Flow fields created by impinging liquid jets and applications in cleaning

Rajesh Kumar Bhagat

Department of Chemical Engineering & Biotechnology
University of Cambridge

This dissertation is submitted for the degree of
Doctor of Philosophy

St John's College, Cambridge
October 2018

I would like to dedicate this thesis to my loving parents . . .

Declaration

I hereby declare that except where specific reference is made to the work of others, the contents of this dissertation are original and have not been submitted in whole or in part for consideration for any other degree or qualification in this, or any other university. This dissertation is my own work and contains nothing which is the outcome of work done in collaboration with others, except as specified in the text and acknowledgements. This dissertation contains fewer than 65000 words including appendices, bibliography, footnotes, tables and equations and has fewer than 150 figures.

Rajesh Kumar Bhagat
October 2018

List of Publications

Published Journal Papers

- Oevermann, D., Bhagat, R.K., Fernandes, R.R. and Wilson*, D.I., 2019. Quantitative modelling of the erosive removal of a thin soil deposit by impinging liquid jets. **Wear**, 422, pp.27-34.

- Bhagat*, R.K., Jha N.K., Linden P.F. and Wilson D.I., 2018. On the origin of the circular hydraulic jump in a thin liquid film. **Journal of Fluid Mechanics**, 851, R5. doi:10.1017/jfm.2018.558

- Chee, M.W.L, Ahuja, T.V, Bhagat, R.K, Taesopapong, N, Wan, S.A, Wigmore, R.L, and Wilson, D.I. 2018. Effect of jet length and surface curvature on cleaning of tank walls. (Manuscript accepted in **Food and Bioproducts Processing**)

- Bhagat, R.K., Perera, A.M. and Wilson*, D.I., 2017. Cleaning vessel walls by moving water jets: Simple models and supporting experiments. **Food and Bioproducts Processing**, 102, pp.31-54.

- Bhagat, R.K. and Wilson*, D.I., 2016. Flow in the thin film created by a coherent turbulent water jet impinging on a vertical wall. **Chemical Engineering Science**, 152, pp.606-623.

- Glover, H.W., Brass, T., Bhagat, R.K., Davidson, J.F., Pratt, L. and Wilson*, D.I., 2016. Cleaning of complex soil layers on vertical walls by fixed and moving impinging liquid jets. **Journal of Food Engineering**, 178, pp.95-109.

Peer reviewed conference papers

- Bhagat*, R.K., Linden P.F. and Wilson D.I. On the origin of the circular hydraulic jump: a differential analysis, **Australian Fluid Mechanics Conference 2018.**

- Bhagat, R.K., Hunter, S.N., Mace F.C.M., Fernandes, R.R., and Wilson* D.I., 2018. Cleaning tanks by impinging liquid jets., **Chemeca 2018.**

Acknowledgements

I would like to thank my supervisor, Prof Ian Wilson for his guidance and support during this work. I conducted some of my research at TU Dresden and I would like to thank Prof Jens-Peter Majschak and Dr Hannes Köhler for this opportunity. I would also like express my gratitude to Prof John Davidson (at CEB) and Prof Paul Linden (at DAMTP); through numerous discussions and their mentorship I have learned a great deal about research and life in general. I am also grateful to the Commonwealth Scholarship Commission and Cambridge Trust for providing the financial support to fund this project.

A big thank must go to the fellow researchers from office M1 and 3.17 for the pleasant and stimulating office environment and the wonderful discussions. I would also like to thank all the IIB and MPhil students that I have worked with. I would also like to thank Mr Lee Pratt and Andy Hubbard from workshop for their help and support. A special thanks to my friend Melissa Chee for her kindness and collaboration. I would also like to thank my friends Aditya Chauhan, Arjun Vijeta, Petar Besevic, Ole Mathis Magens, Romilde Kotzé, Marta Serrani, Eugenia Biral, and Rubens Rosario Fernandes for making my Cambridge experience so pleasant.

In the end, my heartfelt gratitude goes to my family for their love, patient and kindness; it was simply not possible without you. A special thanks to my brother, Sanjoy Bhagat, who has been my teacher and the greatest influence in my life. The acknowledgement will be incomplete without mentioning my sisters; Annapurna, Aparna, Archana and Lili who helped build my character.

Abstract

Title: Flow fields created by impinging liquid jets and applications in cleaning
Name: Rajesh Kumar Bhagat

Cleaning is an essential domestic and industrial operation. It is particularly important in the food and pharmaceuticals sectors, where a large proportion of the total water consumption (as much as 70%) is used just for cleaning. Impinging liquid jets are frequently used for cleaning operations and currently, almost all industrial cleaning systems are based on empirical results. In an effort to develop efficient and sustainable cleaning systems, I have studied the flow field created by impinging liquid jets and their application in cleaning.

On impingement of a liquid jet onto a surface, the liquid spreads radially outwards until it reaches a point where the liquid film changes its thickness abruptly. This transition from a thin film to a thick film is demarcated by a *hydraulic jump*. The supercritical thin film flow is also associated with higher momentum and shear stress, and is therefore, key for cleaning and heat transfer applications. For more than a century, it has been believed that these thin film hydraulic jumps are created due to *gravity*. However, in this dissertation it is shown both experimentally and theoretically, that these hydraulic jumps result from energy losses due to *surface tension* and viscous forces alone and gravity plays no significant role. The new theory allow the size of thin film region (location of the hydraulic jump) to be predicted and manipulated. The location where flow in the thin film becomes turbulent is also considered. The average-velocity and the location demarcating the laminar to turbulent transition were measured and showed good agreement with the model.

The model for cleaning by normally impinging jets (by peeling mechanism) (Wilson et al., 2014) was then extended to consider cleaning by oblique impinging jets and compared with experimental data which showed a good agreement. Finally, cleaning scenarios arising in industrial systems where the liquid jets moves across a soiled surface were modelled. In these scenarios the liquid jet impinges obliquely and moves with varying velocity. A simple mathematical framework was developed for these systems on which more detailed models can build on.

Table of contents

List of figures **xv**

List of tables **xxiii**

1 Background and overview **1**

1.1 Introduction 2

1.1.1 Sinner's circle 4

1.1.2 Cleaning-in-place (CIP) 5

1.2 Overview 7

2 Hydrodynamics of a impinging liquid jet: hydraulic jump **9**

2.1 Introduction 9

2.2 Previous studies 11

2.3 Experimental 13

2.4 Scaling analysis 15

2.5 Theory 17

2.5.1 Force due to surface tension; the normal stress boundary condition 17

2.5.2 Control volume based analysis 20

2.6 Results 22

2.6.1 Effect of surface orientations 22

2.6.2 Effect of fluid properties: surface tension and viscosity 23

2.6.3 Return to scaling 25

2.7 Conclusions 25

3 Energy vs Momentum equation; reconciliation with previous theories **29**

3.1 Introduction 29

3.2 Previous approaches 30

3.3 Theory 33
  3.3.1 Momentum balance 33
  3.3.2 Hydraulic jump/film jump 35
3.4 Results 37
3.5 Conclusions 40

4 Flow field created by impinging liquid jets when liquid film becomes turbulent 41
4.1 Introduction 41
4.2 Model development 44
  4.2.1 Normal impingement of a jet on a vertical surface 45
  4.2.2 Boundary layer formation zone 46
  4.2.3 Laminar film zone (LZ) 50
  4.2.4 Laminar to turbulent transition 51
  4.2.5 Turbulent region (TZ) 53
  4.2.6 Hydraulic jump/ Film jump 54
  4.2.7 Obliquely impinging jet 56
4.3 Experimental 58
4.4 Results and Discussion 60
  4.4.1 Film thickness 60
  4.4.2 Transition radius, r_t 62
  4.4.3 Velocity profile: Perpendicular impingement ($\phi = 90°$) 69
  4.4.4 Oblique impingement ($\phi = 120°$) 71
4.5 Hydraulic jump/Film jump 78
  4.5.1 Horizontal jets impinging perpendicularly 78
  4.5.2 Oblique impingement on a vertical surface 80
  4.5.3 Every man's fluid mechanics 80
  4.5.4 Wall shear stress in the RFZ 83
4.6 Conclusions 85

5 Cleaning by stationary and moving liquid jets 87
5.1 Introduction 87
  5.1.1 Jet dynamics and created liquid film's behaviour 89
  5.1.2 Soil removal 90
  5.1.3 Modelling and optimisation 92
5.2 Experimental 94
5.3 Models 96

5.3.1 Cleaning by static nozzles; full model/intermediate soil model 96
5.3.2 Near field approximation: soils for which the cleaning radius remain small or when $r \sim r_\circ$ 97
5.3.3 Far field approximation; soils for which the cleaning radius is large or when $r \gg r_\circ$ 98
5.3.4 Cleaning by moving nozzle, jet perpendicular to the wall . . . 100
5.4 Cleaning by static nozzle, inclined jets 105
5.5 Cleaning by moving nozzles, inclined jets, moving up or down 107
5.5.1 Case A: D^+/U^- 112
5.5.2 Case B: D^-/U^+ 117
5.5.3 Cleaning by moving nozzles, inclined jets, moving sideways . . 119
5.6 Simple simulations of vessel cleaning 123
5.6.1 Performance indicators 125
5.6.2 Hydraulic energy, E_P 128
5.6.3 Bands: horizontal passes 129
5.6.4 Case Study 130
5.7 Conclusions 134

6 General conclusions and future work 137
6.1 Conclusions 137
6.2 Future work 140

References 143

Appendix A Theory of Hydraulic jumps 149
A.1 Theory 149
A.2 Results and discussion 153
A.3 Conclusions 154

Appendix B Cleaning scenario case study 155

Appendix C Cleaning vessel walls by moving jets: Simple models and supporting experiments 157

List of figures

1.1 Ancient Greek shower (Vase image form Bilder antiken lebens, Hrsg. von Theodor Panofka, 18, 9) Source: http://www.ancientworldalive.com/single-post/2015/10/27/Ancient-Greek-and-Roman-Bathing 1
1.2 Leonardo da vinci's sketches on impact of water jets on a solid surfaces. (Pedretti, 2000) 3
1.3 Leonardo da Vinci's sketch of impact of a water jet on a pool of water 'water in percussion ("in percussione") and in resurgence' ca. 1492. Paris, MS. A, fol.24V 3
1.4 Leonardo da Vinci's sketch about the law of rebound, ca. 1492. Paris, MS. A, fol. 24r 3
1.5 Sinners's circle 5
1.6 CIP operation by a typical Rotary Jet cleaners (Image source: http://www.spray-nozzle.co.uk/resource-links/applications/tank-washing-(cip)/rotary-jet-tank-cleaners) 6

2.1 Hydraulic jumps caused by a water jet impinging normally on surfaces with different orientations. In these three cases the jets are identical, produced from the same nozzle at the same flowrate, $Q = 1\,\mathrm{L\,min^{-1}}$, and the radius of the jump is observed to be independent of the orientation of the surface. 10
2.2 (a) Schematic of the liquid film and hydraulic jump created by an impinging jet. (b) Control volume of film element on which the energy balance is applied. 11
2.3 Schematic of experimental arrangement; liquid jet impinging normally on to a (a) horizontal plate from above, (b) plate inclined at 45°, (c) vertical plate and (d) horizontal plate from below. 14
2.4 Schematic of the experimental setup used for higher Q ($1.3\,\mathrm{L\,min^{-1}} \leq Q \leq 2\,\mathrm{L\,min^{-1}}$) 14

2.5 Dimensionless jump radius plotted against the flow rate for all our experiments with different liquids and surface orientation. 16

2.6 Schematic velocity profiles in a flow with (*a*) 'free surface' and (*b*) a surface with non-zero surface tension γ. The surface tension force retards the flow near the surface giving a non-zero shear stress at the interface (2.4). 18

2.7 Schematic of the differential volume showing the slope of the thin liquid film 19

2.8 Effect of flow rate on jump radius for the four surface orientations. In each case the liquid was pure water. The theoretical prediction (Solid locus) is obtained from setting $g = 0$ (Equation 2.20). 23

2.9 Effect of flow rate on initial jump radius for normal impingement on a horizontal plate from above, for water, water-propanol (WP95/5) and SDBS at $20°C$. Curves are the predictions obtained from solutions of (2.20). The predictions lie within the uncertainty in the experimental measurements. 24

2.10 Measured water bell departure radius, from Jameson et al. (2010), alongside predictions (curves), obtained by solving (2.20) with $g = 0$. The liquids were water-glycerol mixtures WG30/70 and WG10/90. . 24

3.1 Control volume of the film element on which the momentum balance was applied 33

3.2 Schematic, not to scale, showing a cross section of the RFZ and rope in a vertical plate. 36

3.3 Comparison of average velocities obtained from the solution of equation 2.20 and equation 3.9 (Wilson et al. (2012)). 37

3.4 Comparison of the radial distribution of the momentum per unit width, M. Dashed curve show the prediction using Wilson et al. (2012) whereas the solid curve show prediction from the present study. 38

3.5 Comparison of estimated wall shear stress distributions. Dashed curve show the prediction using Wilson et al. (2012) whereas solid curve show prediction from the present study. 39

4.1 Schematic of flow pattern formed by a jet impinging normally on a vertical wall. (*a*) side view through section BB' (*b*) front view. O is the point of impingement, U_o is the jet velocity and d is the jet diameter. 43

4.2 Schematic of cross-section through the radial flow zone and the film jump at $\theta = 90°$ (isometric sectioned view). The different flow zones are: (1) stagnation region; (2) boundary layer formation, shown by dashed line; (3) boundary layer reaches the surface and laminar flow zone starts; (4) laminar to turbulent transition; (5) film jump; (6) rope. O is the point of impingement. 45
4.3 Comparison between equation 4.22, linear, parabolic, cubic velocity profile with the data extracted from experimental velocity profile reported by Stevens and Webb (1993). Different symbols indicates separate data sets with different film thickness 49
4.4 Photograph shows the flow in the RFZ and rope: photograph on glass wall ($Re = 22,200$, $\phi = 90°$, nozzle diameter 2 mm) 55
4.5 Schematics of a liquid jet impinging obliquely on a vertical wall. S is the source point from where liquid spread out radially and O is the point of impingement passing through the center line of the jet 57
4.6 Schematic of the test rig used to study the initial stages of RFZ formation. Labels: P1, P2 – pressure sensors; T – temperature sensor; K – conductivity sensor; FCV – flow control valve) 59
4.7 Comparison of liquid film thickness in the RFZ measured by Stevens and Webb (1993) with the model for the boundary layer zone, equation 4.24. (a) $Re = 53100$, $d = 10.9$ mm; (b) Two different jets were used, with (i) $Re = 37000$, $d = 23$ mm and (ii)$Re = 36100$, $d = 14$ mm. The test liquid was water at room temperature. 61
4.8 Laminar-turbulent transition radius. Comparison of (a) this work with existing correlations: (b) experimental observations of the critical radius for wave breakup alongside the model predictions, equation 4.40. The error bars are standard deviation of measured transition radius. 63
4.9 Photographs of the RFZ and draining films obtained with perpendicular impinging jets, $d = 2.667$ mm and (a) $Re = 15500$ and (b) $Re = 28000$. Dashed line – this work ($d = 2.87$ mm), solid line – this work ($d = 2.67$ mm), equation 4.40; dotted line – Liu et al. (1991) correlation, equation 4.61. 65

4.10 Effect of radial location on local Nusselt number for water jets impinging on a heated surface. Data reproduced from Liu et al. (1991), forRe = (a) 83500, (b) 85500, (c) 48400, (d) 64300, and (e) 71100. Connecting lines between data points are to guide the eye. The vertical dashed lines show the location of $\frac{r_t}{d}$ predicted by equation 4.40. . . . 67

4.11 Time series images of cleaning of Xanthan gum by a impinging water jet. A circular disk and a ring of cleaned region appear near the point of impingement and at a certain radial location in the RFZ, respectively. The experimental images were modified with a false colour to show cleaned regions clearly. These images were extracted from a video provided by Dr. Hannes Köhler from the Technical University of Dresden (TUD). 68

4.12 Cleaning ring radius plotted against jet Reynolds number for cleaning of Xanthan gum coated horizontal plate by a vertical water jet. The curve is the prediction of the laminar to turbulent transition radius, r_t for the respective Reynolds numbers. In the experiments the Re was manipulated by changing both jet diameter and the liquid flow rate. Dr. Hannes Köhler provided the data. 69

4.13 Comparison of experimental estimates of the average velocity $\bar{u}$ obtained from video analysis of the formation of the RFZ with the present model. Vertical glass plate, nozzle diameter 2.67 mm , $Q =$ (a) $1.95\,\mathrm{L\,min^{-1}}$, (b) $2.49\,\mathrm{L\,min^{-1}}$, (c) $3.01\,\mathrm{L\,min^{-1}}$, (d) $3.51\,\mathrm{L\,min^{-1}}$, and (e) $4.01\,\mathrm{L\,min^{-1}}$. 73

4.14 Comparison of estimated average velocity with model predictions for an obliquely impinging water jet ($\phi = 120°$) on a vertical Perspex$^{\mathrm{TM}}$ plate, $d_N = 2.667\,\mathrm{mm}$, for Q = (a) (a) $1.99\,\mathrm{L\,min^{-1}}$, (b) (a) $2.52\,\mathrm{L\,min^{-1}}$; (c) (a) $3.05\,\mathrm{L\,min^{-1}}$; (d) (a) $4.01\,\mathrm{L\,min^{-1}}$; (1) ($\theta = 0°$), (2) ($\theta = 180°$). 77

4.15 Effect of flow rate on the location of film jump for a jet impinging perpendicularly on a vertical surface at $\theta = 90°$. Comparison of measured values and the model, equation 4.51 for $Q = 1.95 - 4.01\,\mathrm{L\,min^{-1}}$, $d_N = 2.667\,\mathrm{mm}$ 79

4.16 Location of the film jump for a jet impinging obliquely on a vertical surface. Comparison of measured and predicted values of R at$\theta = 0°$ and 90°°. Predictions are presented for the turbulent film model presented in this chapter and that of Wang et al. (2013b). $Q = 1.95 - 4.01\,\mathrm{L\,min^{-1}}$, $d = 2.667\,\mathrm{mm}$: angle of impingement $\phi = 100°$ and 120°. 81
4.17 Location of film jump at $\theta = 0°$ and 90° for $Q = 1$,1.2 ,1.4 $\mathrm{L\,min^{-1}}$ and notional angles of impingement 40°, 50° and 60° (equation 4.50). Data taken from Hodgson and Smith (2014). Liquid temperature 37 °C, $d = 2\,\mathrm{mm}$ and $Re = 10600, 12700,$ and 14900. Loci show predictions from this work. 82
4.18 Comparison of the estimated wall shear stress distributions for a jet with $d = 2\,\mathrm{mm}$, $Re = 21000$, flow rate, $Q =$, $2\,\mathrm{L\,min^{-1}}$, $\theta = 90°$ . . . 85

5.1 Schematic of jet cleaning in a cylindrical vessel. O is the point of jet impingement and RFZ is the region of fast moving radial flow. The shaded region represents area wetted by the liquid, with sketch of flow pattern on wall on right. 89
5.2 Schematic of cleaning mechanisms (a) Peeling: Adhesion of soil to the substrate is weaker than cohesive interactions in the soil: the soil detaches as a layer. Promoted by surfactant ingress to the soil/substrate interface. (b) Roll-up: Cohesion within the soil is strong and the soil is insoluble in the cleaning solution. The soil is deformed by fluid flow and/or buoyancy forces, causing it to leave the substrate, which can be enhanced by surfactants. (c) Erosion: Cohesive interactions within the soil are weaker than adhesion to the substrate: shear at the interface removes material. Promoted by agents that weaken the soil. (d) Dissolution: The soil is soluble in the cleaning solution: cohesive interactions within the soil are less favourable than those with the solution. Favoured by thermodynamic factors such as temperature, pH and solvent nature. 91
5.3 Schematic of jet moving downwards with a velocity V and cleaning a vertical wall. O is the point of jet impingement and OP is the point where cleaning strip meet the hydraulic jump. 93
5.4 Picture of the slider or the coater 95

5.5 Predicted evolution of the size of the cleaned region for a coherent water jet impinging perpendicularly on a flat wall (no gravity effects). The results are presented in dimensionless form; $a/r_\circ$ and $t/t_\circ$, where $t_\circ$ is the characteristic time defined as $t_\circ = r_\circ^2/\sigma$. Inset shows initial behaviour. Thin loci show predictions based on the Wilson et al. (2012) flow model: dashed line - near field, equation 5.10; dot-dash line - far field, equation 5.14 ; continuous line - intermediate case, equation 5.6. The heavy locus is the prediction obtained using the numerical model presented in § 4 and Bhagat and Wilson (2016) to calculate M for a water jet at $20°C$ with $r_\circ = 1\,\mathrm{mm}$ and $Re = 22,200$. The discontinuity at F is associated with the transition to turbulence in the film. 100

5.6 (a) Photograph, and (b) model schematic for the region cleaned by a vertical water jet moving from left to right across a plate coated with petroleum jelly. O is the point of impingement and R the radius of the RFZ. 101

5.7 Vector diagram for cleaning front at point P in figure 5.6. Vector PB represents the rate of cleaning along the radial direction and its magnitude taken to be ξ/p^4. Vector PA is the direction of net motion of the interface due to the cleaning and the motion of the nozzle or the target. Here V is the speed of the nozzle or the speed of the target plate. 102

5.8 Predicted shape of cleaning front obtained by integrating equation 5.22. Locus plotted in Cartesian co-ordinates, relative to the point of impingement O (see figure 5.6). Superimposed on the locus are data sets obtained from interrupted experiments, scaled using equation 5.23 to identify a_x from w_c. Data taken from Wilson et al. (2015): Xanthan gum soil cleaned by water at approximately 20°. Conditions: $\Delta P = 1.5$ bar, $V = 10.5\,\mathrm{mm\,s^{-1}}$, $d_N = 1.69\,\mathrm{mm}$. Flow stopped after (A) 30 cm travel, $m_\circ = 1.16\,\mathrm{mg\,cm^{-2}}$; (B) 10 cm travel, $m_\circ = 1.38\,\mathrm{mg\,cm^{-2}}$. Dotted circle shows locus of a circle of radius a_x. Dashed line – numerical solution of Wilson et al. (2015); solid locus – far field case, equation 5.23; dot-dash locus – near field case, equation 5.27. Note that the axes are normalised: a_x for a far field will be larger than a_x for a near field. Figure reproduced from Bhagat et al. (2017). 104

5.9 Evolution of size of cleared region in petroleum jelly layers (see Table 5.1) generated by a water jet ($r_o = 1\,\mathrm{mm}, Q = 2\,\mathrm{L\,min^{-1}}, Re = 21,800$) impinging at angles indicated, plotted in the form suggested by equation 5.33. 108
5.10 Effect of angle of impingement on cleaning rate constant 2σ for petroleum jelly on glass, including the values extracted from the plots in figure 5.9. 109
5.11 Cleaning of PVA layers on glass by water jet impinging at 45°; value of θ given on plots. Data plotted in the form of the near field result, equation 5.33. Layer thickness 33 µm, $Q = 3\,\mathrm{L\,min^{-1}}$, $Re = 32,700$ and $r_\circ = 1\,\mathrm{mm}$. 109
5.12 Effect of flow rate on cleaning rate constant for water jet impinging on PVA layers at an angle of 45°. The data include the values extracted from the plots in figure 5.11. Solid line shows line of best fit to equation 5.33 used to estimate k'. 110
5.13 Schematic of a flow scenario created by a moving water jet inside a tank. The nozzle N rotating in a vertical plane and the point of impingement moving vertically down the wall of a cylindrical vessel of diameter D. ZZ' is the cylindrical axis of symmetry. 111
5.14 Schematics of cleaning by liquid jets impinging moving up or down a wall, above and below the nozzle plane (NH on figure 5.13). D and U refer to the direction of travel of the impingement point O. $V > 0$ or when the jet moves upwards is indicated by U and $V < 0$ is indicated by D. Similarly + and − indicates whether jet is impinging in upward or downward direction or $h > 0$ is referred by + and vice-verse. The two basic flow scenarios arising are when transverse nozzle velocity vector V and a vector along the direction of the jet forms an acute angle D^-/U^+ or obtuse angle D^+/U^- 112
5.15 Schematics of the magnified footprint of an obliquely impinging jet. In relation to relative motion of the nozzle and jet axis, this flow configuration correspond to D^+/U^- 113
5.16 Predicted shapes of cleaning fronts for different angles of impingement, ϕ, for Case A, D^+, U^-(see figure 5.14). Inset shows trend at large $x*$. Dimensionless Cartesian coordinates, $x* = x/a_{x,\phi}$; $y* = y/a_{x,\phi}$. 115
5.17 Effect of angle of jet impingement on dimensionless width of strip cleared by a moving nozzle. 116

5.18 Effect of jet impingement angle on width functions F_V (equation 5.43) and F_ω (equation 5.44) 117
5.19 Predicted shapes of cleaning fronts for different angles of impingement, ϕ, for Case B, D^-, U^+ (see figure 5.14). Dimensionless Cartesian coordinates, $x* = x/a_{x,\phi}$; $y* = y/a_{x,\phi}$. 119
5.20 Model geometry for liquid jet impinging obliquely while nozzle moves normal to the direction of the flow of the liquid jet. 120
5.21 Effect of angle of inclination on the shape of region cleared by nozzle moving normal to liquid jet direction for (a) $\phi \leq 90°$ (b)$\phi \geq 90°$. O is the point of impingement. 121
5.22 Ratio of the width of the cleared region for an inclined jet to that of a perpendicular jet ($\phi = 90°$), for a nozzle moving sideways. Solid line $\breve{}$ polynomial fit,$W^* = 0.0712\phi^6 - 0.6715\Phi^5 + 2.6855\phi^4 - 5.8263\phi^3 + 7.6681\phi^2 - 6.242\phi + 3.4682$, where ϕ is in radians; dashed line, $W^* = \text{cosec}^(3/4)\phi$. Figure reproduced from Bhagat et al. (2017) 122
5.23 Schematic of vessel cleaning pathway (a) vertical strips; (b) geometry; (c) horizontal bands. Figure reproduced from Bhagat et al. (2017) . . 124
5.24 Cleaning by strips: effect of nozzle motion programme on time to clean a cylindrical vessel with hemispherical ends of diameter D and height ΞD with $\Xi = 2, 3, 4$ and 5; w_c at the nozzle plane $= D/20$. $t_{F,ref}$ is the shortest time in the set, obtained here with $L/D = 2$, $q = 1$ and constant w_c. Line pattern indicates motion programme. Each locus is plotted up to $q = \Xi/2$. Figure reproduced from Bhagat et al. (2017) 129
5.25 Cleaning by bands: effect of cleared width at nozzle plane. ϖ is the number of rotations (bands), starting with $\varpi = 1$ at the nozzle plane, and h is the height of the cleared region. Inset shows data presented in scaled form, $h/w_{c,90}$, with logarithmic scale on ordinate axis. Figure reproduced from Bhagat et al. (2017) 130

A.1 Control volume of the differential annular volume of the liquid 151
A.2 Comparison of theoretical prediction obtained using solution of (A.18) (red line) with the experimental results presented in § 2. The dashed line shows the solution of 2.20. 153

List of tables

1.1 Typical water use for cleaning in the food sector (Environmental Technology Best Practice Programme, 1998) 2

2.1 Properties of the liquids used in hydraulic jump tests 15

4.1 Effective angle of impingement for jets inclined at $\phi = 90°$ and 120° as a result of travel across the 200 mm distance between the nozzle and target. 60
4.2 Summary of the effective angle of impingement for $\phi = 40°$, 50°, and 60° with 105 mm distance between the nozzle and target. 82

5.1 Experimental setting for cleaning of petroleum jelly by water jet . . . 106
5.2 Expressions for cycle time for cleaning a vertical cylindrical vessel by successive vertical passes 127
5.3 Case study parameters 131
5.4 Case study performance indicators 133

Nomenclature

Acronyms

Symbols	**Description**
$BLFZ$	Boundary layer formation zone
LZ	Laminar zone
TZ	Turbulent zone
PJ	petroleum jelly
PVA	Polyvinyl acetate
RFZ	Radial flow zone

Dimensionless Numbers

Symbol	**Description**	**Definition**
Re	Reynolds number	$\frac{\rho U_o d}{\mu}$
Re_F	Reynolds number based on film thickness	$\frac{uh}{\nu}$
We	Weber number	$\frac{\rho U_o d}{\mu}$
Nu	Nusselt number	

Greek Symbols

Symbol	**Description**	**Units**
α	Angle between the thin liquid film and the horizontal	

β	Contact angle	degree
χ	Angle to direction of nozzle motion	degree
δ	Boundary layer thickness	m
η	Dimensionless distance normal to the wall	-
η_w	Efficiency of the pump	
γ	Surface tension	$\mathrm{N\,m^{-1}}$
κ	ratio of film thickness to jump radius $\frac{h}{R}$	-
μ	Dynamic viscosity	$\mathrm{kg\,m^{-1}\,s^{-1}}$
ν	Kinematic viscosity	$\mathrm{m^2\,s^{-1}}$
Ω	Angular velocity of nozzle rotation, circumferential	$\mathrm{rad\,s^{-1}}$
Φ	Angle of nozzle inclination	-
ϕ	Angle of inclination of jet to substrate	-
ρ	Density	$\mathrm{kg\,m^{-3}}$
ρ_{pj}	Density of petroleum jelly	$\mathrm{kg\,m^{-3}}$
σ	Cleaning rate parameter	$\mathrm{m^2\,s^{-1}}$
$\sum$	Height of the tank	m
τ_w	Wall shear stress	
θ	Azimuthal angle	-
Ξ	Ratio of vessel wall height to tank diameter	-
ξ	Cleaning rate parameter	$\mathrm{m^5/s}$
π	$\simeq 3.14\ldots$	

Roman Symbols

Symbol	**Description**	**Units**

$\bar{u}$	Average radial velocity	$\mathrm{m\,s^{-1}}$
a	Radial location of cleaning front	m
a^*	Dimensionless cleaning front location	$-$
a_i	Radius when cleaning front is first seen	m
a_x	Distance to cleaning front on jet path	m
A_{pj}	Area of petroleum jelly layer	$\mathrm{m^2}$
$a_{x,\phi}$	distance to cleaning front on jet path, inclination angle ϕ	m
C_D	Nozzle discharge coefficient	$-$
D	Tank diameter	m
d	Jet diameter	m
d_N	Nozzle throat diameter	m
E	Mechanical energy flux per unit width	$\mathrm{kg\,m\,s^{-3}}$
E_p	Pumping energy consumed in cleaning vessel	J
F_ω	Width function, constant ω case	-
F_V	Width function, constant V case	-
g	gravitational acceleration	$\mathrm{m\,s^{-2}}$
H	Liquid film thickness beyond hydraulic jump	m
h	Liquid film thickness	m
K	Lumped parameter	$\mathrm{m^5/s}$
k'	Lumped cleaning rate constant	$\mathrm{m\,s\,kg^{-1}}$
L	Height of the tank	m
M	Momentum flow per unit width	$\mathrm{N\,m}$

M_θ	Momentum flow per unit width along θ streamline	$\mathrm{N\,m}$
N	Number of cycles to clean wall	-
p	Pressure	Pa
Q	Volumetric flow rate	$\mathrm{L\,min^{-1}}$
q	Ratio of nozzle's height	–
R	Hydraulic jump radius	m
r	Radial co-ordinate	m
r_+	Radius where boundary layer is fully developed, equation 4.64	m
$R_\circ$	Scaling jump radius used	m
$r_\circ$	Jet radius	m
r_b	Radius where boundary layer reaches the free surface	mm
r_e	Radial distance from the focus to the boundary of the elliptical projection on an oblique jet	m
r_t	Radius where laminar film becomes turbulent	mm
t	Time	s
t_F	Cleaning time	s
t_{cycle}	Time to complete one cleaning cycle time	s
t_{pj}	Thickness of the petroleum jelly layer	mm
u	Radial velocity	$\mathrm{m\,s^{-1}}$
$U_\circ$	Liquid velocity in the jet	-
u_s	Radial surface velocity	$\mathrm{m\,s^{-1}}$
u_t	Average radial velocity in the film at laminar to turbulent transition radius	$\mathrm{m\,s^{-1}}$

V	Jet velocity/Nozzle's transverse velocity	$\mathrm{m\,s^{-1}}$
Vol	Volume of liquid used	$\mathrm{m^3\,s^{-1}}$
Wt_{after}	Weight of the petroleum jelly layer coated plate	$\mathrm{m^2}$
Wt_{before}	Weight of the plate without petroleum jelly layer	$\mathrm{m^2}$
z	Distance normal to the surface	m

Chapter 1

Background and overview

All early human civilizations started near rivers or near a large source of water. We have always tried to control water and manipulate water flow and by doing so, have discovered hydrology and hydraulic engineering. Tap (or Faucet) producing liquid jets were first used for controlled use of water and beautification in the form of fountains. Subsequently, fueled by their advancement in plumbing and pumping technologies, the ancient Greeks developed the first shower (see figure 1.1) for cleaning and possibly recreational purposes and started the history of cleaning by impinging jets.

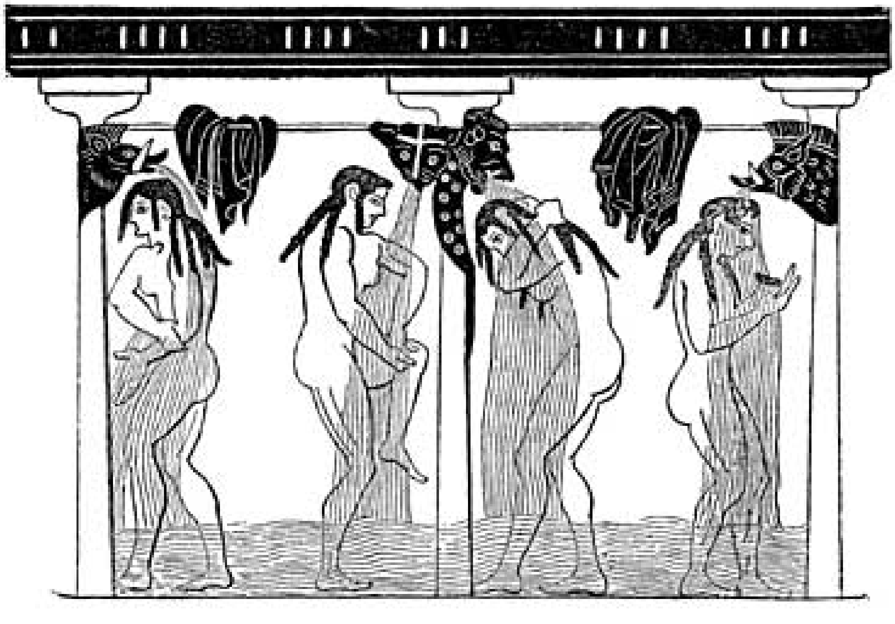

Figure 1.1 Ancient Greek shower (Vase image form Bilder antiken lebens, Hrsg. von Theodor Panofka, 18, 9) Source: http://www.ancientworldalive.com/single-post/2015/10/27/Ancient-Greek-and-Roman-Bathing

An early scientific account of the liquid jet, its impingement on a surface and subsequent flow field including the hydraulic jump can be found in Leonardo da Vinci's sketches and drawings. (see figure 1.2, 1.3 and, 1.4) (Pedretti, 2000). From Leonardo da Vinci's sketches and drawings it is clear that he was obsessed with water. He was fascinated by virtually everything but he studied and tried to understand fluid flow from his youth until his death (Irving, 2018).

The applications of impinging jet, a technology which the ancient Greeks developed, and problem that was discussed by da Vinci and many others since, are still based on empirical results and are inefficient. The main reason for this stagnation is that, we considered water as an unlimited natural resource and this robust ancient technology works. However, with the growing world population, human activities and climate change, water is no longer an unlimited natural resource. Its use for industrial and domestic applications is now subject to availability constraints and ultimately sustainability considerations.

1.1 Introduction

A recent report suggests that in England and Wales, in an average household, 39% of total water consumption is used for personal washing and 24% in WC flushing (Lawson et al., 2018). An average seven and half minute shower consumes $\approx 67\,\mathrm{L}$ of water (Cambridge Water Company, 2018). A recent water crisis in Cape Town highlighted our vulnerability to water resources and distribution (Muller, 2018), where it can cause serious public health issues and even law-and-order problems. High speed impinging jets are frequently used for industrial cleaning. In food and pharmaceutical industries, a large proportion of their total water use is consumed in cleaning operations. In some of the food and drink sectors, cleaning accounts for as much as 70% (dairy sector Ajiero and Campbell (2018)) of the total water use. Table 1.1 presents an overview of the percentage of total water used just for cleaning.

Table 1.1 Typical water use for cleaning in the food sector (Environmental Technology Best Practice Programme, 1998)

Sector	Percentage of water used for cleaning
Bakery	70%
Dairy	70%
Soft drinks	48%
Brewery	45%

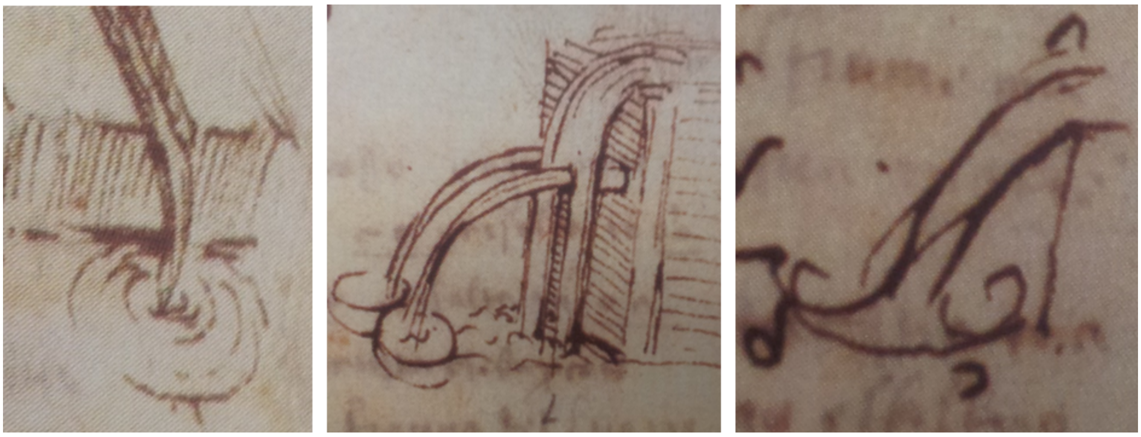

Figure 1.2 Leonardo da vinci's sketches on impact of water jets on a solid surfaces. (Pedretti, 2000)

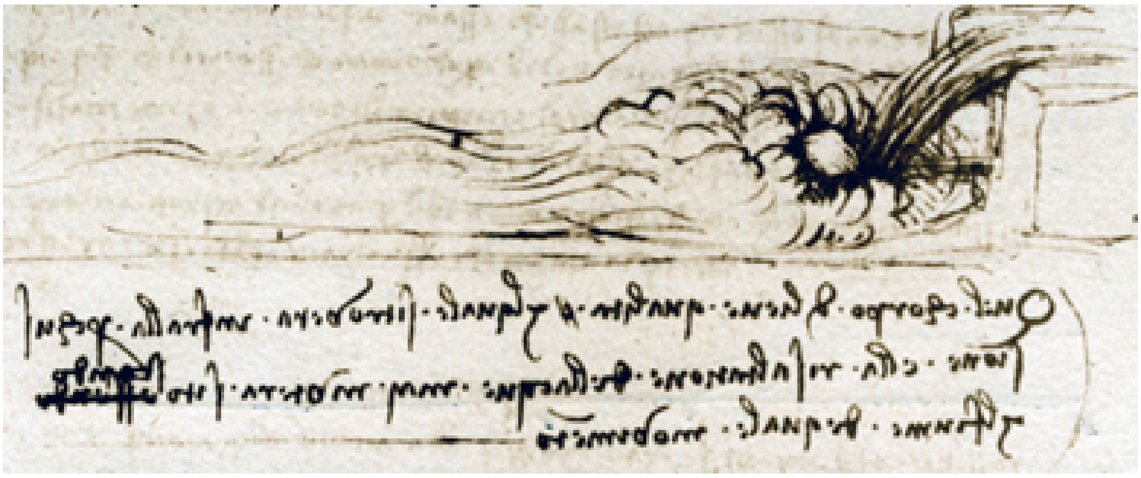

Figure 1.3 Leonardo da Vinci's sketch of impact of a water jet on a pool of water 'water in percussion ("in percussione") and in resurgence' ca. 1492. Paris, MS. A, fol.24V

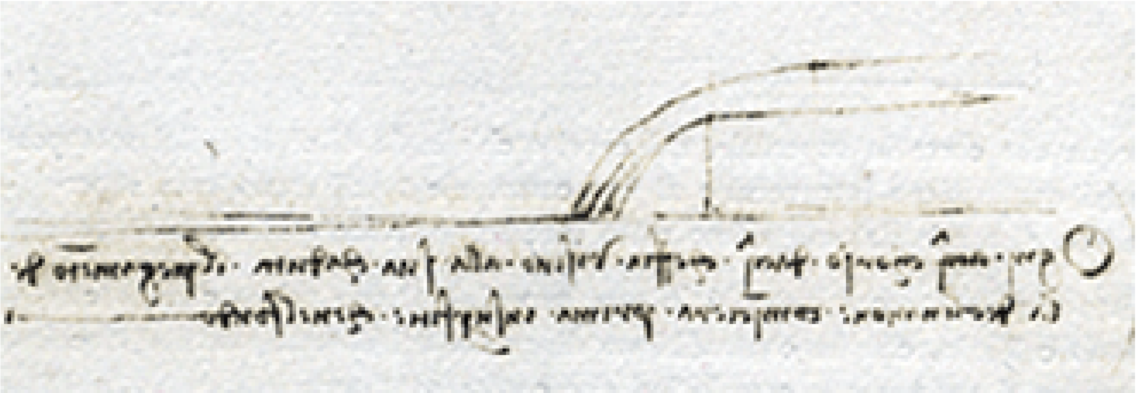

Figure 1.4 Leonardo da Vinci's sketch about the law of rebound, ca. 1492. Paris, MS. A, fol. 24r

Every litre of processed milk requires between 1-10 L of clean water. In the financial year 2014, the total milk production in the UK was $\approx$ 14 million tonnes (Alex, 2016), which implies that total water used for cleaning in the dairy industry in the UK range between 1 to 10 billion L. This comes with an associated cost, both for supply and treatment of the spent water. In areas where water is scarce, such operations are simply not feasible.

Clean water is one of the key resources in the food-water-energy nexus. Prioritisation of clean water to combat thirst means that industry needs to reduce its consumption levels to achieve sustainable operations. The use of water jetting represents a technology which can improve cleaning efficiency while reducing water consumption.

This dissertation aims to understand industrial cleaning using impinging liquid jets. There are two aspects to this problem (1) understanding the hydrodynamics of impinging liquid jets, and (2) its application to industrial cleaning scenarios. The studies therefore set out to understand the hydrodynamics of the impinging liquid jets which is discussed in § 2, 3, and 4. Chapter 5 presents experimental and theoretical studies for industrial cleaning scenarios where liquid jets remain stationary or move and clean surfaces. The conclusions and future work are given in § 6.

1.1.1 Sinner's circle

The main objectives of industrial cleaning systems are speed (cleaning time), efficiency, cost effectiveness, and sustainability. The rules of thumb underlying cleaning activities is expressed as " **Sinner's Circle**" (see figure 1.5). The key variables of Sinner's circle are; (1) Mechanical action, (2) Chemical action, (3) Temperature, and (4) Time. Their cumulative response determine the degree of cleaning *i.e.* higher temperature usually results in more effective cleaning. Likewise for a set degree of cleaning enhancing one aspect reduces other. The application of high speed impinging liquid jets in cleaning produces high shear stress, momentum transfer and hence faster cleaning rates. In Sinner's circle, impinging liquid jets are associated with mechanical action and reduced time. This dissertation focuses mainly on understanding the flow field of impinging liquid jets and their application to cleaning. Sinner's circle is revisited in § 5.

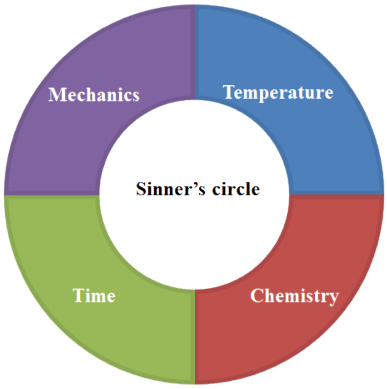

Figure 1.5 Sinners's circle

1.1.2 Cleaning-in-place (CIP)

Cleaning in place (CIP) can be defined as the cleaning of internal or external surfaces of process equipment, pipelines *etc.* without dismantling the equipment, with little or no manual labour. To achieve this objective, high speed liquid jets are directed onto surfaces or cleaning solutions are circulated at higher speed under the turbulent flow conditions (Romney, 1990; Tamime, 2009). CIP systems generally employ spray balls or rotating nozzle(s) ejecting liquid jets (see figure 1.6), which move across the surface and cleans it.

From the perspective of modelling and optimisation, CIP systems with rotating nozzles have three key overlapping elements: (1) hydrodynamics and the flow field of a moving impinging liquid jets, (2) cleaning mechanisms and, (3) geometrical aspects of a moving liquid jet. Considering the complexities of the problem, it is not surprising why design and operation of available CIP systems are currently largely based on empirical relationships. The approach to develop a mathematical framework for modelling of CIP systems is: study the above stated key elements in isolation and couple them to the other elements in stages and finally integrate and develop the model. For instance, understanding the hydrodynamics of a static liquid jet impinging onto a surface will provide the shear stress, momentum and mixing under the flow field. The understanding can then be coupled to the cleaning mechanism to develop a quantitative model for cleaning under the flow condition. For example, Wilson et al. (2014) coupled the hydrodynamics and removal of a specific soil type (immobile soils) to model cleaning by peeling by an impinging liquid jet. They hypothesized that, for cleaning by peeling, the rate of cleaning is proportional to the momentum in the liquid at the cleaning front. In this case, the momentum was estimated by Wilson et al. (2012) hydrodynamic model to obtain the expression for cleaning kinetics.

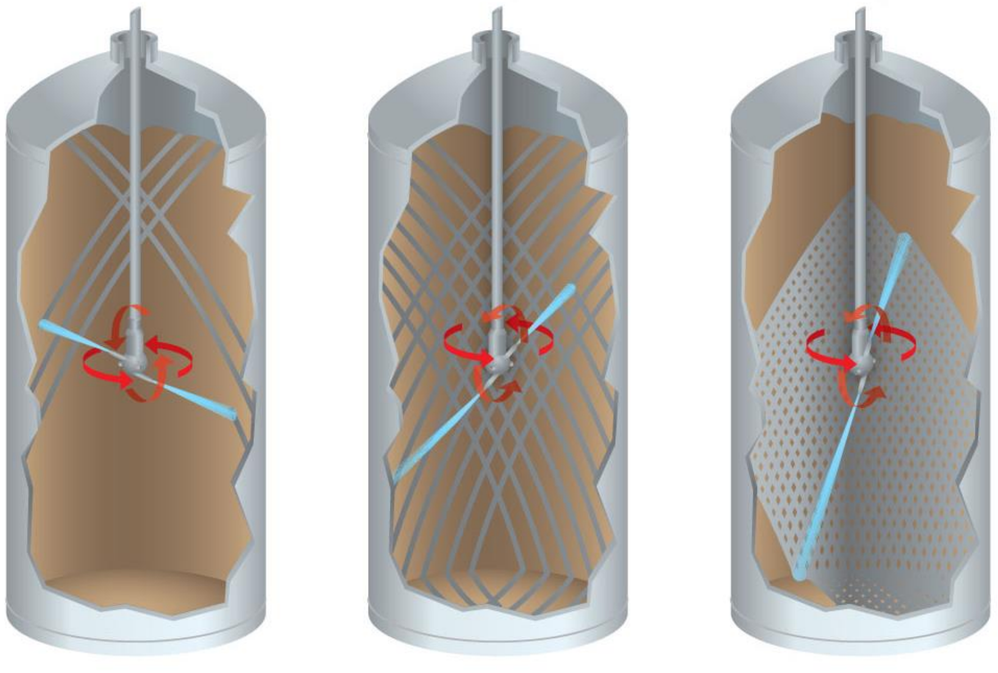

Figure 1.6 CIP operation by a typical Rotary Jet cleaners (Image source: http://www.spray-nozzle.co.uk/resource-links/applications/tank-washing-(cip)/rotary-jet-tank-cleaners)

Wilson et al. (2015) extended this approach with some assumptions, and integrated the static jet cleaning model to moving jet systems, where a liquid jets impinges normally onto the surface and the point of impingement moves steadily across the surface. A better understanding of each key element and their integration into a CIP models offers better understanding of the whole process.

In this dissertation, the main focus is on improving the understanding of the flow field created by impinging liquid jets. I have also worked on developing quantitative relationships for various geometrical scenarios arising in cleaning by static and moving liquid jets. This understanding is coupled with models for cleaning by peeling mechanism. A similar approach could be taken to cleaning by attrition (driven by the local shear stress imposed on a deposit or soil): this is not explored here.

1.2 Overview

The dissertation is divided into four main chapters and a closing chapter with conclusions and recommendation for future work. The chapters do not follow in the chronological order in which the work was conducted. Nevertheless, the adopted modelling strategy in which the key elements could be updated and integrated, allowed the dissertation to be laid in this format and not in the chronological order.

A significant fraction of the chapters from this dissertation have been published; § 2 in the *Journal of Fluid Mechanics* (Bhagat et al., 2018), § 4 in *Chemical Engineering Science* (Bhagat and Wilson, 2016) and § 5 in *Journal of Food and Bioproducts Processing* (Bhagat et al., 2017). I have recorded my coauthor(s)'s contributions in the introduction section of each chapter and, where applicable in the text.

§ 2 discusses the hydrodynamics of an impinging liquid jet and the formation of the hydraulic jumps. In this chapter the mechanical energy equation including surface energy is solved. This chapter provides some new revolutionary insight into the formation of the circular hydraulic jump. Contrary to the previously held view that hydraulic jumps are created due to gravity, it is shown both experimentally and theoretically that the thin film hydraulic jumps (such as in kitchen sinks) are created due to surface tension and gravity does not play significant role. This chapter provides a general mathematical framework which is applicable to all hydraulic jumps, which incorporates the effects of gravity (important for thick film hydraulic jumps, such as occur downstream of a weir, but which is insignificant for thin-film jumps, like those in kitchen sinks). This theory also correctly incorporates the effect of surface tension, which is the dominant effect in thin films. § 2 presents a control volume based analysis; a differential volume based analysis is given in Appendix A, and they show excellent agreement.

Using the mechanical energy based approach,the results from § 2 disapproves the previous momentum based or Navier Stokes equation based approaches of the description of the thin film flow and the hydraulic jump. § 3 revisits the thin film flow from a new momentum based approach and shows agreement with § 2. The the results from § 2 are compared with the Wilson et al. (2012) description of the flow field. It is found that the momentum calculated from both approaches show reasonable agreement and the simple Wilson et al. (2012) model gives a reasonable engineering estimate of the momentum.

§ 4 explores the flow field created by normal and obliquely impinging jets when the thin liquid film becomes turbulent. In this chapter, the flow field is divided into three zones (1) boundary layer formation zone, (2) laminar zone and, (3) turbulent zone. The location demarcating the laminar to turbulent transition is found to be the location where the liquid film thickness is minimum. The transition is then verified by comparison with optical observations, heat transfer and, cleaning data.

§ 5 investigates the cleaning of adherent soil by inclined static and moving liquid jets, where the removal mechanism is peeling. In this chapter, new experimental data and a model for cleaning by obliquely impinging jets are presented and these show good agreement.

Wilson et al. (2015) provided a model for cleaning by normally impinging moving liquid jets. The model is extended for CIP scenarios when the angle of impingement of the jet changes continuously. Models are presented for two different cleaning paths; (1) when the nozzle rotates in a vertical plane and cleans from the top to the bottom or vice-versa, (2) when the nozzle rotates in a horizontal plane following a hoop cleaning track.

The findings are summarised in the § 6, followed by short discussion on avenues for future work.

Chapter 2

Hydrodynamics of a impinging liquid jet: hydraulic jump

2.1 Introduction

It is a common experience to observe that when a jet of water falls vertically from a tap on to the base of a domestic sink, the water spreads radially outwards in a thin film until it reaches a radius where the film thickness increases abruptly. This abrupt change in depth is known as a circular hydraulic jump (see figure 2.1(a)). Beyond the jump, the liquid spreads outward as a thicker film until it reaches the edge of the sink. Up to this point, the hydraulic jump radius remains approximately at the same location (can be seen as Movie 1, https://doi.org/10.1017/jfm.2018.558). Once the liquid reaches the edge of the sink, the boundary condition for the liquid film changes, the downstream liquid film thickness increases and the initial steady hydraulic jump radius moves inwards. The present study explores the steady hydraulic jump before liquid reaches the edge of the plate.

The hydraulic jump has been studied for over four hundred years. An early account was presented by Leonardo de Vinci in the 16th century (Hager (2013)). The Italian mathematician Bidone (1819) published experimental results on the topic and Lord Rayleigh (1914) subsequently provided the first theoretical explanation for the planar hydraulic jump based on inviscid theory.

Figures 2.1(b) and (c), show that the same abrupt change in film thickness occurs on a vertical plane impacted by a horizontal jet and a horizontal plane impacted from below by an upwards directed jet, respectively. Further, as can be seen in figure 2.1, for a given jet diameter and flowrate, the radius of the initial jump is the same in all

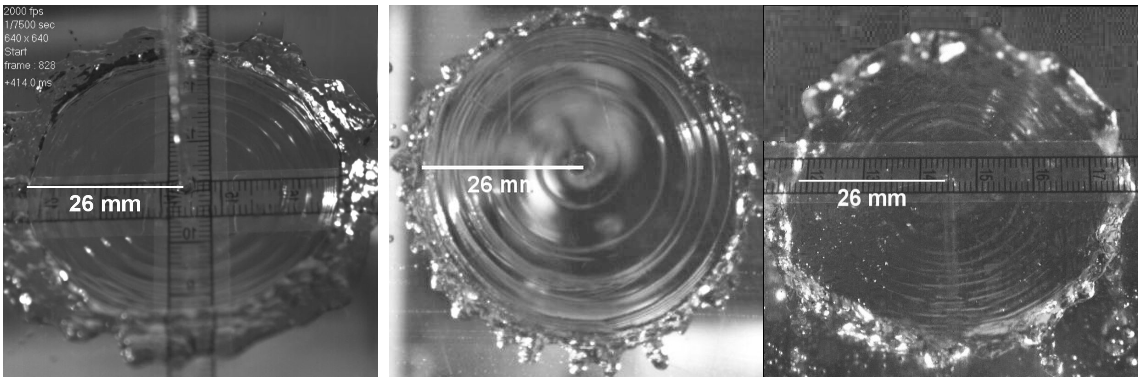

(a) Horizontal surface; jet impinging from above (b) Vertical surface; jet impinging horizontally (c) Horizontal surface; jet impinging from below

Figure 2.1 Hydraulic jumps caused by a water jet impinging normally on surfaces with different orientations. In these three cases the jets are identical, produced from the same nozzle at the same flowrate, $Q = 1\,\mathrm{L\,min^{-1}}$, and the radius of the jump is observed to be independent of the orientation of the surface.

cases, irrespective of the orientation of the surface. From this one can conclude that gravity plays no role in the initial formation of the jump.

To the best of the my knowledge all existing explanations for thin-film hydraulic jumps on the scales under consideration in this chapter, invoke gravity as a significant force in its formation. The work in this chapter demonstrates that this view is incorrect and that the appropriate force balance in these jumps critically involves surface tension and that gravity is unimportant. To achieve this aim the previous theories and experiments are reviewed in § 2.2. The experiments presented in this chapter is described in § 2.3, followed by a scaling analysis in § 2.4, which collapse the experimental data. A detailed theory for the flow is developed in § 2.5. which explains the role of surface tension in the force balance. The theoretical predictions and the experimental data for different surface orientations and fluid properties are compared in § 2.6. Conclusions are reported in § 2.7.

This work has been published in the *Journal of Fluid Mechanics* (Bhagat et al., 2018). I developed the theory, conducted the experiments and analysed the data. My coauthor Dr Narsing Jha helped me perform some circular hydraulic jump experiments. Prof Paul Linden and I developed the scaling relationship. I drafted the manuscript which Prof Linden and I edited. Subsequently, it was also edited by Prof Ian Wilson. Text from the paper appears in this chapter.

2.2 Previous studies

The study presented here concerns with the *initiation* of the jump shown by the schematic in figure 2.2(a), or the hydraulic jump due to impact of a jet normally on an infinite plane. In practice, all experiments involve a plane of finite dimensions and eventually the liquid drains from the edges of the surface. Consequently, the study here is restricted to considerations of the flow before it reaches the edge of the surface, and ignore the changes that occur once the downstream boundary condition changes (The hydraulic jump formation can be seen as Movie 2, https://doi.org/10.1017/jfm.2018.558)

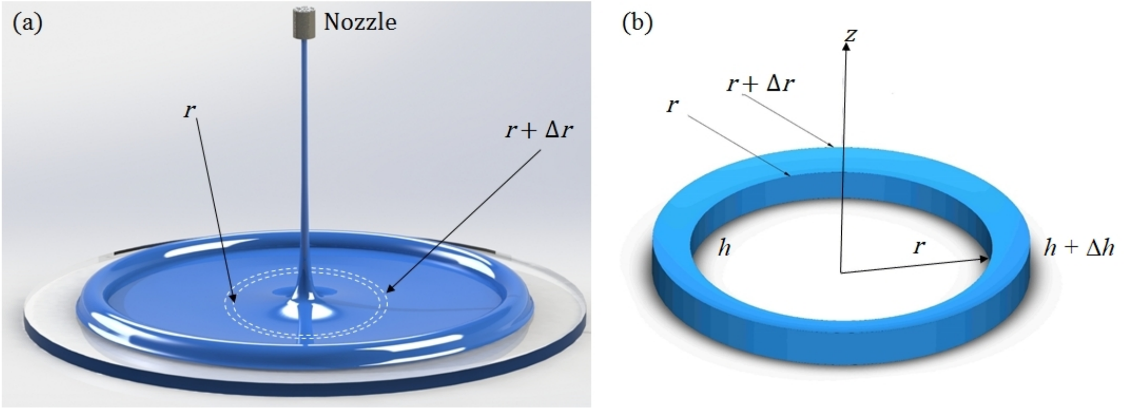

Figure 2.2 (a) Schematic of the liquid film and hydraulic jump created by an impinging jet. (b) Control volume of film element on which the energy balance is applied.

Watson (1964) developed a similarity solution for radial flow in the thin liquid film, which is described further below. He also proposed the first description of a thin-film circular hydraulic jump incorporating viscous friction in the film, ignoring the tangential stress due to surface tension, and balanced the momentum and hydrostatic pressure across the jump. Watson's solution, which involves gravity, requires experimental measurement of the film thickness at the jump location to predict the jump radius, and overpredicts the radius for smaller jumps by as much as 50%. Bush and Aristoff (2003) added surface tension to Watson's theory but stated that its influence was small as they argued its effect was confined to the hoop stress associated with the increase in circumference of the jump. They recognised that addition of surfactant substantially (20%) increased the jump radius but they did not pursue this aspect further, owing to the complications involved with surfactants. Mathur et al. (2007) presented results for hydraulic jumps created by liquid metals where the jump radii were in range of µm. They recognised that jumps on this scale are created due to surface tension but associated with very high curvature and small jump radii. However, they asserted that gravity is the key to all jumps on the scale of the kitchen sink hydraulic jump.

Earlier analyses by Kurihara (1946) and Tani (1949) used thin-film boundary layer equations including gravity to model circular hydraulic jumps. This analysis was critiqued by Bohr et al. (1993) who solved the axisymmetric shallow water equations which again, naturally, included gravity. Bohr et al. (1993) found that the outer solution of the equations became singular at a finite radius. Consequently, they solved the equations inwards from the edge of the plate or the boundary from where liquid drains due to gravity, and connected the inner and the outer solutions for radial flow through a shock. This analysis gave a scaling relation for the jump radius, $R \sim Q^{5/8}\nu^{-3/8}g^{-1/8}$ where Q, ν and g are the jet volumetric flow rate, the kinematic viscosity of the fluid and the acceleration due to gravity, respectively. They argued that the jump could be understood qualitatively in terms of the interplay between gravity, viscosity and the momentum of the liquid. A similar axisymmetric shallow water model was also proposed by Kasimov (2008). Again this study did not consider the initial formation of the jump, but connected the thin film with the deeper flow established as a result of the downstream boundary condition at the edge of the domain.

Two studies considered the case where gravity is unimportant. Godwin (1993) assumed the jet diameter was an important parameter and showed that the jump radius, when independent of gravity, scaled as $R \sim Q^{1/3}d^{2/3}\nu^{-1/3}$, where d is the jet diameter. It can be argued that, since $R \gg d$, the jet diameter is not a relevant parameter which has also been verified experimentally. Avedisian and Zhao (2000) studied the circular hydraulic jump at low gravity in a drop tower. In these experiments, a horizontal plate was submerged in a pool of liquid to impose a constant downstream liquid thickness condition and was impacted by a liquid jet to create a hydraulic jump. They found that, under normal gravity, the jump radius decreased when the depth of the downstream liquid film increased. However, at low gravity, the downstream liquid film height had no effect, and the jump radius increased compared to its value under normal gravity. Capillary waves were also observed, and they concluded that at low gravity the jumps were dominated by viscosity and surface tension.

Hansen et al. (1997) studied surface waves in circular hydraulic jumps. They reported that the hydraulic jump radius scales as $R \propto Q^{0.77}$ for water, and $R \propto Q^{0.72}$ for less viscous oils. They concluded that, on a flat plate without any reflectors, the waves are gravity-capillary waves. Further, in the limit of zero surface tension, Rojas et al. (2013) reported that $R \sim Q^{3/4}\nu^{-1/4}H^{-1/2}g^{-1/4}$, where H is the height of the film downstream of the hydraulic jump.

In the experiments reported in this chapter, it can be observed that, under the same flow conditions, normal impingement of a liquid jet gives a circular hydraulic jump with the same initial radius irrespective of the orientation of the surface (figure 2.1). On a vertical plate, where the spreading liquid film and gravity are coplanar, an approximately circular hydraulic jump is still formed (figure 2.1(b)). The thicker liquid film beyond the hydraulic jump then drains downwards due to gravity and above the point of impingement the location of the jump remains constant in time. The experiments on a surface inclined at 45° also produced circular jumps. A similar lack of dependence of the radius on both vertical and inclined surfaces have also been observed by Wang et al. (2015); Wilson et al. (2012). Similarly, when a jet impinges onto a horizontal surface from below, an abrupt increase in film thickness is also observed (figure 2.1(c)). Under the influence of gravity, the thicker liquid film falls as droplets or as a continuous film forming a water bell (Jameson et al. (2010)). The surface tension of the liquid was changed by preparing homogeneous water-alcohol solutions and a surfactant. A significant change in kitchen sink scale hydraulic jump can be seen by changing the surface tension γ when Q and ν are kept constant (can be seen as Movie 3, https://doi.org/10.1017/jfm.2018.558). The existing treatments are unable to explain this behaviour as they hold that surface tension only becomes significant for much smaller jump radii.

2.3 Experimental

Circular hydraulic jumps were produced by impinging a liquid jet normally on to a planar surface. Both a vertical jet impinging on a horizontal plate from above and below, a horizontal jet impinging on a vertical plate and a jet impinging normally on to a plate inclined at 45° to the horizontal were studied (see figure 2.3). For most experiments the jet nozzle diameter was 2 mm and the jet flow rate Q varied from $0.49 - 2\,\mathrm{L\,min^{-1}}$. For low flow rates ($Q < 1.3\,\mathrm{L\,min^{-1}}$), liquid was supplied from a constant-head apparatus to glass Pasteur pipettes.

Target plates were Perspex$^{\mathrm{TM}}$, glass or Teflon$^{®}$ sheets. The horizontal plate was a 0.25 m diameter circular disk; vertical and inclined planes consisted of a $1 \times 0.4\,\mathrm{m}^2$ rectangular plate. It was found that the jump radius was independent of the plate material and this factor will not consider further. Nozzle diameters of 1 and 3 mm were also used, and no significant difference in the jump radius was observed when measured from the edge of the resulting jet.

For higher flow rates ($Q > 1.3\,\mathrm{L\,min^{-1}}$) a centrifugal pump and a brass nozzle was used (See figure 2.4).

Water was pumped from a 26 L capacity storage tank through a rotameter and a manual control valve before entering the nozzle. The nozzle was fabricated from brass with an orifice diameter of 2 mm. Further details of the setup are given in Wang et al. (2013b). The nozzle could be rotated to give angles of impingement over the range $0 \geq \phi \geq 180°$. In these tests the nozzle was located between 40 to 80 mm from the target so that the jet remained coherent and did not droop. The target was either a transparent Perspex or glass plate.

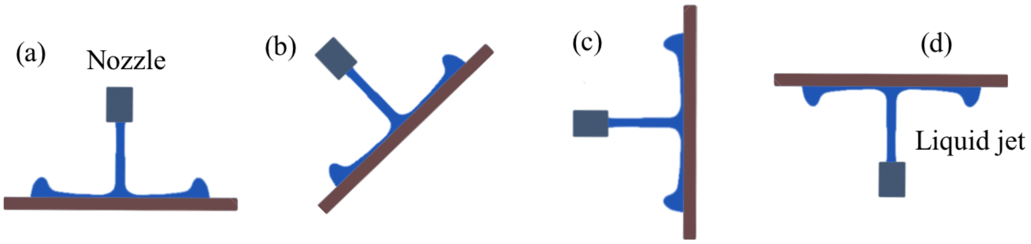
(a)
Nozzle
(b)
(c)
(d)
Liquid jet

Figure 2.3 Schematic of experimental arrangement; liquid jet impinging normally on to a (a) horizontal plate from above, (b) plate inclined at 45°, (c) vertical plate and (d) horizontal plate from below.

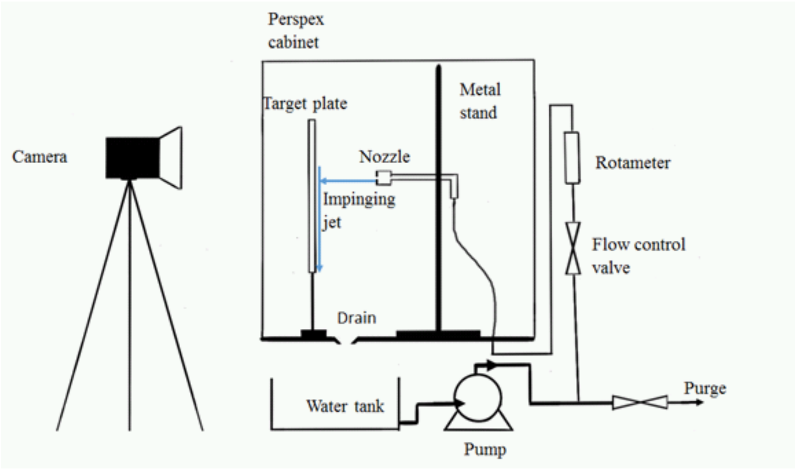
Perspex cabinet
Target plate
Metal stand
Camera
Nozzle
Rotameter
Impinging jet
Flow control valve
Drain
Purge
Water tank
Pump

Figure 2.4 Schematic of the experimental setup used for higher Q ($1.3\,\mathrm{L\,min^{-1}} \leq Q \leq 2\,\mathrm{L\,min^{-1}}$)

Table 2.1 Properties of the liquids used in hydraulic jump tests

Liquid	Reference	T (°C) (°C)	γ ×10^3 ($\mathrm{N\,m^{-1}}$)	ν ×10^6 ($\mathrm{m^2\,s^{-1}}$)	ρ ($\mathrm{kg\,m^{-3}}$)
Water		20	72	1.002	1000
WP95/5	Vazquez et al. (1995)	20	42.5	1.274	989
WP80/20	Vazquez et al. (1995)	20	26	2.30	968
WG30/70	Jameson et al. (2010)	19	67	20.7	1160
WG10/90	Jameson et al. (2010)	28	65	99.3	1240
SDBS	Sun et al. (2014)	20	38	1.00	1000

Transparent graticule tape was mounted on the target to provide in-situ dimension calibration. The experiments performed in this apparatus featured flow rates, with $Q = 1.3 - 2\,\mathrm{L\,min^{-1}}$.

The viscosity and surface tension were varied by using mixtures of water with 1-propanol (5 and 20 w/w%, labelled as WP95/5 and WP80/20, respectively) and water with glycerol (70 and 90 w/w% labelled WG30/70, and WG10/90, respectively). A $3\,\mathrm{mmol\,L^{-1}}$ solution of sodium dodecyl benzene sulfonate (SDBS) was also used. The surface tension was varied by about a factor of three and the kinematic viscosity by a factor of nearly 100. The fluid properties are listed in table 2.1.

An IP65 waterproof fluorescent tube lamp and a halogen lamp illuminated the target. Digital video cameras, Photron Fastcam SA3 and Sony Cyber-Shot DSC-RX100 VA were used to acquire high-speed images of the liquid film and the hydraulic jump at up to 2000 fps. These were subsequently processed using MATLAB and *ImageJ* to obtain the jump radius R as a function of the jet and fluid properties. In total over 150 experiments were conducted. Error bars were determined by the standard deviation of repeated experiments.

2.4 Scaling analysis

Consider the axisymmetric flow shown schematically in figure 2.2. The jump is characterised by its radius R, the liquid film thickness h and the radial velocity u of the film. Based on experimental observations we assert that gravity is unimportant and hence the flow depends on the jet flow rate Q, the jet diameter d, the film thickness h, and the fluid properties i.e. the density ρ, viscosity ν and the surface tension γ. Since observations (e.g. figure 2.1) show that the jump radius $R \gg d$ and we observed no dependence on d, we ignore the jet diameter. We then have six parameters; R, h, ρ, ν, γ and Q (or equivalently u) and three dimensions, giving three dimensionless parameters: a Reynolds number Re, a dimensionless film thickness, κ, and the Weber number, We, given by

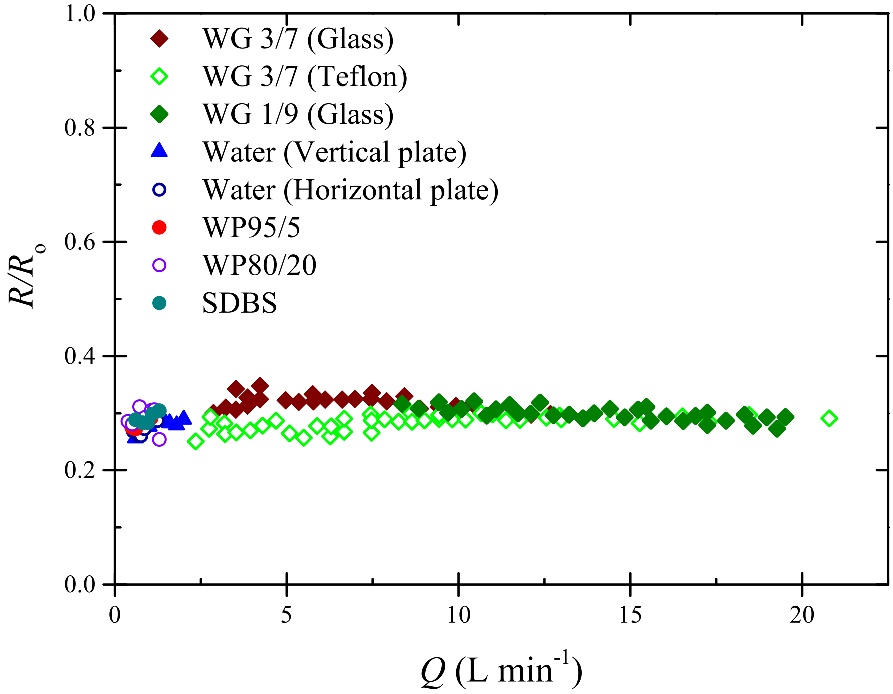

Figure 2.5 Dimensionless jump radius plotted against the flow rate for all our experiments with different liquids and surface orientation.

$$Re = \frac{uh}{\nu}, \quad \kappa = \frac{h}{R}, \quad We = \frac{\rho u^2 h}{\gamma}. \tag{2.1}$$

We assume that the radial flow is balanced by viscous drag, for such flows Watson (1964) showed that $\frac{du}{dr} \propto \frac{-\nu}{h^2}$, which implies

$$\frac{u}{R} \sim \frac{\nu}{h^2} \tag{2.2}$$

Using equation 2.2 and $\kappa = \frac{h}{R}$ implies $\kappa Re_F = \mathcal{O}(1)$, where $Re_F = \frac{uh}{\nu}$, Reynolds number based on the film thickness. Then, if we further assume that the hydraulic jump occurs when momentum equals the surface tension and hence at the jump $We \sim 1$. Now using the fact that continuity implies $Q \sim uhR$, at jump radius $We \sim 1$ and $\frac{u}{R} \sim \frac{\nu}{h^2}$, yields the characteristic length R_0,

$$R_0 = \frac{Q^{\frac{3}{4}}\rho^{\frac{1}{4}}}{\nu^{\frac{1}{4}}\gamma^{\frac{1}{4}}}. \tag{2.3}$$

The measurements of the dimensionless jump radius R/R_0 are plotted against the jet flow rate Q in figure 2.5. This shows that the data from experiments covering the full range of Q, surface material and orientation and fluid properties (table 2.1) all collapse on to the line $\frac{R}{R_0} = 0.289 \pm 0.015$. This collapse of the data, consistent with (equation 2.3), implies that the dominant balance in the formation of thin-film jumps is associated with surface tension and viscous drag, and that gravity is irrelevant. In the next section § 2.5, a more quantitative estimate of the jump radius is developed on the underlying equations of motion.

2.5 Theory

2.5.1 Force due to surface tension; the normal stress boundary condition

Fluid motion is governed by the Navier-Stokes equations which express conservation of momentum in a fluid continuum. For flows with an interface between two fluids, the Navier-Stokes equations or energy equation in differential form do not express the surface tension force acting on the interface. This force is introduced as a normal stress boundary condition at the interface.

Consider a surface S with unit normal $\mathbf{n}$, bounded by a closed contour C with arc length $\mathbf{l}$ in the interface between two immiscible fluids, taken here to be the common case of a liquid and a gas denoted by the subscripts L and G, respectively, with constant surface tension γ. Since the surface tension force acts in a direction perpendicular $\mathbf{n}$ and the contour C, continuity of the normal stress is expressed as

$$\int\limits_S (\mathbf{T}_G - \mathbf{T}_L) \cdot \mathbf{n} dS + \gamma \int\limits_C d\mathbf{l} \times \mathbf{n} \;\; = \;\; 0, \tag{2.4}$$

where $= -p\mathbf{I} + \mu[\nabla\mathbf{u} + (\nabla\mathbf{u})^T]$ is the total stress, with pressure p and velocity $\mathbf{u}$, and μ is the viscosity of the fluid. Using a vector identity and noting that S is an arbitrary surface this gives the dynamic boundary condition

$$(\mathbf{T}_G - \mathbf{T}_L) \cdot \mathbf{n} \;\; = \;\; -\gamma(\nabla_s \cdot \mathbf{n})\mathbf{n}, \tag{2.5}$$

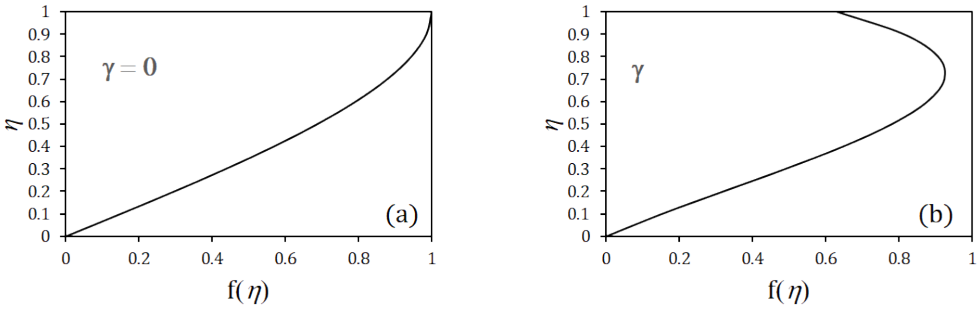

Figure 2.6 Schematic velocity profiles in a flow with (*a*) 'free surface' and (*b*) a surface with non-zero surface tension γ. The surface tension force retards the flow near the surface giving a non-zero shear stress at the interface (2.4).

where $\nabla_s = [\mathbf{I} - \mathbf{nn}].\nabla$ is the surface gradient, relating the jump in the normal stress to the curvature of the surface.

Assuming the *dynamic* viscosity of the air is negligible compared to that of the liquid and denoting pressure in the air as p_G and in the liquid as p_L, (2.4) can be written as

$$\int_S (-p_G + p_L)\mathbf{n} dS + \mu \int_S \mathbf{n}.[\nabla\mathbf{u} + (\nabla\mathbf{u})^T] dS + \gamma \int_C d\mathbf{l} \times \mathbf{n} = 0, \tag{2.6}$$

where $\mathbf{u}$ is the velocity in the liquid.

In the case of a stationary liquid and gas, the middle term of (2.6) is zero and this equation gives the usual Laplace pressure in the liquid associated with the curvature of the surface. In the case of a flowing liquid the surface tension force can be balanced by the viscous stresses at the surface, and for a sufficiently fast flow this can be much larger than the Laplace pressure. This force balance manifests itself through a non-zero velocity shear at the surface as shown in figure 2.6.

Force on an axisymmetric thin film

Following Bush and Aristoff (2003) for an axisymmetric thin film on a planar surface we write the equation of the surface in implicit form

$$J(r, z) = z - h(r) = 0, \tag{2.7}$$

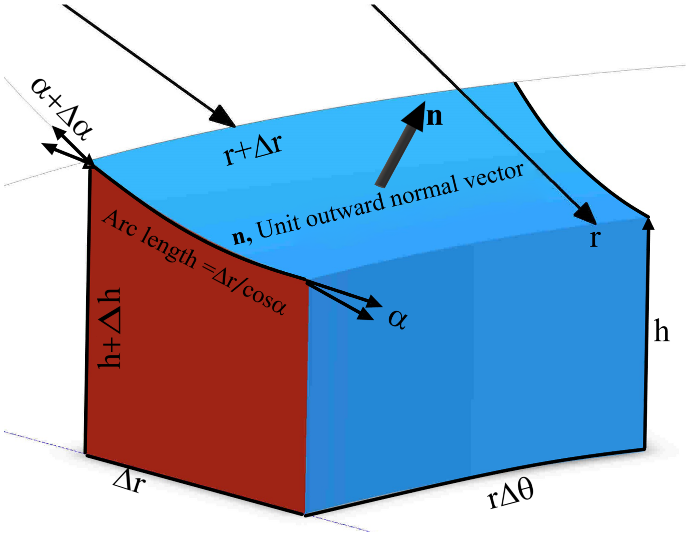

Figure 2.7 Schematic of the differential volume showing the slope of the thin liquid film

which yields the normal vector

$$\mathbf{n}=\frac{\nabla J}{|\nabla J|}=\frac{\hat{\mathbf{z}}-h'\hat{\mathbf{r}}}{(1+h'^2)^{1/2}}, \tag{2.8}$$

where $\hat{\mathbf{r}}$ and $\hat{\mathbf{z}}$ are unit vectors in the radial and wall-normal directions, respectively, and $h'=dh/dr$. We define the angle α as the tangent to the surface defined by $h'=\tan\alpha$. Then $\cos\alpha=\frac{1}{(1+(h'^2)^{1/2}}$ and $\sin\alpha=\frac{h'}{(1+h'^2)^{1/2}}$, and (2.8) can also be written as

$$\mathbf{n}=\hat{\mathbf{z}}\cos\alpha-\hat{\mathbf{r}}\sin\alpha. \tag{2.9}$$

Consider the control volume shown in figure 2.7. Here $d\mathbf{l}=\hat{\theta}rd\theta$ and

$$\begin{aligned}\gamma\int_r^{r+\Delta r} d\mathbf{l}\times\mathbf{n}\\
&= \gamma \textstyle\int_r^{r+\Delta r}\hat{\theta}\times(\hat{\mathbf{z}}\cos\alpha-\hat{\mathbf{r}}\sin\alpha)rd\theta,\\
&= \gamma\left(2\pi r\cos\alpha\hat{\mathbf{r}}+2\pi r\sin\alpha\hat{\mathbf{b}}\right)\Big|_r^{r+\Delta r},\\
&= \gamma\left(2\pi r\cos\alpha\hat{\mathbf{r}}+2\pi r\sin\alpha\hat{\mathbf{b}}\right)\Big|_r^{r+\Delta r},\end{aligned} \tag{2.10}$$

where we have integrated azimuthally from 0 to 2π.

Noting that, since the radial length along the surface is $\frac{dr}{\cos\alpha}$ (figure 2.7) so that $dS=2\pi r\frac{dr}{\cos\alpha}$, then from (2.6) and (2.10) the radial and vertical components of normal stress at the free surface can be written as

$$F_{\gamma,r} \equiv \int_r^{r+\Delta r} \mu\left(\mathbf{n}\cdot[\nabla\mathbf{u}+(\nabla\mathbf{u})^T]\right)\cdot\hat{\mathbf{r}}\left(2\pi r\frac{dr}{\cos\alpha}\right)\Bigg|_h = -\int_r^{r+\Delta r} P\sin\alpha 2\pi r\frac{dr}{\cos\alpha}+2\pi r\gamma\cos\alpha\Bigg|_r^{r+dr}, \tag{2.11}$$

and

$$F_{\gamma,z} \equiv \int_r^{r+\Delta r} \mu\left(\mathbf{n}\cdot[\nabla\mathbf{u}+(\nabla\mathbf{u})^T]\right)\cdot\hat{\mathbf{z}}\left(2\pi r\frac{dr}{\cos\alpha}\right)\Bigg|_h = -\int_r^{r+\Delta r} P2\pi r dr+2\pi r\gamma\sin\alpha\Bigg|_r^{r+dr}, \tag{2.12}$$

where $P = p_L - p_G$. Now recognising that upstream of the hydraulic jump, the liquid film is almost flat which implies that $\alpha \to 0$ and $P \to 0$, equation (2.11) can be written as

$$\mu\left(\int_S \mathbf{n}.[\nabla\mathbf{u}+(\nabla\mathbf{u})^T]dS\right).\hat{\mathbf{r}}\Bigg|_h \approx \gamma\int_C d\mathbf{l}\times\mathbf{n}.\hat{\mathbf{r}} = 2\pi r\gamma\Bigg|_{r+\Delta r} - 2\pi r\gamma\Bigg|_r. \tag{2.13}$$

Consequently, in a control volume approach the force due to surface tension, which in differential form of the governing equation appears as a normal stress boundary condition, can be incorporated as a surface force on the circumference of the control volume (shown in figure 2.2b).

2.5.2 Control volume based analysis

In this section we will adopt a direct method and apply a energy balance on a control volume. We Consider cylindrical co-ordinates r and z, the radial and jet-axial coordinates, respectively, u and w the associated velocity components (figure 2.2), and assume circular symmetry about the jet axis. In order to analyse the flow the *ansatz* developed by Watson (1964) for the velocity within the thin film is used. Then the radial velocity is written as $u = u_s f(\eta)$, $\eta \equiv z/h(r)$ $(0 \le \eta \le 1)$, where η is the dimensionless thickness of the film and u_s is the velocity at the free surface. Using continuity the average velocity $\bar{u} \equiv C_1 u_s$ is defined by

$$\int_0^h urdz = u_s rh\int_0^h f(\eta)d\eta = C_1 u_s rh \equiv \bar{u}rh = \frac{Q}{2\pi} = \text{const.}, \tag{2.14}$$

where $C_1 = \int_0^h f(\eta)d\eta = 0.615$ is a shape factor determined from Watson's similarity solution for which he found the relation,

$$\frac{df(\eta)}{d\eta} = 1.402\left(1 - f(\eta)^3\right)^{\frac{1}{2}} \tag{2.15}$$

The flux of mechanical energy across an annular control volume shown in figure 2.2(b), is balanced from r to $r + \Delta r$ and from 0 to h (where the common factor 2π has been canceled out),

$$\begin{gathered}\left.\frac{(\rho\overline{u^2}\bar{u}rh)}{2}\right|_r - \left.\frac{(\rho\overline{u^2}\bar{u}rh)}{2}\right|_{r+\Delta r} - (\gamma\bar{u}r)\Big|_r + (\gamma\bar{u}r)\Big|_{r+\Delta r} + \\ p\bar{u}rh\Big|_r - p\bar{u}rh\Big|_{r+\Delta r} + \left.\frac{\rho g\bar{u}rh^2}{2}\right|_r - \left.\frac{\rho g\bar{u}rh^2}{2}\right|_{r+\Delta r} - r\tau_w\bar{u}\Delta r = 0,\end{gathered} \tag{2.16}$$

Here $\tau_w = \rho\nu\frac{u_s}{h}f'(0)$ is the wall shear stress and from the velocity profile *ansatz* (equation 2.15), $f'(0) = 1.402$.

The first term is the flux of kinetic energy which is balanced by pressure, gravity and viscous work given in the third, fourth and fifth terms. These are standard and the new term that has been neglected in previous studies is the second term $\gamma\bar{u}r$ which represents the flux of surface energy. This term results from the increase of surface area across the control volume as a result of the change in the circumference from r to $r + \Delta r$.

Dividing (2.16) by Δr, taking the limit $\Delta r \to 0$ and using the fact that $\bar{u}rh =$ constant (see (2.14)) yields,

$$\frac{1}{2}\frac{d(\rho\overline{u^2})\bar{u}rh}{dr} - \frac{d(\gamma\bar{u}r)}{dr} = -\bar{u}rh\frac{dp}{dr} - \frac{1}{2}\rho g\bar{u}rh\frac{dh}{dr} - \tau_w r\bar{u}. \tag{2.17}$$

From the boundary layer velocity profile *ansatz* we write $\overline{u^2} = \int_0^1 u^2 d\eta \equiv C_2 u_s^2$, where $C_2 \equiv \int_0^1 f^2(\eta)d\eta = 0.4755$ is a second shape factor. Then equation (2.17) implies

$$C_2\rho u_s^2 hr\frac{du_s}{dr} - \gamma r\frac{du_s}{dr} - \gamma u_s = -u_s rh\frac{dp}{dr} - \frac{1}{2}\rho g u_s rh\frac{dh}{dr} - \tau_w r u_s. \tag{2.18}$$

Note that the shape factor C_1 cancels out in this equation, and so plays no role. Again using equation (2.14), yields $u_s r\frac{dh}{dr} = -h\frac{d(u_s r)}{dr}$ which can be substituted in equation (2.18), to obtain

$$(C_2\rho u_s^2 h - \gamma - \frac{1}{2}\rho g r h^2)r\frac{du_s}{dr} = -u_s rh\frac{dp}{dr} + \gamma u_s + \frac{1}{2}\rho g u_s h^2 - \tau_w r u_s. \tag{2.19}$$

Finally, rearranging equation (2.19) gives the gradient of the radial velocity

$$\frac{du_s}{dr} = \frac{-u_s rh\frac{dp}{dr} + \gamma u_s + \frac{1}{2}\rho g u_s h^2 - \tau_w r u_s}{(1 - \frac{1}{We} - \frac{1}{Fr^2})(C_2\rho u_s^2 hr)}. \tag{2.20}$$

Wherein the Weber number and Froude number are defined respectively as,

$$We \equiv \frac{C_2 \rho u_s^2 h}{\gamma}, \; Fr \equiv \sqrt{\frac{2C_2 u_s^2}{gh}}. \tag{2.21}$$

It is clear that equation (2.20) is singular when

$$We^{-1} + Fr^{-2} = 1, \tag{2.22}$$

and that the hydraulic jump occurs where this condition is satisfied.

In order to obtain quantitative results, equation (2.20) was solved for u_s using the similarity velocity profile and the initial condition obtained from Watson (1964). The boundary layer first occupies the full depth of the film at the location, r_b, given by $\frac{r_b}{d} = 0.1833 Re^{\frac{1}{3}}$, where the jet Reynolds number $Re = \frac{4Q}{\pi \nu d}$. At this location, which for the present values of $Re \sim 10^4, r_b \ll R$, u_s is set equal to the mean jet velocity, which provides the initial condition to solve equation (2.20) which provides its subsequent radial values. The solution of equation (2.20) is not sensitive to the initial condition obtained using Watson's similarity profile as other boundary layer velocity profiles yield similar values of r_b. The solution of equation (2.20) becomes singular at the location where $We^{-1} + Fr^{-2} = 1$, yielding R. This condition provides a more precise estimate and a physical basis for the scaling argument equation (2.3), and also includes the small effect of gravity, and provides a general theory for formation of a circular hydraulic jump.

2.6 Results

2.6.1 Effect of surface orientations

Figure 2.1 shows that for normal jet impingement the orientation of the surface does not affect the radius of the jump. In figure 2.1(b), for a vertical wall, the jump is very close to circular, which is further evidence that gravity plays no significant role. On vertical plate, the jump radius was measured in the direction where gravity is normal to radial direction. Therefore, for the theoretical prediction gravity was ignored. A direct comparison between the four cases of a horizontal plane impinged from above and below, a vertical plane and a surface inclined at 45° is shown in figure 2.8.

The theoretical curve, obtained ignoring gravity by setting $g = 0$ in (2.20), agrees closely with the data from the vertical, inclined and horizontal plate from above. The observed radius is slightly larger for the horizontal plate impinged from below.

This is presumably because the ultimate transition to dripping flow or a water bell is affected by gravity and occurs after the film initially thickens.

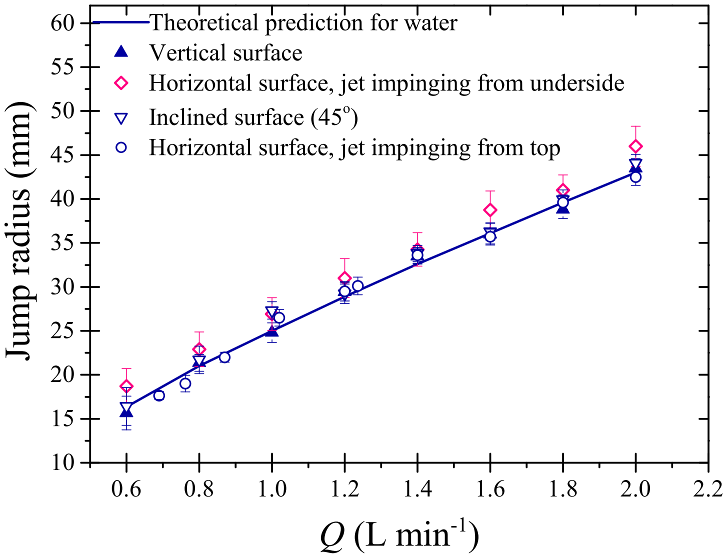

Figure 2.8 Effect of flow rate on jump radius for the four surface orientations. In each case the liquid was pure water. The theoretical prediction (Solid locus) is obtained from setting $g = 0$ (Equation 2.20).

2.6.2 Effect of fluid properties: surface tension and viscosity

Figure 2.9 compares experimental measurements with the predictions of R for pure water, WP95/5 and the aqueous SDBS solution for a jet impinging on a horizontal plate from above. Table 2.1 indicates that SDBS and pure water have similar viscosities but different surface tensions, while WP95/5 and SDBS have different viscosities but similar surface tensions.

Lowering the surface tension (SDBS *cf.* water) increases R while increasing the viscosity (WP95/5 *cf.* SDBS) reduces R. The corresponding theoretical curves obtained from (2.20), again with $g = 0$, shown in figure 2.9, capture these variations with liquid properties and agree with the experimental data.

Figure 2.10 compares data reported by Jameson et al. (2010) for liquid jets of 70 and 90 w/w% glycerol/water solutions, WG30/70 and WG10/90, at 19°C and 28°C, respectively, impinging on the underside of a horizontal surface consisting of either glass or Teflon®. For a given flow rate, the measured departure radius R is smaller for the more viscous solution: the surface tensions are comparable.

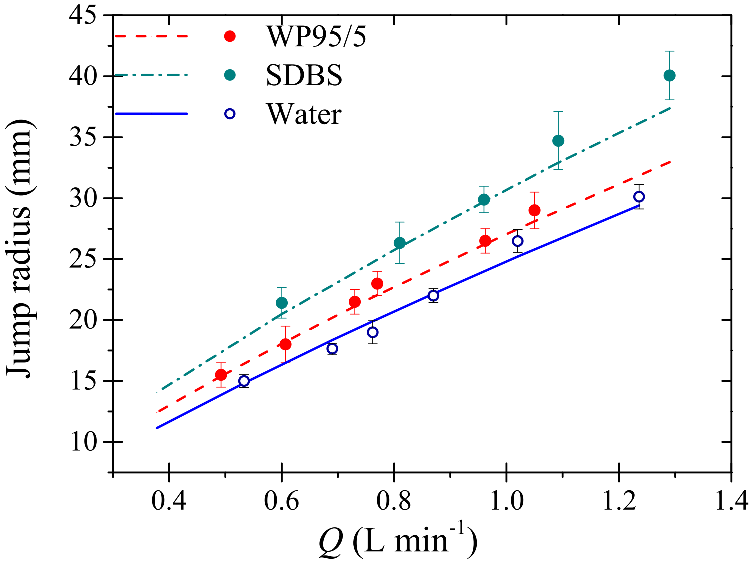

Figure 2.9 Effect of flow rate on initial jump radius for normal impingement on a horizontal plate from above, for water, water-propanol (WP95/5) and SDBS at 20°C. Curves are the predictions obtained from solutions of (2.20). The predictions lie within the uncertainty in the experimental measurements.

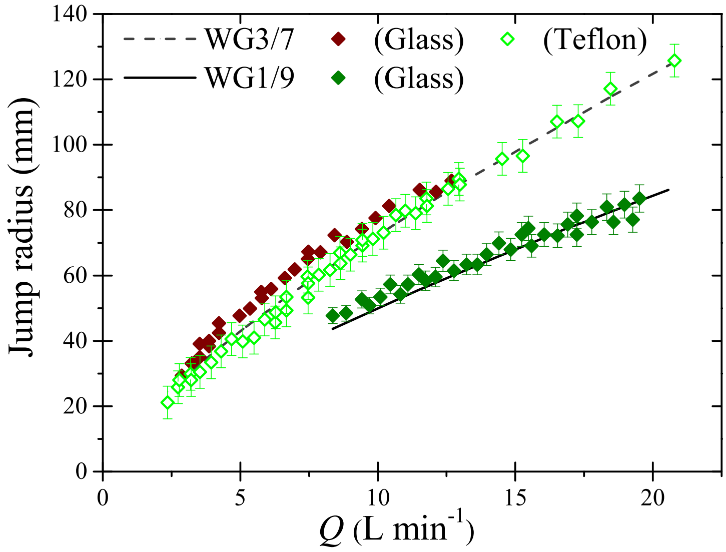

Figure 2.10 Measured water bell departure radius, from Jameson et al. (2010), alongside predictions (curves), obtained by solving (2.20) with $g = 0$. The liquids were water-glycerol mixtures WG30/70 and WG10/90.

The solution to equation 2.20 obtained by setting $g = 0$ slightly underpredict the radius, but they capture the effect of the viscosity changes well. In their theoretical description of the water bell departure radius, Button (2005) expected that R would depend on the surface wettability or the contact angle between the surface and the liquid which they revised in Button et al. (2010), however, their analysis is fundamentally flawed and it is discussed in § 3.3.2. As can be seen in figure 2.10 there is only a very small difference between the glass (hydrophilic) and Teflon® (hydrophobic) surfaces. Although they observed a change in the local contact angle at the rim of the radial flow, the water bell formation radius was at the same location, as predicted by the theory developed here.

2.6.3 Return to scaling

Equation 2.20 can be used to determine the constant in the scaling relation (2.3). Using (2.14), (2.21) and the expression for the wall stress we find that

$$\frac{R}{R_0} = \left(\frac{1}{f'(0)(2\pi)^3} \frac{C_2}{C_1^2} \right)^{\frac{1}{4}} = 0.245, \tag{2.23}$$

which is close to the experimental best fit to the data 0.289 ± 0.015 quoted in § 2.3. Thus, the theory allows us to quantify the scaling relation.

2.7 Conclusions

This chapter ultimately provides a resolution to the question: what gives birth to a circular hydraulic jump in a thin liquid film? A scaling relationship (2.3) was derived which collapses the experimental data and shows that the jump location is determined by the viscosity and the surface tension of the liquid. Using a similarity solution due to Watson (1964), with the addition of surface tension, quantitative predictions of the jump radius R that are in excellent agreement with our measurements for different surface orientations and fluid properties.

The hydraulic jump, or the supercritical to subcritical transition, occurs when $We^{-1} + Fr^{-2} = 1$. From equation (2.20) it can be inferred that the transport of surface energy becomes dominant for the expanding films at larger radii. The LHS of equation (2.19) indicates that the liquid momentum must overcome the hydrostatic pressure and surface tension. The jump is formed where the hydrostatic pressure term $\rho g h^2 r$ and surface force γr are greater than or equal to the momentum. This behaviour was previously attributed to the hydrostatic force alone, which is a special case of the general solution.

Previous analyses have incorporated surface tension but only through the hoop stress, which, we agree, is small on the scale of these jumps and is effectively incorporated in the pressure term in equation (2.16). It is the loss of energy associated with the radial transport of surface energy that implies that the flow can no longer provide the kinetic energy to maintain the thin film. At this point the flow decelerates rapidly, the depth of the flow increases and the hydraulic jump occurs. This is equivalent to the surface tension force associated with curvature of a film of thickness h, and hence this thickness is the relevant length scale in the Weber number used to obtain the scaling relation equation (2.3). Comparing the scaling relation obtained in this chapter, equation (2.3), $R \sim \rho^{1/4} Q^{3/4} \nu^{-1/4} \gamma^{-1/4}$, with the result obtained by Rojas et al. (2013) in the limit of zero surface tension, $R \sim Q^{3/4} \nu^{-1/4} H^{-1/2} g^{-1/4}$, implies that the depth of liquid downstream of the jump scales with capillary length scale $H \sim (\gamma/g\rho)^{1/2}$.

It is also worth noting that the dependence of R on Q and ν our scaling relation ($Q^{3/4}\nu^{-1/4}$) is very similar to that obtained by Bohr et al. (1993) quoted in § 2.2, namely, $Q^{5/8}\nu^{-3/8}$. Consequently, these and other authors were able to fit their data to the latter scaling which involves gravity and not surface tension, since these latter two parameters were not changed between experiments. Similarly, Hansen et al. (1997) found empirically that the jump radius for water, $R \propto Q^{0.77}$ which is close to the obtained scaling relationship, $R \propto Q^{3/4}$. However, they concluded that it is consistent with the scaling relation obtained by Bohr et al. (1993), which predicts $R \propto Q^{5/8}$.

The critical Weber number based on the film thickness at the jump implies that the flow speed is $\sqrt{\gamma/\rho h}$, which is the speed of capillary waves with wavenumbers comparable to the inverse of the film thickness. Consequently, capillary waves play a similar role in this situation to gravity waves in the traditional hydraulic jump.

It should again be emphasised that the study only concerned with the location of the jump *on an infinite plane.* For vertical jet impingement on a horizontal surface, the liquid film eventually reaches and flows off the edge of the surface. At that point there will be another boundary condition resulting from this flow off the edge which will result in information travelling upstream through the subcritical region to the initial jump location. This will effectively flood that control and, in general, the jump will move inwards from its initial location, reducing R. However, on a vertical plate or on impingement of a liquid jet onto a ceiling, the jump will remain at the same location.

Finally, it is worth considering what constitutes a thin film in this context. As shown in equation § 2.3, balancing the deceleration with the viscous drag implies that the film aspect ratio $\kappa \sim Re^{-1}$. For the values of $Re \sim 1000$ in the experiments $h \sim R.10^{-3} \sim 100\,\mu\mathrm{m}$.

Chapter 3

Energy vs Momentum equation; reconciliation with previous theories

3.1 Introduction

In § 2, it was shown that, irrespective of the orientation of the surface, on normal impingement of a liquid jet on to a surface, the liquid film spread radially until a point where the liquid film changes its film thickness abruptly and forms a circular hydraulic jump (figure 2.1). Furthermore, for same flow rate and physical properties, the hydraulic jump occurred at the same location. This experiment unequivocally confirmed that gravity plays no significant role in the formation of a kitchen sink scale hydraulic jump (figure 2.1). It also challenged the previously held views that the abrupt change in liquid film thickness on a horizontal (Bohr et al. (1993); Bush and Aristoff (2003); Watson (1964)), vertical (Wang et al. (2015, 2013b); Wilson et al. (2012)) and on underside (Jameson et al. (2010)) of a surface are different phenomena. Rather, they are related and can be explained by same set of governing equations. Therefore, the existing theories where gravity plays a central role in the formation of hydraulic jump (Bohr et al. (1993); Bush and Aristoff (2003); Watson (1964)) are unlikely to give a reasonable description of the flow field.

In § 2, equation 2.20 was derived by incorporating surface energy into the mechanical energy equation. Equation 2.20 becomes singular at a finite radial location, taking the form, $\frac{du}{dr} \to -\infty$, implying $\frac{dh}{dr} \to \infty$, which yields the location of the hydraulic jump. The criterion for hydraulic jump was found to be; $\frac{1}{We} + \frac{1}{Fr^2} = 1$

which suggests there are two limiting cases.
Case 1: $We \approx 1$ and $Fr \gg 1$. The jump is caused by surface tension, and occurs when the film thickness is small and the momentum per unit width is of the order of the surface tension. For circular hydraulic jumps, the expanding flow field favors this case and most jumps are induced by surface tension.
Case 2: $Fr \approx 1$ and $We \gg 1$ and. When the liquid film thickness is large and the flow of momentum per unit width is high compared to the surface tension, then the jump is initiated by gravity. None of the experiments reported in this paper correspond to this case and for thin films it is effectively $We \approx 1$. The theory also explained, why the film jump/hydraulic jump on a vertical surface and water bell departure radius/hydraulic jump are insensitive of substrate type.

In contrast to earlier theories (see Bohr et al. (1993); Bush and Aristoff (2003); Kasimov (2008); Watson (1964)) which were obtained by solving the Navier Stokes equations, the results shown in § 2 are significantly different in several key aspects. However, in principle, both methods should yield similar results. Therefore, in this chapter, a momentum based approach is adopted to describe the flow field and reconcile the results with previous theories.

The aim is to answer the questions; (i) why previous approaches fail to explain the birth of a hydraulic jumps; (ii) to what extent is the flow field upstream of a hydraulic jump affected by the surface tension, and can previous theories still be used for cleaning and other, such as, heat and mass transfer applications. To achieve this, the assumptions and limitations of the previous theories will be revisited. It is argued that in the case of thin film flows, the slope of the free surface and the force due to surface tension cannot be ignored. To achieve this aim, the previous literature in reviewed in § 3.2. A control volume analysis, applying momentum balance is described in § 3.3 and the role of surface tension, which was ignored previously is highlighted. In § 3.4 the results are compared from previous and the current theories. Conclusions are drawn in § 3.5.

3.2 Previous approaches

Watson (1964) recognised that since the central layer of the liquid film created by impinging jets are thin, the ideas of boundary layer should be applied to describe the flow field. He described the flow as; soon after the impingement of a jet, in the spreading liquid film, a boundary layer will grow from the stagnation point and gradually absorb the whole film, and at a particular radial location the whole film becomes a boundary layer. By balancing the liquid momentum with the viscous force, for large values of r, he found a similarity solution for the laminar boundary layer equations. Watson's governing equations, obtained ignoring the surface tension of the fluid, predicted a smooth film thickness profile. Watson recognized that the Froude number of the flow outside the jump is small and at the location of the hydraulic jump, momentum conservation can be applied. Therefore, balancing momentum with the hydrostatic pressure obtained him a relation for the hydraulic jump. The relation involved depth of the film outside/downstream of the jump, H, jet diameter, d, jump radius, R and other physical parameters; flow rate, Q, kinematic viscosity, ν, and gravity, g. These six parameters, yield four dimensionless groups;

Reynolds number defined as $Re_{Wat} = \frac{Qd}{2\nu}$,

the Froude number equivalent, $\frac{Q^2}{RgH^3}$,

dimensionless radius $\frac{R}{d}$ and $\frac{RgH^2d^2}{4Q^2}$.

Watson ignored the jet Reynolds number, as it is very large and the Froude number equivalent as they would not produce large corrections, he suggested that $\frac{RgH^2d^2}{4Q^2}$ can be related to $(\frac{R}{d})(Re_{Wat})^{-\frac{1}{3}}$. The main shortcomings of Watson's theory are; (1) it is a non-predictive theory. To apply the momentum balance at the location of the hydraulic jump, the height of the film downstream of hydraulic jump needs to be measured;(2) the flow described by Watson ignores the effect of surface tension hence the description of the flow field is inaccurate (see § 2); (3) the theory implies that thin film circular hydraulic jumps are formed due to gravity, which has been proven not to be true (see § 2, figure 2.1).

Bohr et al. solved shallow-water type equations including viscosity and gravity. They wrote the axisymmetric Navier–Stokes equations and averaged these in the vertical direction. This vertically averaged Navier–Stokes equation yielded the shallow-water equations for film thickness and the average radial velocity. The viscous loss term was approximated in terms of average velocity, film thickness and an *ansatz* for the velocity profile. They then applied the constant flux condition and eliminated liquid film thickness from the continuity and momentum equations. This manipulation yielded an ordinary differential equation for velocity as a function of radial location. Then they analysed the solution of this differential equation. They found that outer solutions of their equations become singular at a finite radius and argued that this lack of asymptotic states is a general phenomenon associated with radial flow with a free surface. It is important to recognize that this singularity predicts velocity to be positive infinity ($+\infty$) which is physically impossible. Bohr et al. also suggested that incorporating gravity in Watson's solution will give a similar singularity. They connected the inner and outer solution through a shock and found a scaling relation for the hydraulic jump. Bohr et al. focused mainly on the hydraulic jump and not the flow field.

Azuma and Hoshino (1984*a*) provided an early detailed description of the flow field. They subdivided the flow field into a boundary layer formation zone, a laminar zone and the a turbulent zone. Similarly Lienhard (1995); Liu and Lienhard (1993) studied the flow field created by impinging liquid jets for heat transfer applications. Neither Azuma and Hoshino nor Liu and Lienhard incorporated the effect of surface tension but they were able to predict the measurable physical quantities, for example liquid film thickness and heat transfer coefficient, reasonably well. Since both these theories describe turbulent film, the theories will be discussed in detail in § 4.

Jameson et al. (2010) reported the formation of water bells. To explain the water bells theoretically, Button et al. (2010) used Watson's description of flow and gave a film termination condition or a condition for water bell departure radius. They invoked the theory for disintegration of a liquid sheet (Taylor (1959)) and proposed that at the location of detachment point, the liquid momentum should be balanced by the surface tension. However, their interpretation of Taylor's theory is flawed and discussed in § 3.3.2.

Wilson et al. (2012) studied the flow field created by liquid jets impinging on a vertical plate. They described the flow upstream of the jump as a Nusselt film and named the sudden change in film thickness at a finite radius as the 'film jump'. They suggested that at the location of film jump, the forward momentum balances the force due to surface tension including the contact line. This theory suggested that the film jump location should be sensitive to the nature of the substrate. However, Wang et al. (2013b) found that the measured film jump locations were independent of substrate type.

In § 2 it is shown that the film jump is the same family of event as hydraulic jump and it is insensitive to substrate type and in the limit of large Froude number the condition for a hydraulic jump is $We \approx 1$.

3.3 Theory

3.3.1 Momentum balance

Applying momentum balance to the control volume of fluid shown in figure 3.1 yields,

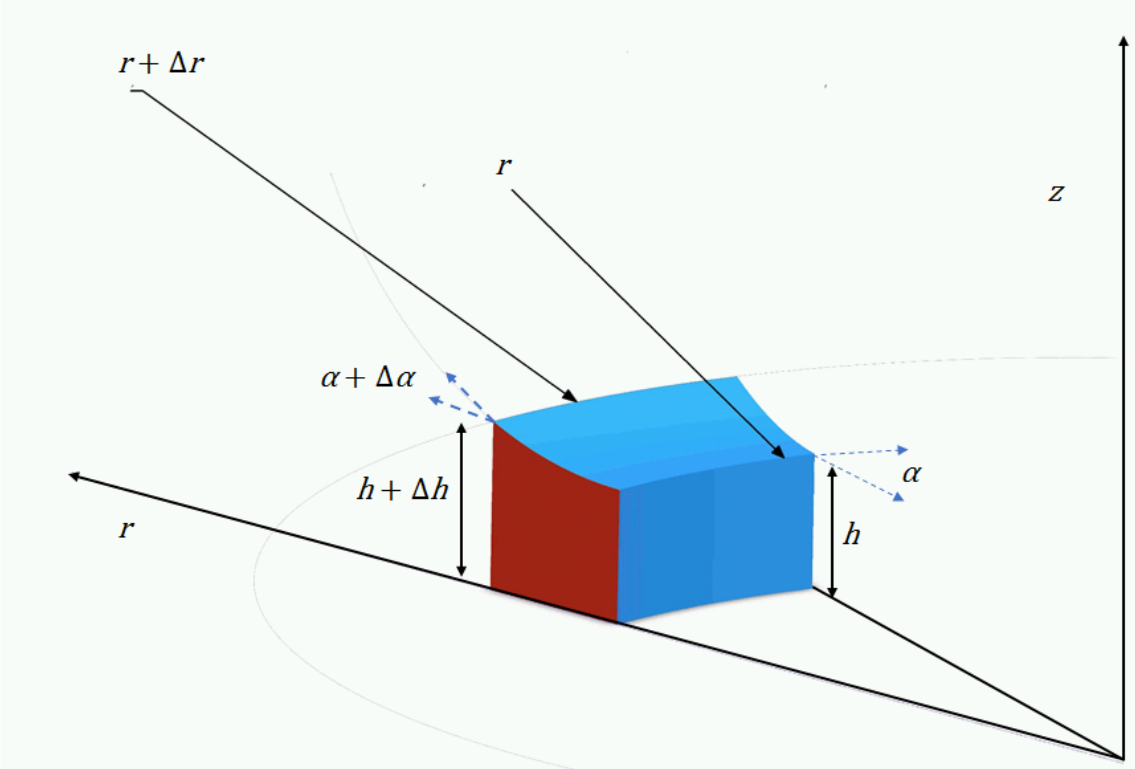

Figure 3.1 Control volume of the film element on which the momentum balance was applied

$$\frac{(C_2\rho u_s^2 h\Delta\theta)}{2}\bigg|_r - \frac{(C_2\rho u_s^2 h\Delta\theta)}{2}\bigg|_{r+\Delta r} - (\gamma\cos(\alpha)r\Delta\theta)\Big|_r + (\gamma\cos(\alpha)r\Delta\theta)\Big|_{r+\Delta r} + prh\Delta\theta\Big|_r - prh\Delta\theta\Big|_{r+\Delta r} + \frac{\rho g r h^2\Delta\theta}{2}\bigg|_r - \frac{\rho g r h^2\Delta\theta}{2}\bigg|_{r+\Delta r} - \tau_w r\Delta\theta\Delta r = 0 \tag{3.1}$$

Here θ is the azimuthal angle and α is the angle subtended by liquid film with horizontal. Dividing both sides by Δr with limits $\Delta r \to 0$, owning to circular symmetry eliminating $\Delta\theta$ and using the constant flux condition $u_s rh =$ constant, yields,

$$C_2\rho u_s r h\frac{du_s}{dr} + \frac{d(\gamma r\cos(\alpha))}{dr} = -rh\frac{dp}{dr} - \frac{1}{2}\rho g r h\frac{dh}{dr} - \tau_w r \tag{3.2}$$

Ignoring γ and α in equation 3.2 would yield an expression which has been used in the conventional theories (see (Bush and Aristoff, 2003; Watson, 1964; Wilson et al., 2012).

$$C_2\rho u_s r h\frac{du_s}{dr} + = -rh\frac{dp}{dr} - \frac{1}{2}\rho g r h\frac{dh}{dr} - \tau_w r \tag{3.3}$$

Equation 3.2 and 3.3 are the momentum balances in the radial direction. Equation 3.3 is a function of r which could be solved with a given initial condition, while equation 3.2 is a function of both r and z (as α is a function of r and z). Again, in the conventional theories, the new term ($\frac{d(\gamma r\cos(\alpha))}{dr}$) has been neglected.

Manipulating equation 3.2 further and taking a dot product with the radial velocity, u_s yields,

$$C_2\rho u_s^2 r h\frac{du_s}{dr} + u_s\gamma\cos(\alpha) + \gamma r u_s\frac{d\cos(\alpha)}{dr} = -u_s r h\frac{dp}{dr} - \frac{1}{2}\rho g u_s r h\frac{dh}{dr} - \tau_w r u_s \tag{3.4}$$

Comparing equations 3.4 with 2.18 implies that $u_s\frac{d(\gamma r\cos\alpha)}{dr} = -\frac{d(\gamma r u_s)}{dr}$ and $u_s\gamma\cos(\alpha) = u_s\gamma$.

This is despite a small growth in α up to the hydraulic jump location; the liquid film remains thin enough that the relation $u_s\gamma\cos(\alpha) \approx u_s\gamma$ still holds. At the location of the hydraulic jump, the radial velocity decreases rapidly and α changes from $\approx 0°$ to $90°$, forming the hydraulic jump. Equation A.6 (see Appendix A) suggests that the vertical component of the velocity in the flow field, w, takes the form of $w = u\frac{dh}{dr}\eta = u_s f(\eta)h'\eta$. Near the hydraulic jump radius, where u rapidly decreases, w can still have a finite value forming hydraulic jump as $\alpha \to 90°$ or $h' \to \infty$. It suggests that the momentum based analysis presented in this chapter is consistent with the energy based analysis presented in § 2.

In § 3.4, the prediction from the current theory is compared with Wilson et al. (2012) flow model. The following key quantities are selected for the comparison: average velocity, $\bar{u}$, momentum per unit width M, and wall shear stress τ_w, which are defined as,

$$\bar{u} = u_s\int_0^1 f(\eta)d\eta \equiv C_1 u_s \tag{3.5}$$

$$M = \int_0^h \rho u^2 dz \equiv C_2 \rho u_s^2 h \tag{3.6}$$

$$\tau_w = \mu \frac{\partial u}{\partial z}\bigg|_{z=0} \tag{3.7}$$

Following the numerical solution of equation 2.20, $\bar{u}$ and M is calculated from equations 3.5 and 3.6 and the wall shear stress is given by,

$$\tau_w = \frac{4.56\pi\mu\bar{u}^2 r}{Q} \tag{3.8}$$

Wilson et al. (2012) described the liquid flow in the radial flow zone as a fully developed Nusselt film and for that the mean liquid velocity is given by,

$$\bar{u}(\text{Wilson et al., 2012}) = \frac{1}{\frac{1}{U_\circ} + \frac{10\pi^2\mu}{3\rho Q^2}\left[r^3 - r_o^3\right]} \tag{3.9}$$

Momentum per unit width, M

$$M(\text{Wilson et al., 2012}) = \frac{6}{5}\rho\bar{u}_{Nu}^2 h \tag{3.10}$$

And the wall shear stress is given by,

$$\tau_w(\text{Wilson et al., 2012}) = \frac{6\pi\mu\bar{u}^2 r}{Q} \tag{3.11}$$

3.3.2 Hydraulic jump/film jump

Button et al. (2010) proposed a model for water bell departure radius in which they balanced the momentum with the surface tension. They invoked Taylor (1959) analysis of disintegration of fluid sheets. Taylor (1959) applied a force balance at the free edge of the bounding liquid sheet and found a relationship for disintegration radius as the location where $M = 2\gamma$. Button et al. (2010) argued that, a moving liquid sheet in air contains two moving surfaces which yields $M = 2\gamma$, adopting the analogy, for moving liquid film with one free surface should yield a balance $M = \gamma$. This analysis is flawed, since unlike liquid sheets with free edge, the water bells are surrounded by the contact line attached to the surface. Hence, correct adaptations of Taylor (1959)'s analysis should yield $M = \gamma(1 - \cos\beta)$, where β is the contact angle between the liquid and the wall (see figure 3.2) which would suggest a dependence on surface wettability. Moreover, Button et al. (2010) wrote '*It was observed experimentally that the liquid formed a local contact angle with the solid surface at the rim of the radial flow. This local contact angle was dependent on the wettability of the surface. Even so, the water bell departure radius was found to be independent of the surface, despite the formation of the local contact angle.*'

In the Wilson et al. (2012) model the location of the film jump is determined by a balance between momentum and surface forces. They estimated the net surface tension force acting at the film jump as $\gamma(1 - \cos\beta)$. Wilson et al. (2012) analysis agrees with Taylor (1959) analysis of disintegration of liquid sheets. However, Wang et al. (2013b) reported that the location of the film jump was independent of the nature of the wall material and could be calculated from their model by using an effective contact angle of 90°.

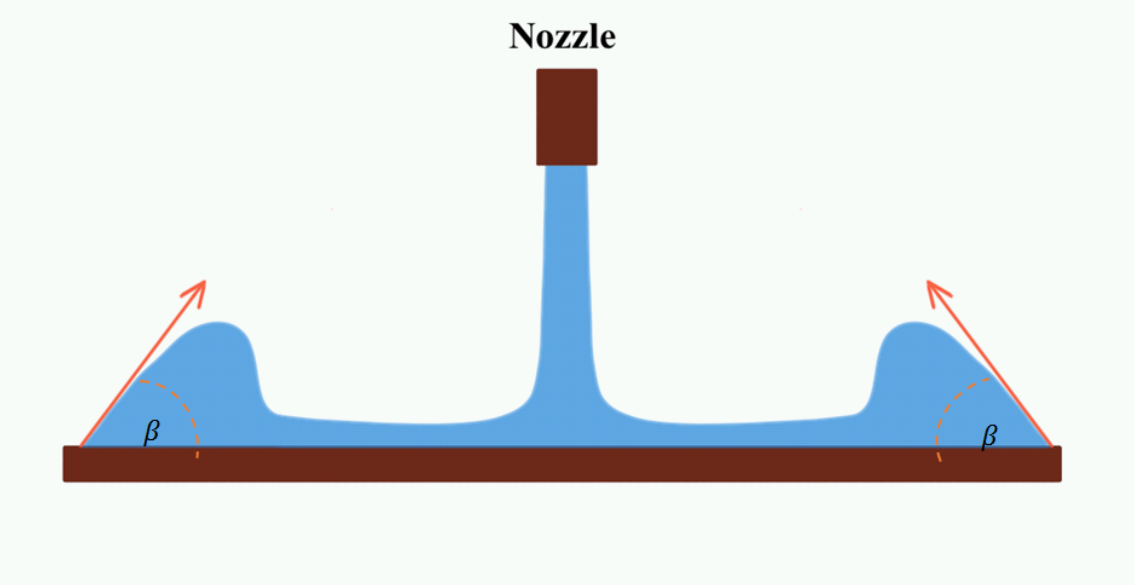

Figure 3.2 Schematic, not to scale, showing a cross section of the RFZ and rope in a vertical plate.

In § 2, it was shown that the condition for a hydraulic jump is; $We^{-1} + Fr^{-2} = 1$ (equation 2.22). It has also been shown that for a kitchen sink scale jump, gravity is unimportant and the effective condition for a jump is $We \approx 1$ which implies that at the location of a hydraulic jump,

$$M = \int_0^h \rho u^2 dz \equiv \gamma \tag{3.12}$$

where M is the momentum per unit width at any radial location. To predict the film jump, Wang et al. (2015) used an effective contact of 90° which essentially satisfies equation 3.12 and hence predicts the hydraulic jump.

3.4 Results

Due to its simplicity and reasonable description of the flow field (see Aouad et al. (2016), Pérez-Mohedano et al. (2015)) and its applicability (see Glover et al. (2016), Damkjær et al. (2017)) Wilson et al. (2012) flow model is being used for comparison with the current theory.

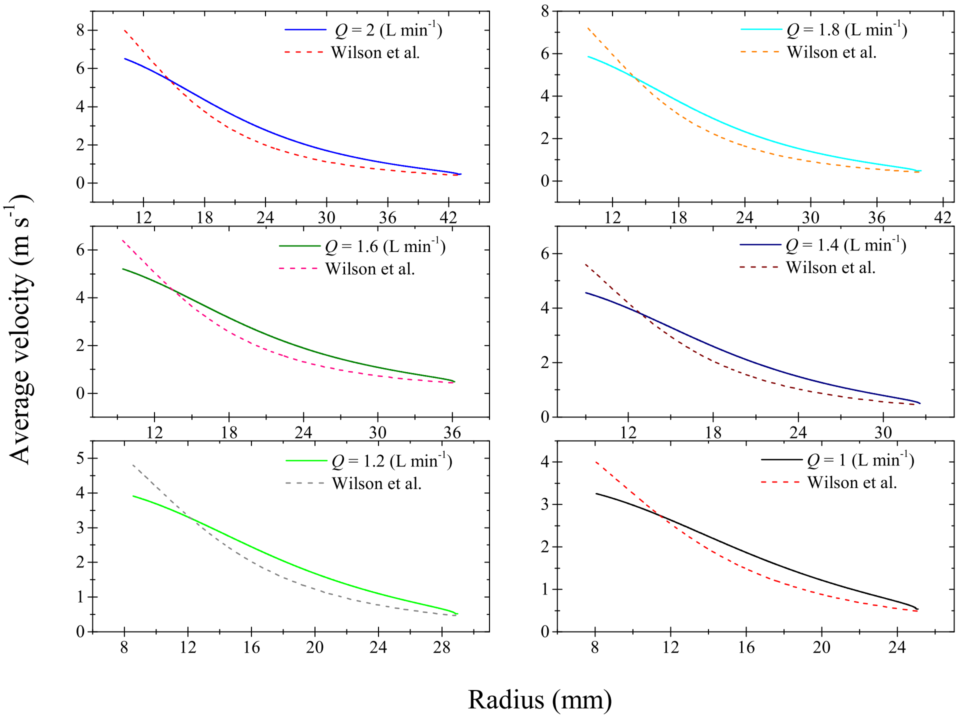

Figure 3.3 Comparison of average velocities obtained from the solution of equation 2.20 and equation 3.9 (Wilson et al. (2012)).

The solution of equation 2.20, with initial condition at $\frac{r_b}{d} = 0.1833Re^{\frac{1}{3}}$, $u_s = U_o =$ mean jet velocity, provides the surface velocity at subsequent radial positions and the mean radial velocity can be calculated from equation 3.5. Similarly the solution of equation 3.9 give Wilson et al.'s prediction of the mean velocity at different radial positions.

Figure 3.3 compares the mean velocity predicted by 3.9 (Wilson et al., 2012) and the present work, 3.5 from the radial position starting from r_b up to the hydraulic jump; and for a range of flow rates ($0.8 - 2\,\mathrm{L\,min^{-1}}$) and a nozzle diameter $d = 2\,\mathrm{mm}$. Equation 2.20 becomes singular at a finite radius, which predicts the hydraulic jump and it is not valid beyond this point, However, equation 3.3 is a continuous function which predicts a finite radial velocity in the range $\frac{d}{2} \leq r < \infty$. For all cases, at a smaller radius, the Wilson et al. model predicts a higher value of velocity which decreases rapidly at subsequent radial positions.

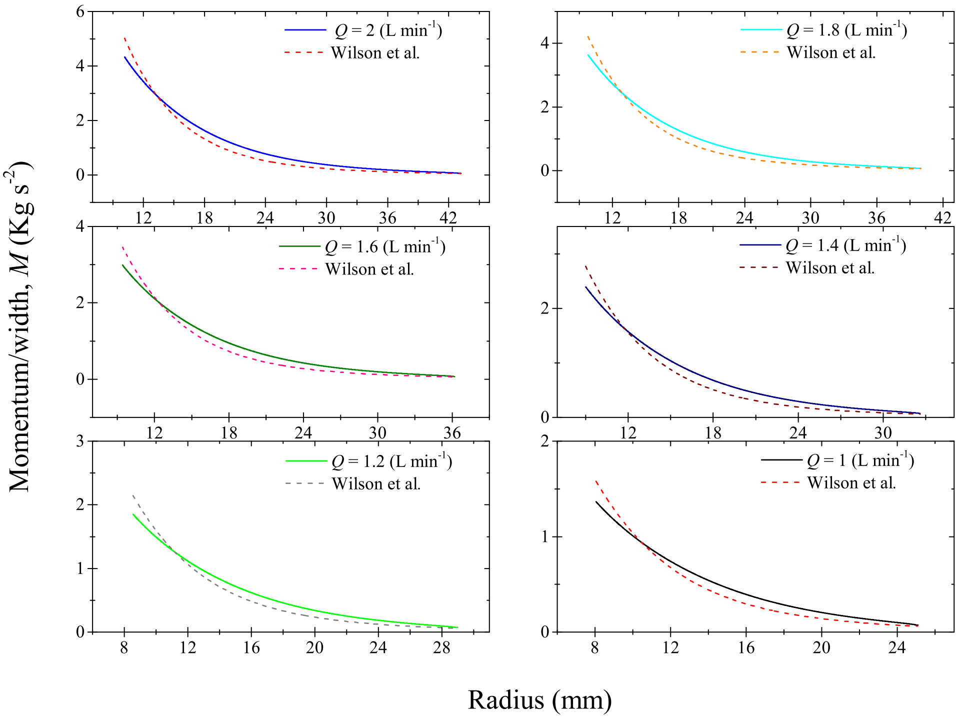

Figure 3.4 Comparison of the radial distribution of the momentum per unit width, M. Dashed curve show the prediction using Wilson et al. (2012) whereas the solid curve show prediction from the present study.

At a larger radius, the mean radial velocity predicted by the present theoretical description has a higher value which, matches with Wilson et al.'s prediction at the location of the hydraulic jump. Moreover, there is an evident difference in the predicted velocities, nevertheless Wilson et al.'s theory gives a reasonable engineering estimate of the velocity which could be easy to implement for its application in cleaning, heat and mass transfer.

Figure 3.4 compares the momentum per unit width, M, as a function of the radial position. Again at smaller radii Wilson et al. (2012) predict slightly higher values of the radial momentum however, the two show a similar value at the location of the hydraulic jump. This implies that both theories satisfy the jump condition given in 3.12 at same radial location, and hence predict the same hydraulic jump radius.

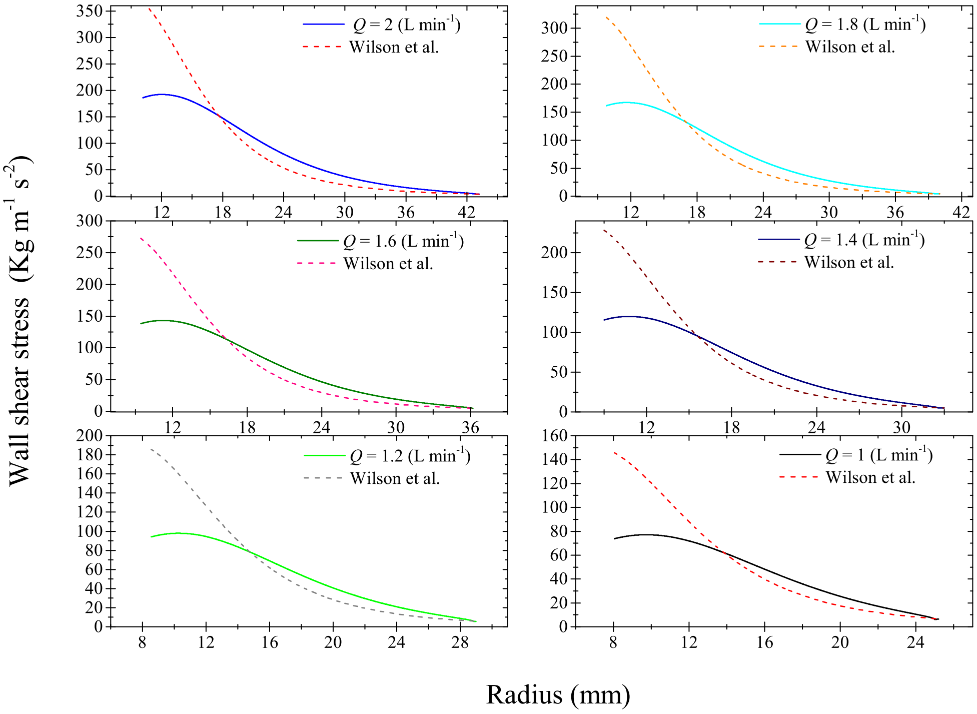

Figure 3.5 Comparison of estimated wall shear stress distributions. Dashed curve show the prediction using Wilson et al. (2012) whereas solid curve show prediction from the present study.

The wall shear stress was calculated using equations 3.8 and 3.11 and compared for a range of flow rates ($0.8 - 2\,\mathrm{L\,min^{-1}}$) and a nozzle diameter $d = 2\,\mathrm{mm}$. At smaller radii, the wall shear stress predictions from Wilson et al. (2012) are almost 2 orders of magnitude higher compared to the present model, which rapidly decreases and give similar value at larger radii. The simple model which ignores the boundary layer formation and the detailed theory presented here do not show good agreement for the wall shear stress. This is further discussed in Section 4.5.4 .

3.5 Conclusions

In § 2, we solved the mechanical energy equation and obtained the governing equation describing the flow field created by impinging liquid jets. In this chapter, it was shown that the momentum based approach agree with the energy based approach. The main aims of the current chapter were to, (1) show that the energy and momentum based approach yield same results, (2) compare the current results with existing literature to reconcile and find the limitation of the existing theories, (3) to find the shortcomings of the existing literature and identify; why existing theories failed to answer the question 'What gives birth to a hydraulic jump?'

The theoretical analysis presented in § 3.3 show that the slope of the liquid film and the force due to surface tension cannot be ignored. At a smaller radius, surface tension does not produce a large correction. However, at a larger radius the liquid momentum per unit width, M, is comparable to the force due to surface tension and produces large corrections. At the location of the hydraulic jump, liquid momentum equals the surface tension.

We compared the average velocity predicted by Wilson et al. (2012) and the current theory, and both theories give similar prediction for the average velocity. In § 4.4.3 we will show that the current theory gives good agreement with experimental data though the Wilson et al. prediction provides reasonable engineering estimate of the average velocity in the liquid film. Similarly, both theories give similar values of momentum per unit width, M. Wilson et al. (2012) gives sufficiently reasonable prediction of the average velocity and momentum, and due to its simplicity, it could be easier to implement it for applications such as cleaning, where the rate of cleaning is proportional to the momentum in the film (Bhagat et al. (2017); Glover et al. (2016); Wang et al. (2013a); Wilson et al. (2014, 2015)).

The prediction for the wall shear stress was compared for both the theories. Wilson et al. consistently gives higher value of the wall shear stress compared to the predictions from the current theory. This is due to the fact that Wilson et al. (2012) flow model ignored the initial development of the boundary layer and assumed a fully developed liquid film from the perimeter of the footprint of the impinging jet and beyond. Therefore, Wilson et al. (2012)'s theory can not be applied for cases where shear stress is the driving force of action, such as an erosive cleaning process.

Chapter 4

Flow field created by impinging liquid jets when liquid film becomes turbulent

4.1 Introduction

§ 3 compares the energy based approach to describe the flow field (See § 2) with the momentum based approach which is widely used in the literature (For example see; Bohr et al. (1993); Bush and Aristoff (2003); Kasimov (2008); Mathur et al. (2007); Watson (1964); Wilson et al. (2012)). The conclusions from § 3 that, although the previous momentum based approach is not accurate, it gives a reasonable estimate of the velocity and momentum in the radial flow zone, RFZ (see figure 4.1). These quantities are widely used for applications such as cleaning and heat transfer, and the momentum based approach ignoring surface tension could be easier to implement for engineering applications. In this chapter, the discussion is extended to higher Reynolds number flows, where the thin liquid film in the RFZ becomes turbulent. The transition to turbulence in the thin liquid film results in higher rates of heat and mass transfer, which is discussed in this chapter.

Turbulent liquid jets (Re > 20000) are widely used for cleaning, with applications ranging from the internal and external surfaces of processing and storage vessels (Burfoot and Middleton (2009)), to kitchenware in dishwashers (Pérez-Mohedano et al. (2015)). Liquid jets impinging on solid surfaces are also employed in process intensification for enhancing local heat transfer rates (Lienhard, 1995) . High speed jets can also be used for cutting (Leach and Walker, 1966). In cleaning applications, knowledge of the flow pattern created by the jet is important for determining local cleaning rates as well as predicting wetting and draining behaviour. § 2 describes '*what gives birth to a hydraulic jump in a thin laminar liquid film*'. The present chapter describes the hydrodynamics of thin liquid films at higher flow rates and jet Reynolds numbers when the liquid film becomes turbulent.

On normal impingement of a horizontal jet onto a vertical surface, liquid spreads radially outwards and changes its film thickness abruptly and forms an approximately circular hydraulic jump (See figure 2.1 b). In this scenario, gravity is coplanar to the direction of flow and it influences the thick liquid film beyond the hydraulic jumps, profoundly. Hence, below the point of impingement, the accelerating liquid film forms a draining film. Above the point of impingement, the slow liquid beyond hydraulic jump, flows circumferentially in a rope (see figure 4.1). Moreover, the hydraulic jump demarcates the region where the liquid velocity is higher and hence shear stress and momentum is higher which is interesting, considering its application in cleaning and heat transfer. It also roughly demarcates the horizontal spread of the liquid on a vertical surface.

Many cleaning applications involve walls which are close to vertical. For high flow rate jets, for which the radial spread is large, the influence of gravity gives rise to less symmetric flow patterns on a vertical wall. This chapter therefore focuses on the flow patterns generated on a vertical wall. When a coherent horizontal jet impinges on a vertical wall, as shown in figure 4.1, the liquid initially spreads out in a thin film in a region which is here labelled the radial flow zone, RFZ. At some radial position the outwards momentum in the film is countered by surface tension or when $We \approx 1$ and a jump is observed: it is here termed the film jump to highlight the flow being on a vertical surface. For high flow rate jets on a vertical plate, the radial spread could be large and unlike the horizontal case, where gravity is perpendicular to the radial velocity, here gravity is coplanar to the flow. Therefore, for a high flow rate jet on a vertical surface, gravity can cause the location of the film jump to vary with azimuthal position, θ. Hence, to describe the variation of film jump in azimuthal direction, the film jump radius will be indicated as R_θ.

Below the level of impingement (marked AA′ on figure 4.1), the rope and radial flow spread out further to generate a falling film which may narrow further downstream.

Morison and Thorpe (2002) reported the first systematic study of liquid jets impinging on vertical walls. Wilson et al. (2012) presented a model for the flow in the RFZ which gave good agreement with Morison and Thorpe's data for the half width of the RFZ (R_{90°) on the plane AA′, in figure 4.1, as well as new experimental data

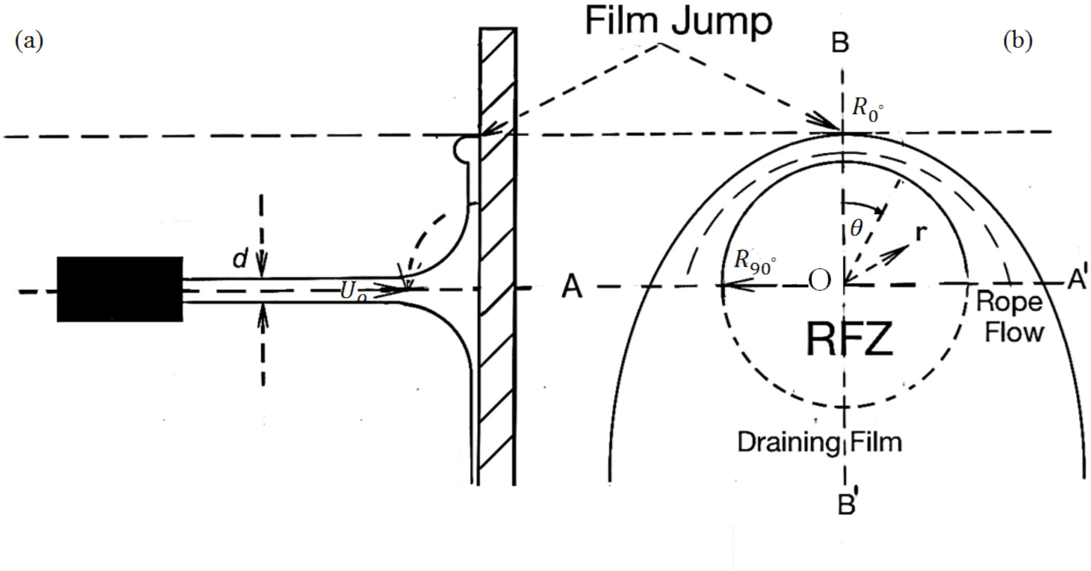

Figure 4.1 Schematic of flow pattern formed by a jet impinging normally on a vertical wall. (a) side view through section BB' (b) front view. O is the point of impingement, U_o is the jet velocity and d is the jet diameter.

sets. The dimensions of the RFZ for obliquely impinging jets and the flow behaviour have since been investigated by Wilson and co-workers (Wilson et al. (2012), Wang et al. (2013a),Wang et al. (2015, 2013b), Aouad et al. (2016)) as well as by other groups (*e.g.* Gordeev et al. (2016)).

In the model of Wilson et al. (2012) the flow in the film is treated as laminar, with a parabolic velocity profile similar to that in Nusselt's analysis of film condensation Nusselt (1916) (see § 3). The location of the film jump was obtained from a balance between the outward flow of momentum in the liquid and the retarding force provided by surface tension. At higher flow rates, approaching those of interest for industrial cleaning applications, their model tended to overpredict the location of the film jump (Wang et al., 2013b). Their model included a contribution from the wall material, via the contact angle β (see § 3.3.2), which was not observed experimentally: moreover, similar RFZ dimensions were found on walls with different wetting characteristics. In § 2, It has been shown that these thin-film hydraulic jumps result from energy losses due to surface tension and viscous forces alone. In the scenario where vertical jets fall on a horizontal surface, gravity is always perpendicular to the radial direction (or gravity is perpendicular to the flow plane) which manifests in the form of gravity waves *viz.* the Froude number is therefore incorporated into the condition for hydraulic jumps; $We^{-1} + Fr^{-2} = 1$. However, in the vertical plane, gravity and radial coordinates are coplanar hence Froude number will disappear from the governing equation and the condition for hydraulic jump becomes $We = 1$.

In the control volume analysis presented in § 2, Watson's similarity velocity profile was used to account for the velocity distribution in the vertical direction. The evolution of velocity profile has not been considered in this analysis. However, at higher flow rates the liquid film is likely to enter the turbulent regime (see Azuma and Hoshino (1984*a*,*b*); Lienhard (2006)) and the laminar film (or Nusselt film behaviour assumed by Wilson et al. (2012)) is unlikely to be valid for the whole film hence, the evolution of the velocity profile must be considered. The aim of this study is to revisit the treatment of the flow of the liquid film in the RFZ for horizontal (and inclined) jets impinging on vertical walls, incorporating the effect of turbulence in the film. The analysis is guided by the results from §3 and § 2, *i.e.* hydraulic jump occurs when $We \approx 1$ and downstream transport of surface energy term dominates only close to the hydraulic jump radius, therefore, in rest of the film it can be ignored. The results are compared with data reported in previous studies in the literature as well as new estimates of the average velocity in the film obtained from observation of the early stages of jet impingement. Several features of the flow in the RFZ, including the transitions in wave behaviour and heat transfer performance reported by Azuma and Hoshino (1984*a*,*b*),; Liu et al. (1991) and Lienhard (1995) are compared with the results from the analysis.

The primary objective was to establish the limit of validity of the previous approaches/models, in addition to providing a description for faster jets.

In most part this work has been published in the journal *Chemical Engineering Science* (Bhagat and Wilson, 2016). I developed the theory, conducted the experiments and analysed data. I drafted the manuscript which Prof Ian Wilson and I edited. Text from this paper appears in this chapter.

4.2 Model development

Figure 4.2 shows an isometric sectioned view (through AA' in figure 4.1) of the flow profile created by normal impingement ($\phi = 90^o$) of a coherent liquid jet on a vertical surface (through the plane AA' in the figure 4.1). Where ϕ is the angle of inclination between the wall and the liquid jet. In figure 4.2, the key regions are labelled: (i) the radial flow zone (RFZ); (ii) the boundary of the radial flow zone, the film jump; (iii) the rope region; and (iv) the draining film. The RFZ is important for cleaning applications as the wall shear stress and momentum in the film are greatest in this region.

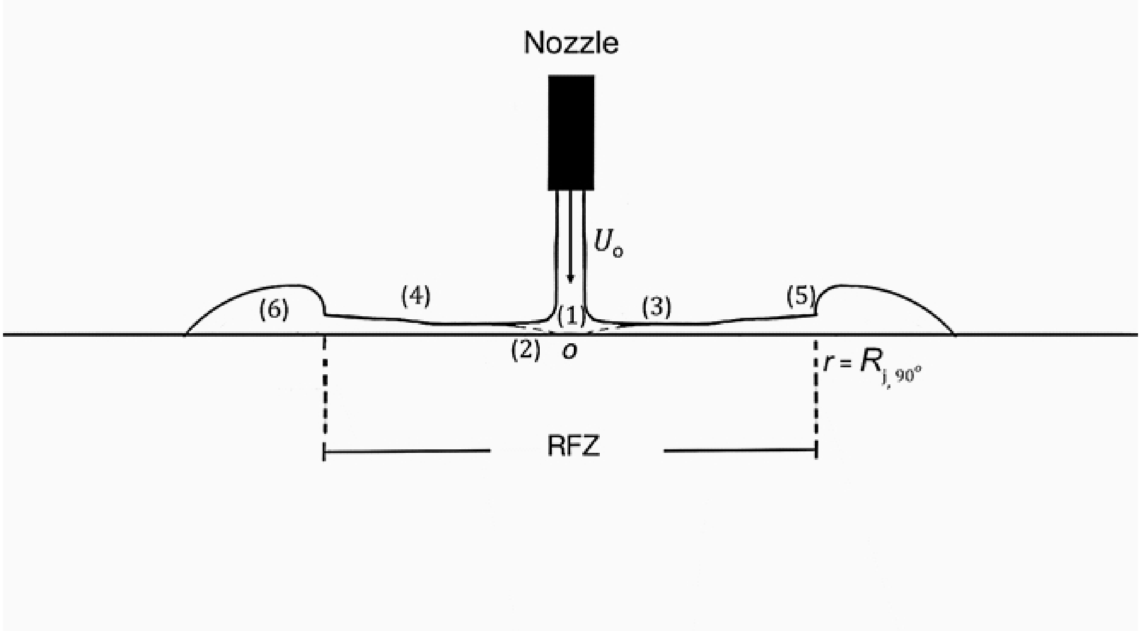

Figure 4.2 Schematic of cross-section through the radial flow zone and the film jump at $\theta = 90°$ (isometric sectioned view). The different flow zones are: (1) stagnation region; (2) boundary layer formation, shown by dashed line; (3) boundary layer reaches the surface and laminar flow zone starts; (4) laminar to turbulent transition; (5) film jump; (6) rope. O is the point of impingement.

The model is presented in three sections. The first section deals with the flow in the film for a jet impinging perpendicularly on a vertical wall. The second considers the formation of the film jump. The third considers the case where the jet impinges obliquely (*i.e.* $\phi < 90^o$ or $\phi > 90^o$).

4.2.1 Normal impingement of a jet on a vertical surface

For the range of flow rates used in the present analysis, the velocity component in the azimuthal direction, v_θ, arising due to gravitational acceleration is small compared to the radial component of velocity $\bar{u}$. Therefore ignoring the component of velocity in the azimuthal direction and applying the boundary layer approximation for a two-dimensional film flow, the governing differential equations for an axisymmetric film flowing radially away from the point of impingement are:

$$\frac{1}{r}\frac{\partial(ur)}{\partial r} + \frac{\partial v}{\partial z} = 0 \qquad \text{(Continuity equation)} \qquad (4.1)$$

$$u\frac{\partial u}{\partial r} + v\frac{\partial u}{\partial z} = \frac{1}{\rho}\frac{\partial p}{\partial r} + \frac{\mu}{\rho}\frac{\partial^2 u}{\partial^2 z} - g\cos\theta \quad \text{(Navier Stokes equation)} \tag{4.2}$$

Cylindrical co-ordinates are used and the boundary conditions are

$$u = v = 0 \qquad atz = 0 \qquad \text{(No slip at wall)}$$

$$\frac{\partial u}{\partial z} = 0 \qquad at \quad z = h \qquad \text{(No shear stress at the free surface)}$$

Conservation of volume yields

$$Q = \int_0^h \int_0^{2\pi} urdzd\theta \tag{4.3}$$

The jets in the present study feature $6300 < Re < 32000$, which lie in the turbulent regime: Landreth and Adrian (1990) discussed the criteria for liquid jets to be turbulent and used PIV measurements on impinging liquid jets to confirm the presence of turbulent characteristics in cases where $Re = 6560$.

The pressure gradient in radial direction, $\frac{\partial p}{\partial r}$, is set to zero (ignoring pressure due to radial curvature (see § 2) and parallel streamlines). Integrating equations 4.1 and 4.2 and applying Leibniz' rule yields the momentum integral equation

$$\frac{1}{r}\int_0^h u^2 rdz - \frac{\mu}{\rho}\frac{\partial u}{\partial r}\bigg|_{z=0} - hgcos\theta \tag{4.4}$$

In the following analysis, mirroring that of Azuma and Hoshino (1984*b*), the film flow is sub-divided into three zones (see figure 4.2): (i) the boundary layer formation zone (BLFZ), (ii) the laminar zone (LZ), and (iii) the turbulent zone (TZ).

4.2.2 Boundary layer formation zone

In the BLFZ, it is assumed that the influence of the wall is restricted to within the growing boundary layer, of thickness δ. Beyond the boundary layer the local velocity is initially that of the jet, U_o: this velocity is not influenced by the wall but is subject to gravitational acceleration, giving,

$$u_s(r) = \sqrt[2]{U_0^2 - 2gr\cos\theta} \tag{4.5}$$

Re-writing equation 4.4 for the BLFZ gives

$$\frac{1}{r}\frac{d}{dr}\int_0^\delta u^2 r dz + \frac{1}{r}\frac{d}{dr}\int_\delta^h u^2 r dz = \frac{-\mu}{\rho}\frac{\partial u}{\partial z}\Big|_{z=0} - hg\cos\theta \tag{4.6}$$

Within the boundary layer, the velocity profile is assumed to be described by a similarity solution of the form

$$u(r,z) = u_s(r)f(\eta) \qquad \text{where} \qquad \eta \equiv \frac{z}{\delta} \tag{4.7}$$

Substituting equation 4.7 into 4.6 and integrating gives

$$\frac{1}{r}\frac{d}{dr}(u_s^2 r\delta)\int_0^1 f^2(\eta)d\eta + \frac{1}{r}\frac{d}{dr}(u_s^2 r(h-\delta)) = \frac{\mu}{\rho}\frac{U_o}{\delta}f'(0) - hg\cos\theta \tag{4.8}$$

writing $\int_0^1 f^2(\eta) = C_2$ and $f'(0) = C_3$ allows equation 4.8 to be re-written as

$$C_2\frac{1}{r}\frac{d}{dr}(U_o^2 r\delta) + \frac{1}{r}\frac{d}{dr}(U_o^2 r(h-\delta)) = \frac{\mu}{\rho}\frac{U_o}{\delta}f'(0) - hg\cos\theta \tag{4.9}$$

Applying conservation of volume (equation 4.3) to the two regions of the film gives

$$Q = r\int_0^{2\pi}\int_0^\delta u dz d\theta + r\int_0^{2\pi}\int_0^\delta u_s dz d\theta \tag{4.10}$$

For small values of r,

$$\int_0^{2\pi}\sqrt[2]{(U_o^2 - 2grcos\theta)}d\theta \approx 2\pi U_o \tag{4.11}$$

Hence, equation 4.10 can be written as,

$$\frac{Q}{2\pi} = rU_o\delta\int_0^1 f(\eta)d\eta + rU_o(h-\delta) \tag{4.12}$$

writing $\int_0^1 f(\eta)d\eta = C_1$ gives,

$$h = \frac{Q}{2\pi rU_o} + \delta(1-C_1) \tag{4.13}$$

Substituting equation 4.13 into 4.9 yields

$$\frac{d(\delta^2)}{dr} = -\frac{2\delta^2}{r} - \frac{2\delta^2 gcos\theta}{U^2}\frac{1-2C_2+C_1}{C_1-C_1} - \frac{2C_3\mu}{\rho U(C_2-C_1)} + \frac{Qgcos\theta\delta}{\pi U_o(C_2-C_1)U^2 r} \tag{4.14}$$

For a given velocity profile, equation 4.14 gives the thickness of the boundary layer at position r and, from equation 4.13, the film thickness, h.

In this analysis, the velocity profile in the boundary layer and in laminar region is assumed to be a fourth order polynomial in z, with

$$u(r,z) = \begin{cases} u_s(r)f(\eta) & \text{if } 0 \leq z \leq \delta \\ u_s(r) & \text{if } \delta < z \leq h \end{cases} \tag{4.15}$$

Where,

$$f(\eta) = a_1 + a_2\eta + a_3\eta^2 + a_4\eta^3 + a_5\eta^4 \tag{4.16}$$

Equation 4.16 must satisfy the following two boundary conditions;

$$f(0) = 0 \qquad \text{no slip condition} \tag{4.17}$$

Ignoring stress due to surface tension, no shear at free surface condition was imposed

$$f'(1) = 0 \qquad \text{free surface condition} \tag{4.18}$$

Beyond the boundary layer, the fluid velocity is the surface velocity, giving

$$f(1) = 1 \qquad \text{surface velocity condition} \tag{4.19}$$

The experimental measurements of the velocity profile in such thin films by Stevens and Webb (1993) show a linear velocity profile (see figure 4.3), $f(\eta) = \eta$ near the wall rather than a parabolic one, $f(\eta) = 2\eta - \eta^2$ (as used by Wilson et al. (2012)) or a cubic, $f(\eta) = \frac{3}{2}\eta - \eta^3$(see Liu et al. (1991); Schlichting et al. (1974)). The remaining two coefficients in equation 4.16 were therefore found by setting the wall behaviour to be linear. This requires

$$C_1 = \int_0^1 f(\eta)d\eta = \frac{1}{2} \tag{4.20}$$

$$C_3 = f'(0) = 1 \tag{4.21}$$

and yields the result.

$$f(\eta) = \eta - \frac{3\eta^2}{2} + 4\eta^3 - \frac{5\eta^4}{2} \tag{4.22}$$

This velocity profile gave good agreement with the Laser Doppler velocimetry results reported by Stevens and Webb (1993) (see figure 4.3). It will also be shown later (see §4.4.2) that the transition from smooth concentric waves to chaotic surface waves observed in experiments is described reasonably well by the model, when the velocity profile in the developing film is described by equation 4.22.

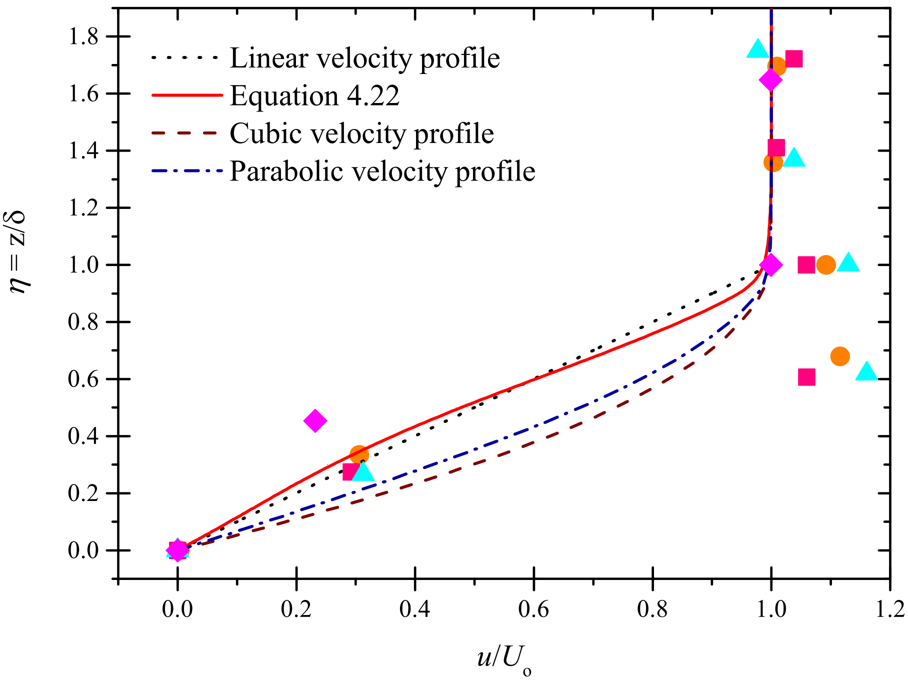

Figure 4.3 Comparison between equation 4.22, linear, parabolic, cubic velocity profile with the data extracted from experimental velocity profile reported by Stevens and Webb (1993). Different symbols indicates separate data sets with different film thickness

Equations 4.14, 4.15 and 4.16 are solved numerically for a given value of θ to give the local film thickness and velocity. For the case where $\theta = 90°$, gravity has no effect and an analytical solution to 4.14 can be obtained, viz.

$$\delta = 2.12\sqrt{\frac{\mu r}{\rho U_o}} \qquad \text{for} \qquad \theta = 90° \tag{4.23}$$

Substituting this result into equation 4.13 gives the film thickness profile along AA′ in the BLFZ,

$$\frac{h}{d} = 0.125\left(\frac{d}{r}\right) + \frac{1.06}{\sqrt[2]{Re}}\sqrt[2]{\frac{r}{d}} \tag{4.24}$$

Equation 4.3 then gives the following relationship between film thickness, h, and average velocity $\bar{u}$ at radial position r:

$$rh\bar{u} = \frac{Q}{2\pi} = \frac{d^2U_o}{8} \tag{4.25}$$

Solving equations 4.24 and 4.25 yields the average velocity in the BLFZ:

$$\bar{u} = \frac{U_o}{8(\frac{r}{d})(0.125(\frac{d}{r}) + \frac{1.06}{\sqrt[2]{Re}}\sqrt{\frac{r}{d}})} \tag{4.26}$$

The radius where the boundary layer reaches the free surface, labelled r_b, and beyond which liquid flows as a fully developed laminar film, is calculated by setting $h = \delta$ in equation 4.13. An analytical result is available for $\theta = 90°$, viz.

$$\frac{r_b}{d} = 0.24\sqrt[3]{Re} \tag{4.27}$$

The film thickness predicted by the above model is similar to that reported by previous workers: Azuma and Hoshino (1984*b*); Liu et al. (1991); Watson (1964)) all reported expressions of the form $\frac{r_b}{d} = \mathcal{O}(\sqrt[3]{Re})$. Watson (1964) obtained $\frac{r_b}{d} = 0.1833(\sqrt[3]{Re})$ for his similarity profile, whilst Liu et al. (1991) found that a cubic velocity profile gave $\frac{r_b}{d} = 0.1773(\sqrt[3]{Re})$

4.2.3 Laminar film zone (LZ)

Beyond r_b the liquid flows in a fully developed laminar film which eventually becomes turbulent (Azuma and Hoshino (1984*a*,*b*)). In the LZ, the velocity profile is again assumed to be described by the fourth order polynomial, for consistency with the $BLFZ$. In the LZ, however, $\eta = \frac{z}{h}$. Equation 4.15 becomes:

$$u = u_s(r)f(\eta) \qquad 0 \le z \le h \tag{4.28}$$

Solving equations 4.4, 4.22, and 4.28 with the initial condition that at $r = r_b$, $u_b = \frac{1}{2}\sqrt[2]{(U_o^2 - 2gr_b\cos\theta)}$, yields the velocity profile in the laminar zone.

$$\frac{d\bar{u}}{dr} = -\frac{(5.7\pi^2\mu\bar{u}^2r^2)}{Q^2\rho} - \frac{0.714gcos\theta}{\bar{u}} \tag{4.29}$$

This requires numerical integration except at $\theta = 90°$, where integrating equation 4.4 with the boundary condition $\bar{u} = \frac{U_o}{2}$ at $r = r_b$ gives

$$\left(\frac{Q}{\pi}\right)^2 \left(\frac{1}{\bar{u}} - \frac{1}{U_o/2}\right) = 1.9\frac{\mu}{\rho}(r^3 - r_b^3) \quad \text{for} \quad \theta = 90° \tag{4.30}$$

The average velocity in the film, $\bar{u}$, is

$$\bar{u} = \frac{U_o}{8\frac{r}{d}\left(\frac{3.792}{Re_j}(\frac{r}{d})^2 + 0.1975(\frac{d}{r})\right)} \tag{4.31}$$

This can be compared with the velocity profile obtained by Wilson et al. (2012), who assumed the film to have a fully developed parabolic velocity profile (*i.e.* a Nusselt film) where $r > \frac{d}{2}$:

$$\left(\frac{1}{\bar{u}} - \frac{1}{U_o/2}\right) = \frac{10\pi^2\mu}{3Q^2\rho}\left(r^3 - \left(\frac{d}{2}\right)^3\right) \tag{4.32}$$

This can be rearranged for comparison with equation 4.31:

$$\bar{u} = \frac{U_o}{8\frac{r}{d}\left(\frac{6.667}{Re}(\frac{r}{d})^2 + \frac{(3Re-20)}{24(Re)}(\frac{d}{r})\right)} \approx \frac{U_o}{8\frac{r}{d}\left(\frac{6.667}{Re}(\frac{r}{d})^2 + 0.125(\frac{d}{r})\right)} \tag{4.33}$$

There is evident similarity between 4.31 and 4.33, providing some insight into the good agreement seen with the Wilson et al. model. It predicts similar trends.

Solving equations 4.25 and 4.31 gives the film thickness in the LZ as

$$\frac{h}{d} = \left(\frac{3.792}{Re}(\frac{r}{d})^2 + 0.1975(\frac{d}{r})\right) \tag{4.34}$$

4.2.4 Laminar to turbulent transition

The laminar film eventually becomes turbulent at radius r_t. Watson (1964) used the approximate result of Lin (1945) to determine the transition radius. Azuma and Hoshino (1984*a*,*b*) and Liu et al. (1991) found that Watson's turbulent model did not give good agreement with their experimental data and both groups presented alternative correlations for $\frac{r_t}{d}$. Azuma and Hoshino set r_t to be the location where the film has granular waves of very small wave-length and they described these waves as sandpaper-like waves (see Azuma and Hoshino (1984*a*,*b*)). Liu et al. (1991) used two criteria: (i) where the smooth laminar film lost its transparency and became a rough light scattering surface; and (ii) where there was a noticeable increase in the local Nusselt number (heat transfer coefficient). The latter results are compared with the new model in figure 4.10. In the experiments, the transition is taken to be where smooth regularly spaced concentric waves become more chaotic. It will be shown that the correlations presented by Azuma and Hoshino (1984*a*,*b*) and Liu et al. (1991) give less good prediction of these features.

Dou (2006) and Dou and Khoo (2010) proposed a mechanism for the laminar-turbulent transition based on flow instability. Duo proposed that the instability in a viscous flow can arise from the relative magnitude of the energy gradient in the transverse z direction to that in the streamline r direction arising from viscous friction. A large energy gradient in the transverse direction can potentially amplify a disturbance while that in the streamline direction can absorb these disturbances. From their analysis they concluded that, for pressure driven flows, an inflection in the velocity profile can give rise to turbulence. For shear driven flows, the condition for the transition is the existence of a zero velocity gradient in the velocity profile of the averaged flow (Dou and Khoo (2010)).

The flow field created by an impinging jet is a shear driven flow, where turbulence is promoted by surface waves, unlike the boundary layer on a flat plate where turbulence starts from the wall (Kline et al. (1967) ;Azuma and Hoshino (1984*a*,*b*); Dou and Khoo (2010)). The experiments which I have conducted, the jet has a varicose shape owing to the Rayleigh-Plateau instability (Rayleigh (1892)), which on impingement creates surface waves on the film (Azuma and Hoshino (1984*a*,*b*)). It has been postulated that the change in surface wave behaviour can be promoted by the existence of a singularity in the variation of energy with film thickness. This can amplify a disturbance and convert a smooth laminar flow into a more chaotic flow: such a location in the film can be a point of transition. It is acknowledged that the hypothesis needs to be proven theoretically and experimentally. The energy flux per unit width of the film is given by;

$$E = \rho \bar{u}^3 h + \rho g r \bar{u} h \cos\theta \tag{4.35}$$

Substituting $\bar{u}$ from equation 4.25 into 4.35

$$E = \rho(\frac{d^2 U_o}{8hr})^3 h + \frac{Q}{2\pi}\rho g \cos\theta \tag{4.36}$$

The variation with film thickness is

$$\frac{dE}{dh} = \frac{\partial E}{\partial r}\frac{dr}{dh} + \frac{\partial E}{\partial h} \tag{4.37}$$

Hence

$$\frac{dE}{dh} = \frac{-3d^6U_o^3}{256r^4h^2}\frac{1}{(\frac{dh}{dr})} - \frac{d^6U_o^3}{128r^3h^3} \tag{4.38}$$

When $\frac{dh}{dr} = 0$ in the laminar region, there is a singularity in $\frac{dE}{dr}$ and this is associated with instability in the film. The condition for instability in film is then

$$\frac{dh}{dr} = 0 \qquad \text{(In laminar region)} \tag{4.39}$$

Solving equations 4.34 and 4.39 yields the transition radius, r_t, for the case where $\theta = 90°$ as

$$\frac{r_t}{d} = 0.2964\sqrt[3]{Re} \tag{4.40}$$

4.2.5 Turbulent region (TZ)

At low jet Reynolds numbers, the film jump may occur before the laminar-turbulent transition. In cases where the film does become turbulent, the velocity profile is assumed to follow a $\frac{1^{th}}{7}$ power law and the wall shear stress, τ_w, is calculated from the Blasius law (Azuma and Hoshino (1984*a*,*b*) Azuma and Hoshino (1984*a*,*b*); Liu et al. (1991); Schlichting et al. (1974)).

$$\frac{u}{u_s} = \eta^{\frac{1}{7}} \tag{4.41}$$

$$\frac{\tau_w}{\rho u_s^2} = 0.225\left(\frac{\mu}{\rho u_s h}\right)^{1/4} \tag{4.42}$$

Ignoring the azimuthal component of velocity and integrating equation 4.3 for a $\frac{1^{th}}{7}$ power law velocity profile (equation 4.41) yields

$$\frac{Q}{2\pi} = \frac{7}{8}u_s rh = \bar{u}rh \tag{4.43}$$

Substituting Equation 4.43 into equation 4.42 gives

$$\frac{\tau_w}{\rho u_s^2} = \frac{0.0366}{\sqrt[4]{Re}}\sqrt[4]{\frac{r}{d}} \tag{4.44}$$

Rearranging equation 4.4 and integrating with respect to η gives

$$\frac{u_s r h}{r}\frac{du_s}{dr}\int_0^1 f^2(\eta)d\eta = -\frac{\tau_w}{\rho} - gh\cos\theta \tag{4.45}$$

Equation 4.45 can be further simplified to

$$\frac{d\bar{u}}{dr} = -0.04706\frac{2\pi}{Q}\frac{\sqrt[4]{r^5}}{\sqrt[4]{Re}}\bar{u}^2 - \frac{64}{63}\frac{g\cos\theta}{\bar{u}} \tag{4.46}$$

At r_t, continuity requires $\bar{u}$ (laminar) $=$ $\bar{u}$ (turbulent) $= u_t$. The velocity distribution can then be calculated.

For $\theta = 90°$, equation 4.46 can be solved with the initial condition, $u_t = 0.422U_o$ at $r = r_t = 0.2964d\sqrt[3]{Re}$. The result is

$$U_o d^2\left(\frac{1}{\bar{u}} - \frac{1}{U_t}\right) = \frac{0.1673}{\sqrt[4]{Re}}\sqrt[4]{r^9}\Big|_{r_t}^{r} \tag{4.47}$$

Rearranging equation 4.47 yields

$$\bar{u} = \frac{U_o}{\frac{0.167}{\sqrt[4]{Re}}\sqrt[4]{\left(\frac{r}{d}\right)^9} + \left(2.37 - 0.0108\sqrt[2]{Re}\right)} \tag{4.48}$$

Substituting for $\bar{u}$ into Equation 4.43 gives the local film thickness:

$$\frac{h}{d} = \frac{0.0209}{\sqrt[4]{Re}}\sqrt[4]{\left(\frac{r}{d}\right)^5} + \left(0.296 - 0.001356\sqrt[2]{Re}\right)\left(\frac{d}{r}\right) \tag{4.49}$$

For angles other than 90°, the velocity is obtained by numerical integration. Examples of the predicted velocity distribution, *i.e.* $\bar{u}$ versus r, are compared with new experimental measurements.

4.2.6 Hydraulic jump/ Film jump

High speed video of the initial stages of formation of the RFZ was used to obtain estimates of $\bar{u}$ for comparison with the above theory. An example of the early stages of a jet impinging perpendicularly on to a vertical wall is provided as (can be seen as video 1 at https://doi.org/10.1016/j.ces.2016.06.011). Initially the liquid spreads out in an almost circular front. After a short period the liquid stops spreading outwards and the rope forms. The location of the film jump at $\theta = 90°$ does not change position with time: the rope falls beyond location $R_{90°}$ (see figure 4.1). At $\theta = 0°$,

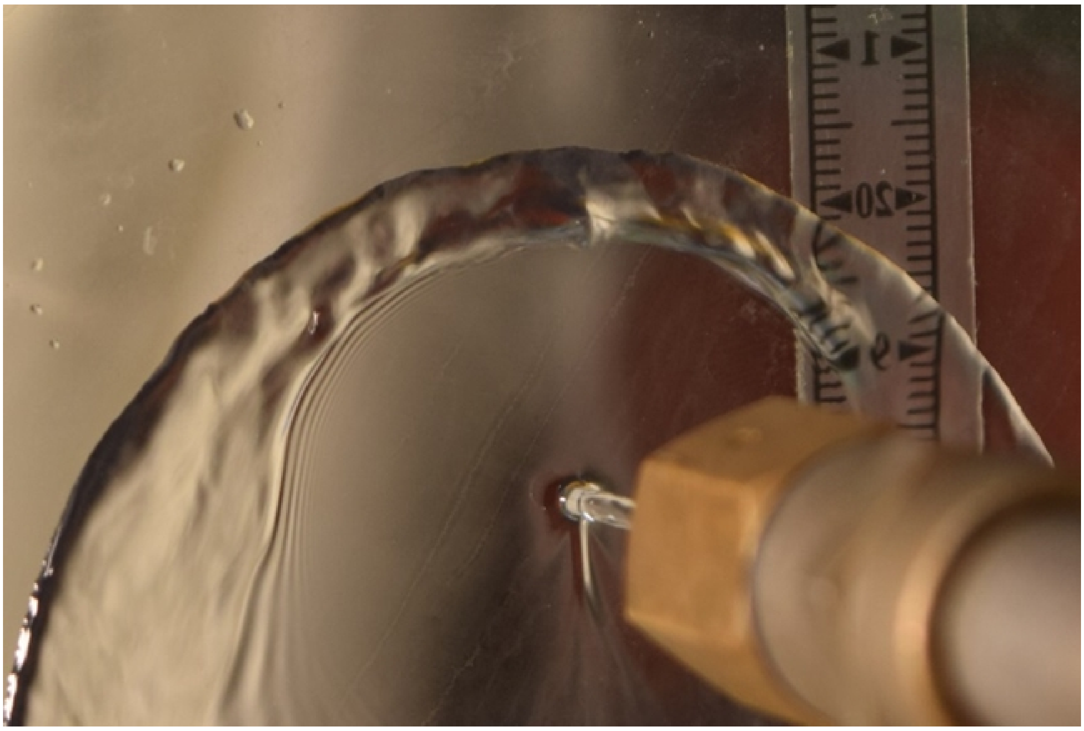

Figure 4.4 Photograph shows the flow in the RFZ and rope: photograph on glass wall ($Re = 22,200$, $\phi = 90°$, nozzle diameter 2 mm)

directly above the point of impingement, once the rope forms gravity causes it to fall back over the spreading film. Therefore, in the upward direction, against gravity, the film jump is first found to occur at the outer edge of the rope and R_{0°, is marked accordingly in figure 4.1. With a hydrophilic wall material the rope spreads outward and the film jump is then located somewhere inside the rope. At R_{90° gravity does not cause the rope to move towards the film jump and the jump is located at the inner edge of the rope.

In 3.3.2, it is shown the criteria for a hydraulic/film jump is,

$$We \approx 1 \tag{4.50}$$

Or when momentum equals the surface tension, for turbulent film therefore, this is where

$$M = \frac{\rho \frac{64}{63} \frac{Q}{2\pi} U_o}{r\left(\frac{0.167}{\sqrt[4]{Re}}\sqrt[4]{\left(\frac{r}{d}\right)^9} + \left(2.37 - 0.0108\sqrt[2]{Re}\right)\right)} = \gamma \tag{4.51}$$

4.2.7 Obliquely impinging jet

The analysis is now extended to a liquid jet impinging obliquely on to a vertical surface. Immediately after impingement, the jet velocity, U_o, remains the same; however, the amount of liquid flow per unit width varies with θ. The azimuthal component of velocity is again omitted from the analysis. However, due to inclination of the jet, the amount of liquid flowing radially depends on θ.

The distribution of flow for an obliquely impinging jet presented by Kate et al. (2007) was used by Wang et al. (2013b) and is used here. Oblique impingement of a circular jet gives an elliptical zone of impact (see Figure 4.5). Kate et al. showed that one of the foci of the ellipse, labelled S on Figure 4.5(b), acts as a source and the liquid moves radially away from this point. The radial distance from the source to the edge of the impingement zone, r_e, subtended by angle θ is

$$r_e = r_o \frac{\sin\phi}{(1 + \cos\theta\cos\phi)} \tag{4.52}$$

where r_o is the radius of the jet. Wang et al. (2013b) showed that the local average velocity in the RFZ is given by

$$r\bar{u}h = \frac{1}{2}U_o r_e^2 \sin\phi \qquad \text{for} \quad r > r_e \tag{4.53}$$

Following the treatment leading to Equations 4.11, 4.12, 4.13 and 4.53, the film thickness in the BLFZ with oblique impingement is given by

$$h = \frac{U_o r_e^2 \sin\phi}{2rU_o} + (1 - C_1)\delta \tag{4.54}$$

Solving equations 4.9 and 4.54 yields the equation for the evolution of boundary layer thickness

$$\frac{d(\delta^2)}{dr} = -\frac{2\delta^2}{r} - \frac{2\delta^2 g\cos\theta}{u_s^2}\frac{(1 - 2C_2 + C_1)}{(C_2 - C_1)} - \frac{2C_3\mu}{\rho u_s(C_2 - C_1)} + \frac{r_e^2 g\delta\sin\phi\cos\theta}{(C_2 - C_1)u_s^2 r} \tag{4.55}$$

Substituting equation 4.54 into 4.53 gives

$$\bar{u} = \frac{\frac{1}{2}U_o r_e^2 sin\phi}{r\left(\frac{U_o r_e^2 sin\phi}{2rU_o} + (1 - c_1\delta)\right)} \tag{4.56}$$

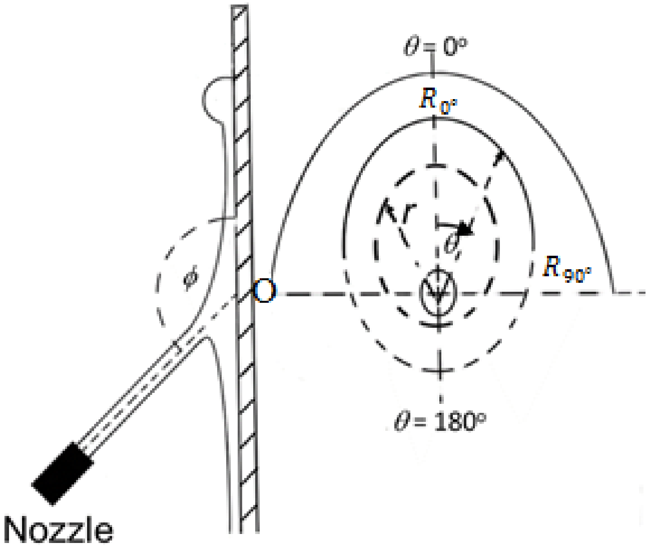
θ = 0°
R0°
r
θ
R90°
O
φ
θ = 180°
Nozzle

(a) **Side and end views, showing non-circular RFZ**

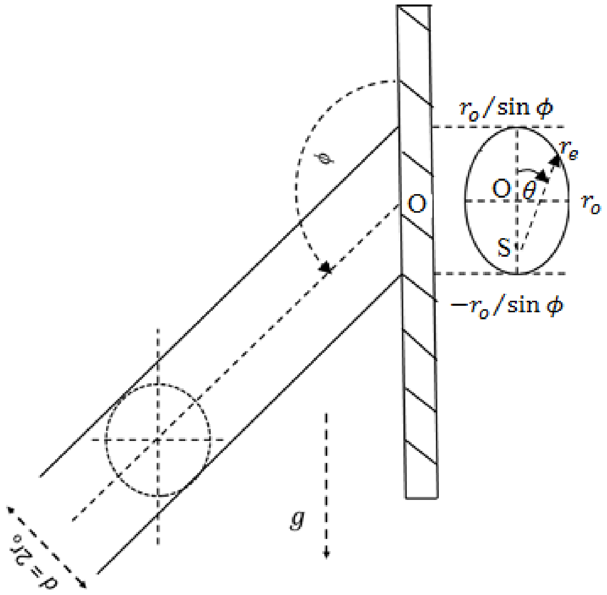
φ
O
r_o / sin φ
r_e
O
θ
r_o
S
−r_o / sin φ
g
d = 2r_o

(b) **End view, showing elliptical impact region**

Figure 4.5 Schematics of a liquid jet impinging obliquely on a vertical wall. S is the source point from where liquid spread out radially and O is the point of impingement passing through the center line of the jet

where h and $\bar{u}$ depend on both θ and ϕ. Similarly, in the LZ, equation 4.29 takes the form

$$\frac{d\bar{u}}{dr} = -\frac{5.7\mu\bar{u}^2 r^2}{\rho(U_o r_e^2 \sin\phi)^2} - \frac{0.714 g \cos\theta}{\bar{u}} \tag{4.57}$$

and for $\theta = 90^\circ$

$$\left(U_o r_e^2 sin\phi\right)^2 \left(\frac{1}{\bar{u}} - \frac{1}{U_o/2}\right) = 1.9\frac{\mu}{\rho}(r^3 - r_b^3) \quad \text{for} \quad \theta = 90^\circ \tag{4.58}$$

For the TZ, equation 4.46 becomes

$$\frac{d\bar{u}}{dr} = -\frac{0.04706}{\left(\frac{1}{2}U_o r_e^2 sin\phi\right)\sqrt[4]{4r_e^2 sin\phi}}\sqrt[4]{\frac{dr^5}{Re}}\bar{u}^2 - \frac{64}{63}\frac{g\cos\theta}{\bar{u}} \tag{4.59}$$

These results for the velocity and film thickness are used to find the location of the film jump, R_θ, which will vary with θ. The predictions are compared with experimental data for $\theta = 0^\circ$ and 180° for a range of flow rates and angle of impingement ϕ.

4.3 Experimental

Two different apparatuses were used in this work. Figure 4.6 shows a schematic of the test rig used for the majority of the experiments. Liquid was pumped from an overhead supply tank through pressure, conductivity and temperature sensors before entering a flow control valve. The pressure upstream of the nozzle was measured to monitor the flow rate. These studies employed a solid stream nozzle of internal diameter 2.667 mm (Lechler GmbH, Type 544) to generate the jet. The nozzle mounting consisted of a 106 mm long section of i.d. 16 mm piping, including a pressure port connection, followed by a 50 mm section of i.d. 11 mm to which the nozzle was connected. This is more representative of industrial cleaning nozzle installations than the very long, smooth entry sections used by workers such as Azuma and Hoshino (1984*a*). The connections can introduce perturbations in the jet. The nozzle mounting allowed rotation so that the angle of impingement could be changed. The nozzle and target were located in a light-tight steel chamber, with illumination provided by externally mounted 1200 W halogen lamps. All the sensors, valves and pump were connected to a computer control and data collection system. A detailed description of this system was also given by Wilson et al. (2015).

The nozzle was positioned 200 mm from the target, which was a 500 × 500 mm^2 and 5 mm thick plate made of Perspex$^{\text{TM}}$ or glass. A graticule tape was fixed on the target to provide in situ scale calibration. A white sheet of paper was mounted on the dry side of the plate in order to give better image resolution and contrast. The target was cleaned, wiped with ethanol, and allowed to dry before each experiment.

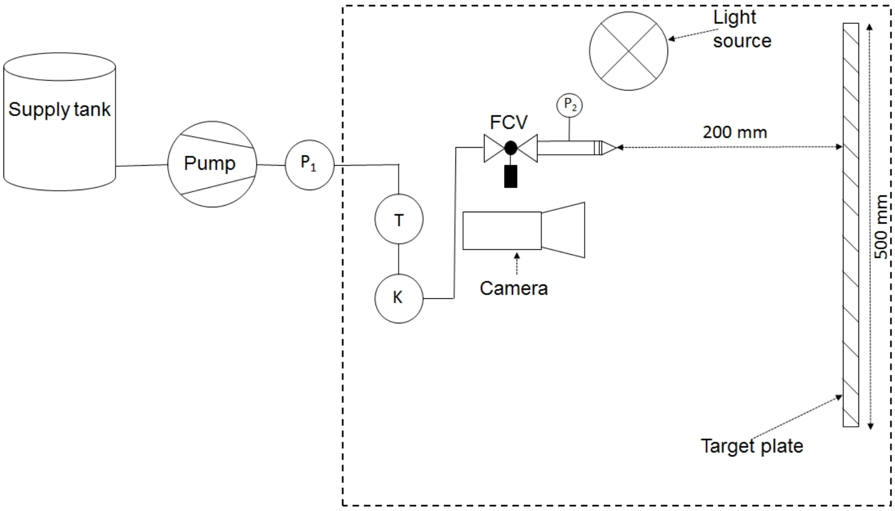

Figure 4.6 Schematic of the test rig used to study the initial stages of RFZ formation. Labels: P1, P2 – pressure sensors; T – temperature sensor; K – conductivity sensor; FCV – flow control valve)

Deionised water at 23°C was used as the test liquid. Initially liquid leaving the nozzle was prevented from reaching the target by a Perspex$^{\text{TM}}$ interrupter plate to allow the flow to reach steady state. After approximately one minute the interrupter plate was removed and the flow pattern created by the jet striking the surface was captured using a high speed camera (Phantom Miro M310) operating at 4300 frames per second. (Can be seen at https://doi.org/10.1016/j.ces.2016.06.011, as videos 1) shows the jet striking the target and the formation of a circular front of liquid which grows and eventually forms a pattern similar to figure 4.1. Images were processed using the NIH ImageJ and Matlab® software.

Although the nozzle was horizontal, gravity could cause the jet to droop a small amount as it traversed the 200 mm to the target. The angle of impingement was therefore slightly less. The effective angle of impingement was calculated and the values are reported in table 4.1.

The second apparatus is described in §2.3. The experiments performed in the second apparatus featured lower flow rates, with $Q = 0.6 - 2\,\text{L}\,\text{min}^{-1}$. An IP65 waterproof fluorescent tube lamp illuminated the target. Photographs and video were taken with a Nikon$^{\text{TM}}$ D 3300 and Photron Fastcam SA3 cameras and image processing was again performed using the ImageJ and MATLAB softwares.

Table 4.1 Effective angle of impingement for jets inclined at $\phi = 90°$ and $120°$ as a result of travel across the 200 mm distance between the nozzle and target.

Flow rate ($\mathrm{L\,min^{-1}}$)	Effective angle of impingement	
	$\phi = 120°$	$\phi = 90°$
1.95	116.7	85.5
2.52	118.0	87.4
3.05	118.6	88.2
3.57	119.0	88.7
4.01	119.2	88.9

4.4 Results and Discussion

The models presented in § 4.2 provide estimates of film thickness, h, and average velocity $\bar{u}$. Both terms are needed to predict the location of the film jump, R, using equation 4.50. Film thicknesses were not measured in the experiments so the models are compared with results from the literature. Model predictions of $\bar{u}$ are compared with the values obtained during the initial growth of the RFZ.

4.4.1 Film thickness

Stevens and Webb (1993) measured the thickness of thin films of water as part of their study of the flow structure in the films with a free surface created by impinging liquid jets. They used Laser-Doppler Velocimetry (LDV) to determine the velocity profile in the film and calculated film thickness from conservation of volume. Figure 4.7(a) shows some of their experimental data alongside the model prediction, equation 4.24. For this jet Reynolds number, of 53100, equation 4.27 predicts the location where the boundary layer to reach the surface of the film at $r_b \approx 9.01d$, indicating that the data originate from the BLFZ.

Similarly, figure 4.7(b) compares the model predictions with data obtained at $Re = 37,000$ and $36,100$ for jet diameters of 23 mm and 14 mm, respectively. The small difference in Re does not give a significant difference in the predicted $\frac{h}{d}$ values.

The predicted values of r_b are $8d$ and $7.93d$ for $Re = 37000$ and 36100, respectively, again lying within the BLFZ. Stevens and Webb did not present error bars with the experimental data. There is good agreement between the experimental results and the model in each case. It is noteworthy that there are no fitted parameters in the model.

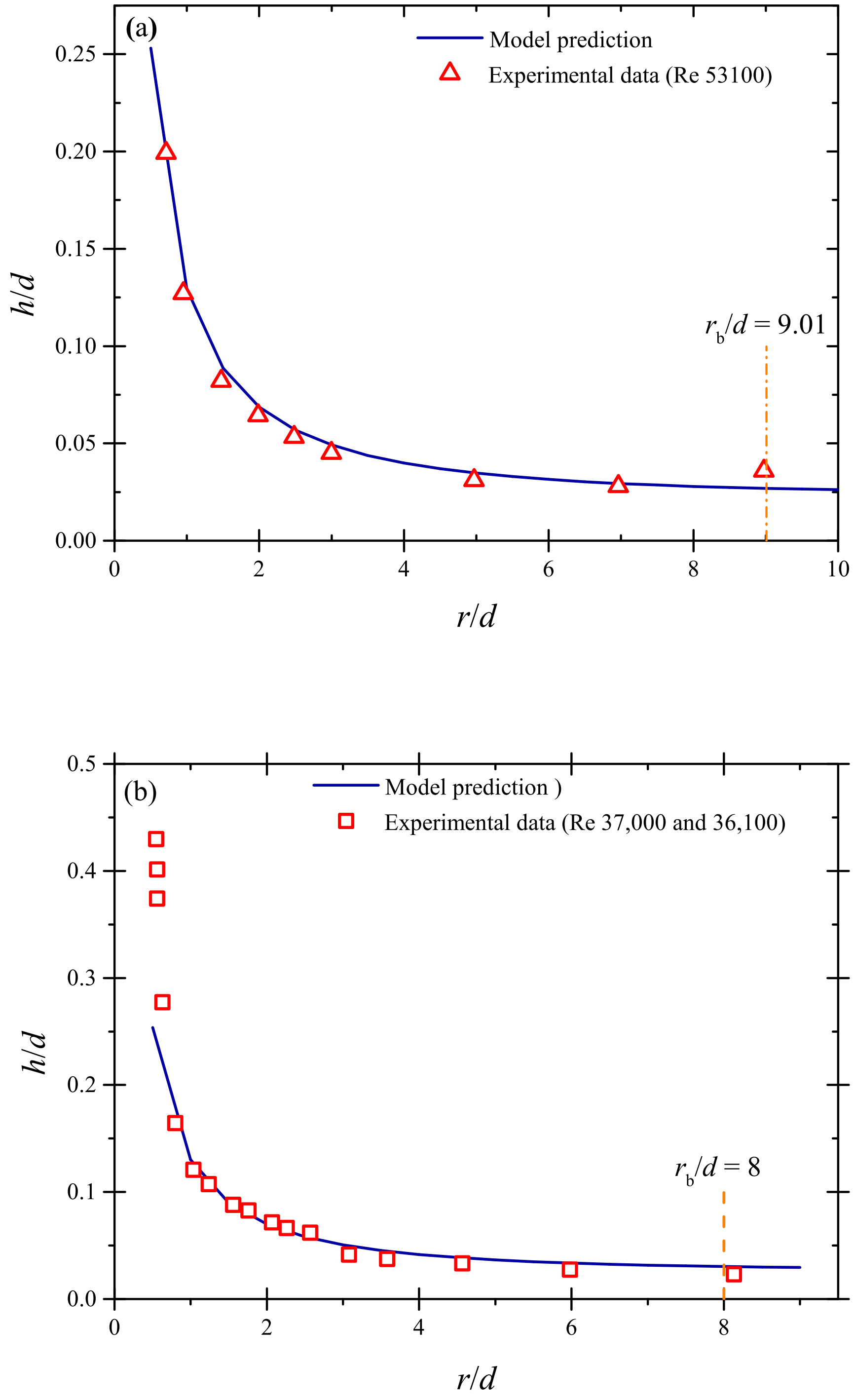

Figure 4.7 Comparison of liquid film thickness in the RFZ measured by Stevens and Webb (1993) with the model for the boundary layer zone, equation 4.24. (a) $Re = 53100$, $d = 10.9$ mm; (b) Two different jets were used, with (i) $Re = 37000$, $d = 23$ mm and (ii)$Re = 36100$, $d = 14$ mm. The test liquid was water at room temperature.

4.4.2 Transition radius, r_t

In the laminar zone, the liquid film thickness initially decreases and reaches a location where it is minimum. At this location $\frac{dE}{dh}$ shows a singularity and we hypothesize that the laminar film becomes unsteady and turbulent effects are expected to dominate. Equation 4.39 gives the location of the transition for the general case, and equation 4.40 for $\theta = 90°$. Azuma and Hoshino (1984*b*) presented the following correlation for the radius of a transition based on their visual observations

$$\frac{r_t}{d} = 730Re^{-0.315} \tag{4.60}$$

Whereas Liu et al. (1991) reported two correlations, one based on visual observation,

$$\frac{r_t}{d} = 1200Re^{-0.422} \tag{4.61}$$

and one based on heat transfer data, viz.

$$\frac{r_t}{d} = 26800Re^{-0.68} \tag{4.62}$$

Figure 4.8(a) compares the present model, for $\theta = 90°$, and the above correlations. The prediction for $\frac{r_t}{d}$ differs noticeably at lower Re. Equations 4.60 and 4.61 show a similar trend but the former is consistently larger by about 15 units. All three (equations (4.60-4.62) predict a decrease in $\frac{r_t}{d}$ with increasing Reynolds number, whereas the current model, equation 4.40, predicts an increasing trend. Equations 4.40, 4.61 and 4.62 predict similar values of $\frac{r_t}{d}$, in the range 9-15, for $Re > 70000$.

Figure 4.8(b) compares the present model predictions, equation 4.40, for $\frac{r_t}{d}$ with our experimental measurements of the location where the smooth concentric waves started to break (see image 4.9).

Two sets of predictions are reported as the jet exhibited a varicose structure, where surface tension caused the diameter to vary periodically before impinging. The maximum and minimum jet diameters were extracted from photographs and used in the prediction. For a 2.66 mm nozzle, the maximum and minimum measured jet diameters were 2.86 and 2.66 mm. The experimental data lie between the values predicted for the minimum and maximum jet diameters and shows good agreement with the model. In the derivation of the criterion for the transition from laminar to turbulent film behaviour, it is postulated, following the work of Azuma and Hoshino (1984*a*) that the transition is accompanied by the loss of regularity in surface waves. The photographs in figure 4.9 show regular concentric waves in the RFZ: further from

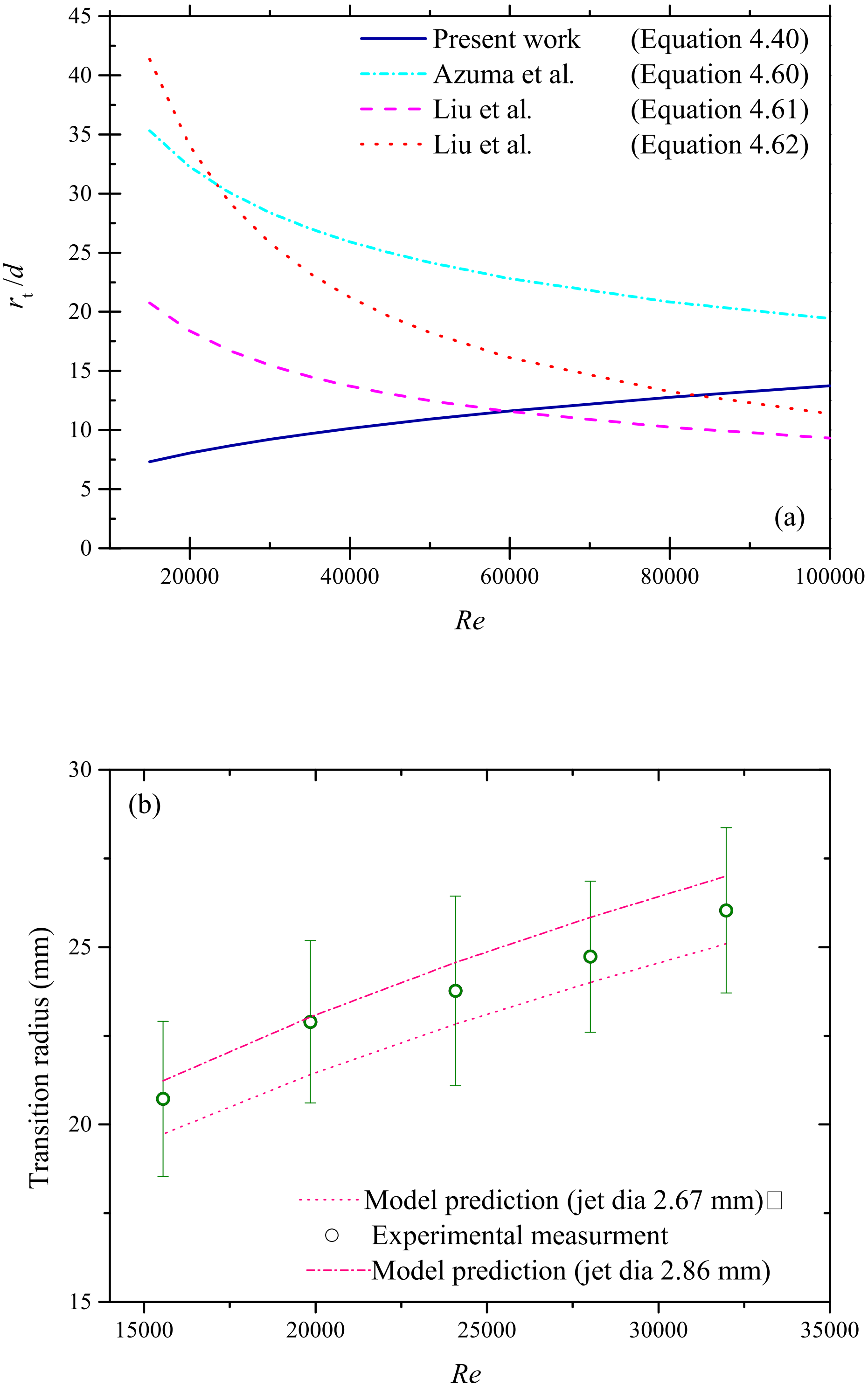

Figure 4.8 Laminar-turbulent transition radius. Comparison of (a) this work with existing correlations: (b) experimental observations of the critical radius for wave breakup alongside the model predictions, equation 4.40. The error bars are standard deviation of measured transition radius.

the point of impingement these are less coherent. The prediction for the transition (equation 4.40) is plotted on the image and shows good agreement with the observed feature. By comparison, the Liu et al. (1991) correlation, equation (4.61, 4.62), consistently overpredicts the transition.

The model also gave good agreement with transitions reported by other workers. Liu et al. (1991) measured the local rate of heat transfer from a hot plate to the film created by an impinging liquid jet. They reported measurements of local heat transfer coefficient. The results are presented in terms of the local Nusselt number, Nu, where the length scale is the jet diameter. The data in figure 4.10 show a general increase in Nu with Re, and a decrease with radial location, $\frac{r}{d}$. At higher Re there is a discontinuity in the decreasing radial trend. Liu et al. attributed this to the transition to a turbulent film. The transition radius predicted by the model, equation 4.40, is marked by a vertical dashed line on the plots and this shows reasonable agreement with the location of the discontinuity. Their plots of local Nusselt number vs $\frac{r}{d}$ show a generally decreasing trend but with a local maximum at $\frac{r_t}{d}$ around 6-10. Their data are compared with the current model in Figure 4.10 (a - e). At higher Re the model gives a reasonably accurate prediction of this local maximum.

Cleaning of water soluble soils such as Xanthan gum by impinging jets shows similar behaviour (Joppa et al., 2018). Figure 4.11 show the evolution of cleaning pattern of a Xanthan gum layer coated plate by impinging liquid jet. A circular cleaned region appears near the point of impingement, which grows in size with time. Simultaneously, a ring shaped cleaned region appears at a particular radial location in the RFZ.

The combination of a circular cleaned region near the point of impingement and a ring cleared of soil further out creates an annulus-shaped foot print of uncleaned material (See figure 4.11 (b-d), where darker areas are the cleaned regions). This cleaning behavior can be attributed to the high shear stress, hence enhances cleaning, near the point of impingement and enhanced mixing at the location where the laminar film becomes turbulent. figure 4.12 compares the experimental measurements of circular cleaned region with the prediction of the laminar to turbulent transition radius. The corresponding theoretical curve obtained from solution of 4.40 shows good agreement with the experimental data. This support my hypothesis that the ring shaped cleaning region appears due to laminar to turbulent and enhanced mixing.

Rao and Trass (1964) measured the local rate of mass transfer for a water jet impinging on a horizontal plate coated with a soluble layer. They reported the local

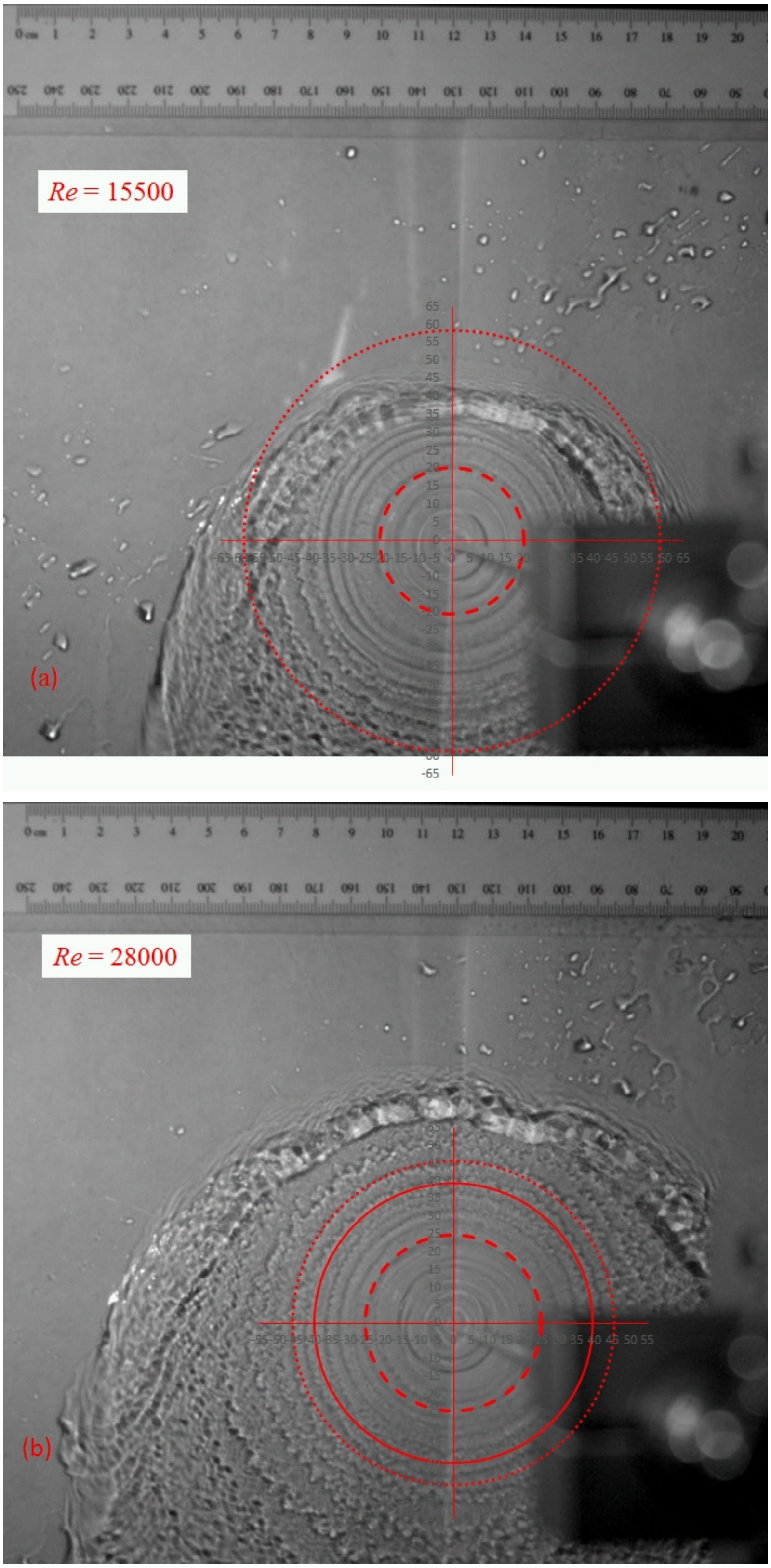

Figure 4.9 Photographs of the RFZ and draining films obtained with perpendicular impinging jets, $d = 2.667$ mm and (a) $Re = 15500$ and (b) $Re = 28000$. Dashed line – this work ($d = 2.87$ mm), solid line – this work ($d = 2.67$ mm), equation 4.40; dotted line – Liu et al. (1991) correlation, equation 4.61.

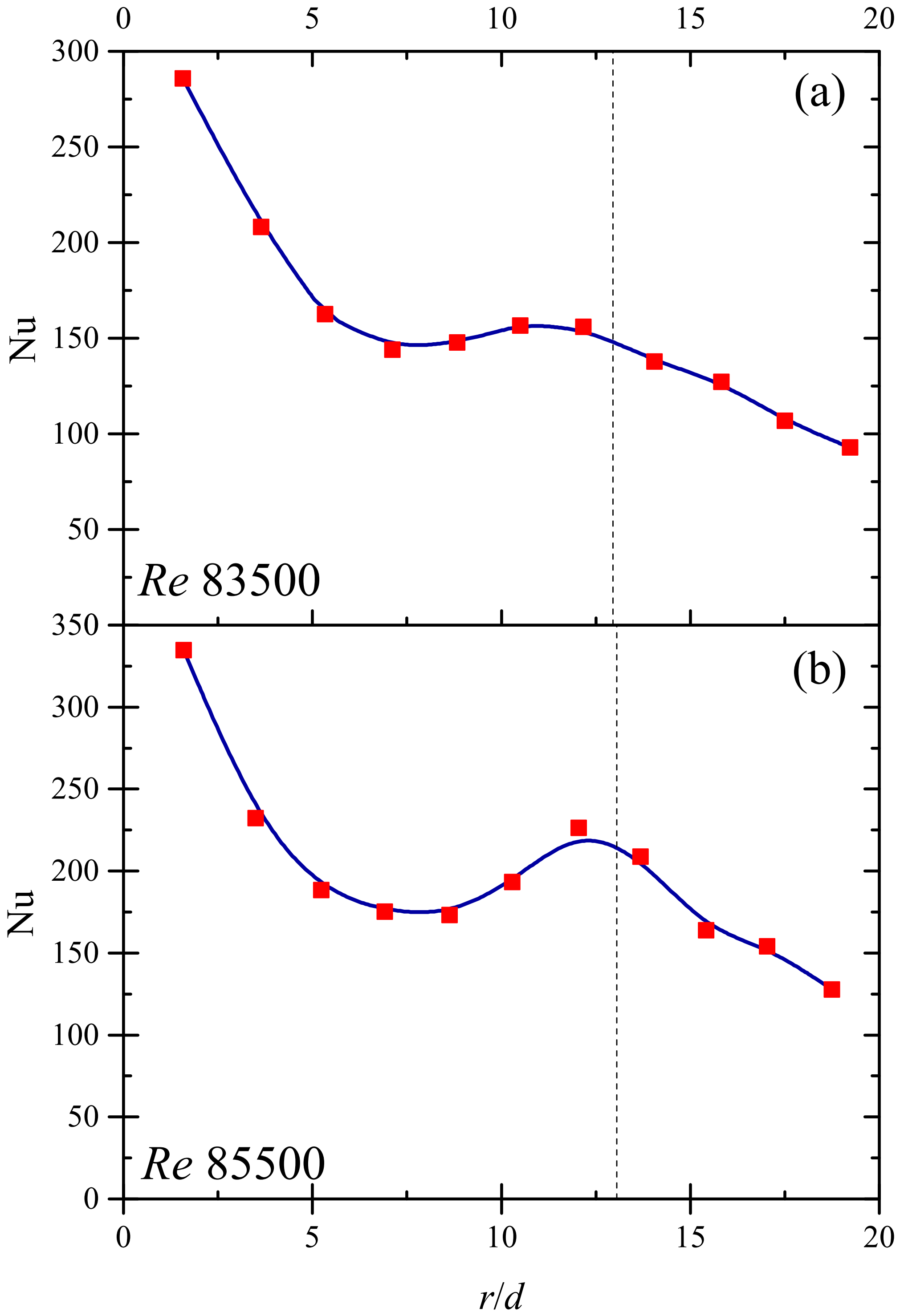
(a)
Re 83500
(b)
Re 85500
Nu
Nu
r/d
0
5
10
15
20
300
250
200
150
100
50
350
300
250
200
150
100
50
0
0
5
10
15
20

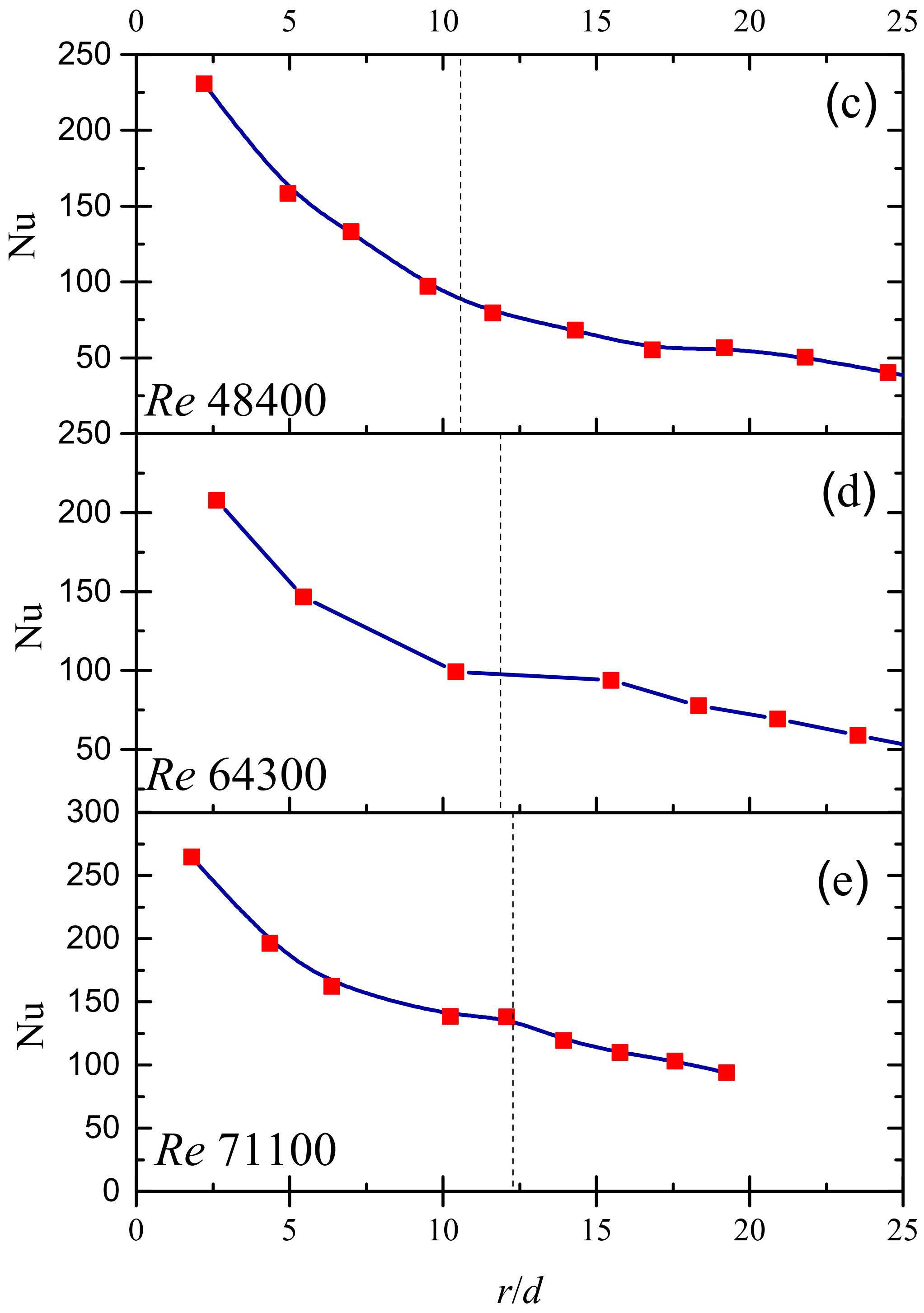

Figure 4.10 Effect of radial location on local Nusselt number for water jets impinging on a heated surface. Data reproduced from Liu et al. (1991), for Re = (a) 83500, (b) 85500, (c) 48400, (d) 64300, and (e) 71100. Connecting lines between data points are to guide the eye. The vertical dashed lines show the location of $\frac{r_t}{d}$ predicted by equation 4.40.

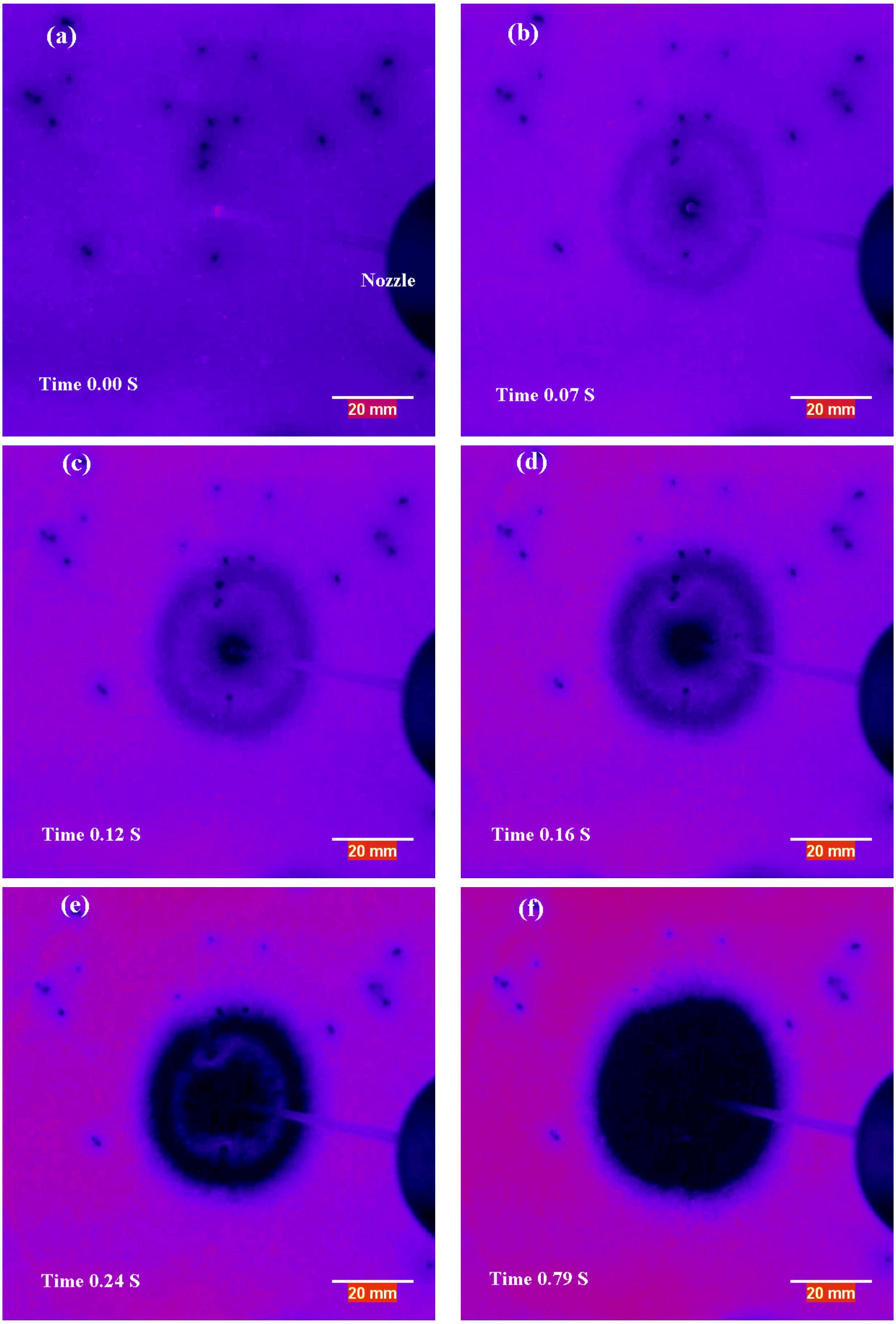
(a)
Nozzle
Time 0.00 S
20 mm
(b)
Time 0.07 S
20 mm
(c)
Time 0.12 S
20 mm
(d)
Time 0.16 S
20 mm
(e)
Time 0.24 S
20 mm
(f)
Time 0.79 S
20 mm

Figure 4.11 Time series images of cleaning of Xanthan gum by a impinging water jet. A circular disk and a ring of cleaned region appear near the point of impingement and at a certain radial location in the RFZ, respectively. The experimental images were modified with a false colour to show cleaned regions clearly. These images were extracted from a video provided by Dr. Hannes Köhler from the Technical University of Dresden (TUD).

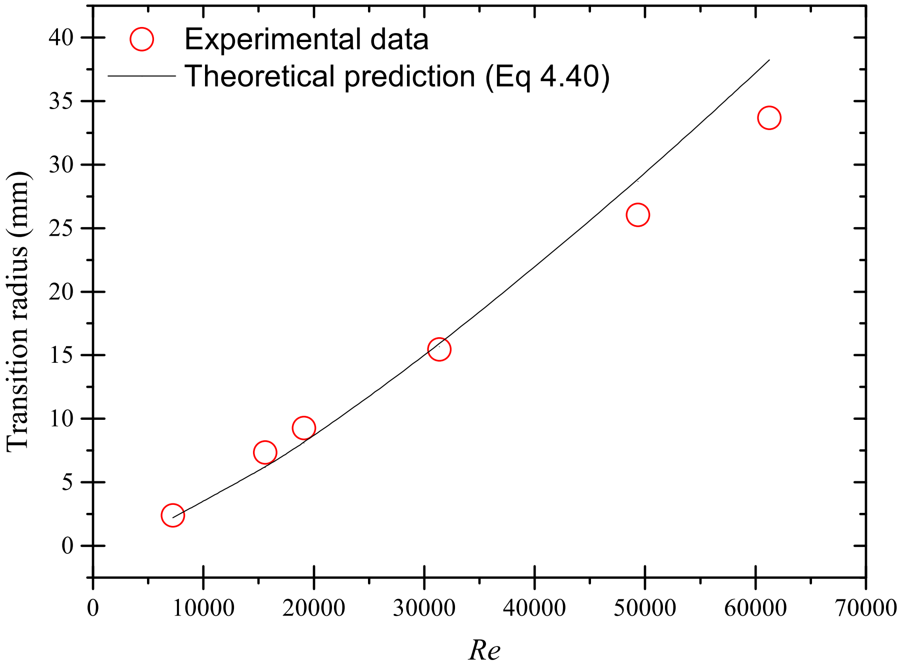

Figure 4.12 Cleaning ring radius plotted against jet Reynolds number for cleaning of Xanthan gum coated horizontal plate by a vertical water jet. The curve is the prediction of the laminar to turbulent transition radius, r_t for the respective Reynolds numbers. In the experiments the Re was manipulated by changing both jet diameter and the liquid flow rate. Dr. Hannes Köhler provided the data.

Sherwood number (a dimenssionless mass transfer coefficient) for a range of Reynolds numbers and jet diameters. At low Re, careful inspection of local Sherwood number vs $\frac{r}{d}$ profiles shows a deviation from the general decreasing trend, similar to that reported by Liu et al. for heat transfer. The location of the deviation is close the transition predicted by the present model.

4.4.3 Velocity profile: Perpendicular impingement ($\phi = 90°$)

Measurements of the velocity profile in these films are complicated by the presence of surface waves. Aouad et al. (2016) measured the surface velocity in the RFZ for jets impinging perpendicularly on vertical walls using particle image velocimetry. They used a dye to limit measurements to the surface region alone. The measured surface velocities were noticeably higher than those predicted by the Wilson et al.'s model and this was attributed to the presence of surface waves.

In the present study the average film velocity was estimated from the initial evolution of the flow pattern until a steady rope was formed. To estimate the average velocity, the high speed videos were analysed to obtain the positional time series of the leading edge of the initially spreading liquid film. The time series data was then processed with a least-squares fit of a high-order polynomial, which allowed to obtain the smoothed time series data. The smoothed data was then numerically differentiated to get a reliable estimate of the average velocity. This method of data processing does not give a reliable estimate of the error, therefore, error bars are not presented (Cousins et al. (2012)).

Also, due to the experimental limitation, at the very beginning, *i.e.* just after the jet impinges and the liquid film spreads very rapidly, reliable time series data could not be obtained, and the velocity could not be estimated.

Figure 4.13 compares the average velocity profile for $\theta = 90°$ obtained from video analysis for flow rates ranging from $Q = 1.95 - 4.01\,\mathrm{L\,min^{-1}}$ and nozzle diameter $d_N = 2.67\,\mathrm{mm}$ ($Re = 15500$ to 32000) with the solutions of equation 2.20, the new model presented in § 4.2, as well as those of Wang et al. (2013b). The latter is based on that of Wilson et al. (2012) and includes the correction for an obliquely impinging jet and gravity. There are no adjustable parameters in either model and the agreement is good in most cases, until the approach to the film jump itself. The agreement is less good for $Re = 32000$ but the general trend is captured.

Comparing the three models, the Wang et al. (2013b)) predictions show consistently less good agreement. The model underpredicts the average velocity at larger radial position but the difference is less than a factor of 2. In several cases the two models (turbulent film and Wang et al. (2015)) bracket the measured velocity, while the solution of equation 2.20 passes through the data.

The theoretical description presented in § 2 does not capture the laminar to turbulent transition and the features arising from this. Nevertheless the solution of 2.20 show better agreement, compared to both the turbulent film model presented in § 4.2 and Wang et al. (2013b). This confirms that the surface energy term plays an important role which should be included for an accurate description of the flow field.

The Wilson et al. (2012)/Wang et al. (2015) model nevertheless provides a reasonable engineering estimate of the average film velocity. It is sufficiently accurate for engineering estimates of phenomena determined by the film such as the location of the film jump and cleaning at $\phi = 90°$ (see Wilson et al. (2014); Glover et al. (2016)). Similarly, the turbulent film model presented in § 4.2 also provides the reasonable estimate of average velocity, film jump and other features, such as enhanced heat transfer (see figure 4.10) and cleaning (see figure 4.11, 4.12) arising from the turbulent transition.

4.4.4 Oblique impingement ($\phi = 120°$)

The obliquely impinging jet presents a stiffer test for the model presented in this chapter as the distribution of liquid as well as the development of the spreading film are tested. Figure 4.14 presents results for different flow rates for a challenging case, where the jet impinges in an upward direction ($\phi = 120°$): Wang et al. (2013b) showed that the widest part of the RFZ was then located above the impingement point. For the value of $\phi = 120°$, r_e is largest at $\theta = 0°$ and smallest for $\theta = 180°$: for a given flow rate the maximum liquid flux occurs at $\theta = 0°$ and the smallest at $\theta = 180°$ and it represents the extreme cases, therefore, chosen for the comparison of velocity. Figure 4.14 presents pairs of plots for each case studied; for $\theta = 0°$ (above the impingement point, where flow is against gravity) and $\theta = 180°$ (downstream of the impingement point). The effective angle of impingement, reported in Table 4.1, was used in the calculations.

There is a noticeable kink in the new model, at the laminar to turbulent transition. This is not evident in the estimated average velocity data. High speed videos were

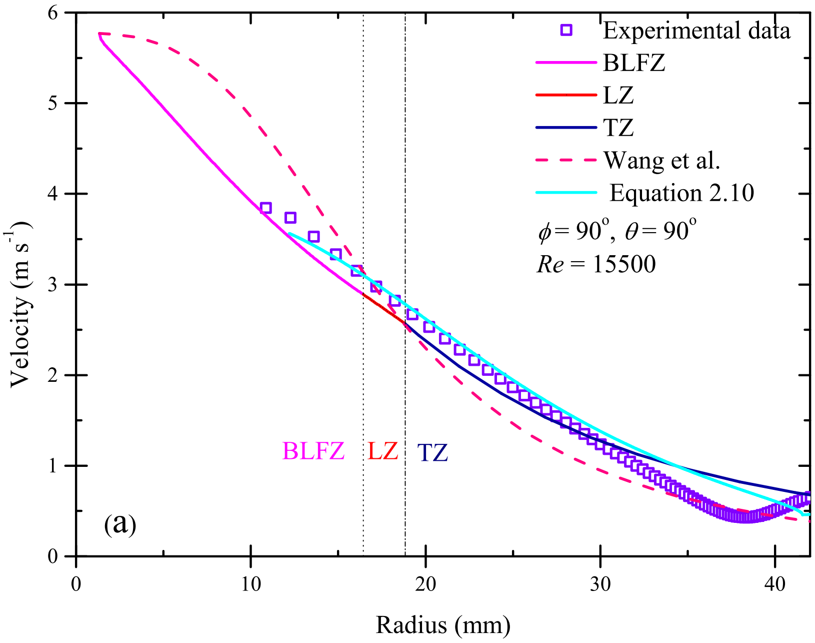

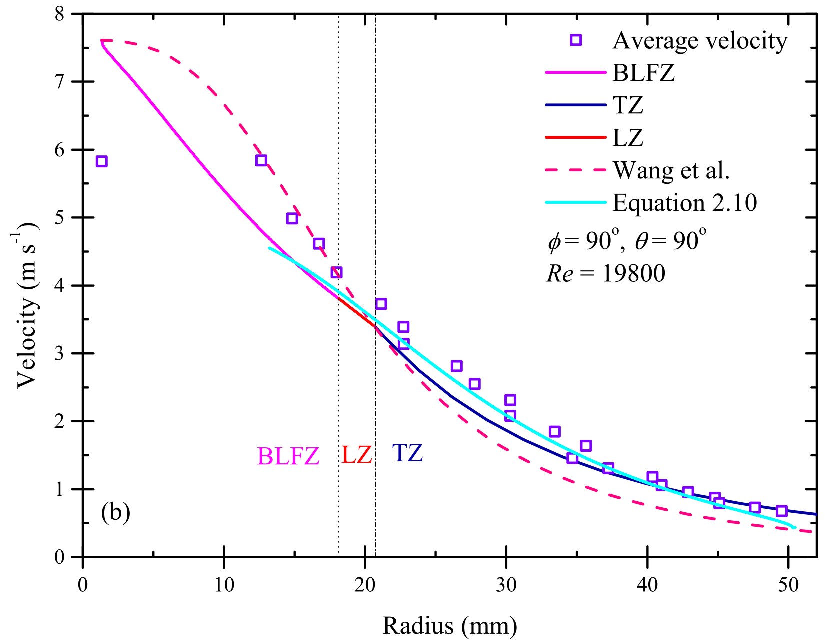
Average velocity
BLFZ
TZ
LZ
Wang et al.
Equation 2.10
$\phi = 90^{\circ}$, $\theta = 90^{\circ}$
$Re = 19800$
BLFZ
LZ
TZ
(b)
Velocity (m s^{-1})
Radius (mm)
0
1
2
3
4
5
6
7
8
0
10
20
30
40
50

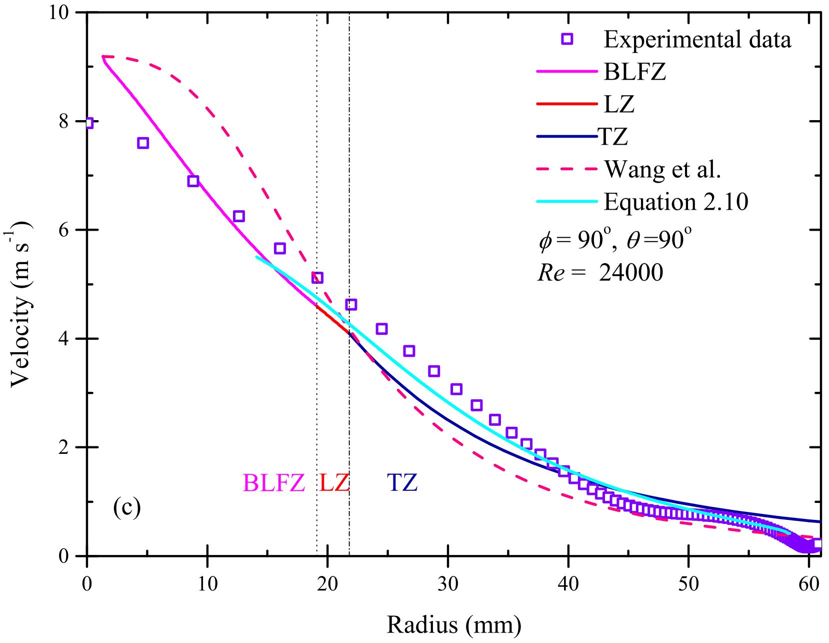
Experimental data
BLFZ
LZ
TZ
Wang et al.
Equation 2.10
$\phi = 90^{\circ}$, $\theta = 90^{\circ}$
$Re = 24000$
BLFZ
LZ
TZ
(c)
Velocity (m s^{-1})
Radius (mm)
0
2
4
6
8
10
0
10
20
30
40
50
60

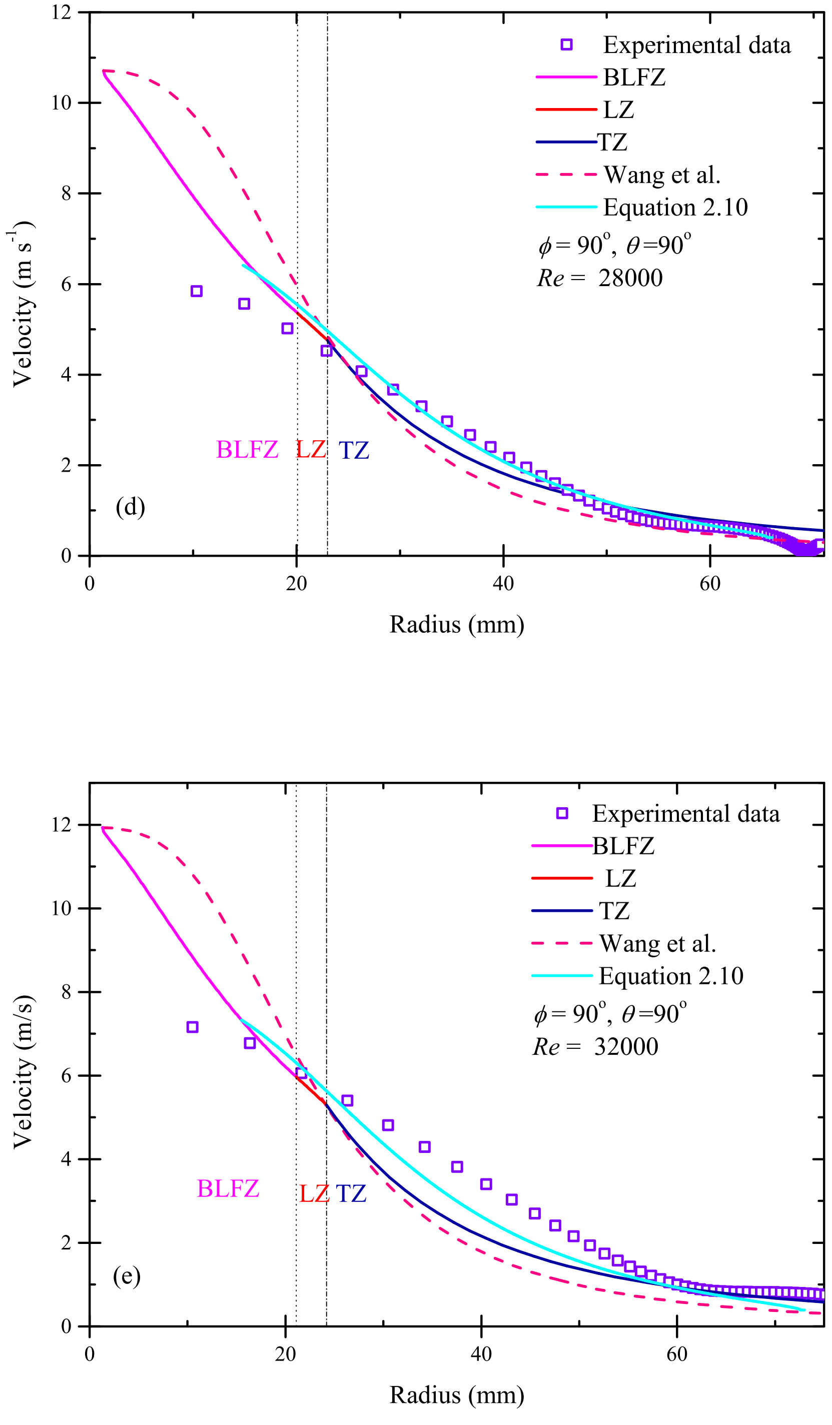

Figure 4.13 Comparison of experimental estimates of the average velocity $\bar{u}$ obtained from video analysis of the formation of the RFZ with the present model. Vertical glass plate, nozzle diameter 2.67 mm , $Q =$ (a) 1.95 L min^{-1}, (b) 2.49 L min^{-1}, (c) 3.01 L min^{-1}, (d) 3.51 L min^{-1}, and (e) 4.01 L min^{-1}.

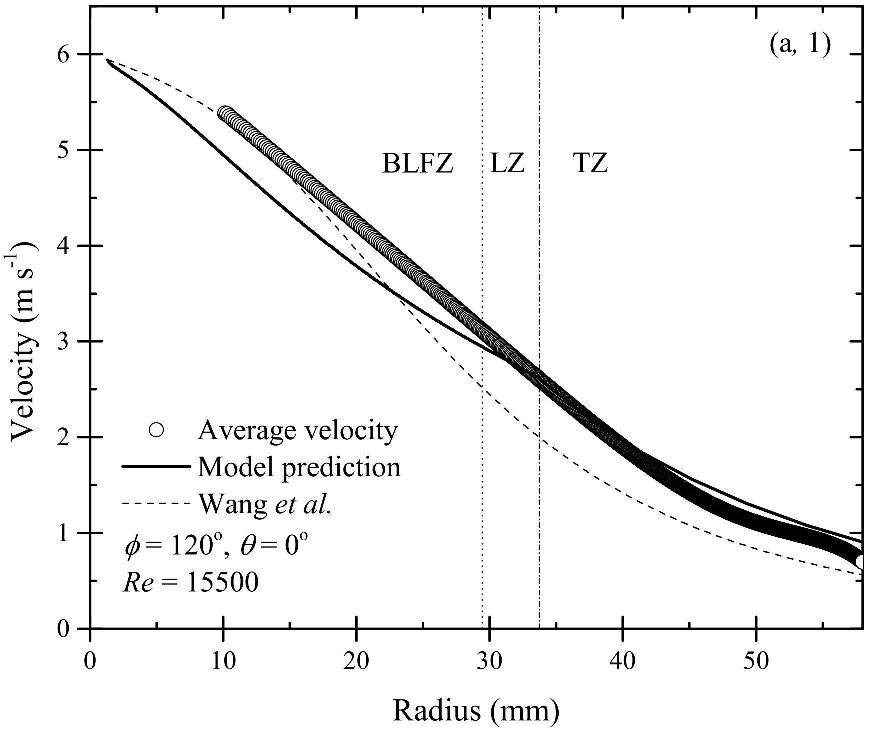
(a, 1)
BLFZ
LZ
TZ
Average velocity
Model prediction
Wang *et al.*
$\phi = 120^{\circ}$, $\theta = 0^{\circ}$
Re = 15500
Velocity (m s^{-1})
Radius (mm)
0
1
2
3
4
5
6
0
10
20
30
40
50

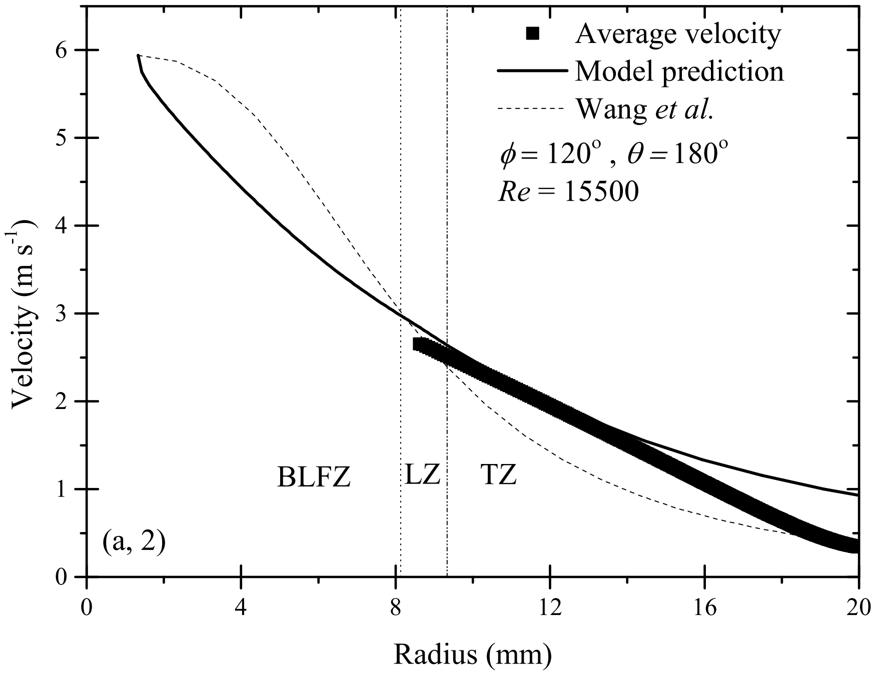
Average velocity
Model prediction
Wang *et al.*
$\phi = 120^{\circ}$, $\theta = 180^{\circ}$
Re = 15500
BLFZ
LZ
TZ
(a, 2)
Velocity (m s^{-1})
Radius (mm)
0
1
2
3
4
5
6
0
4
8
12
16
20

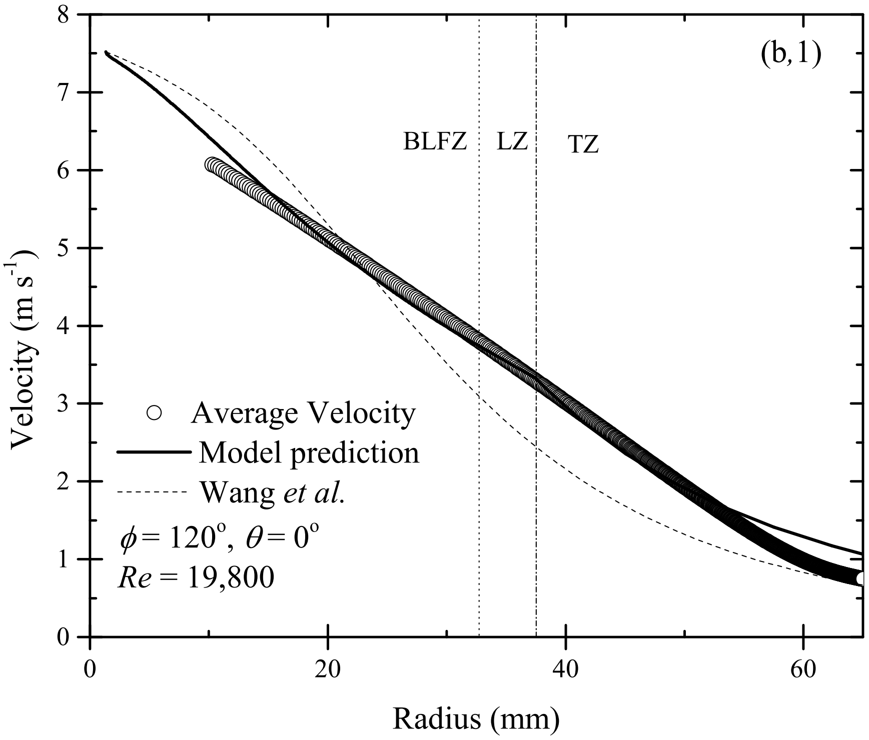
(b,1)
BLFZ
LZ
TZ
Average Velocity
Model prediction
Wang *et al.*
ϕ= 120°, θ= 0°
Re = 19,800
Velocity (m s^{-1})
Radius (mm)
0
1
2
3
4
5
6
7
8
0
20
40
60

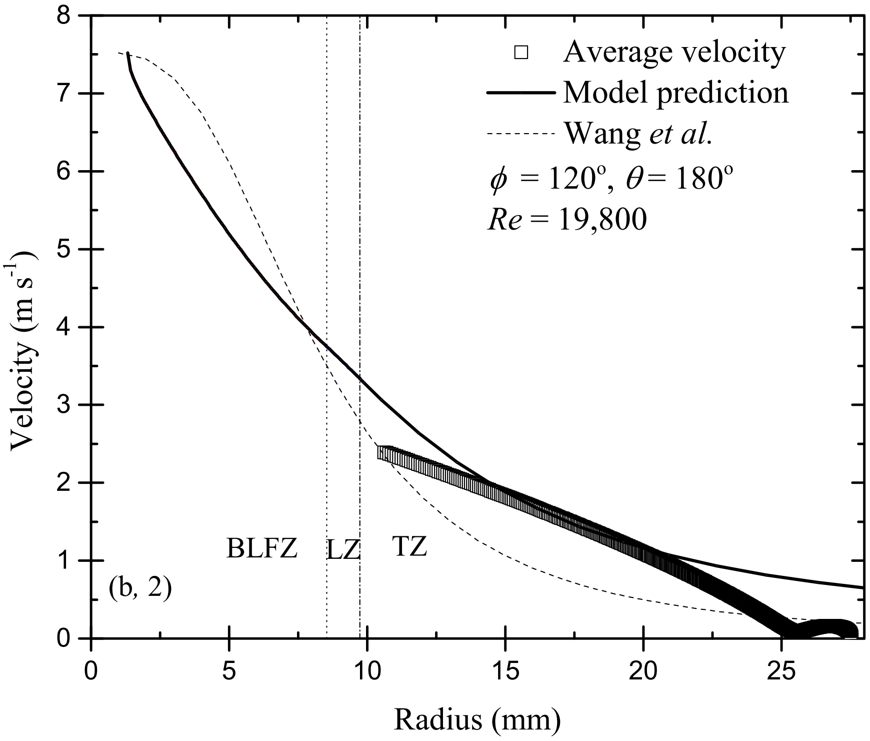
Average velocity
Model prediction
Wang *et al.*
ϕ = 120°, θ= 180°
Re = 19,800
BLFZ
LZ
TZ
(b, 2)
Velocity (m s^{-1})
Radius (mm)
0
1
2
3
4
5
6
7
8
0
5
10
15
20
25

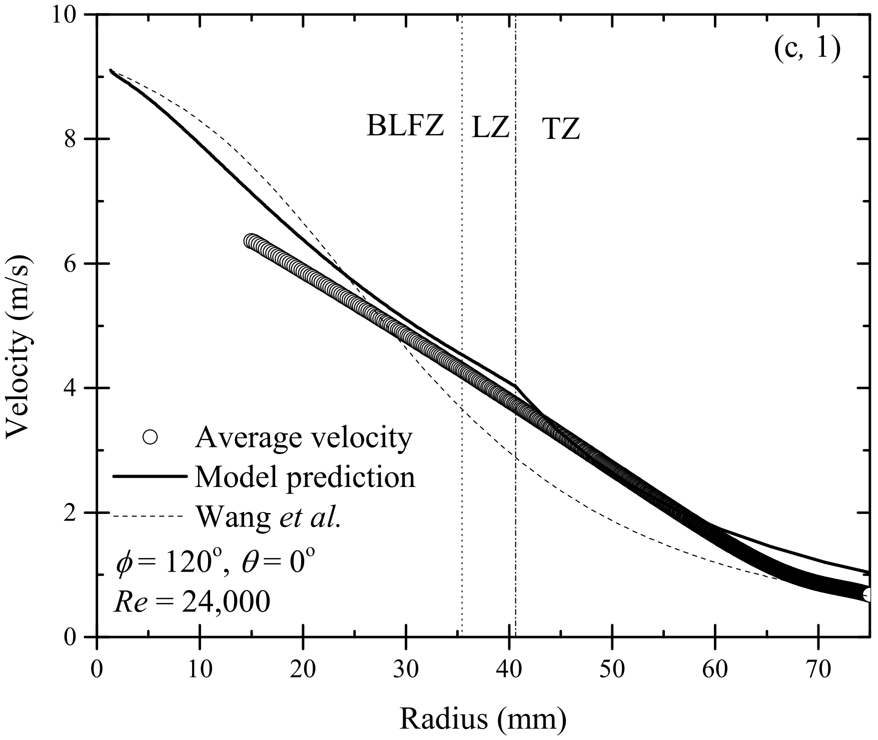
(c, 1)
BLFZ
LZ
TZ
○ Average velocity
Model prediction
Wang *et al.*
$\phi = 120^\circ$, $\theta = 0^\circ$
$Re = 24{,}000$
Velocity (m/s)
Radius (mm)
0
2
4
6
8
10
0
10
20
30
40
50
60
70

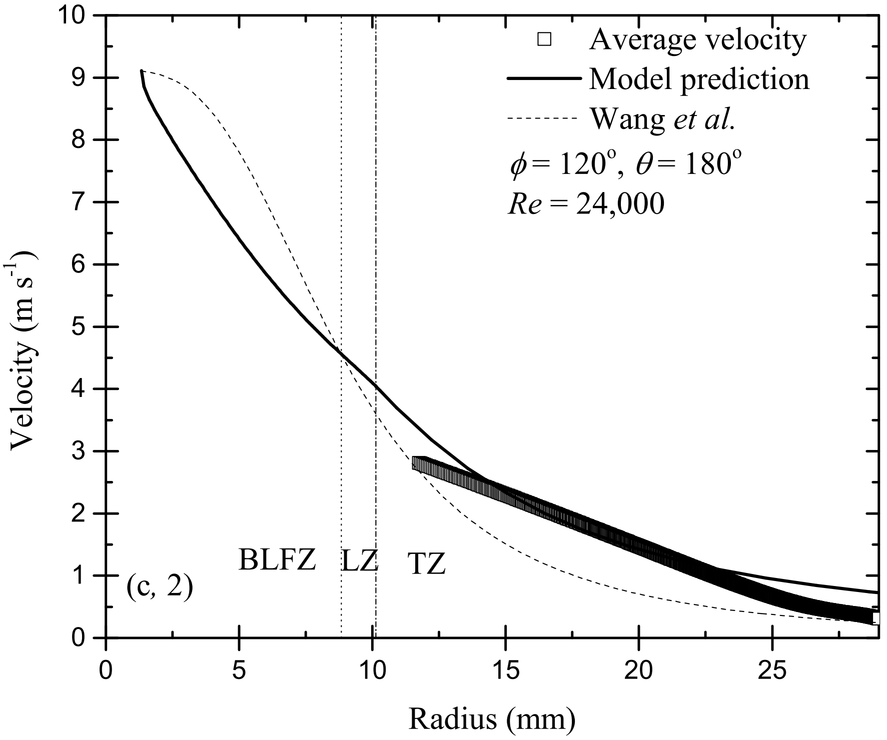
□ Average velocity
Model prediction
Wang *et al.*
$\phi = 120^\circ$, $\theta = 180^\circ$
$Re = 24{,}000$
BLFZ
LZ
TZ
(c, 2)
Velocity ($\mathrm{m\,s^{-1}}$)
Radius (mm)
0
1
2
3
4
5
6
7
8
9
10
0
5
10
15
20
25

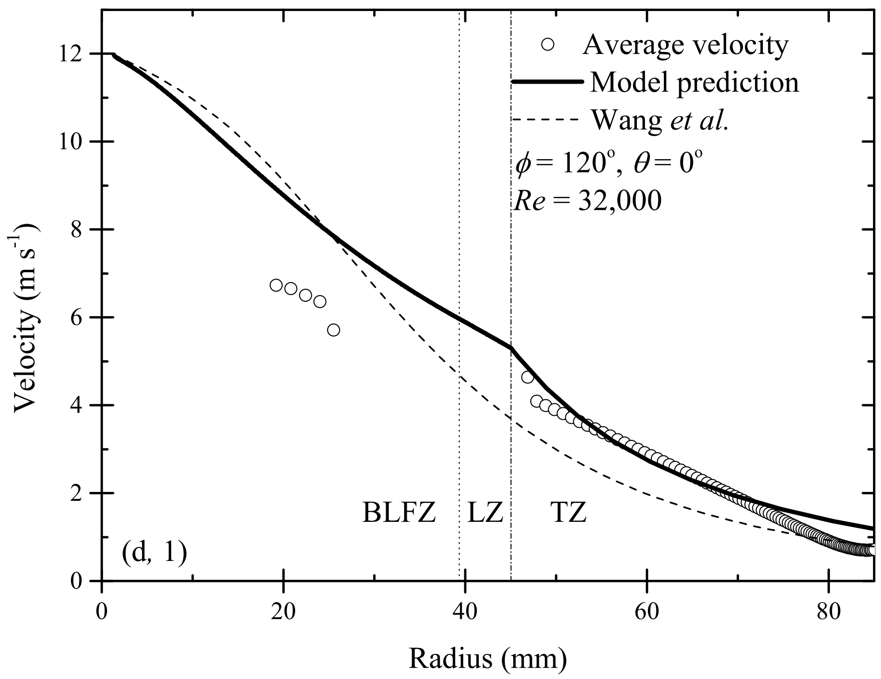

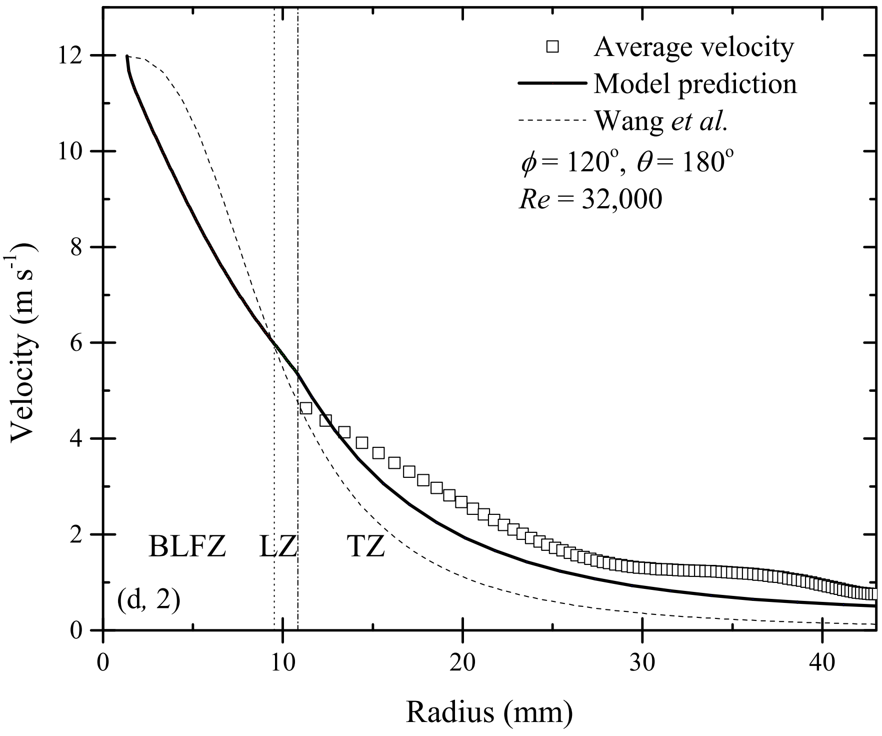

Figure 4.14 Comparison of estimated average velocity with model predictions for an obliquely impinging water jet ($\phi = 120°$) on a vertical Perspex$^{\text{TM}}$ plate, $d_N = 2.667\,\text{mm}$, for Q = (a) (a) $1.99\,\text{L}\,\text{min}^{-1}$, (b) (a) $2.52\,\text{L}\,\text{min}^{-1}$; (c) (a) $3.05\,\text{L}\,\text{min}^{-1}$; (d) (a) $4.01\,\text{L}\,\text{min}^{-1}$; (1) ($\theta = 0°$), (2) ($\theta = 180°$).

analysed to estimate the average velocity and the positional time series of the growth of the film. The smoothed data was then numerically differentiated to obtain reliable time derivatives. Due to data smoothing, the average velocity obtained using this method can not show the expected shuttle kink in the velocity profile. Due to the limitation of the data processing technique, the error in the average radial velocity could not be estimated.

The experimental limitations restricted us to report the velocity measurement data at smaller radius. Particularly, for the oblique configuration, $\phi = 120°$, the direction of least liquid flux is $\theta = 180°$, (see figure 4.5). It is noted that on oblique impingement of the jet, irrespective of the direction of flow the initial liquid velocity remains the same, only the flux of the liquid varies with the direction. In the direction $\theta = 180°$, the film jump terminates quickly. Therefore, it was difficult to get reliable time series data near the point of impingement, hence the velocity could be estimated only for a limited range of radial position.

The theoretical prediction and the experimental data show reasonable general agreement except at larger radii. This was again due to the limitation in the adopted velocity measurement method. Firstly, the governing equations, hence the velocity prediction needs a correction due to surface tension of the fluid (see § 2), particularly at larger radial locations, near the hydraulic jump. Secondly, near the hydraulic/film jump, the radial velocity rapidly decreases and smoothing of the positional time series data using higher order polynomials produces shuttle artifact at larger radius. These artifacts then magnifies on the numerical differentiation and manifests in the form of artifacts in estimated average velocity at higher radius. At smaller radii, the theoretical prediction and the estimate of the average velocity are in excellent agreement while at larger radius they show reasonably good agreement. These are believed to be the first measurements of the average velocity for obliquely impinging jets.

4.5 Hydraulic jump/Film jump

4.5.1 Horizontal jets impinging perpendicularly

The hydraulic jump or film jump is located where the outward flow of momentum is countered by surface tension. Above plane AA′ in figure 4.1, the liquid collects to form the rope and drains under gravity around the RFZ. Below plane AA′, initially, a film jump was clearly observed on wall materials like Perspex (Can be seen at https://doi.org/10.1016/j.ces.2016.06.011, as video 3). However, owing to gravitational acceleration in the downward direction, the film jump eventually gives way to a transition to a draining film in steady state. Therefore, the film jump was only observed above plane AA′. Above AA′ the film jump is not circular: this is partly due to gravity retarding the upwards flow but also due to the dynamics of the rope. At small values of θ (Can be seen at https://doi.org/10.1016/j.ces.2016.06.011, as videos 1 and 2) the film jump and RFZ formed is initially almost circular: over time, the rope grows in size and spreads downwards into the RFZ.

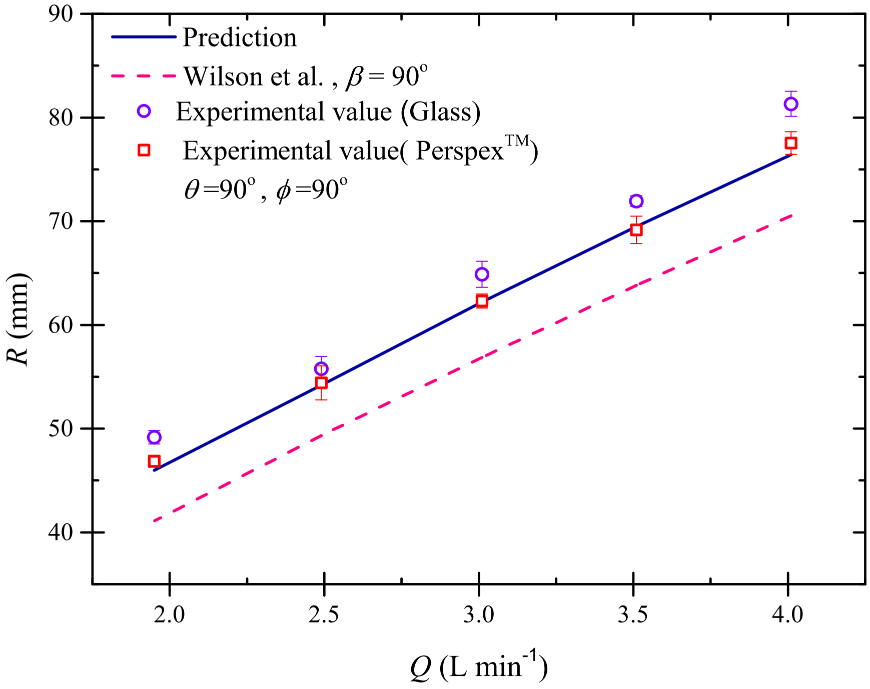

Figure 4.15 Effect of flow rate on the location of film jump for a jet impinging perpendicularly on a vertical surface at $\theta = 90°$. Comparison of measured values and the model, equation 4.51 for $Q = 1.95 - 4.01\,\mathrm{L\,min^{-1}}$, $d_N = 2.667\,\mathrm{mm}$

At larger values of θ such as 90°, the rope spreads outwards, the extent to which it spreads being determined by the nature of the surface, *i.e.* a hydrophilic wall material favouring a wider rope. This observation indicates that the predictions of the location of the film jump should be compared with the outer dimension of the rope at $\theta = 0°$ rather than the inner limit.

Figure 4.15 compares the measured values of R for $\theta = 90°$ ($\phi = 90°$ for flow rates between $1.95 - 4.01\,\mathrm{L\,min^{-1}}$ ($Re = 15500$ to 32000) for equations 4.51 and the

Wilson et al. (2012) model and for two different wall materials, Perspex^{TM} and glass. Following the discussion in § 3.3.2, the latter model uses an effective contact angle of 90°.In all cases the jets are turbulent. The Wilson et al. (2012) model underpredicts R but gives a reasonable estimate, which is consistent with the predictions of average velocity in Figure 4.13. The solution of equation 4.51 gives very good agreement with the data for Perspex but consistently underpredicts the observations on glass, by 2 mm . On glass, which is hydrophilic, the liquid spreads on the surface and there is more noticeable, random, variation in the film jump location. Button et al. (2010) reported a similar, small variation in the departure radius of water bells on glass.

Comparing the models indicates that the new model provides a more reliable prediction for the location of the film jump than those based on the Wilson et al. (2012) approach.

4.5.2 Oblique impingement on a vertical surface

Predicting the location of the film jump for an obliquely impinging jet is, like the average velocity profile, a sterner test of the model. Figure 4.16 compares the experimental measurements of film jump location for $\theta = 0°$ and $90°$ and a range flow rates, $1.95 - 4.01\,\mathrm{L\,min^{-1}}$ and angles of impingement $\phi = 120°$ and $100°$. For $\phi = 120°$, a large portion of the flow travels upward and gives rise to a very unstable rope: the measurements of R were therefore made when the rope was first formed. The difference in flow rates gives rise to R $(\theta = 0°)$ being almost twice R $(\theta = 90°)$. The locus for the Wang et al. (2013b) model shows that it tended to overpredict R $(\theta = 0°)$.

In contrast, the new model gives good agreement with the experimental data for both directions. Similarly good agreement was obtained for other values of θ (data not reported), indicating that it provides a acceptably accurate description of the flow behaviour within the jet for angles of impingement in the range $30° \leq \phi \leq 120°$

4.5.3 Every man's fluid mechanics

The oblique impingement of a liquid jet on a vertical wall is familiar to many in the context of male urination in gentleman's toilets. The model is applied here in a somewhat jocular vein to test its predictive capacity for this everyday phenomenon. A typical adult male urethral orifice is elliptical with dimensions 6 mm × 0.5 mm and delivers $1 - 1.4\,\mathrm{L\,min^{-1}}$ urine (Drake et al. (2014)). Hodgson and Smith (2014) conducted a short study mimicking male urination against a vertical well. They

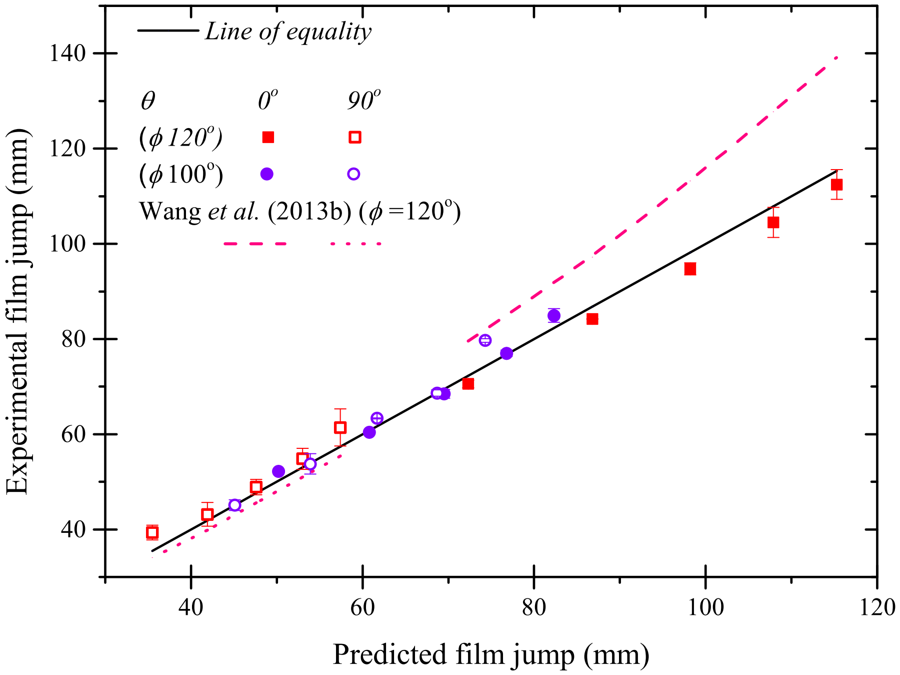

Figure 4.16 Location of the film jump for a jet impinging obliquely on a vertical surface. Comparison of measured and predicted values of R at$\theta = 0^\circ$ and $90^{\circ\circ}$. Predictions are presented for the turbulent film model presented in this chapter and that of Wang et al. (2013b). $Q = 1.95 - 4.01\,\mathrm{L\,min^{-1}}$, $d = 2.667\,\mathrm{mm}$: angle of impingement $\phi = 100^\circ$ and 120°.

established the typical angle of impingement during urination to lie between $30^\circ - 60^\circ$ and measured R_{90° and R_{0° for a 2 mm diameter nozzle at angle of impingements 40°, 50° and 40° against a vertical Perspex$^{\mathrm{TM}}$ sheet. They studied saline solution $16\,\mathrm{g\,L^{-1}}$,(mimicking urine) and water at 37°C at flow rates of 1, 1.2 and $1.4\,\mathrm{L\,min^{-1}}$. The density, viscosity and surface tension of saline solution at 37°C were similar to that of water (given in parentheses), as $1009\,\mathrm{kg\,m^{-3}}$ ($993\,\mathrm{kg\,m^{-3}}$), 0.71 (0.696) mPa.s and $0.0704\,\mathrm{N\,m^{-1}}$ ($0.0701\,\mathrm{N\,m^{-1}}$) respectively (Hodgson and Smith., 2014). The film jump measurements are compared with the present model, equation 4.50, in Figure 4.17. The horizontal distance between the wall and the nozzle was 105 mm and some drooping of the jet due to gravity was encountered. The effective angle of impingement was estimated and the values are given in Table 4.2. The model gives a reasonable prediction of their film jump measurements.

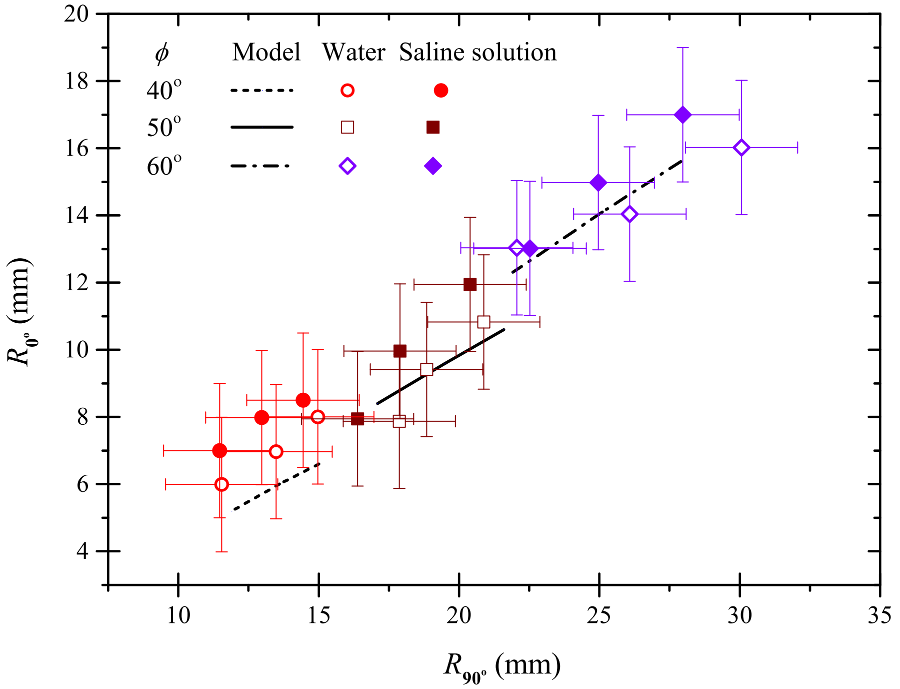

Figure 4.17 Location of film jump at $\theta = 0°$ and $90°$ for $Q = 1\,,1.2\,,1.4\,\mathrm{L\,min^{-1}}$ and notional angles of impingement 40°, 50° and 60° (equation 4.50). Data taken from Hodgson and Smith (2014). Liquid temperature 37 °C, $d = 2\,\mathrm{mm}$ and $Re = 10600, 12700,$ and 14900. Loci show predictions from this work.

Table 4.2 Summary of the effective angle of impingement for $\phi = 40°$, 50°, and 60° with 105 mm distance between the nozzle and target.

Flow rate ($\mathrm{L\,min^{-1}}$)	Effective angle of impingement		
	$\phi = 40°$	$\phi = 50°$	$\phi = 60°$
1	42	51.4	61
1.2	42	51.4	61
1.4	42	51.4	61

The model does not account for splashback, which can cause social problems. Hurd et al. (2013) characterized the splash back from male urination and recommended that practitioners employ a low angle of impingement, ϕ, and a short distance of travel so that the jet impinges as a coherent jet. If the jet is not close enough, jet break-up due to the Rayleigh-Plateau instability results in more splash back. The model confirms that a low value of ϕ will cause the bulk of the liquid to flow downwards. It is left to the reader to explain to practitioners that they should stand close to the wall in order to generate coherent jets.

4.5.4 Wall shear stress in the RFZ

The shear stress imposed by the flow in the film is an important parameter in applications such as heat transfer and in cleaning (where the soiling layer is eroded by the flow). Yeckel and Middleman studied the removal of an oil layer by a water jet impinging perpendicularly downwards on to a horizontal plate (creating a circular hydraulic jump). The shear stress imposed on the oil layer by the water film caused it to thin over time. They presented a two zone model for the flow in the RFZ based on Watson's analysis, with a turbulent film throughout. They obtained the following results for τ_w:

$$\tau_w = \begin{cases} 0.0397\frac{\rho U_o^2}{2} Re^{-0.2}\left(\frac{r}{r_o}\right)^{-0.2} & \text{if } r < r_+ \\ 30.3\frac{\rho U_o^2}{2}\left(\frac{r}{r_o}\right)^{-0.25}\frac{Re^{0.25}}{\left[\left(\frac{r}{r_o}\right)^{2.25}+27.24Re^{0.25}\right]^2} & \text{if } r > r_+ \end{cases} \tag{4.63}$$

where r_+ is their estimate of radius at which the turbulent boundary layer reaches the free surface, given by

$$\frac{r_+}{r_o} = 1.84\sqrt[9]{Re} \tag{4.64}$$

Yeckel and Middleman used the jet radius as the length scale in the jet Reynolds number: equation 4.63 are written in terms of Re as defined above, *i.e.* with jet diameter as the characteristic length scale. The wall shear stress distribution predicted by equation 4.63 for an example case is compared with those obtained from the velocity distributions given by Liu et al. (1991); Wilson et al. (2012) and the current work, § 4.2, in figure 4.18 . The wall shear stress is evaluated in each zone using

$$\tau_w = \mu\frac{\partial u}{\partial z}\bigg|_{z=0} \tag{4.65}$$

(i) For this work, in the BLFZ, differentiating equation 4.15 yields

$$\tau_w = \mu\frac{U}{\delta}f'(\eta)\bigg|_{z=0} \tag{4.66}$$

Using equation 4.23, for $\theta = 90°$, this gives

$$\tau_w = \mu\frac{U_o}{2.12\sqrt[2]{\frac{\mu r}{\rho U_o}}} \tag{4.67}$$

In the laminar zone, the shear stress is given by

$$\tau_w = \mu \frac{U}{h} f'(\eta) \bigg|_{z=0} \tag{4.68}$$

and for $\theta = 90°$,

$$\tau_w = \mu \frac{U_o}{4r\left(\frac{3.792}{Re}(\frac{r}{d})^2 + 0.1975(\frac{d}{r})\right)^2} \tag{4.69}$$

In the turbulent zone, the wall shear stress is calculated from the Blasius law, giving

$$\tau_w = \frac{0.0478\rho}{\sqrt[4]{Re}} \left(\frac{U_o}{\frac{0.167}{\sqrt[4]{Re}} \sqrt[4]{\left(\frac{r}{d}\right)^9} + \left(2.37 - 0.0108\sqrt[2]{Re}\right)} \right) \left(\sqrt[4]{\frac{r}{d}} \right) \tag{4.70}$$

(ii) Liu et al. (1991)
Applying a similar treatment to this flow profile gives
Boundary layer

$$\tau_w = \mu \frac{U_o}{1.786 \sqrt[2]{\frac{\mu r}{\rho U_o}}} \tag{4.71}$$

Laminar zone

$$\tau_w = \mu \frac{0.3U_o}{r\left(\frac{5.147}{Re}(\frac{r}{d})^2 + 0.1713(\frac{d}{r})\right)^2} \tag{4.72}$$

(iii) Wilson et al. (2012) Likewise, the approximation of a Nusselt film yields the result

$$\tau_w = \mu \frac{3U_o}{8r\left(\frac{6.667}{Re}(\frac{r}{d})^2 + \left(\frac{3Re-20}{24Re}\right)(\frac{d}{r})\right)^2} \tag{4.73}$$

The shear stress distribution predicted using Wilson et al.'s description of the flow field, equation 4.73, differs noticeably from the other profiles until larger values of $\frac{r}{d}$, which is in agreement with the results presented in § 3.4. The maximum in τ_w at $\frac{r}{d} \sim 5$ is not present in the other cases as this location lies in the initial region where the boundary layer is still developing: boundary layer development is not considered in the model. The trends in Figure 4.18 indicate that the Wilson et al. model is unlikely to give reliable descriptions of erosive cleaning driven by surface shear stress. The results presented in § 3.4 and in figures 4.13 and 4.14 show that the Wilson et al. (2012) model does however give reasonable estimates for the momentum and $\bar{u}$ in the film, which is the key parameter in the model for adhesive removal (*i.e.* peeling) presented by the same workers (Wilson et al. (2014)).

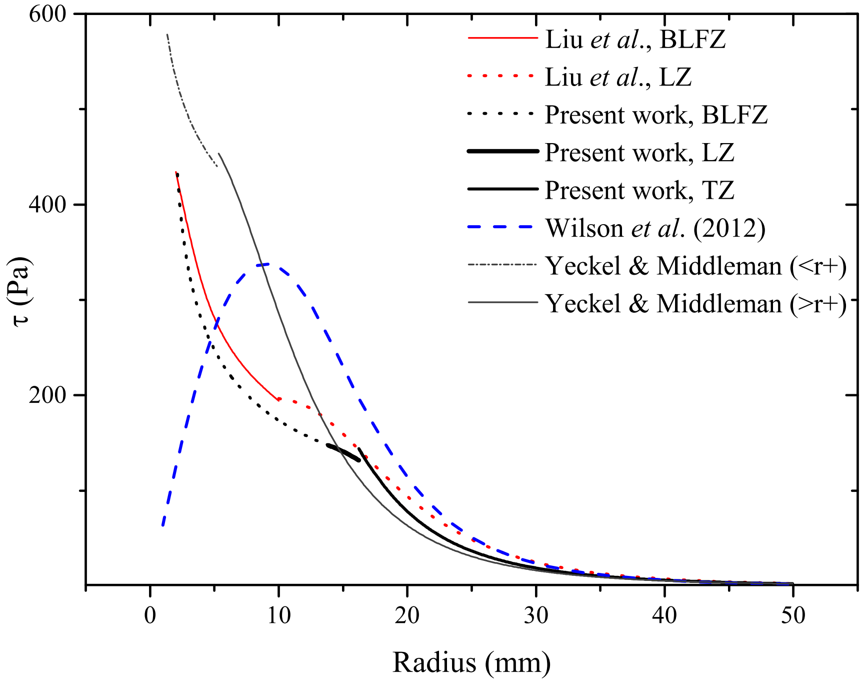

Figure 4.18 Comparison of the estimated wall shear stress distributions for a jet with $d = 2\,\mathrm{mm}$, $Re = 21000$, flow rate, $Q =$, $2\,\mathrm{L\,min^{-1}}$, $\theta = 90°$

Figure 4.18 shows that the current model predicts a similar distribution in τ_w to that of the Liu et al.. The Yeckel and Middleman model predicts a noticeably larger shear stress than the other detailed models for $\frac{r}{d} < 7$: this is because their wall shear stress calculation is for a turbulent film, using the Blasius law, and is higher in this region than the shear stress in a laminar film. Thereafter the trends are similar, with the prediction from the current work, equation 4.69, lying between the other two results. This pattern was observed in other cases considered.

4.6 Conclusions

The flow pattern created by the impingement of a turbulent water jet on a vertical wall was investigated using glass and Perspex$^{\mathrm{TM}}$ walls. The thin film in the radial flow zone was modelled as three regions and the governing equations were solved for each to find the velocity field and the film thickness. The film thickness measurements reported by Stevens and Webb (1993) were used to guide the model: this in turn gave predictions of the average velocity in the film which were compared with new sets of data generated using high-speed video. The analysis yielded predictions for the transition to turbulent flow based on the location where the laminar liquid film can amplify a disturbance and become chaotic.

The postulation for the criterion for transition from a laminar film to a turbulent one is based by work of Dou and Khoo, and relates the transition to the point where there is a minimum in film thickness. In the experiments the transition was assigned to be the distance where concentric transverse surface waves (arising from the jet being varicose due to a Plateau-Rayleigh instability) were replaced by more chaotic structures. This hypothesis requires more rigorous theoretical analysis and is a topic for further study. Nevertheless, the model for turbulent transition gives good agreement with the experimental data.

The measurements of the average velocity in the film were obtained using a new technique. The average velocity is obtained by differentiating the time series data obtained from the leading edge of the initially growing liquid film. It avoids the complications experienced using velocimetry where the influence of waves is significant (see Aouad et al. (2016)). It is relatively robust, independent of liquid optical properties and can be readily applied to different wall materials, angles of inclination and flow rates.

The model gave good agreement with both the historical and new data, for average velocity and location of the film jump. The predictions for obliquely impinging jets were noticeably superior to the model of Wang et al. (2013b) and Wilson et al. (2012). This will allow the rate of cleaning by such jets, using the model of Wilson et al. (2014), to be predicted with greater confidence.

Chapter 5

Cleaning by stationary and moving liquid jets

5.1 Introduction

The previous chapters discuss the hydrodynamics of impinging liquid jets. This chapter explores the application of impinging liquid jets in cleaning. The primary motivation for cleaning by an impinging liquid jet is the maximum utilisation of the available hydrodynamic force/energy in the flow. Liquid jets are frequently used in modern industrial cleaning operations where rotating nozzles are employed to clean the internal and external walls of process equipment and transportation tanks. These rotating nozzles offer advantages over traditional (1) soak and clean techniques, which requires longer down time and and sometimes manual labour and, (2) static spray devices, where the falling film created by these devices does the cleaning (Jensen et al. (2011)).

On impingement of a liquid jet onto a surface, the liquid spreads radially in a thin film until it forms a hydraulic jump. The flow in the thin liquid film is associated with higher liquid velocity, momentum, and shear stress. Figures 3.4 and 4.18 show the momentum per unit width, M, and the wall shear stress distribution in the thin liquid film upstream of the hydraulic jump. From the point of impact up to the hydraulic jump radius, M, and the wall shear stress decreases rapidly.

On normal impingement of a static liquid jet onto a soiled surface, the liquid cleans the surface, forming a circular cleaning front which grows with time. Wilson et al. (2014) proposed a model to describe cleaning by static impinging jets. This model suggested that the rate of cleaning is proportional to the momentum at the cleaning front (see § 5.3). This implies that the driving force for cleaning is the liquid momentum at the cleaning front. In case of a static liquid jet, as the cleaning front grows, the momentum at the cleaning front decreases and hence the cleaning rate decreases rapidly.

However, a liquid jet moving across a soiled surface leaves a trail of cleaned region. In this scenario, if the liquid jet moves slowly, a steady state can be achieved where at the leading edge of the cleaning trail, the rate of cleaning equals the speed of the liquid jet or in case of normal impingement, the nozzle's speed. This implies that, for a given jet velocity, the distance between the point of impingement and the cleaning front remains constant. Hence, the cleaning front remains exposed to a constant momentum.

Near the point of impact, the cleaning rate remains higher and by moving a liquid jet, the cleaning front is always exposed to a higher mechanical force (momentum) as compared to a static jet or a spray ball. Although the moving liquid jets are advantageous over the traditional cleaning systems, they are largely unexplored theoretically. The design and operation of such systems are empirical; mostly based on trial and error. To the best of my knowledge, this is the first study exploring tank cleaning scenarios by moving liquid jets, theoretically. There are two main aspects of modelling cleaning by moving liquid jets; (1) liquid jet dynamics and created liquid film's behaviour and (2) soil removal. This chapter will provide a simple mathematical framework to study cleaning by moving liquid jets, on which future studies with further complexities can build on.

The bulk of this chapter is based on the paper "*Cleaning vessel walls by moving water jets: Simple models and supporting experiments*" by Bhagat, R.K., Perera, A., and Wilson, D.I., which was published in the journal *Food and Bioproducts Processing*, (2017), 102, 31-54. The manuscript was drafted by Prof Ian Wilson. Anira Perera was an undergraduate student who worked with Prof Ian Wilson and me on the mathematical derivation of the moving jet case, when the nozzle moves in a vertical plane, which is presented in § 5.5.1 and § 5.5.2. I then found the analytical solution for these cases. § 5.5.3 on cleaning by moving liquid jets when the nozzle moves sideways creating ring shaped cleaning strips are based on my ideas. I introduced the near and far field approaches. I conducted the data analysis and the new experiments. I extended the normal static jet model for cleaning to obliquely impinging jets and compared it with the experimental data. The figures which I used from the manuscript are clearly cited. The parts where I did not contribute significantly are clearly cited and mentioned in the text. In particular, I note that Section § 5.6 is reproduced from Bhagat et al. (2017) which is mainly based on my coauthor's ideas. I calculated the results for this section. I also participated in the discussions and helped develop the ideas. Text from the paper appears in this chapter. The paper is included in Appendix C.

5.1.1 Jet dynamics and created liquid film's behaviour

A water jet travelling through air is subject to the well known Rayleigh-Plateau instability (Eggers and Villermaux (2008); Weber (1948)). Depending on the tank size and other parameters, the liquid jet may impact the surface as a coherent jet, a varicose shaped jet whose diameter varies strongly or completely broken up jet in the form of droplets. After impacting the surface, the liquid spreads radially outwards in a thin film. In § 4, it has been shown the liquid film goes through various stages, namely; a boundary layer formation zone, a laminar zone, then a turbulent transition and subsequently flow as a turbulent film. The various stages of the liquid film, jet stability add further complexity to the whole analysis. Therefore, for the simplicity of the analysis, it is assumed that the liquid jet remains coherent and the effect of the rotation of the nozzle is ignored. The liquid film is described by Wilson et al.'s simple hydrodynamic model.

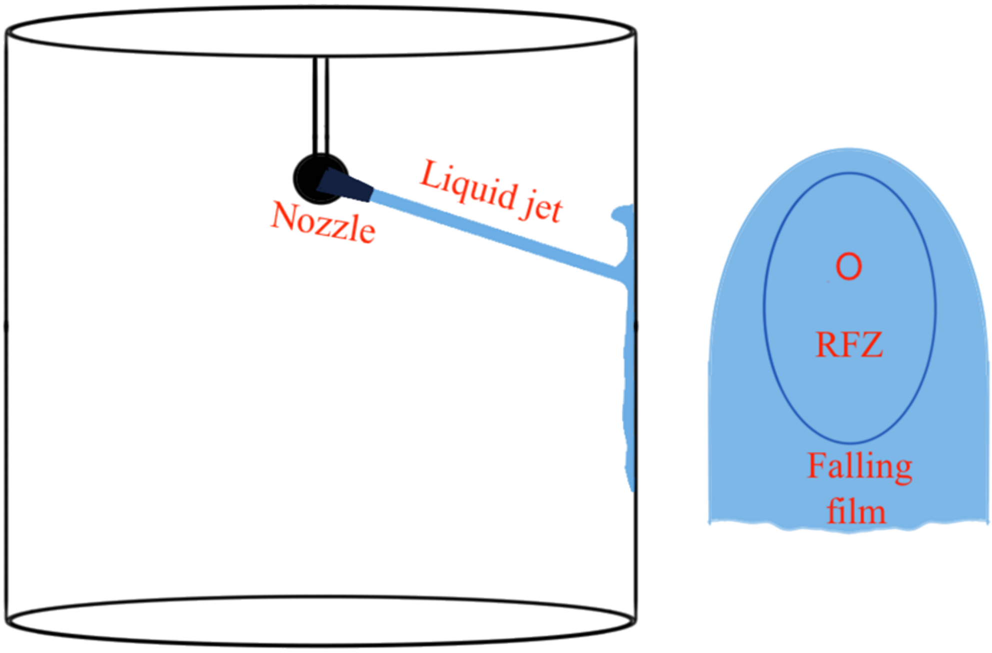

Figure 5.1 Schematic of jet cleaning in a cylindrical vessel. O is the point of jet impingement and RFZ is the region of fast moving radial flow. The shaded region represents area wetted by the liquid, with sketch of flow pattern on wall on right.

The nozzle speed, which is $\mathcal{O}(\mathrm{mm\,s^{-1}})$, is much smaller compared to the mean velocity in the liquid film hence it is assumed that the nozzle's motion does not influence the liquid film.

5.1.2 Soil removal

The removal of a soil layer by the flow of a cleaning solution is determined by its chemical composition, physical structure (dry, wet, crystalline no-crystalline), relative interaction (cohesive or adhesive forces) and solubility. The main objective of industrial as well as domestic (dish washers) cleaning techniques is to clean as fast as possible at as less cost as possible; it should take the least amount of time and should be environmentally friendly. Classical cleaning is described in terms of four key parameters, which forms Sinner's circle(Tamime, 2009) are; (1) mechanical action, (2) chemical actions, (3) temperature and, (4) time. Wilson (2005) reviewed the cleaning mechanisms to remove fouling layers whereas Fryer and Asteriadou (2009) classified food soils in terms of mechanical and chemical action. Mechanical action relates to flow rate while chemical action relates to reagents and detergents.

In terms of the mechanical action, the flow field of an impinging liquid jet can be subdivided into three regions namely (1) the stagnation zone, (2) the radial flow zone, RFZ, and (3) the flow beyond the hydraulic jump. In the immediate vicinity of the point on the solid surface where the liquid jet approach toward the surface subdivide and spread away is the region of flow called stagnation zone. In the stagnation zone, a point of intersection of the center line of the jet and the solid surface is know as a *stagnation point*. At the stagnation point, even without no slip boundary condition the flow velocity is zero. At this point the force present is normal in nature. Between $r = 0$ to the jet radius r_o, the vorticity created at the boundary diffuse away from the surface which is pushed back or convected towards the surface by the liquid jet. Hence, vorticity generated at the boundary remains confined in a layer adjacent to the boundary (Batchelor, 2000). This creates a boundary layer in the stagnation zone. In the rest of the radial flow zone up to the hydraulic jump, the shear stress decreases with r rapidly (see figure 4.18). Beyond the hydraulic jump, liquid flow slowly in a thick draining film and the shear stress is low in this region.

In relation to the cleaning by impinging liquid jets, Bhagat et al. (2017) presented an alternative food soil characterisation which is shown schematically in figure 5.2. In this characterisation, the mode of cleaning is determined by the soil properties and their interaction with the flow. Soils are classified as (1) mobile soils; the soils which deform when subjected force and, (2) immobile soil; which does not deform but undergo rupture and breakage. A soil generally gets removed by a combination of cleaning mechanisms. In the different region of mechanical action, one or the other cleaning mechanism dominates. For example; in the RFZ, where momentum and shear force are high, a soil may get dislodged due to peeling (immobile soil behaviour) however, in the draining film region the soil may behave as a mobile soil and be removed by dissolution. Similarly, chemical reagents and temperature can change the soil's response to flow and after exposure to these a soil's property can change from being immobile to mobile.

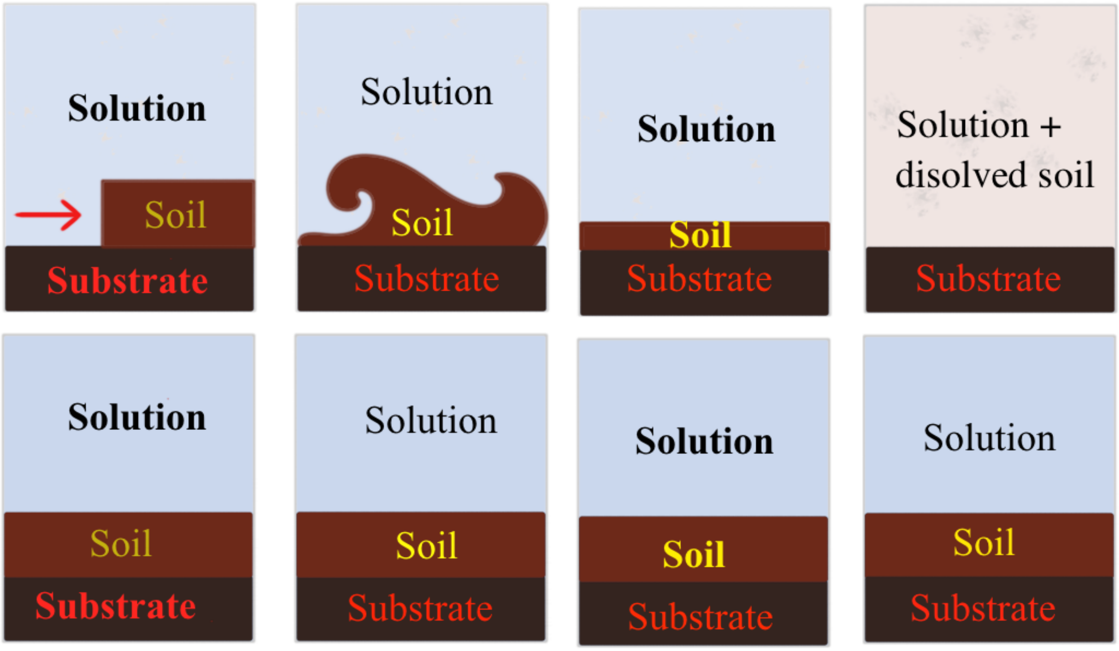
Solution
Soil
Substrate
Solution
Soil
Substrate
Solution
Soil
Substrate
Solution +
disolved soil
Substrate
Solution
Soil
Substrate
Solution
Soil
Substrate
Solution
Soil
Substrate
Solution
Soil
Substrate

(a) **Peeling Immobile soil**

(b) **Roll-up Mobile soil**

(c) **Erosion Immobile soil**

(d) **Dissolution Mobile soil**

Figure 5.2 Schematic of cleaning mechanisms (a) Peeling: Adhesion of soil to the substrate is weaker than cohesive interactions in the soil: the soil detaches as a layer. Promoted by surfactant ingress to the soil/substrate interface. (b) Roll-up: Cohesion within the soil is strong and the soil is insoluble in the cleaning solution. The soil is deformed by fluid flow and/or buoyancy forces, causing it to leave the substrate, which can be enhanced by surfactants. (c) Erosion: Cohesive interactions within the soil are weaker than adhesion to the substrate: shear at the interface removes material. Promoted by agents that weaken the soil. (d) Dissolution: The soil is soluble in the cleaning solution: cohesive interactions within the soil are less favourable than those with the solution. Favoured by thermodynamic factors such as temperature, pH and solvent nature.

Another major aspect of cleaning which is related to the interaction and time dependent behaviour between the cleaning liquid and the soil is 'soaking'. If a soil is exposed to a cleaning fluid which changes either physical or chemical structure of the soil which results in its adhesive, cohesive strength or solubility of the soil, can promote or make it harder to clean. Exposure to the cleaning fluid can also change the cleaning mechanism, for example, if the solubility of a soil is pH dependent, by manipulating the pH of the cleaning fluid and exposure time, one can manipulate the cleaning mechanism and rate. Likewise, if a surfactant penetrates through a soiling layer to the soil/substrate interface, it can promote adhesive failure (Ali et al. (2015)). This time dependency introduces further complexity, as the extent of contact with the cleaning solution is determined by the distribution of liquid, *i.e.* behaviour at impingement and film drainage (see Aouad et al. (2016)).

5.1.3 Modelling and optimisation

One of the key elements in developing a mathematical framework to predict and optimise cleaning by impinging liquid jets, is the understanding of the different cleaning mechanisms shown in figure 5.2. To some extent, models capable of predicting cleaning by a static impinging liquid jet by different mechanism are available. The remaining knowledge gap is to apply the current understanding of cleaning by static impinging jets to moving liquid jets, which are widely used in industry.

For cleaning by static liquid jets Wilson et al. (2014) proposed a model for cleaning by the peeling mechanism in which they hypothesised that the rate of cleaning is proportional to the momentum at the cleaning front. They showed that the model could predict cleaning for a number of different soils. Yeckel and Middleman (1987) looked at cleaning of an oil layer by impinging liquid jets where the main mechanism of cleaning is erosion. They proposed that the shear stress at the interface between water and the oil promotes motion and thinning of the oil layer. Hsu et al. (2011) and Walker et al. (2012) looked at other soils with complex rheologies in similar setup. Meng et al. (1998) and Leu et al. (1998) studied cleaning by high pressure (69-311 MPa) water jets, where erosion is caused by the impingement of high velocity droplets. Scholtz and Trass (1970) studied convective mass and heat transfer which could be extended to cleaning by dissolution mechanism for different materials.

Wilson et al. (2015), Glover et al. (2016) studied cleaning by normally impinging liquid jets moving across the soil surface and cleaning. Considering the far field approximation of liquid flow (see § 5.3.3) they developed an analytical solution to predict the width of the region cleared by these jets. This model, in principle, could give the time required to clean a tank, provided the liquid jet impinges normally. However, in practice, from a fixed position in the tank, the nozzle(s) rotates and spray the water jet which move across the surface creating different cleaning patterns (see figure 1.6). This implies that the angle of impingement changes continuously (see figure 5.1).

This chapter presents a simplified modelling approach to the problem of cleaning by moving liquid jets. Wilson et al. (2014) used the the far field approximation for the hydrodynamics, which is exact in the outer periphery of the RFZ. This implies that the model cannot explain cleaning in the inner regions (closer to the point of impingement) of the RFZ. However, for a relatively weak food soil, the far field approximation could be a reasonable approximation. Figure 5.3 shows a cleaning scenario in which a nozzle moves downwards with velocity $|V|$ creating a trail of cleaned region. In the frame of the liquid jet, the soil approaches the leading edge of the cleaning trail, X, with velocity V. At this point the rate of cleaning is equal to the jet velocity V. Vector OP indicates a typical streamline which is diverging from vector V and point P is the furthest point where OP is of the size of the hydraulic jump. For a weak food soil, cleaning rates near point P (indicated in the highlighted region) will determine the final width of the cleaned region.

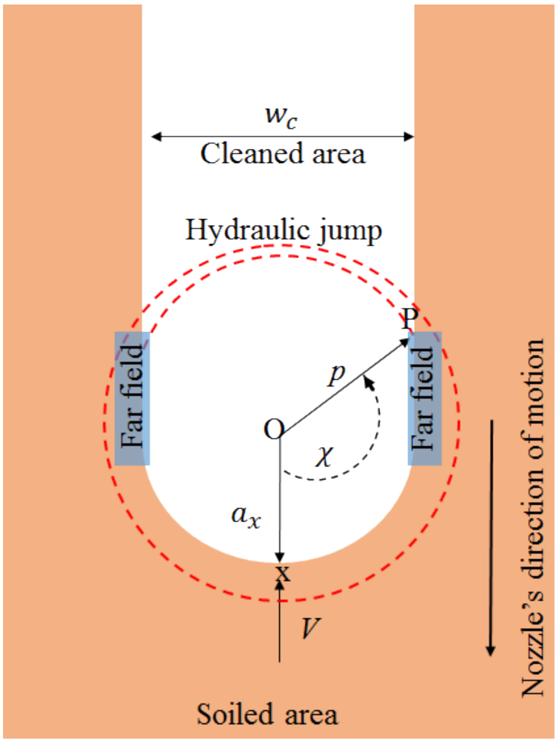

Figure 5.3 Schematic of jet moving downwards with a velocity V and cleaning a vertical wall. O is the point of jet impingement and OP is the point where cleaning strip meet the hydraulic jump.

For a relatively weak food soil and at a low nozzle velocity V, this region is likely to be in the far field region implying that far field hydrodynamics will dictate the final width of the cleaned region. For the case when the nozzle moves in upward direction, the cleaning strip will continuously be in contact of the liquid and far field hydrodynamics will determine the final cleaning width. Hence for rest of the analysis, the hydrodynamics are described by the far field approximation. In this chapter, the radial flow zone is divided into three regions; (1) intermediate region, (2) near field and, (3) far field. The model for cleaning (by peeling mechanism) by static perpendicular as well as inclined liquid jets, is extended to all three regions. The approximations used to model the cleaning by a moving liquid jet are listed below:
(1) § 2 shows that in the RFZ, gravity does not play any significant role, and even on vertical plates, the RFZ remains approximately circular. Therefore, in the RFZ, gravity is ignored.
(2) Gravity and rotation of the nozzle do not affect the liquid jet and it travels through air as a straight ray.
(3) The liquid jet remains coherent (no break-up or splash-back from the surface)
(4) The soil layer is uniform
(5) Only the peeling mechanism is considered
(6) The flow field in the RFZ is described by the simple Wilson et al. (2012) laminar film model

5.2 Experimental

The models developed in the next section are compared with data obtained from experimental studies of cleaning by impinging water jets. The data presented in figure 5.8 has been published previously in Wilson et al. (2015). The experimental data for Polyvinyl acetate (PVA) layers on polymethylmethacrylate (Perpex®) sheets in figures 5.11 and 5.12, and petroleum jelly on glass in figures 5.9 and 5.10, are new sets of data. The latter data sets were obtained using the apparatus described by Wilson et al. (2014) and by Glover et al. (2016). Detailed descriptions of the experimental configuration and operating protocols are given in these papers, §2.3 and § 4.3. Layers of petroleum jelly were prepared by spreading the soft solid material across a 300 mm wide × 500 mm long and 5 mm thick glass sheet using a spreader tool. The spreader tool consist of a aluminum blade attached to frame which could be rolled on attached roller wheels (see figure 5.4). Two identical screws of known pitch adjust the level of the blade and hence can create a gap between the blade and the substrate to be coated. A surplus amount of material to be coated (petroleum jelly or the PVA) was spread on the surface and made as even as possible using a window cleaning spreader. Then, the slider is placed at one end of the substrate behind the surplus amount of soil and pulled across the sheet to the other end, leaving a uniform coating layer. The procedure is also described by Glover et al. (2016). PVA layers were prepared on Perspex®sheets and allowed to dry for 24 h before testing. The thickness of the PVA layers was measured using a deep throat micrometer. To measure the petroleum jelly layers thickens; the substrate was weighed before and after spreading the layer. After spreading the layer, the area covered by petroleum jelly layer was found using image analysis and the thickness of the layer t_{PJ} was determined using

$$t_{pj} = \frac{Wt_{after} - Wt_{before}}{\rho_{pj} \times A_{pj}} \tag{5.1}$$

Where t_{pj}, Wt_{after}, Wt_{before}, ρ_{pj}, and A_{pj} are the thickness of the layer, weight of the plate after coating, weight of the plate before coating, density of the petroleum jelly and the coated area respectively.

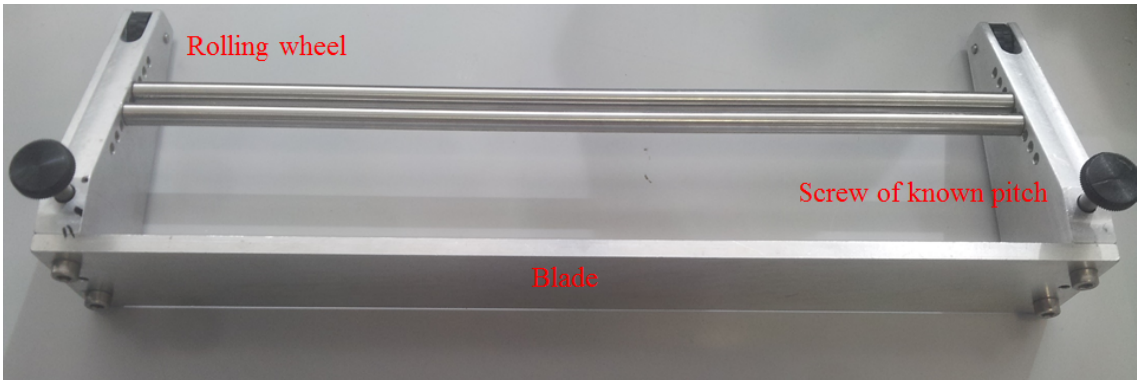

Figure 5.4 Picture of the slider or the coater

The sheet was mounted vertically on a frame located within a test chamber whose walls were transparent. Distilled water was pumped from a reservoir at a set and measured flow rate through a nozzle to create a coherent jet. The flow rates used range from $1 - 3\,\mathrm{L\,min^{-1}}$. The nozzle was positioned 28 cm from the sheet so that the jet was coherent at the point of impingement. The jet diameter could be changed by using nozzles with similar configuration but different diameter. After impinging, the water spread out and drained down the sheet, after which it was collected and recycled. The experiments were performed at ambient temperature, which varied from 18 to $20°C$ in the tests reported here. The experimental setup is described in detail in §2.3 and § 4.3.

The use of transparent sheets meant that the evolution of the cleaned region could be monitored by a video camera (Nikon D3200) located outside the test chamber. Transparent graticule tape was attached to the dry side of the sheet to provide a calibration for extracting dimensions from the images. An interrupter plate was initially placed between the nozzle and the soiled sheet when the flow was started until a steady, coherent jet was obtained. The interrupter plate was then removed and the change in cleaned region size extracted by analysis of the videos.

5.3 Models

The model for peeling (*i.e.* adhesive removal) of soil layers by impinging jets for stationary nozzles presented by Wilson et al. (2014) and its extension to moving nozzles (Wilson et al. (2015)) is summarised and extended to the cases where the jet is not impinging perpendicularly. In these models, the force imposed by the spreading liquid film within the RFZ is considered sufficient to detach the soil from the substrate. When a jet impinges perpendicularly on a wall, with negligible effect of gravity, a circular cleaned region of radius a grows over time. The local rate of film removal is given by

$$\frac{da}{dt} = k'M \tag{5.2}$$

where a is the measure of the size of the cleaned area, M is the local rate of momentum flow per unit width of cleaning front, and k' is a rate constant which incorporates any dependency on soil strength, interaction with the substrate, and thickness.

5.3.1 Cleaning by static nozzles; full model/intermediate soil model

From Equation 3.9 and 3.10, the momentum per unit width, M, at radius r is given by

$$M = \frac{3\rho Q}{5\pi}\frac{1}{r}\left(\frac{1}{\frac{1}{U_\circ} + \frac{10\pi^2\mu}{3\rho Q^2}\left[r^3 - r_o^3\right]}\right) \tag{5.3}$$

alternatively Equation 5.3 can also be written as

$$M = \frac{3\rho Q}{5\pi}\frac{U_\circ}{r}\left(\frac{1}{1 - \frac{20}{3Re} + \frac{20}{3Re}\frac{r^3}{r_\circ^3}}\right) \tag{5.4}$$

This expression assumes a well-developed parabolic velocity profile within the film, which is not valid for small r. This assumption was criticized in § 3 and § 4 and shown to be reasonable for larger values of r. Nevertheless, the model gives a reasonable engineering estimate of the momentum, M, and for the simplicity of the analysis, the model has been implemented to predict cleaning. Substituting equation 5.3 into 5.2 yields,

$$\frac{da}{dt} = k'\frac{3\rho Q}{5\pi}\frac{1}{a}\left(\frac{1}{\frac{1}{U_\circ} + \frac{10\pi^2\mu}{3\rho Q^2}\left[a^3 - r_o^3\right]}\right) \tag{5.5}$$

Separating the variables,

$$\left(\frac{1}{U_\circ} - r_o^3\frac{10\pi^2\mu}{3\rho Q^2}\right)\int_{a_i}^{a} a'da' + \frac{10\pi^2\mu}{3\rho Q^2}\int_{a_i}^{a} a'^4 da' = k'\frac{3\rho Q}{5\pi}dt \tag{5.6}$$

Integrating equation 5.6 yields

$$\left(\frac{1}{U_\circ} - r_o^3\frac{10\pi^2\mu}{3\rho Q^2}\right)(a^2 - a_i^2) + \frac{10\pi^2\mu}{3\rho Q^2}(a^5 - a_i^5) = k'\frac{3\rho Q}{5\pi}\Delta t \tag{5.7}$$

Here a_i is the initial cleaned radius. For high Reynolds number flows, a careful examination of equation 5.4 suggests two limiting cases; regime 1 (near field) when $a \sim r_o$ and regime 2 (far field) when $a \gg r_o$, and in the intermediate regions, where full model must be used.

5.3.2 Near field approximation: soils for which the cleaning radius remain small or when $r \sim r_\circ$

In the limiting case when $r \sim r_\circ$ and the jet Reynolds number, Re, is high, equation 5.4 can be approximated by

$$M \approx \frac{3\rho Q}{5\pi}\frac{U_o}{r} \tag{5.8}$$

The liquid jets used in cleaning operations are generally high Reynolds number jets. The above approximation is valid only in the region when $\frac{20}{3Re}\frac{r^3}{r_\circ^3} \ll 1$ which implies that $\frac{r}{d} \ll 0.265Re^{1/3}$, the cleaning front is located near the point of impingement and the boundary layer in the film is not fully developed. This is consistent with the theory presented in § 4 on the boundary layer formation zone where equation 4.27 demarcating the boundary layer to the laminar zone is given by $\frac{r}{d} < 0.24Re^{\frac{1}{3}}$. From equation 5.2, rate of cleaning was estimated to be

$$\frac{da}{dt} = k' \frac{3\rho Q}{5\pi} \frac{U_o}{a} = \frac{\sigma}{a} \tag{5.9}$$

where σ is a group of parameters and it sets the cleaning timescale. Integrating equation 5.9 from the point where adhesive breakthrough is first noticed, a_i, at time t_i, to time t gives

$$(a^2 - a_i^2) = 2\sigma(t - t_i) \tag{5.10}$$

The cleaned region is expected to increase with $\Delta t^{1/2}$ (a parabolic growth law). After some time a will reach the limit of validity of Equation 5.8.

5.3.3 Far field approximation; soils for which the cleaning radius is large or when $r \gg r_\circ$

This is the scenario considered by Wilson et al. (2014). In the limit of $r \gg r_\circ$, equation 5.3 can be approximated to

$$M = \frac{9\rho^2 Q^3}{50\pi^3 \mu} \left(\frac{1}{r(r^3 - r_o^3)} \right) \tag{5.11}$$

Substituting equation 5.11 in 5.2 yields the rate of cleaning for large radii,

$$\frac{da}{dt} = k'M = k' \frac{9\rho^2 Q^3}{50\pi^3 \mu} \left(\frac{1}{a(a^3 - r_o^3)} \right) \tag{5.12}$$

Integrating 5.12 w.r.t. time yields

$$\left[\frac{a^5}{5} - r_\circ^2 \frac{a^2}{2} \right]_{a_i}^{a} = k' \frac{9\rho^2 Q^3}{50\pi^3 \mu} (t - t_i) \tag{5.13}$$

For $r \gg r_\circ$ such that $a^5 \gg r_\circ^3 a^2$ and when a_i and t_i are of the $\mathcal{O}(0)$, Wilson et al. (2014) approximated it further and found the relation

$$a \approx \left(k' \frac{9\rho^2 Q^3}{50\pi^3 \mu} \right)^{1/5} (t - t_i)^{1/5} = K \Delta t^{0.2} \tag{5.14}$$

Here, K is a lumped cleaning constant dependent on mass flow rate. Adopting a similar approximation equation 5.12 can be written as

$$\frac{da}{dt} = k'M \approx k' \frac{9\rho^2 Q^3}{50\pi^3 \mu} \left(\frac{1}{a^4} \right) = \frac{\xi}{a^4} \tag{5.15}$$

The evolution of a is then noticeably different from equation 5.9.

Figure 5.5 compares the evolution of the cleaned area predicted by equations 5.6, 5.10 and 5.14, in terms of scaled time $t/t_\circ = t\sigma/r_\circ^2$ (the time scaling can be obtained from equation 5.10), for the values employed in the experiments of Glover et al. (2016): water at $20°C$, $r_\circ = 1\,\mathrm{mm}$, $Q = 2\,\mathrm{L\,min^{-1}}$ and $U_\circ = 10.8\,\mathrm{m\,s^{-1}}$, giving $Re = 21800$ with $a_i = r_\circ$. The full model deviates from the near field prediction around $a/r_\circ = 14$, at $t/t_\circ = 4000$, and follows the far field trend from $a/r_\circ = 20$. Beyond $a/r_\circ = 30$ the difference between the latter two models is small and decreases with time.

Also plotted on the figure is the locus obtained when M is calculated using the detailed model of the hydrodynamics of the radial film including a turbulent film in § 4. This shows similar behaviour to the full model up to $a/r_\circ = 40$. The models deviate thereafter owing to the fact that the detailed model considers three different flow regimes including turbulent film whereas Wilson et al.'s simple model does not account for either boundary layer formation or turbulence. The discontinuity in the detailed model, marked F on the inset, is the location of the transition from laminar to turbulent behaviour in the film. Nevertheless, the Wilson et al. (2012) model give a reasonable prediction of the cleaning behaviour and has the advantage of yielding tractable analytical solutions: the detailed model always requires numerical enumeration. Also for cleaning applications, it is reasonable to assume that for static jet cleaning the region of interest is the initial region of fast cleaning. In figure 5.5, in first $t/t_\circ \approx 1600$, the cleaning radius grow to $a/r_\circ = 25$ however in next 18200 scaled time unit $a/r_\circ$ becomes 25 to 50. In this initial region the simple Wilson et al. (2012) models give reasonable engineering estimate of momentum and cleaning. The Wilson et al. model is therefore used in the following sections which consider the influence of features such as varying angle of impingement and soil behaviour.

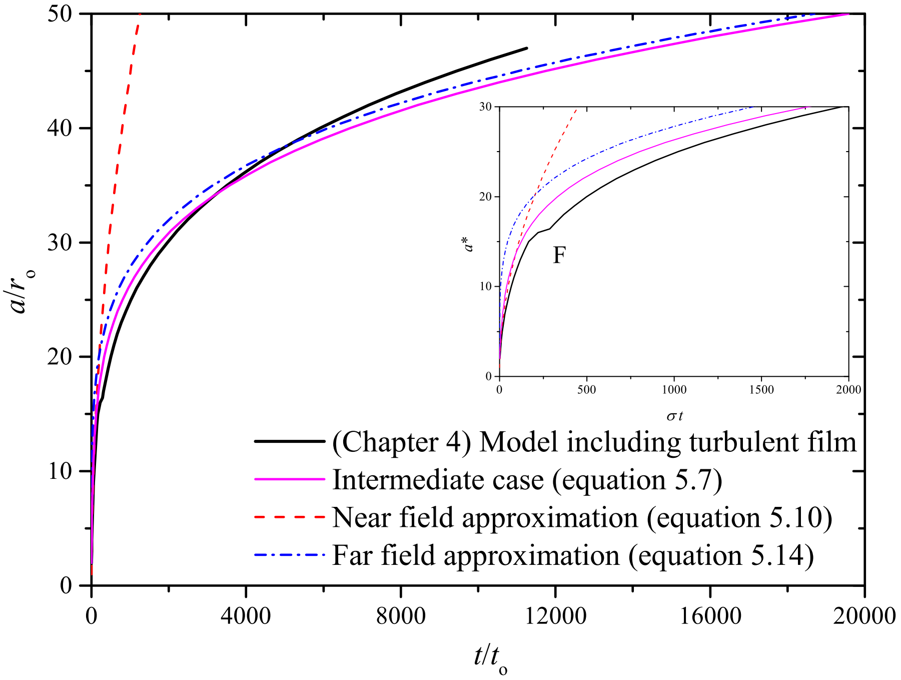

Figure 5.5 Predicted evolution of the size of the cleaned region for a coherent water jet impinging perpendicularly on a flat wall (no gravity effects). The results are presented in dimensionless form; $a/r_\circ$ and $t/t_\circ$, where $t_\circ$ is the characteristic time defined as $t_\circ = r_\circ^2/\sigma$. Inset shows initial behaviour. Thin loci show predictions based on the Wilson et al. (2012) flow model: dashed line - near field, equation 5.10; dot-dash line - far field, equation 5.14 ; continuous line - intermediate case, equation 5.6. The heavy locus is the prediction obtained using the numerical model presented in § 4 and Bhagat and Wilson (2016) to calculate M for a water jet at $20°C$ with $r_\circ = 1\,\text{mm}$ and $Re = 22,200$. The discontinuity at F is associated with the transition to turbulence in the film.

5.3.4 Cleaning by moving nozzle, jet perpendicular to the wall

In this case the nozzle moves, the jet strikes the wall perpendicularly, and the point of impingement moves across the soiled surface at velocity V. The photograph in figure 5.6(a) shows a roughly elliptical front ahead of the point of impingement followed by a cleared strip downstream, of width w_c. Wilson et al. (2015) modelled this using the construction in figure 5.6(b). They changed the frame of reference so that the point of impingement was static and the soil moved towards the jet at velocity V. Velocity V is equal to the speed of translation of the nozzle, which they labelled v_{jet}.

For jets generated by rotating nozzles, V varies with angular position and this is considered in the process analysis later.

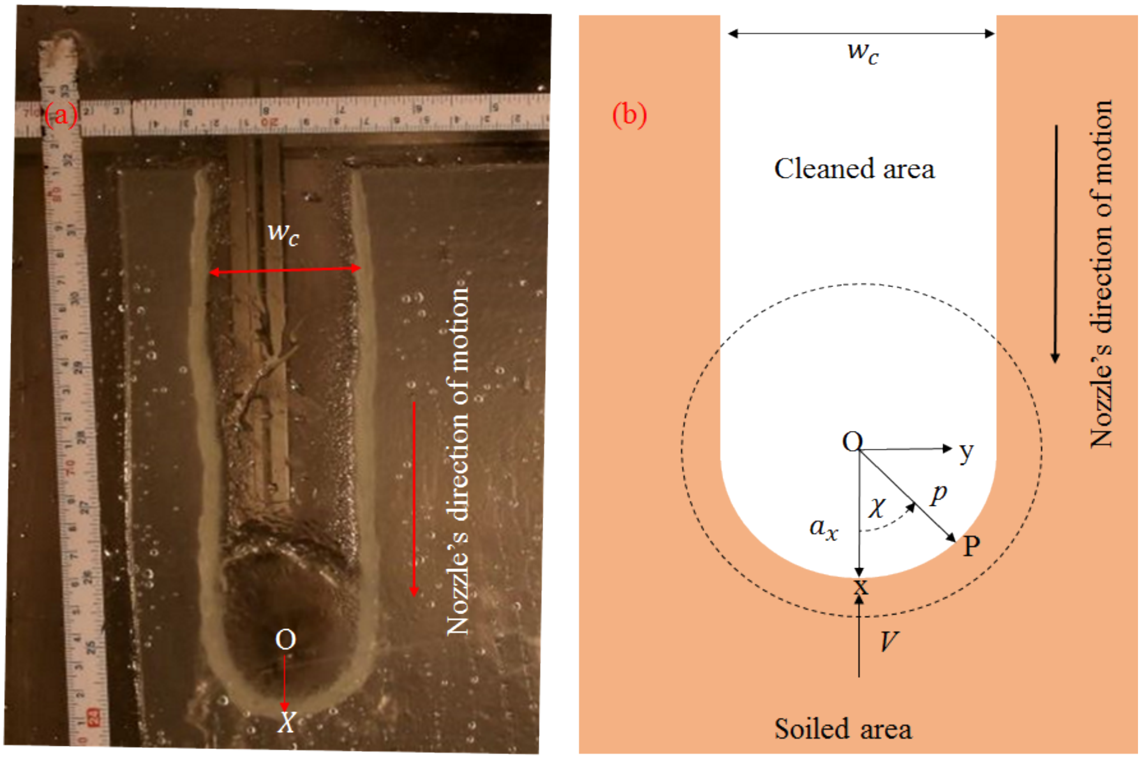

Figure 5.6 (a) Photograph, and (b) model schematic for the region cleaned by a vertical water jet moving from left to right across a plate coated with petroleum jelly. O is the point of impingement and R the radius of the RFZ.

Point X, located in this case a distance a_x directly ahead of the jet, is a stationary point where the rate of cleaning is equal to the rate at which soil material is convected towards it, at V. At point P, oriented at angle χ to the direction of nozzle movement and at distance p from the origin, vector addition is required to resolve the relationship between the rate of cleaning at P to V (see figure 5.7). When the radial velocity of the liquid, u, is much greater than V, the locus of p is described by the non-linear differential equation

$$\frac{dp}{d\chi} = \left(\frac{da}{dt}\right)_P \frac{p}{V \sin \chi} - \frac{p}{\tan \chi} \tag{5.16}$$

The analysis of Wilson et al. (2015) is revised and extended to other cases

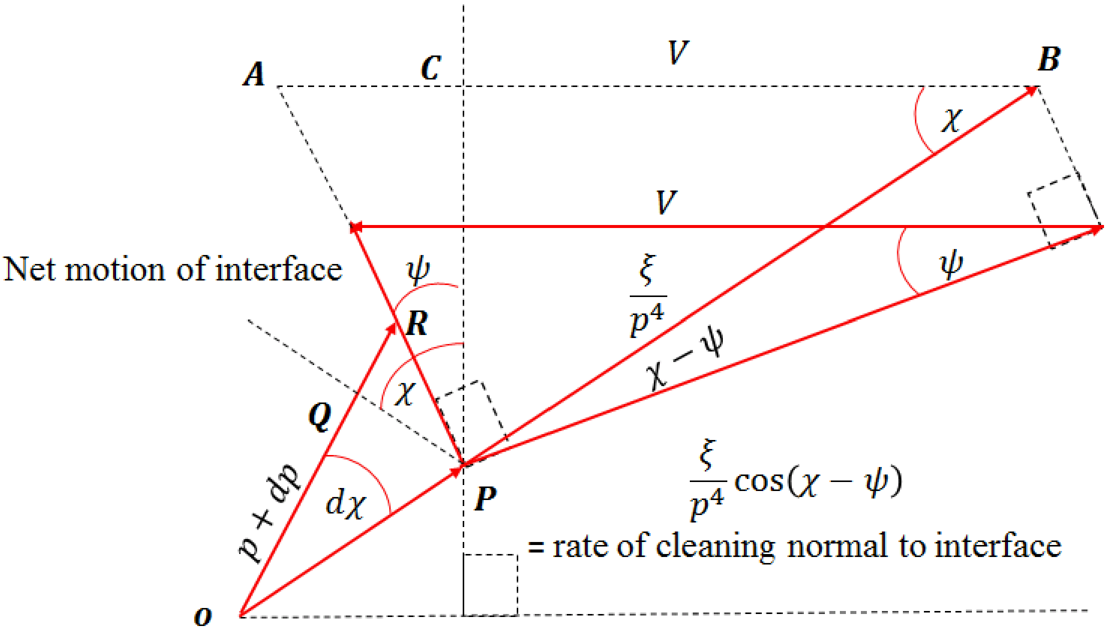

Figure 5.7 Vector diagram for cleaning front at point P in figure 5.6. Vector PB represents the rate of cleaning along the radial direction and its magnitude taken to be ξ/p^4. Vector PA is the direction of net motion of the interface due to the cleaning and the motion of the nozzle or the target. Here V is the speed of the nozzle or the speed of the target plate.

Far field case

Wilson et al. (2015) considered the far field scenario, where $p \gg r_\circ$ described by equation 5.15. At X, with $a_x \gg r_\circ$,

$$\frac{da}{dt} = V = \frac{\xi}{a_x^4} \tag{5.17}$$

and

$$a_x = \left(\frac{9}{50}\right)^{1/4} \left(\frac{k'\dot{m}^3}{\rho\pi^3\mu}\right) \left(\frac{1}{V}\right) \tag{5.18}$$

Elsewhere $da/dt = \xi/p^4$ and equation 5.16 becomes

$$\frac{dp}{d\chi} = \frac{\xi}{Vp^3 \sin\chi} - \frac{p}{\tan\chi} \tag{5.19}$$

They integrated 5.19 numerically and obtained the result $w_c = 2.94a_x$. Bhagat et al. (2017) provided an analytical solution of the differential equation. Substituting for

ξ/V from equation 5.17 gives

$$\frac{dp}{d\chi} = \frac{a_x^4}{p^3 \sin\chi} - \frac{p}{\tan\chi} \tag{5.20}$$

This can be written in dimensionless form by setting $p^* = p/a_x$

$$\frac{dp^*}{d\chi} = \frac{1}{p^{*3} \sin\chi} - \frac{p^*}{\tan\chi} \tag{5.21}$$

Multiplying each side by p^{*3} and rearranging gives

$$p^{*3}\frac{dp^*}{d\chi} + \frac{p^{*4}}{\tan\chi} = \frac{1}{\sin\chi} \tag{5.22}$$

Writing $z = p^{*4}$ and using an integrating factor of $\sin^4\chi$ with the boundary condition $p^* = 1$ at $\chi = 0$ leads to the solution

$$p^{*4}\sin^4\chi = \frac{4}{3}\cos^3\chi - 4\cos\chi = \frac{8}{3} \tag{5.23}$$

Inspection of equation 5.23 yields the following results: (i) At $\chi = 0$, $p^* = 1$ and in the limit of small χ the RHS $\rightarrow \chi^4$, as required.
(ii) The co-ordinates of the cleaning locus (x, y) relative to the point of impingement are given by $x = p^* \cos\chi$ and $y = p^* \sin\chi$. Equation 5.23 allows y to be calculated directly and x is obtained from $x = y\cot\chi$. It can be shown that as $\chi \rightarrow \pi$, $y \rightarrow \frac{2}{\sqrt[4]{3}} = 1.52$. Figure 5.8 shows the shape of the cleaning front superimposed on the data sets reported by Wilson et al. (2015) as well as their numerical solution, which was obtained using the modified Euler method. The two integrations are almost identical until $\chi \approx 127°$, after which the numerically calculated width started to narrow. The difference in cleared width is small, equation 5.23 giving $w_c = 3.04a_x$ *cf.* $2.94a_x$, i.e. *a* 3.5% difference. Applying this result to the data sets for cleaning Xanthan gum presented by Wilson et al. (2015) yielded a k' value of $0.0018\,\mathrm{m\,s\,kg^{-1}}$ *cf.* their reported value of $0.002\,\mathrm{m\,s\,kg^{-1}}$: both values agreed with the value of k' obtained from static cleaning tests within experimental uncertainty.

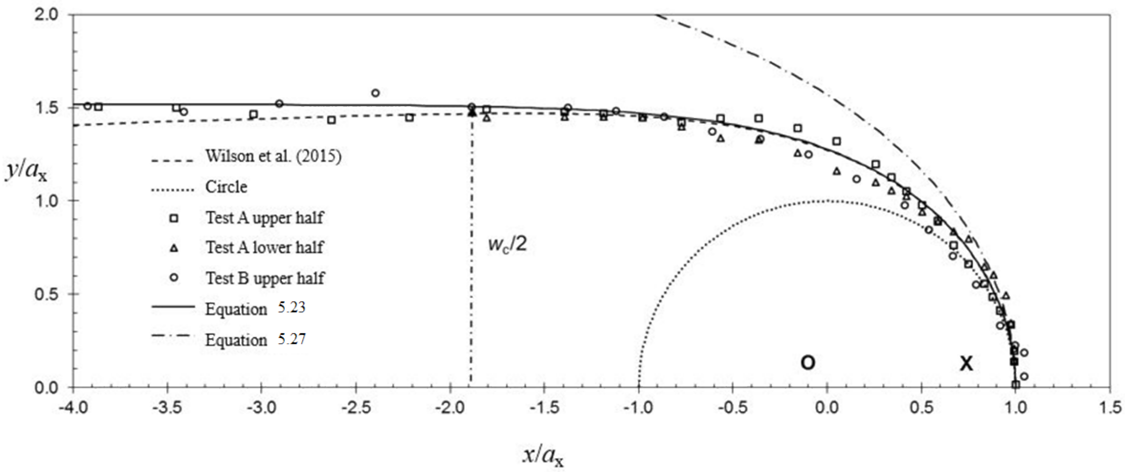

Figure 5.8 Predicted shape of cleaning front obtained by integrating equation 5.22. Locus plotted in Cartesian co-ordinates, relative to the point of impingement O (see figure 5.6). Superimposed on the locus are data sets obtained from interrupted experiments, scaled using equation 5.23 to identify a_x from w_c. Data taken from Wilson et al. (2015): Xanthan gum soil cleaned by water at approximately 20°. Conditions: $\Delta P = 1.5$ bar, $V = 10.5\,\mathrm{mm\,s^{-1}}$, $d_N = 1.69\,\mathrm{mm}$. Flow stopped after (A) 30 cm travel, $m_\circ = 1.16\,\mathrm{mg\,cm^{-2}}$; (B) 10 cm travel, $m_\circ = 1.38\,\mathrm{mg\,cm^{-2}}$. Dotted circle shows locus of a circle of radius a_x. Dashed line – numerical solution of Wilson et al. (2015); solid locus – far field case, equation 5.23; dot-dash locus – near field case, equation 5.27. Note that the axes are normalised: a_x for a far field will be larger than a_x for a near field. Figure reproduced from Bhagat et al. (2017).

Near field case

The near field case, where a is small, also arises when V is large such that that a_x is small. Again, at X, with $a_x \sim r_\circ$, using equation 5.9

$$\frac{da}{dt} = V = \frac{\sigma}{a_x} \tag{5.24}$$

At P equation 5.16 gives

$$\frac{dp}{d\chi} = \frac{\sigma}{V \sin\chi} - \frac{p}{\tan\chi} \tag{5.25}$$

Or in dimensionless terms,

$$\frac{dp*}{d\chi} = \frac{1}{\sin\chi} - \frac{p*}{\tan\chi} \tag{5.26}$$

With $p^* = 1$ at $\chi = 0$. The solution is

$$p^* = \chi \mathrm{cosec}\chi \tag{5.27}$$

and the locus of the cleaning front is given by $(\chi \cot \chi, \chi)$. This is plotted alongside the solution for the far field on figure 5.8. The width of the cleared region increases steadily with distance from X, noticeably more than the far field case, and approaches a limit of $w_c^* = 2\pi$ as $\chi \to \pi$. The difference arises from the slower loss of momentum in the film (from the assumption that $u \approx U_\circ$). At larger distances, e.g. far downstream where $\theta \to \pi$, this assumption will no longer be valid, and numerical methods must be used to include the transition region in the velocity profile. The full model can be obtained following similar procedure as shown above and it is shown in the paper by Bhagat et al. (2017).

5.4 Cleaning by static nozzle, inclined jets

The previous sections describe the evolution of the circular area cleaned by a stationary jet impinging perpendicularly and normal impingement of a moving liquid jet on the soiled surface, where dimension a lies within the RFZ (the models do not apply beyond the hydraulic/film jump). The § 4.2.7 presents the detailed flow field including boundary layer and turbulent film created by obliquely impinging jets. However, the cleaning models presented in this chapter are based on the simplified Wilson et al. and Wang et al. model. Wang et al. (2015) modified the Wilson et al. (2012) model for flow in the thin film to include inclination of the jet relative to the wall, by including the flow distribution presented by Kate et al. (2007). The Wang et al. flow model is combined with the model for peeling to predict cleaning by an inclined jet. In the next section these are extended to describe removal by an inclined moving jet.

Consider a coherent liquid jet of radius r_o and mean velocity U_o impinging on a flat surface at angle ϕ, as shown in figure 5.15. Gravity is not considered so the orientation of the wall is not important. The footprint of the jet is an ellipse, with flow following streamlines moving radially away from the source S which is located a distance $r_o \cot \phi$ upstream of the point of impingement O. The upstream direction is positive in Cartesian co-ordinates.

Consider a streamline inclined at angle θ to the upstream direction. The radial distance from S to the edge of the ellipse (where the mean velocity of the flow is U_o), r_e, is given by equation 4.52 ($r_e = r_o \frac{\sin \phi}{(1+\cos \theta \cos \phi)}$). Beyond r_e, continuity links the local film depth, h, and mean velocity at location r via equation 4.53 ($r\bar{u}h = \frac{1}{2} U_o r_e^2 \sin \phi \qquad \text{for } r > r_e$)

Table 5.1 Experimental setting for cleaning of petroleum jelly by water jet

Set angle of impingement ϕ	Effective angle of impingement	Layer thickness (µm)
45°	43.6°	340 ± 50
90°	88.6°	340 ± 50
110°	108.5°	322 ± 50
135°	133.4°	409 ± 50

The mean velocity in the film at $r > r_e$ is given by

$$\frac{1}{\bar{u}} = \frac{1}{U_\circ} + \frac{10\nu}{3U_\circ^2 r_e^4 \sin\phi^2}\left(r^3 - r_e^3\right) \tag{5.28}$$

The corresponding momentum flow per unit width of cleaning front in the θ direction, M_θ, is given by

$$M_\theta = \frac{3}{5}\rho U_\circ r_e^2 \sin\phi \frac{\bar{u}}{r} \tag{5.29}$$

For the weaker soil case (assuming $U_o \gg \bar{u}; r^3 \gg r_e^3$: equation 5.15), this gives

$$M_\theta = \left[\frac{9}{50}\frac{\rho}{\nu}U_\circ^3 \sin\phi^3\right]\frac{1}{r^4} \tag{5.30}$$

The rate of cleaning along the streamline inclined at θ is then

$$\frac{da}{dt} = \left[\frac{9k'}{50}\frac{\rho}{\nu}U_\circ^3 \sin\phi^3\right]\frac{1}{a^4} = \left[\frac{3\sigma}{10\nu}\frac{r_e^6}{r_\circ^2}U_\circ \sin\phi^3\right]\frac{1}{a^4} \tag{5.31}$$

and the corresponding result for the near field case is

$$\frac{da}{dt} = \left[\frac{9k'}{50}\rho r_e^2 U_\circ^2 \sin\phi\right]\frac{1}{a} = \left[\sigma\frac{r_e^2}{r_\circ^2}\sin\phi\right]\frac{1}{a} \tag{5.32}$$

In each case σ is calculated using the mass flow rate in the jet.

New experimental data obtained for inclined and perpendicular jets impinging on petroleum jelly and PVA layers are compared with the near field result, equation 5.32, which suggests that plots of a^2 vs. t should be linear, with a gradient that is determined by ϕ and θ:

$$\Delta a^2 = 2\left[\sigma\frac{r_e^2}{r_\circ^2}\sin\phi\right]\Delta t = 2\sigma_{\theta\phi}\Delta t \tag{5.33}$$

There was some variation in petroleum layer thickness, from 320 −400µm (Table 5.1). The Table also includes the true angle of impingement, calculated from the effect of gravity on the jet trajectory. There is a systematic shift of 1.5° arising from the apparatus. The effective angle of impingement was used in the calculations.

Figure 5.9 shows the results for different combinations of ϕ and θ obtained with petroleum jelly layers on glass plotted in the form $(\Delta a^2)^{1/2}$ vs $(\Delta t)^{1/2}$. All the plots show the linear trend predicted by equation 5.33 and the gradient gives an estimate of $2\sigma_{\theta\phi}$. The gradients are plotted against $(r_e/r_\circ)(Q/r_\circ)\sqrt{\sin\phi}$ in figure 5.10 to isolate the contributions from ϕ, θ and flow rate. The data lie on a straight line passing through the origin, confirming that the model can account for the variation in azimuthal flow rate resulting from non-perpendicular impingement. The gradient of the line of best fit in figure 5.10 gives an estimate of k' of $0.027\,\mathrm{m\,s\,kg^{-1}}$. Wilson et al. (2014) reported a value of $k' = 0.001\,\mathrm{m\,s\,kg^{-1}}$ for a noticeably stiffer petroleum jelly.

Further validation of the model is provided by studies on PVA layers employing water jets impinging at 45° conducted by Wang (2014). The data from the initial phase of cleaning for different values of θ are plotted in figure 5.11 and show good agreement with the near field result. The values of $2\sigma_{\theta\phi}$ extracted from these plots as well as those collected for two other flow rates are plotted against $(r_e/r_\circ)(Q/r_\circ)\sin^{1/2}\phi$ in figure 5.12. The data again lie on a straight line, confirming that the model accounts for the effect of flow rate, for a different soiling material. The cleaning rate constant estimated in this case was $0.000\,13\,\mathrm{m\,s\,kg^{-1}}$, making this PVA soil the hardest to clean of those considered here.

5.5 Cleaning by moving nozzles, inclined jets, moving up or down

Figure 5.13 shows a flow scenario created by a liquid jet moving in a vertical plane inside a cylindrical tank. In this scheme, the nozzle rotates in a vertical plane which enables the liquid jet to create a vertical strip of cleaned region, The impingement point O moves across the surface from the bottom to the top of the tank. At any given point, the angle of impingement changes continuously. To model cleaning by moving liquid jets, a number of assumptions are outlined in § 5.1.3. Apart from those, the curvature of the tank wall is not considered as the liquid film is thin and the typical curvature of the industrial tanks are small (The curvature of the tank is defined as 1/radius of the tank and typical radius are $\mathcal{O}(\mathrm{m})$). Breakup of the jet

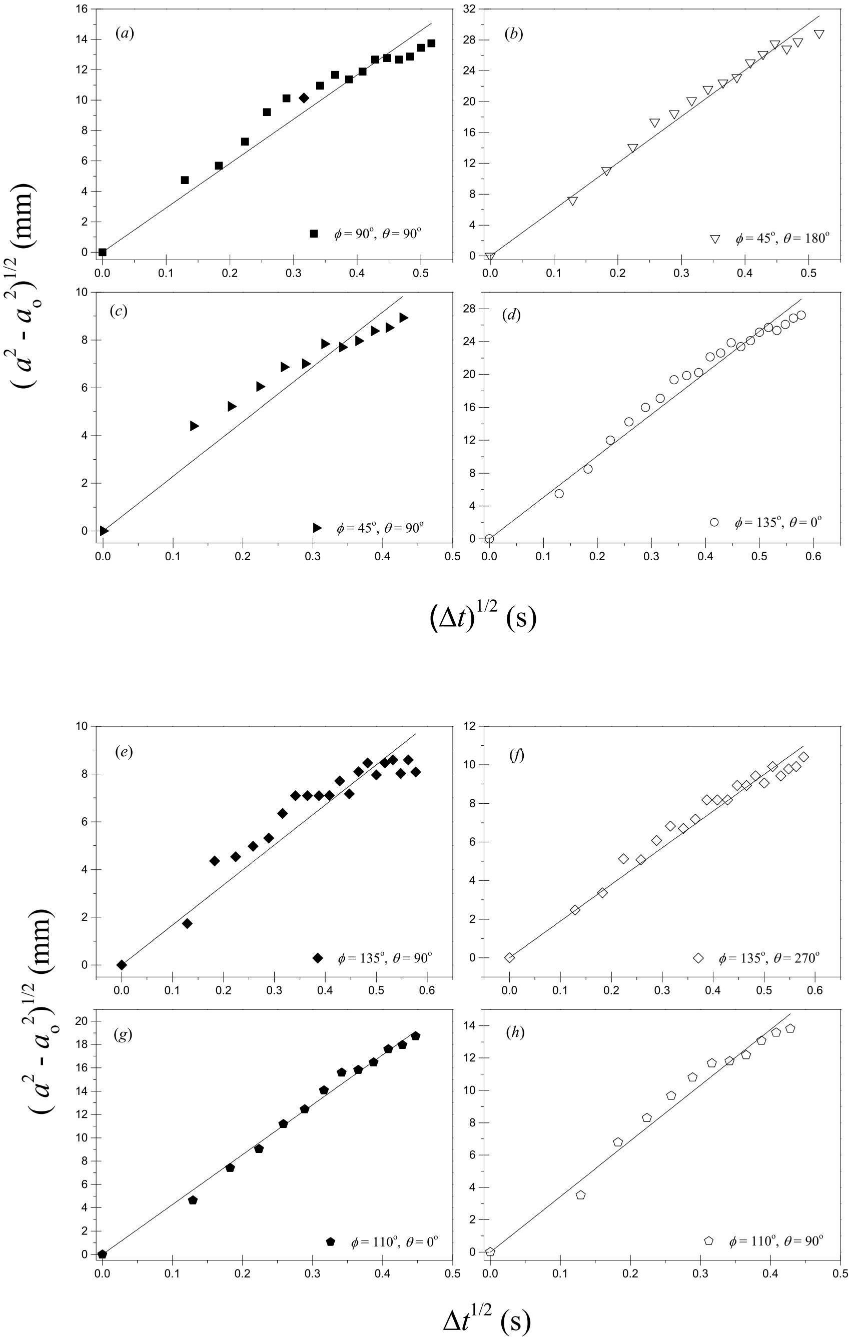

Figure 5.9 Evolution of size of cleared region in petroleum jelly layers (see Table 5.1) generated by a water jet ($r_o = 1\,\text{mm}, Q = 2\,\text{L}\,\text{min}^{-1}, Re = 21,800$) impinging at angles indicated, plotted in the form suggested by equation 5.33.

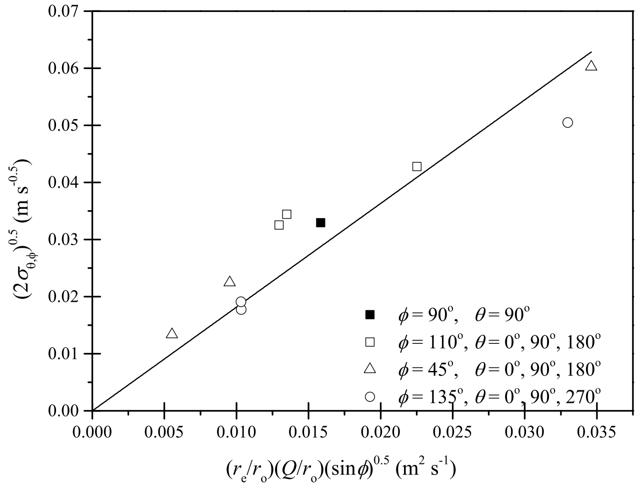

Figure 5.10 Effect of angle of impingement on cleaning rate constant 2σ for petroleum jelly on glass, including the values extracted from the plots in figure 5.9.

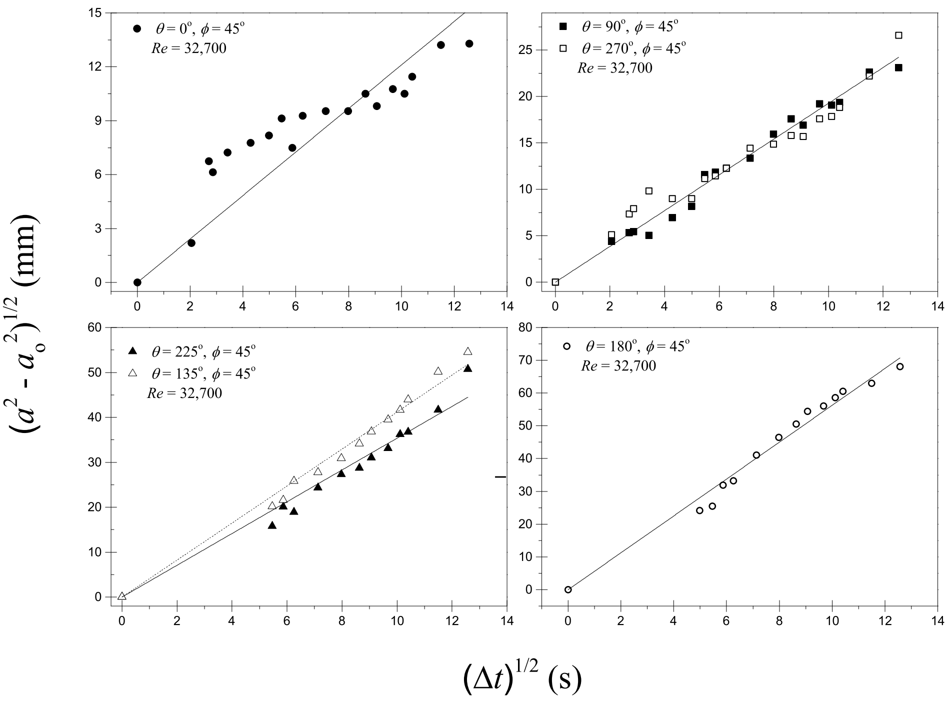

Figure 5.11 Cleaning of PVA layers on glass by water jet impinging at 45°; value of θ given on plots. Data plotted in the form of the near field result, equation 5.33. Layer thickness 33 µm, $Q = 3\,\mathrm{L\,min^{-1}}$, $Re = 32,700$ and $r_\circ = 1\,\mathrm{mm}$.

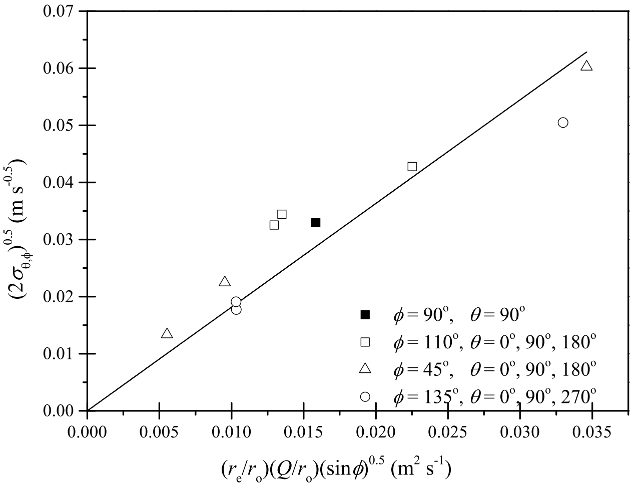

Figure 5.12 Effect of flow rate on cleaning rate constant for water jet impinging on PVA layers at an angle of 45°. The data include the values extracted from the plots in figure 5.11. Solid line shows line of best fit to equation 5.33 used to estimate k'.

as it travels to the wall and gravity effects are not considered. However, in real life applications it will have an effect (see Damkjær et al. (2017)). Ignoring gravity and the effect of the rotation of nozzle gives rise to two basic flow configurations. On oblique impingement of a liquid jet, the liquid flows dominantly in one direction and in combination with the transverse nozzle velocity V the following two flow scenarios are; (1) the transverse nozzle velocity V and dominant flow direction are the same, or the transverse nozzle velocity vector V and a vector along the liquid jet's axis forms an acute angle (U^+/D^-) and, (2) they are in the opposite direction or form a obtuse angle (U^-/D^+). The flow scenarios are shown schematically in figure 5.14.

As the nozzle moves up or down along the wall, the angle of inclination, Φ, changes. In § 5.1.3 it is shown that for weaker food soils, the far field approximation provides a reasonable estimate of the final cleaned width (see figure 5.8). For rest of the analysis, the hydrodynamics are described by the far field approximation. The result for a near field and the intermediate case can be obtained following the same approach, noting that the latter requires cumbersome algebra which may be better suited to numerical methods. Three scenarios are considered:

(i) Constant speed: the point of impingement moves up or down the wall at V or $-V$. As drawn on figure 5.13, $V = -\frac{dL}{dt}$.

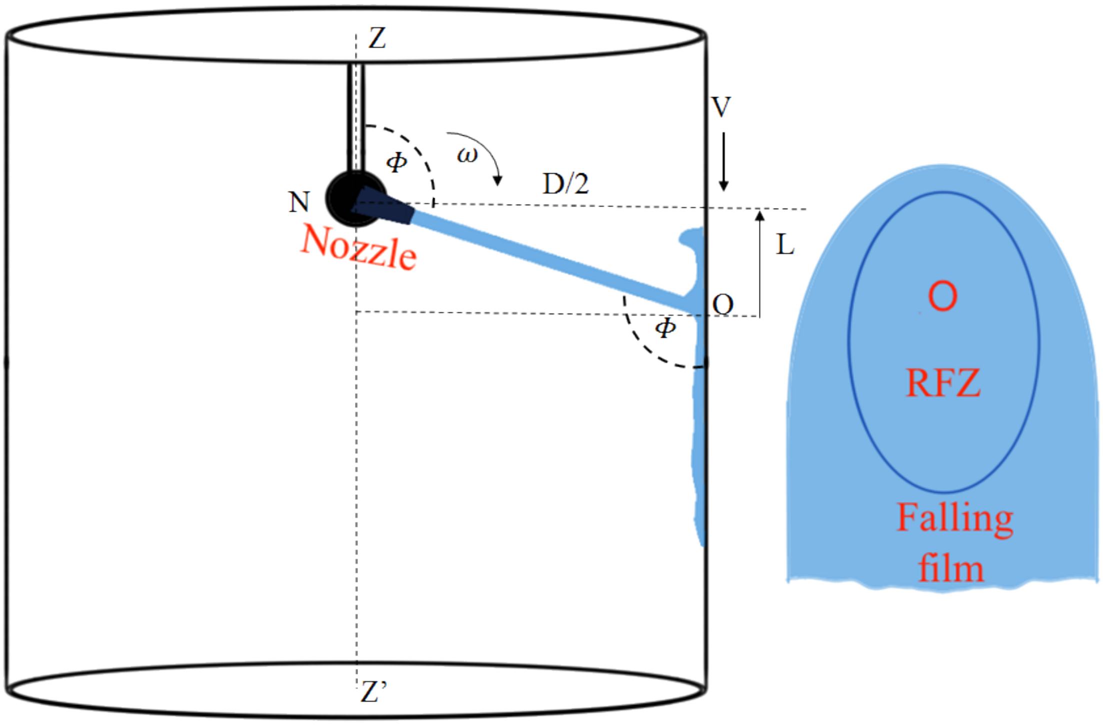

Figure 5.13 Schematic of a flow scenario created by a moving water jet inside a tank. The nozzle N rotating in a vertical plane and the point of impingement moving vertically down the wall of a cylindrical vessel of diameter D. ZZ' is the cylindrical axis of symmetry.

(ii) The nozzle rotates at constant angular velocity $\omega = d\Phi/dt$, where Φ is the angle from the vertical defined in figure 5.13. We assume there is no azimuthal rotation, so O moves down one wall and up the opposite wall (one might think of the cutting pattern followed by lawnmowers or combine harvesters).

$$V = -\frac{dL}{dt} = -\frac{d}{dt}(\frac{1}{2}D\cot\Phi) = -\frac{D\omega}{2}\mathrm{cosec}^2\Phi = -V_N\mathrm{cosec}^2\Phi \qquad (5.34)$$

where V_N is the traverse speed at the nozzle plane. Computer controlled nozzles may proceed around one or more axes at varying rates, and the analysis presented here can be extended to such motions.

(iii) The nozzle velocity varies with Φ in order to give a cleared region of constant width. The conditions require to achieve this are considered later (equation 5.45).

Figure 5.14 shows the four scenarios that can arise. Labels D and U refer to the direction of the jet on the wall (down and up, respectively), while $+$ and $-$ refer to the location of the point of impingement relative to the nozzle plane. These are paired: in D^+ and U^- the point corresponding to X is located upstream of

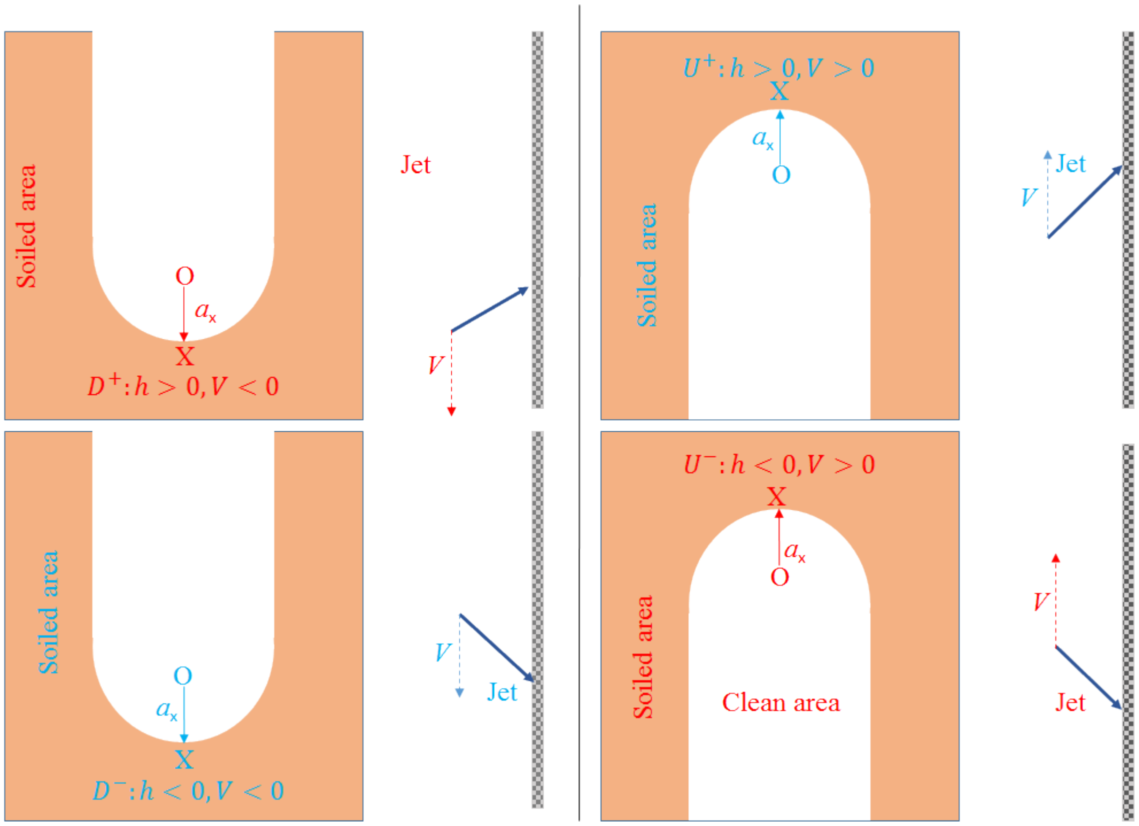

Figure 5.14 Schematics of cleaning by liquid jets impinging moving up or down a wall, above and below the nozzle plane (NH on figure 5.13). D and U refer to the direction of travel of the impingement point O. $V > 0$ or when the jet moves upwards is indicated by U and $V < 0$ is indicated by D. Similarly + and − indicates whether jet is impinging in upward or downward direction or $h > 0$ is referred by + and vice-verse. The two basic flow scenarios arising are when transverse nozzle velocity vector V and a vector along the direction of the jet forms an acute angle D^-/U^+ or obtuse angle D^+/U^-

the impingement point, at $\theta = 0°$ in figure 5.15, while in D^- and U^+ it is located downstream, at $\theta = 180°$ in figure 5.15.

5.5.1 Case A: D^+/U^-

The source S is located a distance $r_o \cot\phi$ behind the point of impingement, so any plots of the shape of the cleaning front should be corrected for this contribution. It is ignored in the idealised cases presented here as r_o is expected to be small and the factor does not contribute significantly to the calculation for the cleared width.

Consider U^-, as the geometry is that in figure 5.15. The angle of inclination, ϕ, is acute: $0 < \phi < 90°$. Most of the liquid is flowing in the opposite direction to the

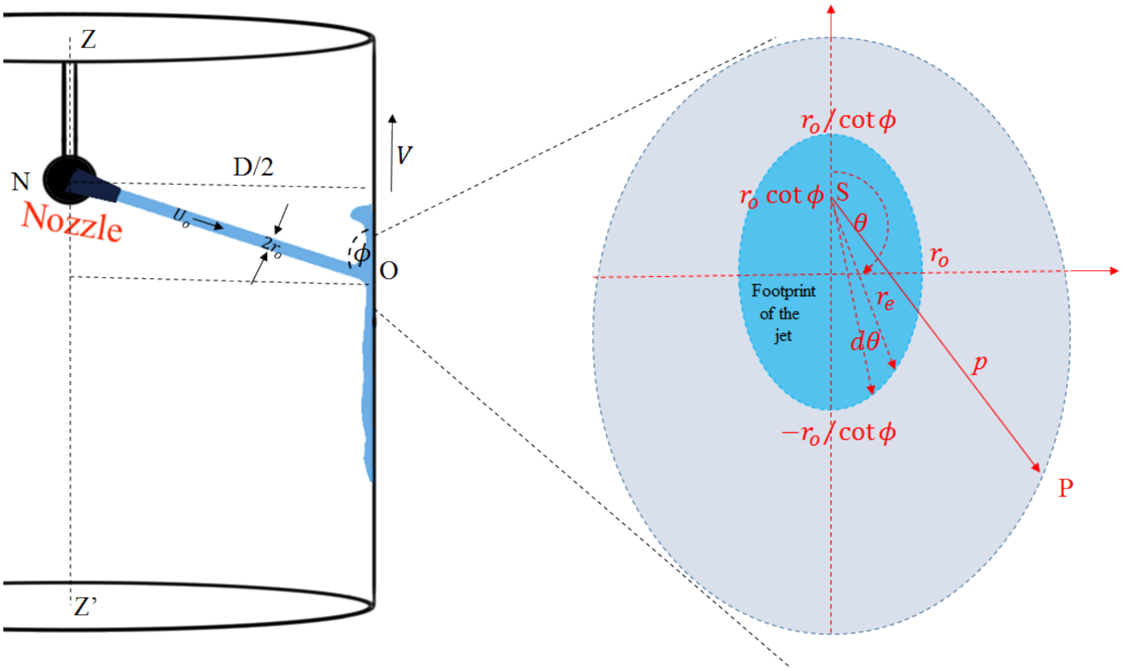

Figure 5.15 Schematics of the magnified footprint of an obliquely impinging jet. In relation to relative motion of the nozzle and jet axis, this flow configuration correspond to D^+/U^-

path of the jet so the distance OX will be short. Angles χ and θ are coincident in this case and the expressions that follow are written in terms of θ as this emphasises the effect of flow pattern. For D^+ the sense is reversed and the same construction applies, but with ϕ defined with respect to the downward direction. At the stagnation point $\theta = 0°$ and X lies on the same side of O as the source S. At X, $|V| = \frac{da}{dt}$ and equation 4.52 gives (noting that $\cot\phi$ is positive)

$$r_e = r_o \frac{\sin\phi}{(1+\cos\phi)} \tag{5.35}$$

The cleaning rate for the far field case is then calculated using equation 5.15. Discarding the magnitude brackets on V, the following result for $a_{x,\phi}$, the distance between S and X for angle of inclination ϕ, is obtained:

$$a_{x,\phi} = \left(\frac{9k'}{50}\right)\left(\frac{\rho}{\nu} r_\circ^6 U_\circ^3\right)\left[\frac{\sin^9\phi}{(1+\cos\phi)^6}\right] V^{-1/4} \tag{5.36}$$

The parameters have been grouped into terms related to the soil, the jet, the angle of inclination and nozzle, respectively. The term in square brackets decreases strongly as ϕ decreases (the jet impinges more obliquely) as more of the jet flow is then directed towards the $\theta = 180°$ streamline, and $a_{x,\phi}$ is consequently smaller.

Comparing the cleaning rate at angle θ to that at $\theta = 0°$, and noting that $\frac{da}{dt} = \frac{\xi}{p^4}$ (Equation 5.31), yields

$$\frac{\left(\frac{da}{dt}\right)_\theta}{V} = \frac{\xi(\theta)/p^4}{\xi(0)/a_{x,\phi}^4} = \frac{r_e^6(\theta)}{r_e^6(0)}\frac{a_{x_\phi}^4}{p^4} \tag{5.37}$$

$$\implies \frac{\xi(\theta)}{\xi(0)} = \frac{r_e^6(\theta)}{r_e^6(0)} = \left(\frac{1+\cos\phi}{1+\cos\phi\cos\theta}\right)^6 \tag{5.38}$$

ξ therefore increases with θ, as more flow is directed outwards from the source as the point on the cleaning front moves round from X. After scaling, the equivalent expression to equation 5.22 is obtained

$$p^{*3}\frac{dp^*}{d\theta} + \frac{p^{*4}}{\tan\theta} = \left[\frac{1+\cos\phi}{1+\cos\phi\cos\theta}\right]^6 \frac{1}{\sin\theta} \tag{5.39}$$

An analytical solution can again be obtained using an integrating factor of $\sin^4\theta$, *viz.*

$$p^*\sin\theta = \sqrt{2}\left\{(1+\cos\phi)^6\int_0^\theta \frac{\sin^3\theta'}{(1+\cos\phi\cos\theta')^6}d\theta'\right\}^{1/4} \tag{5.40}$$

The integral can be evaluated using a dummy variable $j = \sec\phi + \cos\phi$ and yields

$$\begin{aligned} p^* &= \sqrt{2}\frac{(1+\sec\phi)^{3/2}}{\sin\theta}\left\{\left[\frac{-1}{3(\sec\phi+\cos\theta')^3} + \frac{\sec\phi}{2(\sec\phi+\cos\theta')^4} + \frac{1-\sec^2\phi}{5(\sec\phi+\cos\theta')^5}\right]_0^\theta\right\}^{1/4} \\ &= \left(\frac{2}{15}\right)^{1/4}\frac{(1+\sec\phi)^{3/2}}{\sin\theta}\left\{\left[\frac{-\sec^2\phi - 5\sec\phi\cos\theta' - 10\cos^2\theta' + 6}{(\sec\phi+\cos\theta')^5}\right]_0^\theta\right\}^{1/4} \end{aligned} \tag{5.41}$$

Figure 5.16 shows the cleaning front shape predicted for various values of ϕ, within the likely working range, taken to be $10° < \phi < 90°$. The origin $(0, 0)$ is the source S. Near X the shape is again curved and the width of the cleared region increases with θ, approaching a limiting width as $\theta \to \pi$. The distance taken to reach the limit depends on ϕ, as shown by the inset on the figure. With small ϕ, i.e. very oblique jets, the model predicts that the cleared region grows outwards for a considerable distance downstream. The flow distribution model is unlikely to be valid in this range, however, as a non-elliptical flow pattern may be formed (see Kate et al. (2007))

and the jet may bounce off the surface if the surface material is hydrophobic (Kibar et al. (2010)).

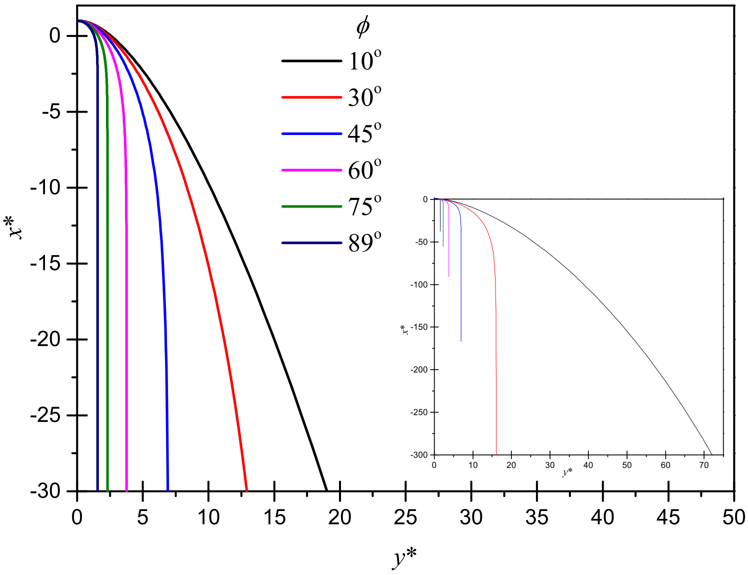

Figure 5.16 Predicted shapes of cleaning fronts for different angles of impingement, ϕ, for Case A, D^+, U^-(see figure 5.14). Inset shows trend at large $x*$. Dimensionless Cartesian coordinates, $x* = x/a_{x,\phi}$; $y* = y/a_{x,\phi}$.

The dimensionless width of the cleaned region is obtained by setting $\theta = \pi$ in equation 5.41 and finding $p^* \sin\theta$, giving

$$\begin{aligned} w_c^* = \frac{w_c}{a_{x,\phi}} &= 2\sqrt{2}(1+\sec\phi)^{3/2}\left\{\frac{1}{30}\left(\frac{4-\sec\phi}{(\sec\phi-1)^4}+\frac{4+\sec\phi}{(\sec\phi+1)^4}\right)\right\} \\ &= \left(\frac{32}{15}\right)^{1/4}(1+\sec\phi)^{3/2}\left\{\left(\frac{4-\sec\phi}{(\sec\phi-1)^4}+\frac{4+\sec\phi}{(\sec\phi+1)^4}\right)\right\}^{1/4} \end{aligned} \tag{5.42}$$

where $a_{x,\phi}$ depends on the mode of operation, *i.e.* whether V is constant or varies with ϕ. Figure 5.17 shows that w_c^* decreases as ϕ becomes more oblique, in contrast to the effect of ϕ on $a_{x,\phi}$. Combining equations 5.36 and 5.42 gives

$$\begin{aligned} w_{c,\phi} &= \left(\frac{48}{125}\frac{k'\rho^2Q^3}{\pi^3\mu}\right)\left(\frac{1}{V}\right)^{1/4}\left\{\left(\sin^3\phi\tan^6\phi\right)\left(\frac{4-\sec\phi}{(\sec\phi-1)^4}+\frac{4+\sec\phi}{(\sec\phi+1)^4}\right)\right\}^{1/4} \\ &= \left(\frac{48}{125}\frac{k'\rho^2Q^3}{\pi^3\mu}\right)\left(\frac{1}{V}\right)^{1/4}F_V(\phi) \end{aligned} \tag{5.43}$$

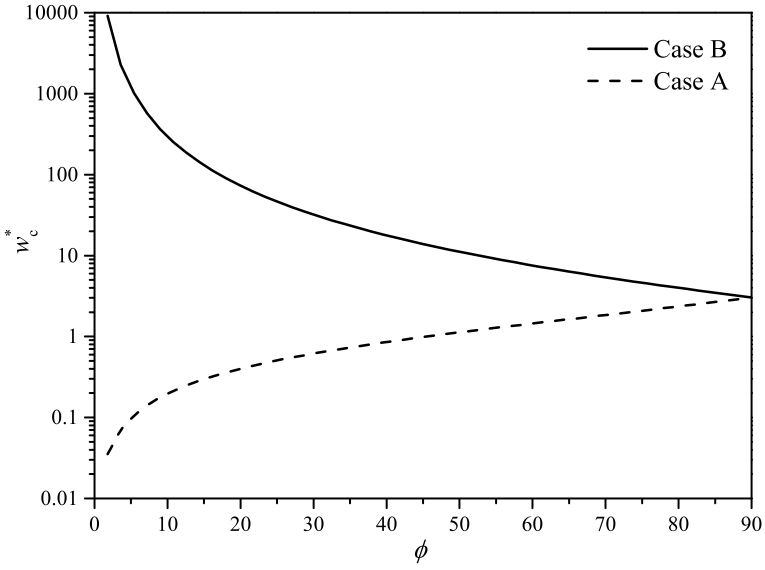

Figure 5.17 Effect of angle of jet impingement on dimensionless width of strip cleared by a moving nozzle.

for the case where V is constant, and

$$\begin{aligned} w_{c,\phi} &= \left(\frac{48}{125}\frac{k'\rho^2Q^3}{\pi^3\mu}\right)^{1/4}\left(\frac{\sin^2\phi}{V_N}\right)^{1/4}\left\{\left(\sin^3\phi\tan^6\phi\right)\left(\frac{4-\sec\phi}{(\sec\phi-1)^4}+\frac{4+\sec\phi}{(\sec\phi+1)^4}\right)\right\}^{1/4} \\ &= \left(\frac{48}{125}\frac{k'\rho^2Q^3}{\pi^3\mu}\right)^{1/4}\left(\frac{1}{V_N}\right)^{1/4}F_\omega(\phi) \end{aligned} \tag{5.44}$$

for the case where the nozzle rotates at constant angular velocity, with V_N the traverse speed at the nozzle plane (NH in figure 5.13; $|V_N| = D\omega/2$). The plots of F_V and F_ω in figure 5.18 show that a constant traverse speed gives a more uniform cleared width, decreasing by about 30% as the angle of impingement reaches 10°, whereas the constant rotational speed results in a 70% reduction over this range.

Equation 5.43 suggests that a uniform cleared width could be obtained by using a traverse speed of the form

$$\begin{aligned} V &\propto \left(\sin^3\phi\tan^6\phi\right)\left(\frac{4-\sec\phi}{(\sec\phi-1)^4}+\frac{4+\sec\phi}{(\sec\phi+1)^4}\right) \\ &\propto \sin\phi\left(1+\frac{\cos^2\phi}{5}\right) \end{aligned} \tag{5.45}$$

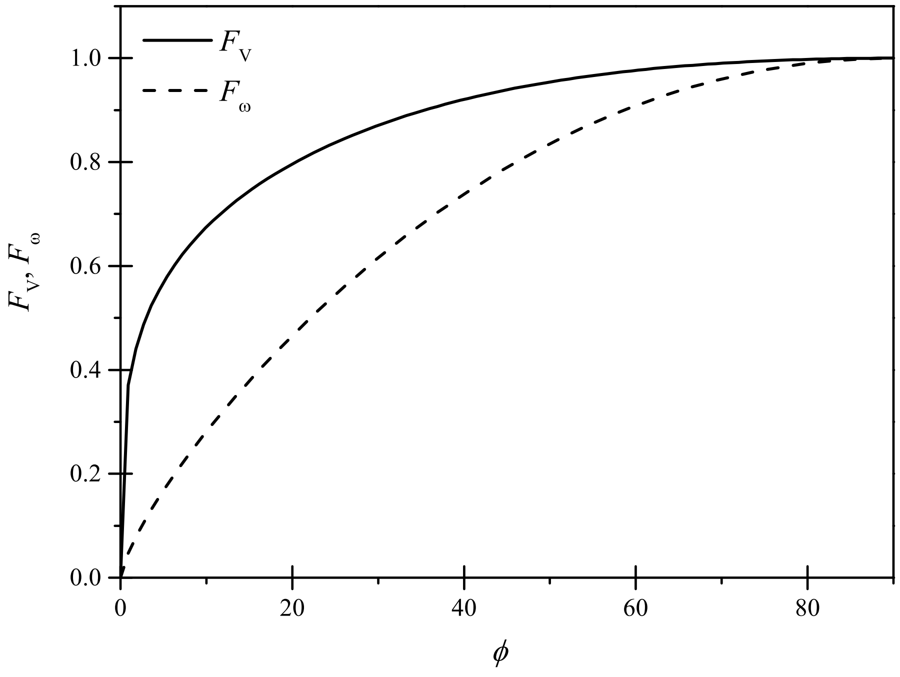

Figure 5.18 Effect of jet impingement angle on width functions F_V (equation 5.43) and F_ω (equation 5.44)

The variation is approximately sinusoidal as $V \propto \sin\phi\left(1+\frac{\cos^2\phi}{5}\right) \approx \sin\phi$. There would be a lower limit to the velocity used in practice as low values of ϕ are likely to correspond to the jet crossing the base or top of the vessel rather that a vertical wall, and the cleared areas will overlap more extensively. This aspect is covered in the Simulation section.

5.5.2 Case B: D^-/U^+

Consider D^- as this allows ready comparison with figure 5.15. The angle of impingement, ϕ, is again $0 < \phi \leq 90°$. At the stagnation point, $\theta = 180°$, $|V| = \frac{da}{dt}$ and equation 4.52 gives (noting that $\cos\phi$ is again positive)

$$r_e = r_o \frac{\sin\phi}{(1-\cos\phi)} \tag{5.46}$$

The corresponding result for $a_{x,\phi}$ is

$$a_{x,\phi} = \left(\frac{9k'}{50}\right)\left(\frac{\rho}{\nu} r_\circ^6 U_\circ^3\right)\left[\frac{\sin^9\phi}{(1-\cos\phi)^6}\right] V^{-1/4} \tag{5.47}$$

In contrast to Case A, equation 5.36, the term in square brackets increases strongly as ϕ decreases (the jet impinges more obliquely) as more of the jet flow is directed along the $\theta = 180°$ streamline towards the stagnation point.

The shape of the cleaning front is calculated in a similar fashion to Case A but it is convenient to write equation 5.23 with the angle of inclination of the streamline to the downstream direction, χ, now equal to $\pi - \theta$, such that X is located at $\chi = 0$: Comparing the cleaning rate at angle θ to that at $\theta = 0$, and noting that $\frac{da}{dt} = \frac{\xi}{p^4}$ (equation 5.31), yields

$$\frac{dp}{d\chi} = \left(\frac{da}{dt}\right)_P \frac{p}{V \sin\chi} - \frac{p}{\tan\chi} \tag{5.48}$$

The ξ term again depends on χ, with

$$\frac{\left(\frac{da}{dt}\right)_\chi}{V} = \frac{\xi(\chi)/p^4}{\xi(0)/a^4_{x,\phi}} = \frac{r_e^6(\chi)}{r_e^6(0)} \frac{a^4_{x_\phi}}{p^4} \tag{5.49}$$

$$\implies \frac{\xi(\chi)}{\xi(0)} = \frac{r_e^6(\theta - \pi - \chi)}{r_e^6(\theta - \pi)} = \left(\frac{1 - \cos\phi}{1 - \cos\phi\cos\chi}\right)^6 \tag{5.50}$$

yielding *cf*. equation 5.41)

$$p^* = \left(\frac{2}{15}\right)^{1/4} \frac{(\sec\phi - 1)^{3/2}}{\sin\theta} \left\{ \left[\frac{\sec^2\phi - 5\sec\phi\cos\chi' + 10\cos^2\chi' - 6}{(\sec\phi - \cos\chi')^5} \right]_0^\chi \right\}^{1/4} \tag{5.51}$$

Figure 5.19 shows the cleaning front shape predicted for the range $10° \leq \phi < 90°$.

The cleaned region reaches its asymptotic width close to the source, in contrast to Case A. As the jet impinges more obliquely, the asymptotic width is reached ahead of the point of impingement.

The width of the cleaning front narrows noticeably with increasing ϕ, again differing from Case A, with w_c^* given by

$$w_c^* = \left(\frac{32}{15}\right)^{1/4} (\sec\phi - 1)^{3/2} \left\{ \left(\frac{4 - \sec\phi}{(\sec\phi - 1)^4} + \frac{4 + \sec\phi}{(\sec\phi + 1)^4} \right) \right\}^{1/4} \tag{5.52}$$

Figure 5.19 shows that w_c* decreases strongly with increasing ϕ. The product $w_c^* \times a_{x,\phi}, \phi$, however, is identical to that for Case A (Equations 5.43 and 5.44), so that the ultimate width of the cleaned strip is independent of the direction of nozzle motion and is determined by the angle of impingement and the traverse speed. It is acknowledged that this finding is unlikely to apply for Case A when ϕ is small, where the distance to reach the asymptotic width, downstream of the point of impingement, may be large and detailed geometrical computation must be performed.

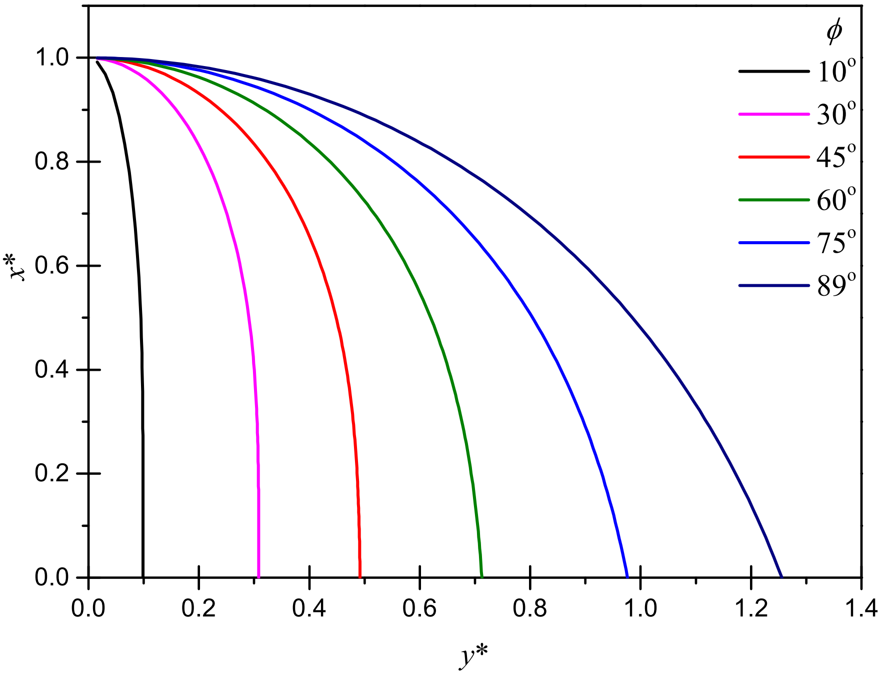

Figure 5.19 Predicted shapes of cleaning fronts for different angles of impingement, ϕ, for Case B, D^-, U^+ (see figure 5.14). Dimensionless Cartesian coordinates, $x* = x/a_{x,\phi}$; $y* = y/a_{x,\phi}$.

5.5.3 Cleaning by moving nozzles, inclined jets, moving sideways

This combination arises when a jet moves in a spiral pattern within a vessel, moving slowly upwards or downwards while the nozzle rotates in the azimuthal plane. The motion of the nozzle in the azimuthal direction and along the vertical axis is perpendicular to the radially ejecting liquid jet. The model for the moving jet, equation 5.16, is combined with that for an inclined jet (figure 5.15) for the far field case. The geometry is summarised in figure 5.20. Angle χ is again relative to the direction of motion of the nozzle, OX: angle θ is zero in the upstream direction of the flow, and $\chi = \theta + \pi/2$

At X, $\chi = 0$ and $\theta = \pi/2$: equation 4.52 gives $r_e = r_\circ \sin\phi$, so equation 4.52 gives

$$\frac{da}{dt} = V = \left[\frac{3\sigma}{10\nu} r_\circ^4 U_\circ \sin^9\phi\right] \frac{1}{a_{x,\phi}^4} \tag{5.53}$$

The subscript ϕ on $a_{x,\phi}$ is used to flag that this dimension depends on the angle of inclination. At P, noting that $\cos\theta = \sin\chi$ when calculating r_e from equation 4.52, equation 5.31 becomes

$$\left(\frac{da}{dt}\right)_P = V \frac{a_{x,\phi}^4 \sin^3\phi}{p^4} \left(\frac{\sin\phi}{1 + \cos\phi\sin\chi}\right)^6 \tag{5.54}$$

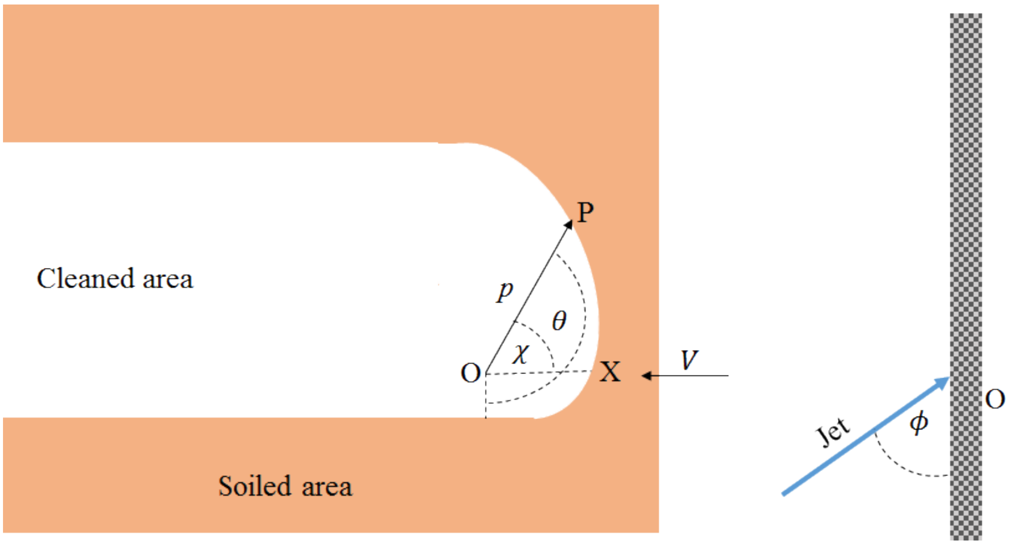

Figure 5.20 Model geometry for liquid jet impinging obliquely while nozzle moves normal to the direction of the flow of the liquid jet.

Substituting this result into equation 5.16 and using dimensionless variables as before gives

$$p^{*3}\frac{dp^*}{d\chi} + \frac{p^{*4}}{\tan\chi} = \mathrm{cosec}\chi \left[\frac{\sin\phi}{1 + \cos\phi\sin\chi}\right]^6 \tag{5.55}$$

Using the integrating factor of $\sin^4\chi$ gives

$$\frac{1}{4}\frac{d(p^{*4}\sin^4\chi)}{d\chi} = \sin^3\chi \left(\frac{\sin\phi}{1 + \cos\phi\sin\chi}\right)^6 \tag{5.56}$$

with boundary condition $p^* = 1$ at $\chi = 0$. The shape of the cleared region becomes asymmetric as the angle of inclination differs from perpendicular. Equation 5.55 was integrated in Matlab from $\chi = 0$ to π, and from $\chi = 0$ to $-\pi$, to obtain the

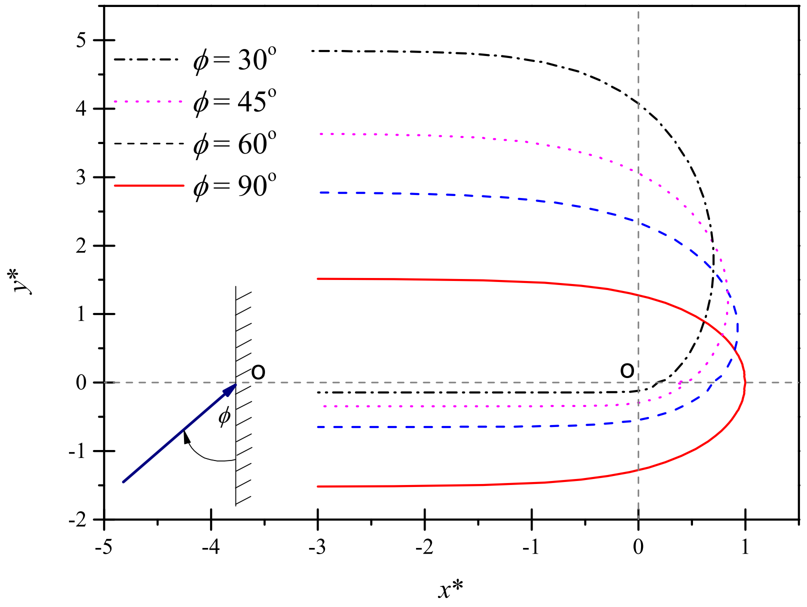

(a) **Upward directing jet:** $\phi \leq 90°$

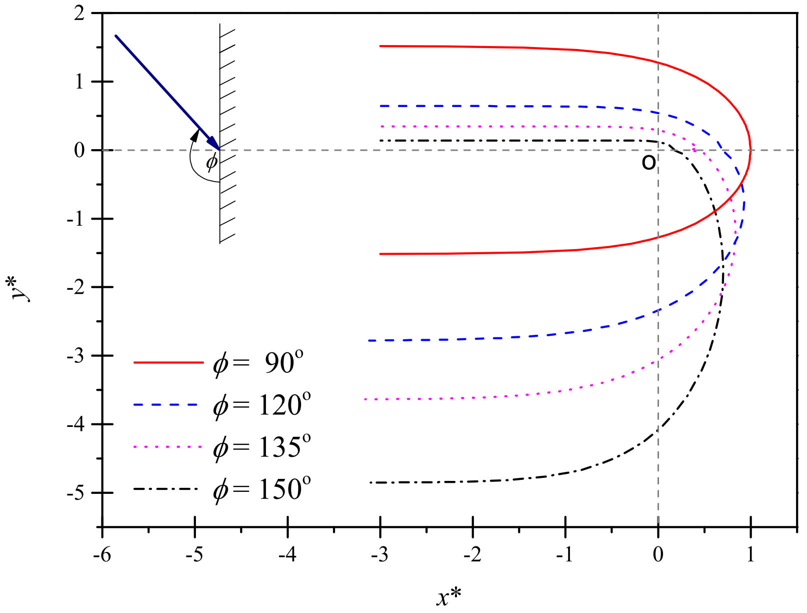

(b) **Downward directing jet:** $\phi \geq 90°$

Figure 5.21 Effect of angle of inclination on the shape of region cleared by nozzle moving normal to liquid jet direction for (a) $\phi \leq 90°$ (b)$\phi \geq 90°$. O is the point of impingement.

components of the cleared width above and below the impingement plane, $w_{c,\phi}^{+*}$ and $w_{c,\phi}^{-*}$, respectively. Figure 5.21 shows the effect of ϕ on the shape and width of the cleared zone, where the dimensions have been normalised with respect to $a_{x,90}$ (i.e. perpendicular impingement) for ease of comparison.

The width of the cleared zone increases as the angle becomes more oblique. The combined width, $w_{c,\phi}^{+*}$ and $w_{c,\phi}^{-*}$, was calculated for the range of values of ϕ of interest ($30° < \phi < 150°$) and the results are presented in the form of the parameter $W^* = (w_{c,\phi}^{+*} + w_{c,\phi}^{-*})/3.04a_{x,90°}$ in figure 5.22. The plot shows that w^* could be fitted to a 6^{th} order polynomial in ϕ (with $R^2 = 1$), or to an acceptable degree of accuracy by the expression

$$W^* = \frac{w_{c,\phi}}{w_{c,90°}} = \text{cosec}^{3/4}\phi \tag{5.57}$$

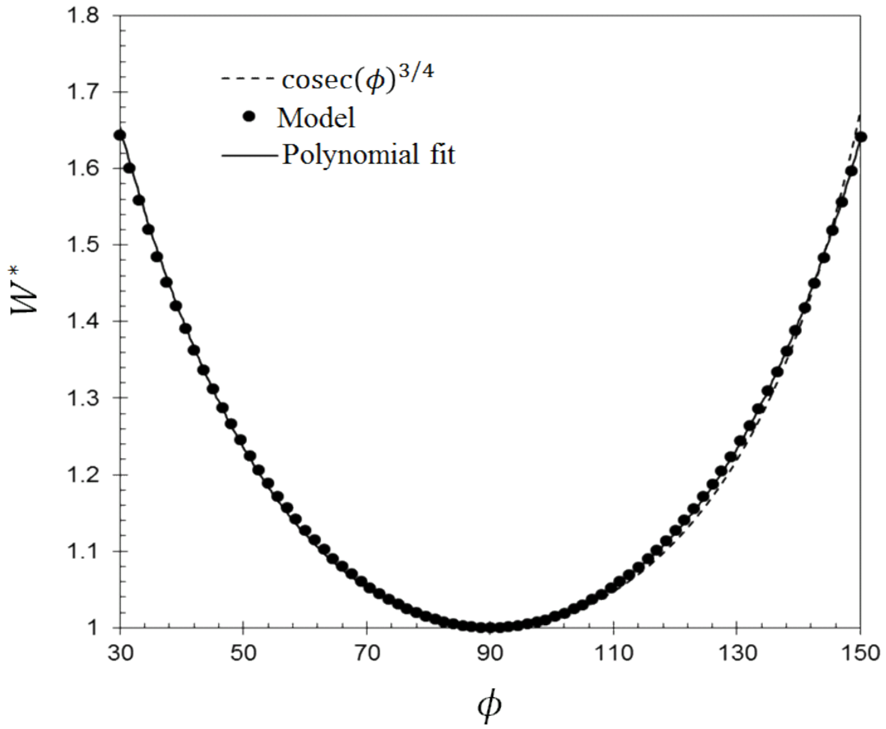

Figure 5.22 Ratio of the width of the cleared region for an inclined jet to that of a perpendicular jet ($\phi = 90°$), for a nozzle moving sideways. Solid line ˘ polynomial fit,$W^* = 0.0712\phi^6 - 0.6715\Phi^5 + 2.6855\phi^4 - 5.8263\phi^3 + 7.6681\phi^2 - 6.242\phi + 3.4682$, where ϕ is in radians; dashed line, $W^* = \text{cosec}^(3/4)\phi$. Figure reproduced from Bhagat et al. (2017)

5.6 Simple simulations of vessel cleaning

§ 5.6 is reproduced from Bhagat et al. (2017) and I would like to acknowledge that this is mainly based on my coauthor's ideas. I had participated in the discussions and had made some corrections. I calculated the results for this section.

The results predicting the width of the region cleared by the jet can be used to estimate the length of time and other resources required to remove the soil from the wall of a vessel. This section present some simple models for calculating a set of performance indicators similar to those proposed by Köhler et al. (2015) for the case of a vertical cylindrical vessel with hemispherical ends. There are a number of simplifying assumptions made in the analysis, which could be revised in a detailed numerical model.

Two types of trajectory are considered, shown schematically in figure 5.23. The nozzle is located on the axis of a vertical cylinder of diameter D. It is assumed that the curvature of the wall has no effect on the cleaning behaviour. The diameter of the hemispherical ends is also D and the height of the wall is Σ. For the purpose of comparing cycle times Ξ is introduced as the ratio of the height to diameter. The nozzle is located at distance qD from the top of the wall. The jet is assumed to travel as a ray, i.e. it remains coherent (no breakup, constant velocity), does not bend or droop. Since the nozzle is located on the axis, the angle of impingement of the jet is ϕ in the plane of the jet motion and normal to the wall in the transverse direction. It is acknowledged that these assumptions are unlikely to hold in practice (see Damkjær et al. (2017)) but the knowledge of jet breakup and its impact on cleaning rate in these situations is not sufficiently advanced for more accurate predictions to be made at the current time. The aim of these calculations is to establish a framework for comparing different designs and operating protocols.

Furthermore, cleaning is assumed to occur by adhesive breakdown, *i.e.* peeling, alone: there is no change in k' with time or wetting history. For many soils of practical interest, the ease with which the material can be removed from the wall is related to the time for which the soil has been in contact with the cleaning solution. In such cases, the flow path of the liquid down and along the wall would need to be modelled in parallel and k' adjusted according to the length of time that the soil has locally been in contact with the cleaning solution. The flow of liquid in the falling film could also promote cleaning if the soil became sufficiently weak or soluble.

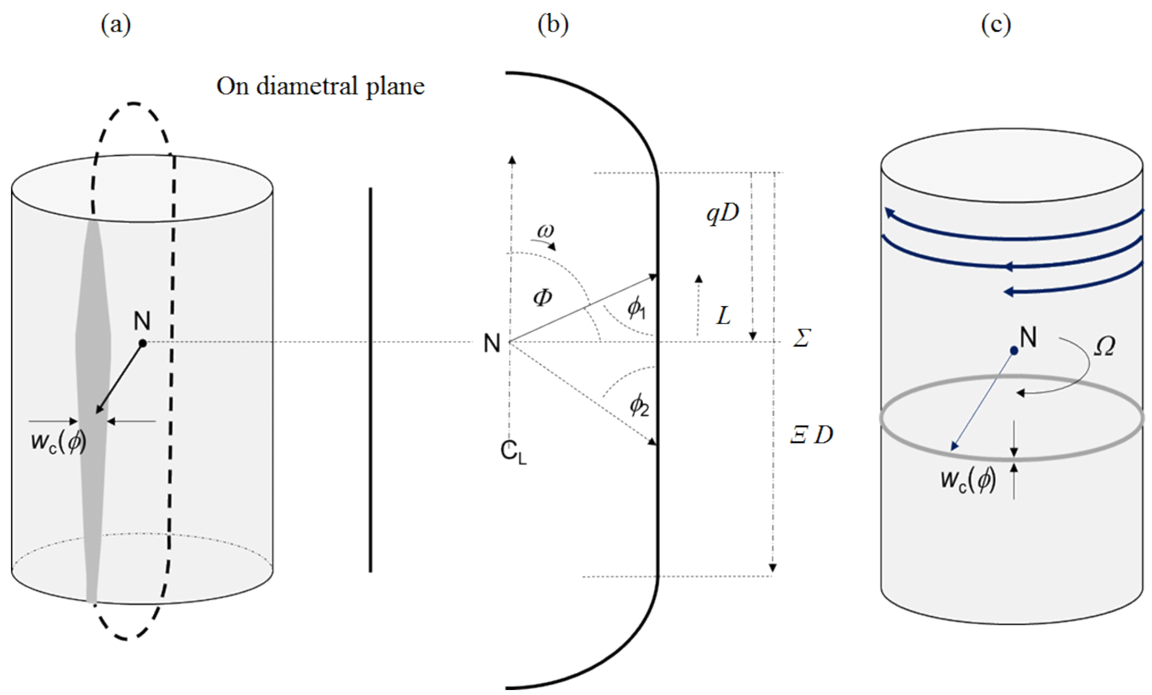
(a)
(b)
(c)
On diametral plane
N
$w_c(\phi)$
N
C_L
ω
Φ
ϕ_1
ϕ_2
qD
L
Σ
ΞD
N
Ω
$w_c(\phi)$

Figure 5.23 Schematic of vessel cleaning pathway (a) vertical strips; (b) geometry; (c) horizontal bands. Figure reproduced from Bhagat et al. (2017)

5.6.1 Performance indicators

Strips – vertical passes

In this case the point of impingement moves vertically up one wall and down the opposite wall, moving to the side by a small amount during each pass so that in the subsequent transit the cleared region touches that created by the previous transit at the point of narrowest width (see figure 5.23(a)). At other points the cleared regions overlap. The finding that the width of the cleared region depends on ϕ alone (for modest ϕ) means that the number of cycles is set by the angle subtended at the nozzle by the top and bottom of the wall, labelled ϕ_1,min and ϕ_2,min respectively, which are in turn determined by Ξ and q. This symmetry indicates that the range of values of q to consider is $0 \leq q \leq \Xi/2$, so that $\phi_{1,min} \leq \phi_{2,min}$. The construction in figure 5.23(b) gives

$$\phi_{2,min} = \arctan\left(\frac{1}{2(\Xi - q)}\right) \tag{5.58}$$

The number of complete cycles (up one side and down the other) required to clean the vessel wall, N, is given by

$$N = \frac{\pi D}{2W_{c,\phi_{2,min}}} \tag{5.59}$$

It is assumed that the ends of the vessel are cleaned by the repeated passes. For a given soil, nozzle design and flow rate, the distance $W_{c,\phi_{2,min}}$ is determined by the nozzle rotation, and three possible behaviours are considered, namely (i) constant nozzle angular velocity, ω; (ii) constant traverse speed on vessel wall, V; and (iii) variable speed, set to give a constant width of cleared region (see equation 5.45). For the purposes of comparison, it is convenient to use a common speed of jet transit at the nozzle plane, V_N, such that $\omega = \frac{2V_N}{D}$. The time to complete a cycle, t_{cycle}, is then

$$t_{cycle,\omega} = \frac{2\pi}{\omega} = \frac{\pi D}{V_N} \tag{5.60}$$

$$t_{cycle,V} = \frac{2\Xi D + \pi D}{V_N} = \frac{D}{V_N}(2\Xi + \pi) \tag{5.61}$$

Equation 5.61 is only valid for a hemisphere of diameter D. The cycle time for constant traverse speed is therefore longer, but figure 5.18 indicates that this programme gives a wider cleared region so fewer passes are needed for equal V_N. For case (iii), the speed over the hemispherical ends needs to be specified. This was set at the value reached at the top and bottom of the cylindrical wall where it joined the ends, giving (see Appendix B)

$$t_{cycle,W} = \frac{D}{V_N}\left\{\frac{\pi}{2}(\mathrm{cosec}\phi_{1,min} + \mathrm{cosec}\phi_{2,min}) + \frac{1}{4}\left[\ln(\mathrm{cosec}\Phi - \cot\Phi) - \cot\Phi\,\mathrm{cosec}\phi\right]_{\phi_{1,min}}^{\pi-\phi_{2,min}}\right\} \tag{5.62}$$

The three performance indicators can then be evaluated. Two schemes can be considered: one including cleaning of the hemispherical ends, using the results for t_{cycle} in equations 5.60-5.62, and a second for cleaning of the vertical wall alone, for comparison with the next scenario. The cycle times for each case are summarised in Table 5.2.

Cleaning time, t_F

This is the total time taken to remove all the material from the vertical walls, given by

$$t_F = N \times t_{cycle} \tag{5.63}$$

Volume of liquid used, Vol

This is the amount of liquid that is projected from the nozzle. In practice the liquid is likely to be recirculated, so this gives the maximum amount required, *e.g.* where all the liquid goes to drain

$$Vol = t_F \times Q \tag{5.64}$$

Table 5.2 Expressions for cycle time for cleaning a vertical cylindrical vessel by successive vertical passes

Scenario	Constant ω	Constant $V = V_N$	Constant cleaned width*
Parameter or Indicator			
Cycle time, complete cycle	$\frac{\pi D}{V_N}$	$\frac{D}{V_N}(2\Xi + \pi)$	$\frac{D}{V_N}\frac{\pi}{2}(\text{cosec}\phi_{1,min} + \text{cosec}\phi_{2,min})$ $+\frac{D}{4V_N}\left[\ln(\text{cosec}\Phi - \cot\Phi) - \cot\Phi\text{cosec}\phi\right]_{\phi_{1,min}}^{\pi-\phi_{2,min}}$ (Equation B.8)
Cycle time, vertical wall only	$\frac{D}{V_N}(\phi_{1,min} + \phi_{2,min})$	$\frac{D}{V_N}(2\Xi)$	$\frac{D}{4V_N}\left[\ln(\text{cosec}\Phi - \cot\Phi) - \cot\Phi\text{cosec}\phi\right]_{\phi_{1,min}}^{\pi-\phi_{2,min}}$ (Equation B.5)

*Cleaned width set at that obtained at $\phi = 0$, with $V = V_N$.

5.6.2 Hydraulic energy, E_P

The width of the cleared region is related to the flow rate of the jet, which requires pumping. If the discharge coefficient of the nozzle is C_D, and the combined efficiency of the pump and motor is η_p, the hydraulic energy expended in cleaning is given by (ignoring friction losses in piping and valves etc., which could be included via a multiplying factor)

$$\begin{aligned} E_P &= t_F \times Q \times \frac{1}{\eta_p} \times \Delta P \\ &= t_F \times Q \times \frac{1}{\eta_p} \times \frac{8Q^2\rho}{\pi^2 d_N^4 C_D^2} \\ &= t_F \times Q^3 \times \times \frac{8\rho}{\pi^2 d_N^4 C_D^2 \eta_p} \end{aligned} \tag{5.65}$$

The effect of jet flow rate differs between the performance indicators. Equation 5.44 indicates that $W_{c,\phi} \propto (\rho \times Q)^{3/4}$ for a given geometry and nozzle motion programme, so $t_F \propto (\rho \times Q)^{-3/4}$ and decreases noticeably with increasing mass flow rate. In contrast, Vol is weakly dependent on jet flow rate ($Vol \propto (\rho \times Q)^{1/4}$) while E_P increases strongly ($E_P \propto (\rho \times Q)^{9/4}$).

The effect of vessel geometry ($\Xi = 2, 3, 4$ and 5, $0.25 < q < \Xi/2$) and nozzle speed programme is compared in figure 5.24. The width of the cleared region at the nozzle plane is set at $D/20$ and $w(\phi)$ for the constant V and constant ω programmes is calculated using F_V and F_ω, respectively (noting that F_V and $F_\omega \neq 1$ at the nozzle plane). Time is in arbitrary units ($t.u.$) and the performance indicators are normalised with respect to the case, $\Xi = 2, q = 1, V_N =$constant $= 1D/t.u.$ and $\omega = 2t.u.$ In the plots the cleaning time is normalised by the smallest value of t_F. Dimensions are introduced in the Case Study.

For each speed programme the cleaning time is shortest with the nozzle is located at $q = \Xi/2$, i.e. the symmetrical case. The cleaning time increases with Ξ, resulting from the additional area to be cleaned and the effect of angle of impingement on the width of the cleaning region: for constant w_c operation, the velocity decreases noticeably further away from the nozzle plane. The Figure shows that the constant speed case gives consistently poor performance compared to constant ω (which is typical of those used in multi-axis cleaning devices) and constant w_c (which requires a more complex drive arrangement).

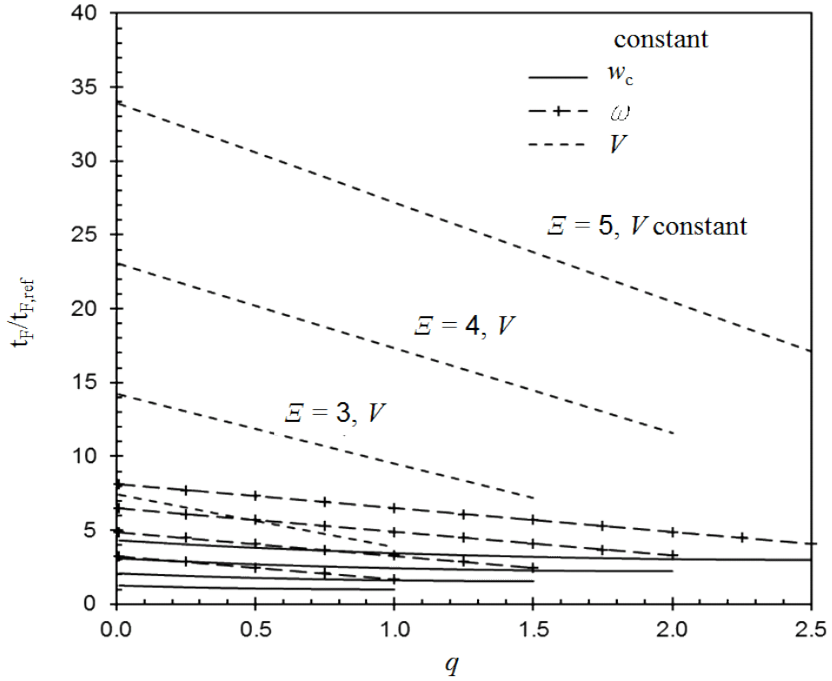

Figure 5.24 Cleaning by strips: effect of nozzle motion programme on time to clean a cylindrical vessel with hemispherical ends of diameter D and height ΞD with $\Xi = 2, 3, 4$ and 5; w_c at the nozzle plane $= D/20$. $t_{F,ref}$ is the shortest time in the set, obtained here with $L/D = 2$, $q = 1$ and constant w_c. Line pattern indicates motion programme. Each locus is plotted up to $q = \Xi/2$. Figure reproduced from Bhagat et al. (2017)

5.6.3 Bands: horizontal passes

The nozzle rotates in the azimuthal plane at constant angular velocity, ω (see figure 5.23(c)). Cleaning of the hemispherical ends is not considered here. Two scenarios are:

(i) Descending nozzle: in this idealised configuration, the nozzle descends (or ascends) after each rotation so that the jet always impinges at an angle of inclination of 90° and the circumferential traverse speed across the surface is constant, at $V_N = \frac{1}{2}\Omega D$. The width of the cleared region is constant, at $W_{c,90^\circ}$, and t_F is given by $\frac{2\pi}{\Omega} \times \frac{LD}{W_{c,90^\circ}} = \frac{\pi L D^2}{V_N W_{c,90^\circ}}$.

(ii) Nozzle in fixed position. After each rotation ϕ is adjusted so that the next band touches the previous band. The width of the band, $w_{c,\phi}$, is given by Equation 5.57. In this case the circumferential velocity is constant, at V_N. The first rotation, at $\phi = 90^\circ$, gives a band with height $l_1 = w_{c,90^\circ}/2$ above and below the nozzle plane. The angle of impingement corresponding to this height, ϕ_1, is given by

$\phi_1 = \arctan(D/2l_1)$, and is used to estimate the width of the next band and thence the height, *i.e.* $l_2 = l_1 + w_{c,\phi_1}$. A numerical root search would be required to identify ϕ_{i+1} for each band. The progress of cleaning for successive bands is presented in figure 5.25 for different values of initial band width. As the angle of jet impingement becomes more acute, the width of the cleared band increases, in contrast to the above case of stripes at constant angular velocity. Whereas the stripes case favours the nozzle being located at the centre of the vessel, this result suggests that the nozzle should be located towards the top of the vessel. There will, in practice, be limits to how far up the vessel the nozzle should be located: considerations of jet breakup and jet rebound have already been mentioned.

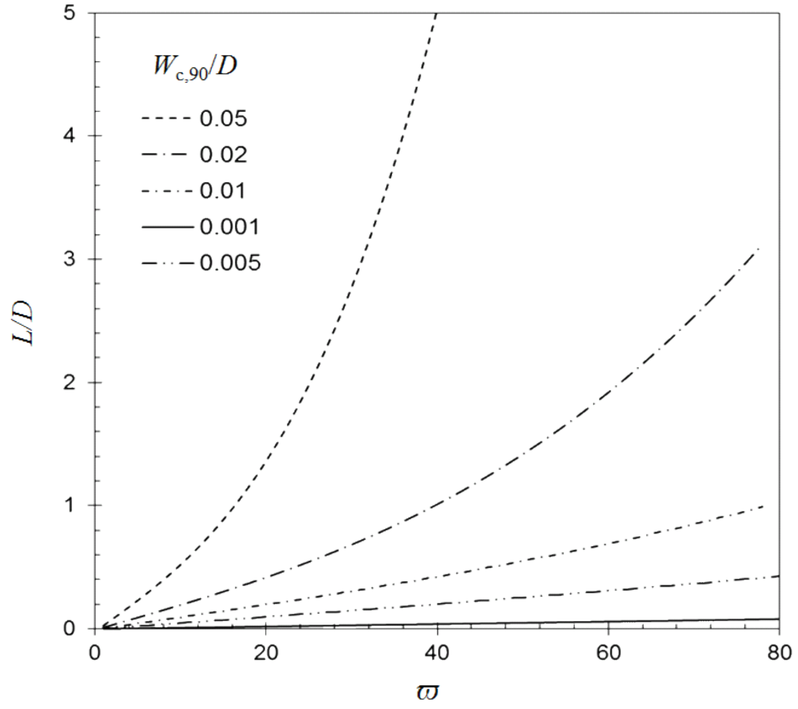

Figure 5.25 Cleaning by bands: effect of cleared width at nozzle plane. ϖ is the number of rotations (bands), starting with $\varpi = 1$ at the nozzle plane, and h is the height of the cleared region. Inset shows data presented in scaled form, $h/w_{c,90}$, with logarithmic scale on ordinate axis. Figure reproduced from Bhagat et al. (2017)

5.6.4 Case Study

The two modes of operation are now compared for an idealised case, namely a cylindrical vessel with diameter 2 m and a 2 m high vertical wall. Only the cleaning of the cylindrical sides is considered. A 2.66 mm diameter nozzle is located at the midpoint of the vessel, with flow characteristics taken from a commercial nozzle specification (*Lechler Catalogue* (2011)). The case study parameters are summarised in Table 5.3. Three flow rates were considered and the value of V_N was based on a nozzle rotation speed of $4\,\mathrm{min}^{-1}$.

Table 5.3 Case study parameters

Feature	Parameter	Value
Vessel geometry	Diameter, D	$2\,\mathrm{m}$
	Height, ΞD	$6\,\mathrm{m}$
	Nozzle location, qD	$3\,\mathrm{m}$
	ϕ_{min}	$18.4°$
	Volume (cylinder)	$18.3\,\mathrm{m}^3$
Nozzle	Diameter	$2.66\,\mathrm{mm}$
Flow rate	$\Delta P = 1$ barg	$4.45\,\mathrm{L\,min}^{-1}$
	$\Delta P = 2$ barg	$6.30\,\mathrm{L\,min}^{-1}$
	$\Delta P = 5$ barg	$9.96\,\mathrm{L\,min}^{-1}$
Angular velocity	ω	4 rpm
	Ω	4 rpm
Linear velocity at nozzle plane	V_N	$0.42\,\mathrm{m\,s}^{-1}$
Hydraulic efficiency	η_p	0.75
Cleaning rate constant	Temperature ($°C$)	k'
	20°	0.027
	30°	0.23
	40°	2.54
	50°	13.3

The value of k' is based on that obtained above for petroleum jelly. The effect of using higher temperature, which is one factor in Sinner's circle, was included by increasing k' by the factor reported by Wilson et al. (2014) for a different petroleum jelly. The thermal energy required to heat the water is added to the hydraulic pumping requirement, E_P, to give the total energy requirement, E_{total}. This allows the benefit generated by using hot water to be quantified. Capital costs of the heater are not considered.

Table 5.4 summarises the results for three stripes scenarios, with constant angular velocity (labelled ω), traverse speed (V) and cleared width (w_c) and two bands scenarios, namely one where the nozzle moves up and down while rotating at constant angular velocity (Ω), and one where the nozzle is located at the centre of the vessel (mid, where $q = \Xi/2$). The latter was used to allow comparison with the scenario. Results were also generated for the scenario where the nozzle was located at the top of the vessel, and gave cleaning times approximately 25% faster.

The results are sensitive to the value of L but general trends can be identified. Constant cleared width operation scenario gave consistently longer times and consequently poorest performance as measured by the other indicators. This result differs from that shown in figure 5.24 because the time taken to move across the top and base of the vessel is not considered in the case study calculations. The order of cleaning times is then $V > \Omega > \omega >$ mid: the latter two, which are simplest to achieve in practice, are similar. Increasing the temperature results in a noticeable reduction in cleaning time and consumption of liquid. The former results in a reduction in hydraulic energy and, for the parameters of this case study, the associated increase in thermal energy requirement does not alter this trend. Otherwise the use of higher pressure results in shorter cleaning times but higher liquid consumption. Comparing the extremes for the most attractive (mid) scenario, operating at $20°C$ and 1 bar achieves cleaning in 17.5 minutes and requires 79 L of liquid and of energy: the corresponding values for $60°C$ and 5 bar are 2.5 min, 25 L and 19 k. Cost factors need to be introduced to determine the financial benefit.

This case study demonstrates how the models developed in this chapter could be applied to assess the performance of different cleaning strategies, including the use of chemical agents to modify k'. Since k' can be identified from batch cleaning tests, the areas requiring further investigation are confirmation of the moving inclined jet models; determination of the effect of jet travel distance on jet trajectory, breakup, and cleaning performance (as well as the influence of jet rotation); and the impact of soaking on cleaning behaviour.

Table 5.4 Case study performance indicators

P(Bar)	T ($^\circ C$) Mode	t_F(min)					Vol(L)					E_p(kJ)					†E_{total}(kJ)				
	Constant	V	ω	w_c	Ω	‡mid	V	ω	w_c	Ω	mid	V	ω	w_c	Ω	mid	V	ω	w_c	Ω	mid
1	20	31.9	23.6	46.8	25.0	17.5	142	105	208	111	78	16.9	12.5	24.8	13.2	9.3	16.9	12.5	24.8	13.2	9.3
1	30	18.7	13.8	27.4	14.6	10.5	83	61	122	65	47	9.9	7.3	14.5	7.7	5.6	13.4	9.9	19.6	10.4	7.5
1	40	10.3	7.6	15.0	8.0	6.0	46	34	67	36	27	5.4	4.0	8.0	4.2	3.2	9.2	6.8	13.6	7.2	5.4
1	60	6.8	5.0	9.9	5.3	4.5	30	22	44	24	20	3.6	2.7	5.3	2.8	2.4	8.6	6.4	12.7	6.7	5.7
2	20	24.6	18.2	36.1	19.2	14.0	155	115	227	121	88	36.9	27.3	54	29	21	36.9	27.3	54	29	21.0
2	30	14.4	10.7	21.1	11.3	8.5	91	67	133	71	54	21.6	16.0	32	17	13	25.4	18.8	37	20	15.0
2	40	7.9	5.8	11.6	6.2	5.0	50	37	73	39	32	11.9	8.8	17	9.3	7.5	16.0	11.9	23	12.5	10.1
2	60	5.2	3.9	7.7	4.1	3.5	33	24	48	26	22	7.8	5.8	11	6.1	5.3	13.3	9.9	20	10.4	8.9
5	20	17.4	12.9	25.6	13.6	10.0	174	129	255	136	100	103	76.6	152	81	59	103	76.6	152	81	59
5	30	10.2	7.6	15.0	8.0	6.0	102	75	149	80	60	61	44.8	89	47	36	65	48.0	95	51	38
5	40	5.6	4.1	8.2	4.4	3.5	56	41	82	44	35	33	24.6	49	26	21	38	28.0	56	30	24
5	60	3.7	2.7	5.4	2.9	2.5	37	27	54	29	25	22	16.3	32	17	15	28	20.8	41	22	19

† $E_{total} = E_P + \rho Vol C_p (T/^\circ C - 20)$

‡ mid: $q = \Xi/2$, nozzle is located at the centre of the vessel

5.7 Conclusions

The main goal of the study presented in this chapter was to develop a mathematical framework for modelling industrial and domestic cleaning (Dish washer) operations. The problem can be subdivided into three overlapping sub-problems; (1) understanding the hydrodynamics of the flow field created by impinging liquid jets, (2) coupling the hydrodynamics and cleaning mechanisms to obtain cleaning models and, (3) integrating and modifying these cleaning models in the light of the dynamics arising from the motion of the nozzle.

Damkjær et al. (2017); Glover et al. (2016); Wilson et al. (2014, 2015) studied cleaning by the peeling mechanism by a static impinging liquid jet which suggests that the rate of cleaning is proportional to the liquid momentum at the cleaning front *i.e.* $\frac{da}{dt} = k'M$. Here, the term M couples the hydrodynamics and the cleaning mechanism *i.e.*, in this case peeling. In § 3 and § 4, it was established that the Wilson et al. (2012) description of flow field gives a reasonable engineering estimate of the momentum M and the main advantage of this model is its simple mathematical formulation. For the ease of analysis and to obtain an analytical solution, they approximated the flow model and it is found to be valid only at the peripheral regions of the RFZ.

However, it is identified that in the Wilson et al. (2012) flow model, the mathematical expression for momentum should be approximated by three sets of equation, suggesting three regions, namely; near field, far field and, intermediate region. Through a series of results presented in this chapter, it is shown that the Wilson et al. (2014) model for cleaning by peeling by an impinging liquid jet can be used to predict the extent of cleaning by jets created by stationary and moving nozzles. In a laboratory setup, the stationary jet experiments are easier to conduct and they provide vital insight to understand the cleaning mechanisms. For example, for cleaning by the peeling mechanism, stationary jet experiments provide the cleaning rate parameter k' which can subsequently be used for comparison and application with cleaning by moving jets. The near field and the far field region approximations for cleaning was confirmed using experimental data. The stationary jet cleaning model was extended, for the first time, to cleaning where the jet impinges at an angle off the perpendicular. The shape of the cleared region is no longer circular and the model predictions were in good agreement with new experimental data obtained with layers of petroleum jelly. It was shown that model can account for the variation in the azimuthal flow rate.

In cleaning-in-place-systems (CIP), the nozzle rotates about two axes which enables the liquid jet(s) to sweep across, creating different jet path pattern on the vessel surface. With appropriate geometric manipulation, the modelling approach presented in this chapter can be applied to assess the effectiveness and impact of CIP jet path trajectories in cleaning.

Wilson et al. (2015) gave solution for cleaning by peeling the mechanism for normal moving jets, for which they used the far field approximation for the flow field. The model is extended to other cases, namely the near field. In CIP applications, the moving jet impinges obliquely, with a continuously changing angle of impingement. For those cases, new solutions have been obtained. It is found that the angle of impingement and nozzle's direction of motion affects the shape and the total cleared area significantly.

A series of velocity programmes were investigated, and the impact on resources (time taken, liquid consumption, energy requirement) calculated. The most favourable programme was found to depend on the geometry of the vessel.

The case study indicates how the modelling approach could be used to design or develop cleaning-in-place programmes for specific soils. There are a number of aspects where further work is required in order to generate accurate results. Experimental data are required for an inclined jet with a moving impingement point, as well more information about the effect of jet breakup, splatter, and rebound. Extension of the model to spiral trajectories, reflecting those employed in practice, is also required.

Chapter 6

General conclusions and future work

6.1 Conclusions

The main aim of this work was to understand the flow fields created by impinging liquid jets and their use in cleaning applications, particularly CIP processes.

§ 2 deals with understanding of the hydrodynamics. For centuries, it was believed that the kitchen sink scale hydraulic jumps are created due to gravity. The experiments and the theory presented in § 2 overturned this gravity-based theory and ultimately provided a theoretical resolution to the question: what gives birth to a hydraulic jump? Experiments were conducted in which water jets were fired upwards and sideways onto flat surfaces, and witnessed exactly the same hydraulic jumps as those obtained when the jet flowed downwards. These experiments unequivocally disapproved the previous gravity-based theories since changing the orientation of surface changes the relative direction of gravity to the liquid flow. Despite these changes in orientation the shape and the size of the hydraulic jump remains approximately the same. A control volume analysis was conducted in which the total mechanical energy including surface tension was considered. Through this energy balance, it was found that the derivative of the radial velocity with respect to the radius becomes singular ($\frac{du}{dr} \rightarrow -\infty$) at a finite radial location. This implies that, at this location, the radial velocity changes rapidly and produces the hydraulic jump. The condition for the hydraulic jump, or the supercritical to subcritical transition was shown to be; $We^{-1} + Fr^{-2} = 1$.

For thin film cases, Fr does not play any significant role and the condition for hydraulic jump is $We \approx 1$. This also answered the question which has been debated for some time about that, why the hydraulic jump on a vertical wall or the departure radius, observed when a liquid jet hits a ceiling from the underside, are unaffected by the nature of the substrate. The primary conclusion from the study presented § 2 was that these thin-film hydraulic jumps result from energy loss due to surface tension and viscous forces alone. At the location of the hydraulic jump, surface tension and viscous forces balance the momentum in the liquid film and gravity plays no significant role. The findings reported here shed new light on thin film flows and the incorporation of surface tension into liquid flows which has often being puzzling. For example, Bush and Aristoff (2003) looked at the influence of surface tension on circular hydraulic jumps and concluded that, '*While the influence of surface tension is generally weak in terrestrial experiments, it becomes appreciable for jumps of small radius and height. Moreover, its influence will be heightened dramatically in a microgravity setting, or when internal jumps arise between immiscible fluids of comparable density.*' Since the theory presented by Bush and Aristoff (2003) was one of the most accepted views, this clearly shows a lack of fundamental understanding and a knowledge gap which the study presented in § 2 has overcome.

Previous treatments of the hydraulic jump had employed the solutions based on the Navier-Stokes equation, or a momentum balance obtained by integrating this equation. In § 3 a momentum balance was applied on the relevant control volume which showed an agreement with the energy based theory described in § 2. It was also found that the surface energy term, which had previously been ignored, dominates only in the peripheral region of the RFZ *i.e.* close to the hydraulic jump. Hence, despite the fundamental difference, in most of the RFZ the new theory and the previous theories (*e.g.* Wilson et al. (2012)) gives a similar value of momentum. Button et al. (2010) presented a model for the water bell departure radius (*i.e.* the case when water jet was fired upward onto a ceiling) was revisited. The analysis of Button et al.'s model which was based on Taylor's analysis was found to be flawed.

§ 4 considered with the case where the thin liquid film in the RFZ becomes turbulent. The thin film in the RFZ was divided into three regions, namely the boundary layer flow zone, the laminar zone, and the turbulent zone. Governing equations were written and solved for the boundary layer flow zone and the laminar zone. The condition for the laminar to turbulent transition was found to be the location where the liquid film thickness reaches a minimum. Beyond that point, the flow was modelled using a $1/7^{th}$ power law velocity profile.

Three different data sets for the laminar to turbulent transition, (1) direct optical observation, (2) enhanced heat transfer coefficient and (3) enhanced cleaning by dissolution mechanism were compared with the predictions and found to be in agreement. Measurements of the average velocity in the film were obtained using a new technique. It avoids the complications experienced using PIV where the influence of waves is significant (as reported by Aouad et al. (2016)). It is relatively robust, independent of liquid optical properties and can be readily applied to different wall materials, angles of inclination and flow rates. The experimental data for the average velocity were compared with predictions from the models presented in § 2 and § 4. The data showed good agreement with turbulent film model, and better agreement with the theory presented in § 2. Similarly, Stevens and Webb (1993) measured the liquid film thicknesses and these were compared with the model's prediction. The data and the prediction showed excellent agreement.

§ 5 reported a collaborative effort which developed a mathematical framework for modelling jet cleaning scenarios that arise in CIP operations. The problem was subdivided into three overlapping sub-problems; (1) understanding the hydrodynamics of impinging liquid jets,(2) coupling hydrodynamics and cleaning mechanisms to obtain cleaning models, and (3) integrating and modifying the cleaning model in the light of the dynamics arising from motion of the nozzle. The conclusion from § 3 was that the Wilson et al. (2012) flow model gives a reasonable engineering estimate of the momentum in the RFZ. Given its simplicity, it was used to describe the flow field. It was identified that in the Wilson et al. (2012) flow model, the mathematical expression for momentum can be approximated by three sets of equation, suggesting three regions, namely; near field, far field and, the full model or intermediate region. Similarly, the Wang et al. (2015) flow model was approximated for the near field case and it was coupled with the Wilson et al.'s cleaning model to obtain an expression for cleaning by obliquely impinging jets. The predictions from the modified model were then compared with the experimental data and showed good agreement. The jet cleaning (by peeling) model was used to predict performence of a moving jet operating under different translation paths. Considering two different CIP flow scenarios, models were developed for (1) when the nozzle moves in a vertical plane creating vertical cleaned stripes, and (2) when the nozzle rotates in a horizontal plane creating circular cleaned stripes. Using these models, a simple simulation for vessel cleaning and a case study was presented.

6.2 Future work

§ 2 provided a theoretical resolution to the question; '*What gives birth to a hydraulic jump?*'. However, several questions still remain to be answered.

In § 2 for the control volume analysis, Watson's similarity velocity profile was used to account for the distribution of the velocity in the z direction. Watson (1964) obtained this velocity profile ignoring surface tension and assuming zero shear stress at the liquid-air interface. However, the analysis presented in § 2.5.1 conclusively shows that this approach is not correct and the normal stress boundary condition must be applied at the interface. Particularly, in the peripheral region of the RFZ, the momentum M and the force due to surface tension are comparable; the similarity velocity profile cannot represent the true velocity profile. Therefore, to understand the evolution of the velocity profile, Navier-Stokes equations with the normal stress boundary condition should be solved. The velocity profile is important in the shear-driven cleaning as the shear stress imposed on the surface depends on the velocity profile. Similarly, the differential analysis presented in Appendix A should be modified and the contribution from surface tension should be incorporated directly using the boundary condition at the interface.

After the birth of a hydraulic jump on a finite plate, liquid continues to spread outwards and will eventually reach the edge of the plate. At this point, the boundary condition changes: the liquid film thickness downstream of the hydraulic jump increases and the hydraulic jump radius moves inwards. This phenomenon is currently unexplored and could be a fruitful area for further work to understand hydraulic jumps.

Hydraulic jumps are conventionally studied by applying a momentum balance at the jump location where hydrostatic pressure is balanced by the momentum of the fluid (Bush and Aristoff, 2003; Watson, 1964). In these studies, the height of the film downstream of the hydraulic jump was measured experimentally. The control volume analysis presented in § 2 yielded a condition for the formation of a hydraulic jump, in which the flow downstream of the hydraulic jump did not appear. A momentum balance across the hydraulic jump will yield the height of the film downstream of the hydraulic jump and this estimate could be compared with experiments.

The analysis presented in § 2 for the circular hydraulic jump can be extended to thin film planar hydraulic jumps, where predictions can again be compared to experimental measurements.

In § 4, although the empirical relationship demarcating the laminar to turbulent transition in the RFZ explains the experimental data, it is not rigorous. The empirical findings in this study provide a new understanding about this transition, nevertheless the precise mechanism for the transition remains unknown. In general, however, it appears to be related to the instability in the capillary waves (see figure 4.9). In light of the theory presented in this dissertation, stability analysis should be performed and the laminar to turbulent transition should be re-investigated. This is particularly important for cleaning applications as the current model yields a discontinuity in the wall shear stress which is puzzling.

The analysis presented in § 5 was for cleaning by the peeling mechanism. The hydraulic model can now be applied to study other cleaning mechanisms. The extension will require different approaches to those employed in § 5. For example, in case of cleaning by erosion mechanism where wall shear stress is the important parameter, it will not be possible to frame the rates in term of steady state condition at the leading edge of the cleaning front.

In § 5 one of the key assumptions was that the liquid jet remains coherent. In large industrial tanks, the liquid jets are often non-coherent and they impact the wall as a series of droplets. The rotation of the nozzles adds further complexities. Considerably more work will need to be done to establish the effect of jet breakup and the rotation of the nozzle on the hydrodynamics and cleaning performance of large scale jets.

Another aspect to consider is the soaking and swelling related phenomena which change the cleaning rate parameter k' and introduce temporal dynamics into cleaning studies. This complex behaviour can arise in many real systems, driven by cleaning solution and chemistry. In a computer controlled moving nozzle system with a camera attached to the nozzle, and by an *in situ* calibration, the cleaning rate parameter k' can constantly be fed to the system. The *in situ* calibration can be obtained by the following method; in case of cleaning by moving liquid jets, at the leading edge of the cleaning trail, the rate of cleaning equals the speed of the liquid jet, which implies $k'M(a_X) = V$. This expression provides a simple alternate way to obtain the cleaning rate parameter k'. Different nozzle speeds would yield different a_x values which then can be plotted as V *vs* $M(a_X)$ and the slope of this linear curve will yield k'. In a moving jet system, transverse nozzle velocity changes continuously and the image analysis from the camera mounted on the nozzle could provide the *in situ* calibration. This could be vital for the optimal cleaning of soils for which the cleaning rate parameters are time dependent and change due to soaking or other chemical or physical changes in the soil while the cleaning operation is underway.

CIP literature contains several studies where pulsed liquid flow have yielded enhance cleaning performance (*e.g.* Augustin et al. (2010), Fuchs et al. (2017)). The hydrodynamics and performance of pulsed liquid jets have not been studied in depth to date, and the current knowledge is largely emperical. This is an area of research and one where the findings of this work could provide a basis for a quantitative framework.

References

Ajiero, I. and Campbell, D. (2018), ‘Benchmarking water use in the uk food and drink sector: Case study of three water-intensive dairy products’, *Water Conservation Science and Engineering* **3**(1), 1–17.

Alex, B. (2016), ‘UK Dairy Industry Statistics’, *House of Commons Library, Briefing Paper* **2721**.

Ali, A., Alam, Z., Ward, G. and Wilson, D. I. (2015), ‘Using the scanning fluid dynamic gauging device to understand the cleaning of baked lard soiling layers’, *Journal of surfactants and detergents* **18**(6), 933–947.

Aouad, W., Landel, J., Dalziel, S. B., Davidson, J. and Wilson, D. I. (2016), ‘Particle image velocimetry and modelling of horizontal coherent liquid jets impinging on and draining down a vertical wall’, *Experimental Thermal and Fluid Science* **74**, 429–443.

Augustin, W., Fuchs, T., Föste, H., Schöler, M., Majschak, J.-P. and Scholl, S. (2010), ‘Pulsed flow for enhanced cleaning in food processing’, *Food and Bioproducts Processing* **88**(4), 384–391.

Avedisian, C. and Zhao, Z. (2000), The circular hydraulic jump in low gravity, *in* ‘Proc R Soc Lond A Math Phys Sci’, Vol. 456, The Royal Society, pp. 2127–2151.

Azuma, T. and Hoshino, T. (1984*a*), ‘The radial flow of a thin liquid film: 1st report, laminar-turbulent transition’, *Bulletin of JSME* **27**(234), 2739–2746.

Azuma, T. and Hoshino, T. (1984*b*), ‘The radial flow of a thin liquid film: 3rd report, velocity profile’, *Bulletin of JSME* **27**(234), 2755–2762.

Batchelor, G. K. (2000), *An introduction to fluid dynamics*, Cambridge university press.

Bhagat, R. K., Jha, N. K., Linden, P. F. and Wilson, D. I. (2018), ‘On the origin of the circular hydraulic jump in a thin liquid film’, *Journal of Fluid Mechanics* **851**, R5.

Bhagat, R., Perera, A. and Wilson, D. I. (2017), ‘Cleaning vessel walls by moving water jets: Simple models and supporting experiments’, *Food and Bioproducts Processing* **102**, 31–54.

Bhagat, R. and Wilson, D. I. (2016), 'Flow in the thin film created by a coherent turbulent water jet impinging on a vertical wall', *Chemical Engineering Science* **152**, 606–623.

Bidone, G. (1819), 'Le remou et sur la propagation des ondes', *Report to Académie Royale des Sciences de Turin, séance* **12**, 21–112.

Bohr, T., Dimon, P. and Putkaradze, V. (1993), 'Shallow-water approach to the circular hydraulic jump', *Journal of Fluid Mechanics* **254**, 635–648.

Burfoot, D. and Middleton, K. (2009), 'Effects of operating conditions of high pressure washing on the removal of biofilms from stainless steel surfaces', *Journal of food engineering* **90**(3), 350–357.

Bush, J. W. and Aristoff, J. M. (2003), 'The influence of surface tension on the circular hydraulic jump', *Journal of Fluid Mechanics* **489**, 229–238.

Button, E. (2005), *The dynamics of water bells, Honours thesis, Mathematics & Statistics,*, University of Melbourne.

Button, E. C., Davidson, J. F., Jameson, G. J. and Sader, J. E. (2010), 'Water bells formed on the underside of a horizontal plate. part 2. theory', *J. Fluid Mech.* **649**, 45–68.

Cambridge Water Company (2018), 'How much water do you use'.
URL: *http://www.cambridge-water.co.uk/customers/how-much-water-do-you-use, Accessed 06 October 2018*

Cousins, T. R., Goldstein, R. E., Jaworski, J. W. and Pesci, A. I. (2012), 'A ratchet trap for leidenfrost drops', *Journal of Fluid Mechanics* **696**, 215–227.

Damkjær, N. F., Adler-Nissen, J., Jensen, B. and Wilson, D. (2017), 'Flow pattern and cleaning performance of a stationary liquid jet operating at conditions relevant for industrial tank cleaning', *Food and Bioproducts Processing* **101**, 145–156.

Dou, H.-S. (2006), 'Mechanism of flow instability and transition to turbulence', *International Journal of Non-Linear Mechanics* **41**(4), 512–517.

Dou, H.-S. and Khoo, B. C. (2010), 'Criteria of turbulent transition in parallel flows', *Modern Physics Letters B* **24**(13), 1437–1440.

Drake, R., Vogl, A. W., Mitchell, A. W., Tibbitts, R. and Richardson, P. (2014), *Gray's Atlas of Anatomy E-Book*, Elsevier Health Sciences.

Eggers, J. and Villermaux, E. (2008), 'Physics of liquid jets', *Reports on progress in physics* **71**(3), 036601.

Environmental Technology Best Practice Programme (1998), 'Reducing the cost of cleaning in the food and drink industry, gg 154 guide'.
URL: *http://infohouse.p2ric.org/ref/23/22893.pdf, Accessed 06 October 2018*

Fryer, P. and Asteriadou, K. (2009), 'A prototype cleaning map: a classification of industrial cleaning processes', *Trends in Food Science & Technology* **20**(6-7), 255–262.

Fuchs, E., Helbig, M., Pfister, M. and Majschak, J.-P. (2017), 'Increasing the cleaning efficiency of the cleaning-in-place method by applying discontinuous liquid jets', *Chemie Ingenieur Technik* **89**(8), 1072–1082.

Glover, H., Brass, T., Bhagat, R., Davidson, J., Pratt, L. and Wilson, D. (2016), 'Cleaning of complex soil layers on vertical walls by fixed and moving impinging liquid jets', *Journal of Food Engineering* **178**, 95–109.

Godwin, R. P. (1993), 'The hydraulic jump ("shocks"and viscous flow in the kitchen sink)', *Am. J. Phys.* **61**(9), 829–832.

Gordeev, S., Groeschel, F. and Stieglitz, R. (2016), 'Numerical analysis of high-speed lithium jet flow under vacuum conditions', *Fusion Engineering and Design* **109**, 1669–1673.

Hager, W. H. (2013), *Energy dissipators and hydraulic jump*, Vol. 8, Springer Science & Business Media.

Hansen, S., Hørlück, S., Zauner, D., Dimon, P., Ellegaard, C. and Creagh, S. (1997), 'Geometric orbits of surface waves from a circular hydraulic jump', *Phys. Rev. E* **55**(6), 7048.

Hodgson, P. and Smith, M. (2014), *Flow patterns and cleaning behaviour of impinging liquid jets*, CET IIB Research Project Report, Department of Chemical Engineering and Biotechnology, University of Cambridge.

Hsu, T. T., Walker, T. W., Frank, C. W. and Fuller, G. G. (2011), 'Role of fluid elasticity on the dynamics of rinsing flow by an impinging jet', *Physics of Fluids* **23**(3), 033101.

Hurd, R., Hacking, K., Haymore, B., Truscott, T. et al. (2013), Urinal dynamics, *in* 'APS Division of Fluid Dynamics Meeting Abstracts'.

Irving, L. (2018), 'Leonardo's watery chaos'.
URL: *https://www.ias.edu/ideas/2018/lavin-leonardos-watery-chaos, Accessed 06 October 2018*

Jameson, G. J., Jenkins, C. E., Button, E. C. and Sader, J. E. (2010), 'Water bells formed on the underside of a horizontal plate. part 1. experimental investigation', *Journal of Fluid Mechanics* **649**, 19–43.

Jensen, B., Nielsen, J., Falster-Hansen, H. and Lindholm, K. (2011), 'Tank cleaning technology: innovative application to improve clean-in-place (cip)', *EHEDG Yearbook* **2012**, 26–30.

Joppa, M., Köhler, H., Kricke, S., Majschak, J., Fröhlich, J. and Rüdiger, F. (2018), 'Simulation der strahlreinigung: Diffusionsmodell für quellbare verschmutzungen'.
URL: *urn:nbn:de:bsz:14-qucosa-236389*

Kasimov, A. R. (2008), ‘A stationary circular hydraulic jump, the limits of its existence and its gasdynamic analogue’, *Journal of Fluid Mechanics* **601**, 189–198.

Kate, R., Das, P. and Chakraborty, S. (2007), ‘Hydraulic jumps due to oblique impingement of circular liquid jets on a flat horizontal surface’, *Journal of Fluid Mechanics* **573**, 247–263.

Kibar, A., Karabay, H., Yiğit, K. S., Ucar, I. O. and Erbil, H. Y. (2010), ‘Experimental investigation of inclined liquid water jet flow onto vertically located superhydrophobic surfaces’, *Experiments in fluids* **49**(5), 1135–1145.

Kline, S. J., Reynolds, W. C., Schraub, F. and Runstadler, P. (1967), ‘The structure of turbulent boundary layers’, *Journal of Fluid Mechanics* **30**(4), 741–773.

Köhler, H., Stoye, H., Mauermann, M., Weyrauch, T. and Majschak, J.-P. (2015), ‘How to assess cleaning? evaluating the cleaning performance of moving impinging jets’, *Food and Bioproducts Processing* **93**, 327–332.

Kurihara, M. (1946), ‘On hydraulic jumps’, *Proceedings of the Report of the Research Institute for Fluid Engineering, Kyusyu Imperial University* **3**(2), 11–33.

Lawson, R., Marshallsay, D., DiFiore, D., Rogerson, S., Meeus, S., Sanders, J. et al. (2018), ‘The long term potential for deep reductions in household water demand’.

Leach, S. and Walker, G. (1966), ‘The application of high speed liquid jets to cutting’, *Proc. R. Soc. London, Ser. A* **260**, 295–308.

Lechler Catalogue (2011).
URL: *www.lechler.de/is-bin/intershop.static/WFS/LechlerUK-Shop-Site/LechlerUK-Shop/en_GB/PDF_UK/General%20Industry/05_Vollstrahl_e_2011_solid%20stream%20nozzles.pdf., Accessed = 11 August, 2016*

Leu, M.-C., Meng, P., Geskin, E. and Tismeneskiy, L. (1998), ‘Mathematical modeling and experimental verification of stationary waterjet cleaning process’, *Journal of Manufacturing Science and Engineering* **120**(3), 571–579.

Lienhard, J. (1995), ‘Liquid jet impingement’, *Annual Review of Heat Transfer* **6**(6).

Lienhard, J. (2006), Heat transfer by impingement of circular free-surface liquid jets, *in* ‘Proceedings of 18th National and 7th ISHMT-ASME Heat and Mass Transfer Conference, Guwahati, India’.

Lin, C. (1945), ‘On the stability of two-dimensional parallel flows. ii. stability in an inviscid fluid’, *Quarterly of Applied Mathematics* **3**(3), 218–234.

Liu, X. and Lienhard, J. (1993), ‘The hydraulic jump in circular jet impingement and in other thin liquid films’, *Exp. Fluids* **15**(2), 108–116.

Liu, X., Lienhard, J. and Lombara, J. (1991), ‘Convective heat transfer by impingement of circular liquid jets’, *Journal of heat transfer* **113**(3), 571–582.

Lord Rayleigh, O. (1914), On the theory of long waves and bores, *in* ‘Proc. R. Soc. Lond. A’, Vol. 90, The Royal Society, pp. 324–328.

Mathur, M., DasGupta, R., Selvi, N., John, N. S., Kulkarni, G. and Govindarajan, R. (2007), 'Gravity-free hydraulic jumps and metal femtoliter cups', *Phys. Rev. Lett.* **98**(16), 164502.

Meng, P., Geskin, E., Leu, M.-C., Li, F. and Tismeneskiy, L. (1998), 'An analytical and experimental study of cleaning with moving waterjets', *Journal of manufacturing science and engineering* **120**(3), 580–589.

Morison, K. and Thorpe, R. (2002), 'Liquid distribution from cleaning-in-place sprayballs', *Food and bioproducts processing* **80**(4), 270–275.

Muller, M. (2018), 'Cape town's drought: don't blame climate change'.

Nusselt, W. (1916), 'Die oberflachenkondensation des wasserdampfes, vdi-zeitschrift 60: 542-575', *Google Scholar* .

Pedretti, C. (2000), *Leonardo Da Vinci: The Codex Leicester–notebook of a Genius*, Museum of Applied Arts & Sciences.

Pérez-Mohedano, R., Letzelter, N., Amador, C., VanderRoest, C. and Bakalis, S. (2015), 'Positron emission particle tracking (pept) for the analysis of water motion in a domestic dishwasher', *Chemical engineering journal* **259**, 724–736.

Rao, V. and Trass, O. (1964), 'Mass transfer from a flat surface to an impinging turbulent jet', *The Canadian Journal of Chemical Engineering* **42**(3), 95–99.

Rayleigh, L. (1892), 'On the instability of a cylinder of viscous liquid under capillary'.

Rojas, N., Argentina, M. and Tirapegui, E. (2013), 'A progressive correction to the circular hydraulic jump scaling', *Phys. Fluids* **25**(4), 042105.

Romney, A. (1990), *CIP: cleaning in place.. ed. 2*, Society of Dairy Technology.

Schlichting, H. et al. (1974), *Boundary-layer theory*, Springer.

Scholtz, M. and Trass, O. (1970), 'Mass transfer in a nonuniform impinging jet: Part i. stagnation flow-velocity and pressure distribution', *AIChE Journal* **16**(1), 82–90.

Stevens, J. and Webb, B. (1993), 'Measurements of flow structure in the radial layer of impinging free-surface liquid jets', *International journal of heat and mass transfer* **36**(15), 3751–3758.

Sun, N., Shi, L., Lu, F., Xie, S. and Zheng, L. (2014), 'Spontaneous vesicle phase formation by pseudogemini surfactants in aqueous solutions', *Soft Matter* **10**(30), 5463–5471.

Tamime, A. Y. (2009), *Cleaning-in-place: dairy, food and beverage operations*, Vol. 13, John Wiley & Sons.

Tani, I. (1949), 'Water jump in the boundary layer', *J. Phys. Soc. Jpn.* **4**(4-6), 212–215.

Taylor, G. I. (1959), 'The dynamics of thin sheets of fluid. iii. disintegration of fluid sheets', *Proc. R. Soc. Lond. A* **253**(1274), 313–321.

Vazquez, G., Alvarez, E. and Navaza, J. M. (1995), 'Surface tension of alcohol water+ water from 20 to 50. degree. c', *J. Chem. Eng. Data* **40**(3), 611–614.

Walker, T. W., Hsu, T. T., Frank, C. W. and Fuller, G. G. (2012), 'Role of shear-thinning on the dynamics of rinsing flow by an impinging jet', *Physics of Fluids* **24**(9), 093102.

Wang, T. (2014), *PhD dissertation,*, University of Cambridge.

Wang, T., Davidson, J. F. and Wilson, D. I. (2015), 'Flow patterns and cleaning behaviour of horizontal liquid jets impinging on angled walls', *Food and Bioproducts Processing* **93**, 333–342.

Wang, T., Davidson, J. and Wilson, D. (2013a), 'Effect of surfactant on flow patterns and draining films created by a static horizontal liquid jet impinging on a vertical surface at low flow rates', *Chemical Engineering Science* **88**, 79–94.

Wang, T., Faria, D., Stevens, L., Tan, J., Davidson, J. and Wilson, D. (2013b), 'Flow patterns and draining films created by horizontal and inclined coherent water jets impinging on vertical walls', *Chemical Engineering Science* **102**, 585–601.

Watson, E. (1964), 'The radial spread of a liquid jet over a horizontal plane', *Journal of Fluid Mechanics* **20**(3), 481–499.

Weber, C. (1948), *On the breakdown of a fluid jet.*

Wilson, D. (2005), 'Challenges in cleaning: recent developments and future prospects', *Heat Transfer Engineering* **26**(1), 51–59.

Wilson, D. I., Atkinson, P., Köhler, H., Mauermann, M., Stoye, H., Suddaby, K., Wang, T., Davidson, J. and Majschak, J.-P. (2014), 'Cleaning of soft-solid soil layers on vertical and horizontal surfaces by stationary coherent impinging liquid jets', *Chemical Engineering Science* **109**, 183–196.

Wilson, D. I., Köhler, H., Cai, L., Majschak, J.-P. and Davidson, J. (2015), 'Cleaning of a model food soil from horizontal plates by a moving vertical water jet', *Chemical Engineering Science* **123**, 450–459.

Wilson, D., Le, B., Dao, H., Lai, K., Morison, K. and Davidson, J. (2012), 'Surface flow and drainage films created by horizontal impinging liquid jets', *Chemical engineering science* **68**(1), 449–460.

Yeckel, A. and Middleman, S. (1987), 'Removal of a viscous film from a rigid plane surface by an impinging liquid jet', *Chemical Engineering Communications* **50**(1-6), 165–175.

Appendix A

Theory of Hydraulic jumps

A.1 Theory

We consider a cylindrical co-ordinates r and z, the radial and jet-axial coordinates, respectively, u and w the associated velocity components (figure 2.2), and assume circular symmetry about the jet axis. In the boundary layer approximation, the equations are governing steady flow in a thin film are

$$\frac{\partial(ru)}{\partial r} + \frac{\partial(rw)}{\partial z} = 0, \tag{A.1}$$

$$u(\frac{\partial u}{\partial r}) + w(\frac{\partial u}{\partial z}) = \nu\frac{\partial^2 u}{\partial z^2}. \tag{A.2}$$

The no slip boundary conditions at the substrate is

$$u = w = 0, \qquad at \quad z = 0, \tag{A.3}$$

For constant jet flow rate Q the radial velocity satisfies $2\pi r\int_0^h u\,dz = Q$. In order to analyse the jump we use the similarity velocity profile's *ansatz* developed by Watson (1964) for the velocity within the thin film which is derived assuming no shear stress at the free surface

$$\frac{\partial u}{\partial r} = 0, \qquad at \quad z = h. \tag{A.4}$$

This assumption ignores the shear stress at the free surface which arises due to the surface tension of the liquid and should formally be introduced through the normal stress boundary condition at the interface, which here is introduced by surface energy balance on the annular control volume (shown in figure A.1). Therefore, the radial velocity can be written as $u = u_s f(\eta)$, $\eta \equiv z/h(r)$ $(0 \leq \eta \leq 1)$, where η is the dimensionless thickness of the film and u_s is the velocity at the free surface. Using continuity we define the flux-average velocity $\bar{u} \equiv C_1 u_s$ by

$$\int_0^h urdz = u_s rh \int_0^h f(\eta)d\eta = C_1 u_s rh \equiv \bar{u}rh = \frac{Q}{2\pi} = \text{const.}, \tag{A.5}$$

where $C_1 = \int_0^h f(\eta)d\eta = 0.6137$ is a shape factor determined from the similarity solution.

Integrating equation A.1 from 0 to h and using 2.14 yields

$$w = u\frac{dh}{dr}\eta = u_s f(\eta)h'\eta \tag{A.6}$$

Writing A.1 in the form

$$\frac{1}{2}\rho(u^2 + w^2)\frac{\partial(ru)}{\partial r} + \frac{\partial(rw)}{\partial z} = 0 \tag{A.7}$$

using A.7 and the circular symmetry of the system allows the mechanical energy equation to be written as

$$\frac{\partial}{\partial r}(ur\frac{1}{2}\rho(u^2 + w^2)) + \frac{\partial}{\partial z}(wr\frac{1}{2}\rho(u^2 + w^2)) = -ur\frac{dp}{dr} - \rho gur\frac{dh}{dr} + ru\mu(\frac{\partial^2 u}{\partial z^2}) \tag{A.8}$$

The mechanical energy equation (A.8) does not have a surface energy term as the differential element of fluid does not include the free surface. However, on integration of (A.8) from $z = 0$ to the free surface $z = h$, we need to add the surface energy term. This is calculated as follows.

The rate of change of surface energy at a radial location r and in a differential volume $2\pi rh\Delta r$ is $2\pi\gamma r\frac{\Delta r}{\Delta t}$ and in the limit $\Delta r \to 0$

$$2\pi\gamma r\frac{\Delta r}{\Delta t} = 2\pi\gamma r\bar{u}. \tag{A.9}$$

Assuming circular symmetry around the jet axis, we can write the rate of change of surface energy per unit angle as $\gamma r\bar{u}$. In the limit $\Delta r \to 0$, a balance on the flux of surface energy across the annular control volume (figure A.1), yields

$$2\pi\gamma r\frac{\Delta r}{\Delta t} = 2\pi\gamma r\bar{u}. \tag{A.10}$$

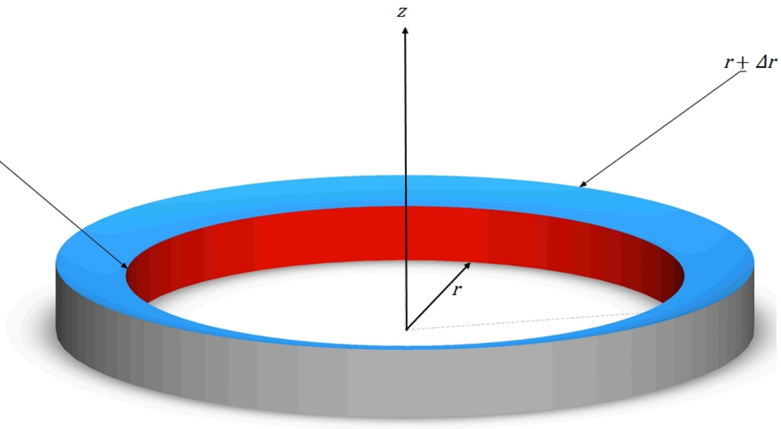

Figure A.1 Control volume of the differential annular volume of the liquid

Assuming circular symmetry around the jet axis, we can write the rate of change of surface energy per unit angle as $\gamma r \bar{u}$. In the limit $\Delta r \to 0$, a balance on the flux of surface energy across the annular control volume (figure A.1), yields

$$\lim_{\Delta r\to 0} \frac{(\gamma \bar{u} r)\Big|_{r+\Delta r} - (\gamma \bar{u} r)\Big|_{r}}{\Delta r} = \frac{d(\gamma \bar{u} r)}{dr}. \tag{A.11}$$

Substituting (A.6) in (A.8) and integrating the LHS of the equation w.r.t z and adding the surface energy term, yields

$$\int_0^h \frac{\partial}{\partial r}\left(\frac{\rho r u^3}{2}(1+(h'\eta)^2)dz\right) + \int_0^h \frac{\partial}{\partial z}\left(\frac{\rho r u^3}{2}h'\eta(1+(h'\eta)^2)dz\right), \tag{A.12}$$

$$\int_0^h \frac{\partial}{\partial r}\left(\frac{\rho r u^3}{2}(1+(h'\eta)^2)dz\right) + \frac{\rho r u_s^3}{2}h'\eta(1+h'^2). \tag{A.13}$$

Applying Leibniz's integral rule yields,

$$\frac{d}{dr}\int_0^h\left(\frac{\rho r u^3}{2}(1+(h'\eta)^2)\right)dz = \frac{d\left(\frac{\rho r h u^3}{2}\right)}{dr}\int_0^1 f^3(\eta)(1+(h'\eta)^2)d\eta. \tag{A.14}$$

Now using the fact that $u_s r h =$ constant, (A.14) can be written as

$$\frac{d}{dr}\int_0^h\left(\frac{\rho r u^3}{2}(1+(h'\eta)^2)\right)dz = \rho u_s^2 h r\frac{du_s}{dr}\int_0^1 f^3(\eta)(1+(h'\eta)^2)d\eta. \tag{A.15}$$

Similarly integrating the RHS of (A.8) w.r.t z and adding the surface energy term from (A.11) yields

$$-\int_0^h ur\frac{dp}{dr}dz - \int_0^h \rho gur\frac{dh}{dr}dz + \int_0^h ru\mu(\frac{\partial^2 u}{\partial z^2})dz + \frac{d(\gamma\bar{u}r)}{\partial r}. \tag{A.16}$$

Then, using relation $u_s rh =$ constant implies $u_s r\frac{dh}{dr} = -h\frac{d(u_s r)}{dr}$, yields

$$-u_s rh\frac{dp}{dr}\int_0^1 f(\eta)d\eta - \rho g h^2\left(r\frac{du_s}{dr}+u_s\right)\int_0^1 f(\eta)d\eta + \frac{\mu r u_s^2}{h}\int_0^1 f(\eta)f''(\eta)d\eta + \gamma\frac{d(\bar{u}r)}{dr}. \tag{A.17}$$

Finally putting together the LHS of (A.15) and the RHS of (A.17) and using the relation $\bar{u} = C_1 u_s$ gives

$$\frac{du_s}{dr} = \frac{-u_s rhC_1\frac{dp}{dr} + C_1\gamma u_s + C_1\rho g u_s h^2 - \frac{\mu r u_s^2}{h}\int_0^1 f(\eta)f''(\eta)d\eta}{(1-\frac{1}{We}-\frac{1}{Fr^2})\left(\rho u_s^2 hr\int_0^1 f^3(\eta)(1+(h'\eta)^2)d\eta\right)}. \tag{A.18}$$

Here, the Weber number and Froude number are defined as, respectively,

$$\begin{aligned} We &\equiv \frac{\rho u_s^2 h\int_0^1 f^3(\eta)(1+(h'\eta)^2)d\eta}{C_1\gamma}, \\ ,Fr &\equiv \sqrt{\frac{u_s^2\int_0^1 f^3(\eta)(1+(h'\eta)^2)d\eta}{C_1 gh}}. \end{aligned} \tag{A.19}$$

Equation (A.18) was solved with the initial condition obtained from Watson's analysis of the growth of the boundary layer (Watson, 1964). The boundary layer first occupies the whole film at r_{bl}, given by $\frac{r_{bl}}{d} = 0.1833\sqrt[3]{Re}$, where d is the nozzle diameter and the jet Reynolds number $Re = \frac{\rho U_o d}{\mu}$. At this location u_s is set equal to the mean jet velocity. Inside the jump radius h' remains very small therefore, to obtain an approximate solution upstream of the hydraulic jump, in (A.18) and (A.19), h' was set to zero. From Watson solution, we can calculate $\int_0^1 f(\eta)^3 d\eta = 0.4$ and $\int_0^1 f''(\eta)f(\eta)d\eta = 1.179$. Substituting the integrands in (A.18) and solving it with initial condition at $r = r_{bl}$, $u_s = U_o$ provides the subsequent radial values of the surface velocity. The location where $We^{-1} + Fr^{-2} = 1$, (A.18) becomes singular and there is a discontinuity in the film velocity and the liquid film thickness changes abruptly. Therefore, the condition for hydraulic jump is,

$$We^{-1} + Fr^{-2} = 1. \tag{A.20}$$

A.2 Results and discussion

Equation (A.20) shows that the hydraulic jump depends on the local We and Fr numbers. In § 2, it has been shown that in the case of thin-film hydraulic jump, Fr remains very high and the criterion is set by the Weber number. Subsequently, the surface tension and the viscosity of the test liquids was systematically changed and it was shown that the theory gives excellent agreement with the experimental data. Here, the theoretical prediction is compared with the experimental data for different surface orientations. Figure A.2 compares the theoretical prediction obtained by the solution of (A.18), whereas the dashed (blue) line represents the theoretical prediction obtained from the solution of equation 2.20. The two predictions overlap and show excellent agreement with the experimental data.

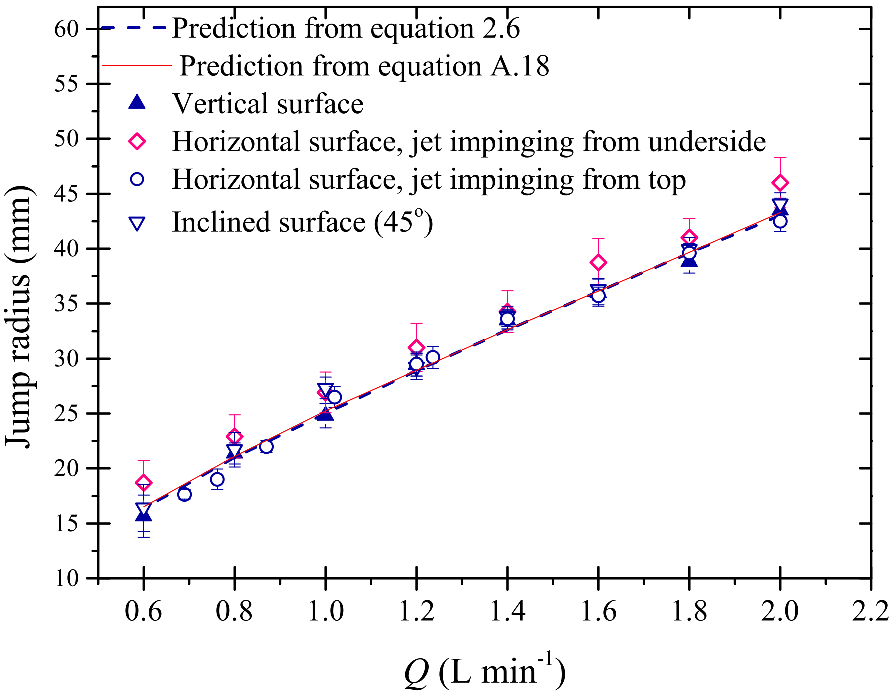

Figure A.2 Comparison of theoretical prediction obtained using solution of (A.18) (red line) with the experimental results presented in § 2. The dashed line shows the solution of 2.20.

A.3 Conclusions

The general theoretical treatment, including gravity and surface tension, presented here show that the condition at a circular hydraulic jump is $We^{-1} + Fr^{-2} = 1$. In case of thin films, gravity does not play any significant role and the hydraulic jumps are created due to surface tension alone and the effective condition for a thin film hydraulic jump is $We \approx 1$. This calculation agrees with the conclusions drawn in § 2 and with both the flux average control volume analysis presented in § 2 and the differential analysis presented in this paper are in agreement.

Appendix B

Cleaning scenario case study

Consider a nozzle moving clockwise, with Φ the angle from the vertical (Figure 5.23(b)), defined by

$$\tan\Phi = \frac{D}{2L} \tag{B.1}$$

The velocity at which the point of impingement moves up or down the surface is

$$V = -\frac{dL}{dt} = \frac{D}{2}\mathrm{cosec}^2\Phi\frac{d\Phi}{dt} \tag{B.2}$$

For constant cleared width, quation 5.44 suggests that $|V| \approx V_N \sin\phi$, where ϕ is the acute angle at the point of impingement. Above $N\Sigma$, $\Phi = \phi_1$ while below $N\Sigma$, $\pi - \Phi = \phi_2$. Equation B.2 becomes

$$\frac{D}{2}\mathrm{cosec}^2\Phi\frac{d\Phi}{dt} = V_N sin\Phi \tag{B.3}$$

Giving

$$\Delta t_{wall} = \frac{D}{2V_N}\int_{\phi_{1,min}}^{\pi-\phi_{2,min}} \mathrm{cosec}^3\Phi d\Phi \tag{B.4}$$

$$\Delta t_{wall} = \frac{D}{4V_N}\left[\ln(\mathrm{cosec}\Phi - \cot\Phi) - \cot\Phi\mathrm{cosec}\phi\right]_{\phi_{1,min}}^{\pi-\phi_{2,min}} \tag{B.5}$$

With

$$\tan\phi_{1,min} = \frac{1}{2q} \tag{B.6}$$

$$\tan\phi_{2,min} = \frac{1}{2(\Xi - q)} \tag{B.7}$$

The jet is assumed to move across the upper and lower hemispherical ends at speeds $V_N \sin\phi_{1,min}$ and $V_N \sin\phi_{2,min}$, respectively, giving the time for one cycle as

$$t_{cycle,W} = \frac{D}{V_N}\left\{\frac{\pi}{2}(\mathrm{cosec}\phi_{1,min} + \mathrm{cosec}\phi_{2,min}) + \frac{1}{4}\left[\ln(\mathrm{cosec}\Phi - \cot\Phi) - \cot\Phi\,\mathrm{cosec}\phi\right]_{\phi_{1,min}}^{\pi-\phi_{2,min}}\right\} \tag{B.8}$$

Appendix C

Cleaning vessel walls by moving jets: Simple models and supporting experiments

https://www.sciencedirect.com/science/article/pii/S0960308516301638